



Departament d'Enginyeria
Electrònica

UNIVERSITAT POLITÈCNICA DE CATALUNYA

DEVELOPMENT AND VALIDATION OF THE THERMAL DIAGNOSTICS INSTRUMENTATION IN LISA PATHFINDER

THESIS SUBMITTED IN FULFILLMENT OF THE
REQUIREMENTS FOR THE DEGREE OF DOCTOR

JOSEP SANJUÁN MUÑOZ

ADVISORS: JUAN RAMOS CASTRO
JOSÉ ALBERTO LOBO GUTIÉRREZ

Barcelona, May 2009

*El físico tiene que estudiar el lugar de la
misma manera que el infinito, a saber:
si es o no es, de qué modo es, y qué es.*

Aristóteles, *Física*, 208^a25-28

Contents

Agraïments	v
Acronym list	vii
1 Introduction	1
1.1 Gravitational waves	1
1.2 Ground-based GW detectors	3
1.2.1 Resonant mass detectors	3
1.2.2 Interferometric detectors	3
1.3 LISA mission overview	5
1.4 LISA Pathfinder mission overview	9
1.5 Diagnostics in the LTP	15
1.5.1 Thermal disturbances in the LTP	15
1.5.1.1 Noise effects inside the GRS	16
1.5.1.2 Noise effects inside the OMS	19
1.5.2 Temperature measurement subsystem sensitivity requirement	19
1.6 Structure of the thesis	20
2 The LTP temperature measurement subsystem	23
2.1 State of the art	23
2.2 Temperature sensors	24
2.2.1 Resistance temperature detectors (RTDs)	25
2.2.2 NTC thermistors	25
2.3 Signal processing chain	27
2.3.1 Principle of measurement	27
2.3.2 Analog signal processing	29
2.3.2.1 Wheatstone bridge circuit	29
2.3.2.2 Drive bridge circuit	33
2.3.2.3 Self-heating effect error considerations	34
2.3.2.4 Multiplexers, amplification and low-pass filter	35
2.3.2.5 Analog-to-digital conversion stage	39
2.3.3 Digital signal processing	39
2.3.4 Theoretical noise equivalent temperature	41
2.3.5 Temperature coefficient and uncertainty	42
2.3.6 Scales changing scheme	43
2.4 Thermal diagnostic items positioning and connections	44
2.4.1 Temperature sensors location	45
2.4.2 Heaters location	46
2.4.3 Summary of sensors and heaters location	47

3	Interactions with LTP subsystems	49
3.1	Thermistors magnetic polarisation	49
3.1.1	Force fluctuations in the TM due to magnetic field and magnetic field gradient	51
3.1.2	Magnetic field and magnetic field gradient in the TM due to NTCs. Measurement of the magnetic properties of the NTCs	53
3.1.3	NTCs magnetic characterisation	53
3.1.4	Numerical calculations	55
3.1.5	NTCs first magnetisation curve	57
3.1.6	Excess TM noise calculations	59
3.2	Interferences in the thermistors in the GRS	61
3.2.1	Analog signal processing chain	61
3.2.2	Signal demodulation process	63
3.2.3	Digital filtering and downsampling	66
3.2.4	Generalisation for any frequency	67
3.2.5	Experimental results	68
3.2.6	Permitted amplitudes of the interferences	69
3.2.6.1	Sine wave interferences	69
3.2.6.2	Electrical ground fluctuations	70
4	Test bed design for the TMS validation	73
4.1	Test bed for the LTP requirements	73
4.1.1	Insulator design: theoretical analysis	74
4.1.2	Insulator sizing	75
4.1.3	Heat leakage through thermistors' cables	77
4.2	Test bed for the LISA MBW	81
4.2.1	Solution: differential measurements	81
4.2.2	Test bed non-idealities	82
4.2.3	Temperature control design	86
4.2.3.1	Feedforward filter design	87
4.2.3.2	Feedback-feedforward control	91
5	TMS performance tests	93
5.1	Tests in the LTP measurement bandwidth	93
5.1.1	Prototype TMS test	93
5.1.2	Engineering model test	98
5.1.2.1	Excess noise due to non-ideal analog-to-digital conversion	103
5.1.2.2	Excess noise in the thermistors	105
5.1.3	Flight model test	107
5.2	Tests in the LISA MBW	108
6	Performance improvements of the TMS	111
6.1	ADC non-linear errors correction	111
6.1.1	Non-ideal quantisation noise	111
6.1.1.1	ADC bit error description	113
6.1.1.2	Dither signal effect in ideal quantisers	114
6.1.1.3	Dither signal effect on non-ideal quantisers	116
6.1.1.4	INL effect on general signals	118
6.1.2	Mitigation of ADC errors	120
6.1.2.1	Gaussian noise dither injection	120
6.1.2.2	Triangular wave dither injection	122
6.1.3	Test set up and results	124
6.1.3.1	Test set up	124

6.1.3.2	Test results	125
6.2	Floor noise reduction	127
6.2.1	Thermistor nominal resistance	128
6.2.2	Power increase in thermistors	129
7	Thermal experiments in the GRS	135
7.1	Estimation of errors on parameters: the Cramér-Rao bound	135
7.2	Purpose of the thermal experiments in the GRS	136
7.3	Thermal coupling within the LTP dynamics	138
7.3.1	Available hardware description	140
7.3.2	Signals definition	141
7.3.3	Parameters estimation	143
7.3.4	Estimation of α	143
7.3.5	Resolving radiation pressure and radiometer effect	145
7.4	Simulations	150
7.4.1	x -axis LTP dynamics	150
7.4.2	Implementation in Simulink	152
7.4.3	Thermal excitation and parameters estimation	154
8	Conclusion	161
A	Temperature coefficient and uncertainty analysis	165
A.1	Voltage level adaption	165
A.1.1	Voltage follower	165
A.1.2	Voltage divider	167
A.2	Drive bridge circuit	168
A.2.1	Resistors	168
A.2.2	Operational amplifiers	169
A.3	Wheatstone bridge	170
A.4	2-wire configuration	171
A.5	Multiplexers	172
A.6	Instrumentation amplifier	173
A.7	Low-pass filter	174
A.8	Analog-to-digital converter	176
A.9	Temperature sensor	177
A.10	TC and uncertainty of the measurement chain	177
B	Heaters in the GRS	179
B.1	Thermistor temperature increase due to the SHE	180
B.2	Second-order model for the thermistor response	185
C	Bit rate reduction	189
D	Spectral density function for the fluctuating force due to magnetic disturbances	193
E	Insulator construction	195
F	Heater transfer function	197
F.1	Frequency-domain analysis	197
F.2	Time-domain analysis	198

G	Transfer functions and noise sources of the x-axis LTP dynamics	201
G.1	Drag-free control and low-frequency suspension	201
G.2	Noise sources	202
G.3	Closed-loop transfer functions and noise apportioning	203
G.3.1	Drag-free control: o_1	204
G.3.2	Low-frequency suspension control: o_Δ	205
G.4	DF and LFS controls: implementation in discrete domain	206
G.5	Position to acceleration conversion	207

Gràcies també a la Isabel i la Delfi que des de la distància també m'han ajudat a poder quadrar els comptes. Finalment, un record pel Txepo, ara a Tarragona, amb qui vaig coincidir els primers anys a l'Institut i amb qui vaig compartir tants *pintxos* al Tritón.

Com no podria ser d'altra manera, haig d'agraïr profundament als meus pares tot el suport i facilitats que sempre m'han donat per seguir estudiant. Moltes gràcies al meu pare qui segurament fou, juntament amb el meu avi, els que incitaren en mi la curiositat pels *trastos* a la casa de Cardona. Molt més que gràcies a la meva mare, sempre tant preocupada per mi i pendent de tot allò que a mi se m'escapa. Gràcies també a la Virgina, al Juanma i al Gerard i als amics d'Olesa i de l'ETSEIB.

Finalment, el meu més sentit agraïment a la Laia, qui ha estat aguantant-me (a mi i al portàtil) durant tots aquests anys. Gràcies per tot el suport i confiança del món i per animar-me en el nou periple que ens espera plegats. Tot i que falten les paraules, gràcies per contribuir amb la teva alegria a que tot sempre fos més fàcil.

L'elaboració d'aquesta tesi ha estat finançada pel Ministerio de Educación y Ciencia mitjançant una beca de formació de personal d'investigació (FPI) associada als projectes "Contribución española al LTP a bordo de la misión LISA Pathfinder", ESP2004-01647 i ESP2007-61712.

Olesa de Montserrat,
Maig de 2009

Acronym list

ACE	Advanced composition explorer
ADC	Analog-to-digital converter
AWG	American wire gauge
CFRP	Carbone fiber reinforced plastic
CGS	Carlo Gavazzi space
CMRR	Common mode rejection ratio
CRB	Cramér-Rao bound
CTTC	Centre tecnològic de comunicacions de Catalunya
DAC	Digital-to-analog converter
DAU	Data acquisition system
DDS	Data and diagnostic subsystem
DF	Drag-free
DMU	Data management unit
DNL	Differential non-linearity
DPU	Data processing unit
EH	Electrode housing
EM	Engineering model
ESA	European space agency
FB	Feedback
FEE	Front-end electronics
FEEP	Field emission electric propulsion
FEM	Finite element method
FF	Feedforward
FM	Flight model
FMC	First magnetisation curve

FPGA	Field programmable gate array
FS	Full-scale
GRS	Gravity reference sensor
GW	Gravitational wave
HS	High-stability
IA	Instrumentation amplifier
IEEC	Institut d'estudis espacials de Catalunya
IIR	Infinite impulse response
INL	Integral non-linearity
LCA	LTP core assembly
LIGO	Laser interferometer gravitational-wave observatory
LISA	Laser interferometer space antenna
LPF	LISA pathfinder
LSB	Least significant bit
LTP	LISA technology package
MBW	Measurement bandwidth
MSB	Most significant bit
NASA	National aeronautics and space administration
NEBW	Noise equivalent bandwidth
NET	Noise equivalent temperature
NTC	Negative temperature coefficient
OA	Operational amplifier
OB	Optical bench
OBC	On-board computer
OMS	Optical metrology system
OW	Optical window
PDU	Power distribution unit
PSD	Power spectral density
RTD	Resistance temperature detector
SAR	Successive approximation register
SC	Spacecraft
SHE	Self-heating effect

SNR	Signal-to-noise ratio
SQUID	Superconducting quantum interference device
STFT	Short-time Fourier Transform
TC	Temperature coefficient
TDI	Time-delay interferometry
TM	Test mass
TMS	Temperature measurement subsystem
UPC	Universitat Politècnica de Catalunya
VE	Vacuum enclosure

Chapter 1

Introduction

This thesis focuses on a very specific issue: the measurement of temperature at the micro-Kelvin level in the frequency range of the milli-Hertz. Such measurements are required as a part of a space mission intended to put to test key technologies for a space borne gravitational wave detector. The technological mission is LISA Pathfinder (LPF), which is devoted to pave the way to the LISA (Laser Interferometer Space Antenna) mission. LISA is a space-based gravitational wave observatory with the primary scientific goal of detecting and observing gravitational waves (GWs) from astronomical sources in a frequency range of 0.1 mHz to 0.1 Hz. Observation of gravitational waves will be a new way to explore the Universe and it will convey new rich information about its structure and evolution. However, the detection of GWs at low frequency requires differential measurements of distances of pico-meters between two bodies separated by 5 million kilometres. In view of the very demanding requirements LISA must attain, a precursor mission, LISA Pathfinder, has been decided to be launched first.

The work presented in this thesis is devoted to the measurement of the thermal perturbations in the main subsystems of LISA Pathfinder. Such measurements, as the whole mission itself, will be useful as a debugging tool for LISA. Before entering into the details of the issues related to the measurement of temperature and its purpose on-board LISA Pathfinder, an introduction about the nature of the gravitational waves and the efforts made to detect them since the 1960s is required. In this chapter we give a brief description of the gravitational wave properties and an overview of the on-ground based detectors: resonant mass detectors and interferometric detectors. Later, an overview of LISA and LISA Pathfinder missions is presented. Finally, the thermal effects in critical subsystems of LISA Pathfinder are discussed and they are used to define the requirements of the temperature measurement subsystem.

1.1 Gravitational waves

In the Newtonian Gravitation theory, gravitational fields propagate instantly to remote places, no matter how distant from the source. This is of course untenable, as it would appear that gravity is not subject to the laws of causality every other interaction complies with. A consistent alternative to the Newtonian Gravitation theory is the Einstein's General Theory of Relativity where gravitational waves (GWs) describe the propagation of gravitational fields. GWs were predicted by Einstein in 1916 as a consequence of the General Theory of Relativity. They are originated in a source of gravitational field whose structure varies with time, for instance, when a mass distribution moves in an asymmetric way. In this case the gravitational field variation propagates away into the surrounding space at some finite speed and thus, a body at a certain distance will feel such variation after some finite time. Gravitational perturbations travel outwards as ripples of the

spacetime geometry and, therefore, they distort the spacetime geometry¹. The basic properties of GWs are: (i) travel through empty space at the speed of light, (ii) have two polarisations modes ('+' and '×') and (iii) are transverse to the propagation direction [93]. Consequently, the distance between freely falling bodies changes in the perpendicular direction of the passing GW in two different polarisations —see Figure 1.1— and this is exactly the key aspect to measure them. GWs were already inferred by Hulse and Taylor in 1978 [69, 136]. They measured the decrease of the rotation period of a binary pulsar (PSR 1913+16) discovered in 1974, and attributed the observed loss of energy of the system to gravitational radiation [137].

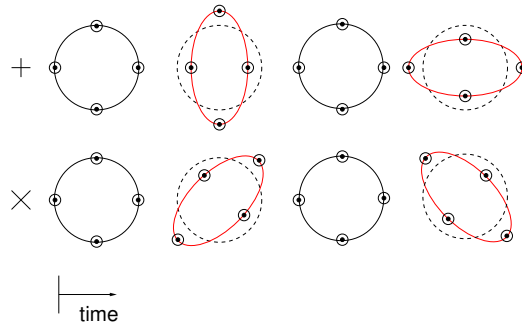


Figure 1.1: Freely falling macroscopic bodies (represented as black dots)—GW interaction. The GW direction is perpendicular to the plane of the circles. Both polarisation modes are shown ('+' and '×').

The main problem of measuring GWs is the exceedingly small relative change in the distance between freely floating bodies due to a passing GW where the current (or potential) detectors can be placed (on Earth or at some point in outer space close to the Earth). The amplitude of a GW is given by the strain, h , which is defined as ${}^{2\delta}L/L$ and represents the relative distance change between two test bodies separated by an initial distance L . For gravitationally bounded systems, an order of magnitude estimation of the strain, h , can be calculated as² [127]

$$h \sim \frac{\ell}{R} \left(\frac{GM}{\ell c^2} \right)^2 \quad (1.1)$$

where M is the mass of the source, R is the distance from the source, ℓ is the linear size of the source and $G = 6.67 \cdot 10^{-11} \text{ m}^3 \text{ kg}^{-1} \text{ s}^{-2}$ and $c = 3 \cdot 10^8 \text{ m s}^{-1}$ are the gravitational constant and the speed of light, respectively. For GW detectors on Earth the values for the strain, h , are $\sim 10^{-18}$ in the most favourable conditions³.

Like electromagnetic waves the GW spectrum covers a wide frequency range: from 10^{-16} Hz (quantum fluctuations in the very early Universe) to GWs radiating in the kilo-Hertz (and higher). The GW spectrum can be divided into four rather different bands [68]: (i) the *ultra low frequency* band (10^{-18} Hz to 10^{-13} Hz); (ii) the *very low frequency* band (10^{-9} Hz to 10^{-7} Hz); (iii) the *low frequency* band (10^{-5} Hz to 1 Hz); and (iv) the *high frequency* band (1 Hz to 10^4 Hz).

On the one hand, the detection of GWs in the *high frequency* band is covered by the on-ground detectors —see §1.2. The candidate sources to be detected by these instruments are rotating neutron stars (due to small ellipticities in their structure), massive objects like binary systems of neutron stars or black holes (specially, the last epoch of the inspiral process) and supernova explosions [68]. On the other hand, the *low frequency* band will be covered by the space-based GW detector: Laser Interferometer Space Antenna (LISA) —see §1.3— which has a list of guaranteed binary systems if

¹The geometry is, thus, determined by the distribution of mass and energy and it cannot be determined *a priori*.

²More specifically, it is proportional to the source's quadrupole moment acceleration, $\dot{Q}_{ij}(t)$.

³If we assume the free floating bodies are at a distance of $L=1$ km, the change in distance is of $5 \cdot 10^{-16}$ m.

the design sensitivity of the detector is achieved. These binary systems are known as the *verification binaries* [134]. Among the binary systems, the large amount of white dwarf binaries detectable by LISA produce a background confusion noise around the 5 mHz. LISA also will be able to detect GWs coming from several other sources such as super massive black holes (SMBHs) [15] and extreme mass ratio inspirals (EMRIs) [55].

1.2 Ground-based GW detectors

At present two different types of detectors have been used for the detection of GWs. They are resonant mass detectors and interferometric detectors [109] and both work in the *high frequency* band. The following sections describe how they work and their main properties.

1.2.1 Resonant mass detectors

Large efforts have been done since the early 1960s in the detection of GWs. J Weber [156, 157] initiated his work by means of resonant mass detectors. The development of such detectors has continued until today achieving sensitivities almost three orders of magnitude (in amplitude) higher than those exhibited by the first ones. Resonant mass detectors are solid bodies (cylinders or spheres) designed specifically to have a very high Q mechanical resonator [52, 46]. This resonance is excited by the passing GW —see Figure 1.2—, thus enabling detection.

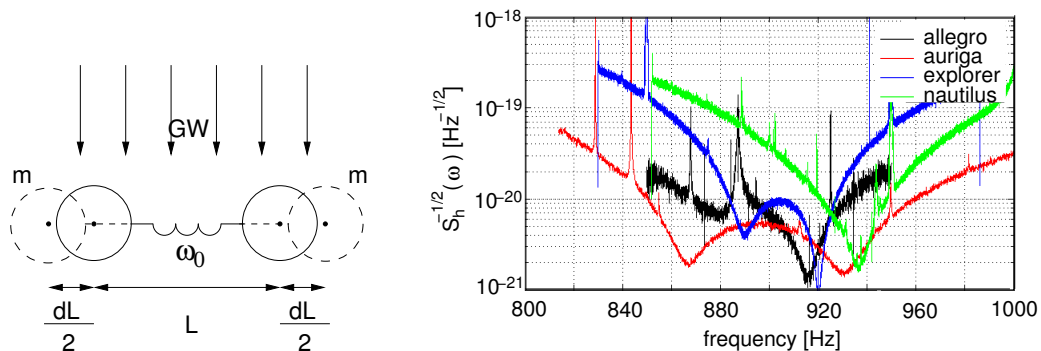


Figure 1.2: Left: resonant mass detector scheme. The gravitational wave Fourier component at a frequency ω_0 is amplified by the spring-masses system. Right: strain sensitivities of different resonant mass detectors [108].

Current resonant mass detectors⁴ reach very impressive strain sensitivities: $\sim 10^{-21} \text{ Hz}^{-1/2}$ ($\sim 10^{-21} \text{ m Hz}^{-1/2}$ in distance since they are around one meter long) at the kilo-Hertz frequency range with a bandwidth of tens of Hertz —see Figure 1.2.

1.2.2 Interferometric detectors

An alternative method to detect GWs rose in the early 1970s. This method was based on laser interferometry and, more specifically, in the classical Michelson interferometer. Roughly speaking, such detectors measure the phase differences between two laser beams reflected in two bodies caused by the motion of the bodies when passing a GW —see Figure 1.3 (left). The change of phase, $\delta\phi$,

⁴Allegro in USA [64], Auriga in Italy [162], Explorer in Switzerland [10], Nautilus in Italy [9], Niobe in Australia [17], MiniGRAIL in the Netherlands [36] and Mario Schenberg in Brazil [4].

in a Michelson interferometer of arm-length L due to a passing GW is [85]

$$\delta\phi = 2 \frac{\omega_{\text{laser}}}{\omega_{\text{GW}}} h_+ \sin \frac{\omega_{\text{GW}} \tau}{2}, \quad (\omega_{\text{GW}} \ll \omega_{\text{laser}}) \quad (1.2)$$

where ω_{laser} is the angular frequency of the laser light, ω_{GW} is the angular frequency of the GW, and τ is the round-trip time: $\tau = 2L/c$ with $c = 3 \cdot 10^8 \text{ m s}^{-1}$ the speed of light and L the arm-length of the interferometer. The optimum arm-length is $L = \pi c / \omega_{\text{GW}}$ and the transfer function of the antenna rolls off at frequencies above the inverse of the round-trip time τ ($= 2L/c$) — see Figure 1.6.

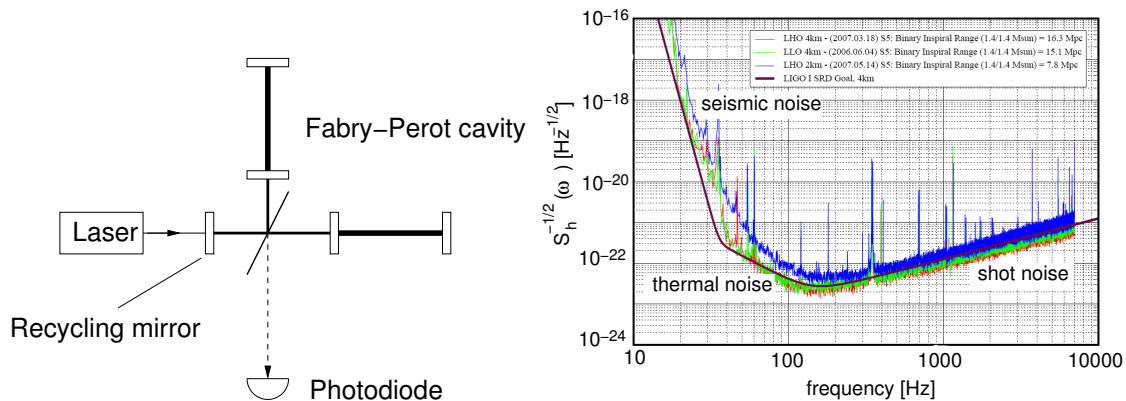


Figure 1.3: Left: schematic of a GW detector using Fabry-Perot cavities and power recycling. Right: sensitivity curves of the LIGO detector. The solid black trace is the design sensitivity [108].

However, the high sensitivity demanded to the interferometers complicates their design. The configurations adopted are the power-recycled Michelson interferometer with Fabry-Perot cavities in the arms [3, 1, 32], and the dual recycling technique [87, 91]. The use of these techniques increase the interaction time between the light and the GW and reduces the photon shot noise. The sensitivity of ground-based GW interferometric detectors is limited by different sources of noise (seismic noise, thermal noise, photoelectron shot noise, gravity gradient noise and quantum effects). These factors prevent the detection of GWs in the low frequency range, essentially, due to gravity gradient and seismic noise. At high frequency the shot noise dominates the measurement [88] — see Figure 1.3. The ground-based interferometric detectors are summarised in Table 1.1.

detector	arm-length	strain sensitivity
GEO600 [87]	0.6 km	$\simeq 7 \cdot 10^{-22} \text{ Hz}^{-1}$
LIGO Hanford [130]	2 km	$\simeq 4 \cdot 10^{-23} \text{ Hz}^{-1}$
LIGO Hanford [130]	4 km	$\simeq 2 \cdot 10^{-23} \text{ Hz}^{-1}$
LIGO Livingston [130]	4 km	$\simeq 2 \cdot 10^{-23} \text{ Hz}^{-1}$
TAMA300 [135]	0.3 km	$\simeq 3 \cdot 10^{-21} \text{ Hz}^{-1}$
VIRGO [2, 3]	3 km	$\simeq 5 \cdot 10^{-23} \text{ Hz}^{-1}$

Table 1.1: Ground-based interferometers sensitivities.

Second generation instruments for the LIGO detector are planned [138], which promise an order of magnitude increase in broadband strain sensitivity, i.e., $\sim 2 \cdot 10^{-24} \text{ Hz}^{-1/2}$. This means an increase in the probability of detecting GWs by a factor of 1000.

So far the high frequency band of the GW spectrum is covered by the ground-based detectors. On the contrary, the low frequency band remains still uncovered since ground-based detectors are

not able to work at frequencies below 1 Hz due to seismic noise. Hence, the logical solution to avoid such limitations is to place an interferometric GW detector in space, where the gravity noise is strongly reduced and the length of the arm can be orders of magnitude longer than in Earth. This detector is the so called Laser Interferometry Space Antenna (LISA) which has been designed to detect GWs with high signal-to-noise ratio in the milli-Hertz range. An overview of this mission and its precursor mission, LISA Pathfinder (LPF), are given in the next sections.

1.3 LISA mission overview

The primary objective of the LISA mission [14] is to detect GWs from massive black holes and galactic binaries⁵ in the low frequency range, i.e., from 0.1 mHz to 0.1 Hz. More specifically, the main purpose of the mission is to learn about the formation, growth, density and surroundings of massive black holes (from $10^6 M_\odot$ to $10^8 M_\odot$). Observations of these sources can provide unique new information about these objects, and would test General Relativity and black hole theory to unprecedented accuracy. Low frequency GW detection is not possible to interferometric ground-based detectors due to the local gravitational noise (moving objects, seismic movements, gravity gradient noise, meteorological phenomena, etc.) and due to the short interferometer arm-length (few kilometers). Nevertheless, a space-based detector is free from such noise sources and can have very long arm-length, hence, it should be able to work in the low frequency range, where the most certain and powerful GW sources radiate (large scale mass motions imply typically long time scales). Figure 1.4 shows the expected sensitivity for LISA and LIGO and the expected sources of gravitational waves at different frequencies.

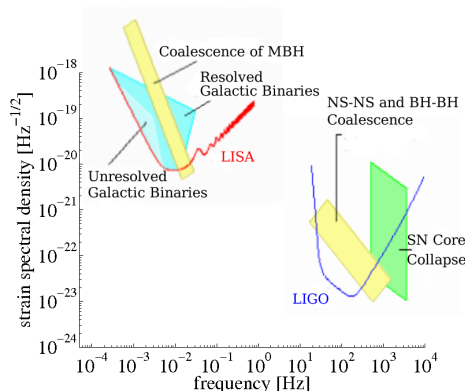


Figure 1.4: Strain sensitivities and gravitational wave sources for LISA and LIGO [14].

The LISA mission consists in three identical spacecraft separated by $5 \cdot 10^6$ km (in comparison, the longest arm-length of a ground-based detector is 4 km, the LIGO detector) forming an equilateral triangle. This triangular constellation turns around the Sun in an Earth-like orbit about 20° behind the Earth. The plane of this triangle needs to have an inclination of 60° with respect to the ecliptic to provide the most stable size of the triangle —see Figure 1.5 (left).

⁵Pairs of close white dwarfs, pairs of neutron stars, pairs of neutron star-black hole, etc.

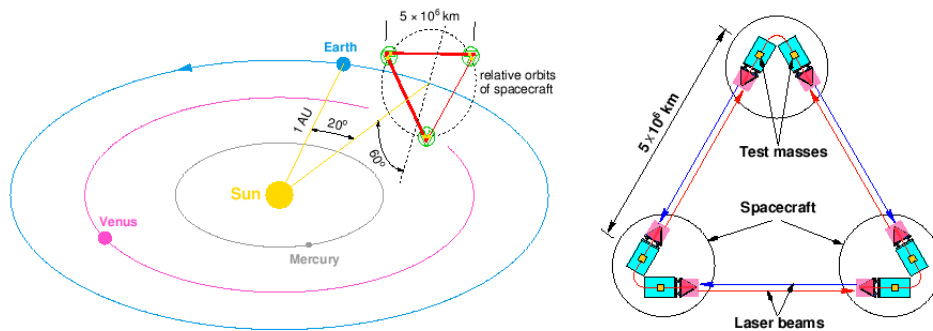


Figure 1.5: Left: orbit LISA configuration. Right: LISA's equilateral triangle configuration.

The distances between the vertexes of the equilateral triangle shown in Figure 1.5 are not constant since the LISA constellation is affected by the gravitational field of the Solar System. Actually, the arm-lengths and the angles of the triangle change $\sim 120\,000$ km (peak-to-peak) and $\sim 1^\circ$ per year, respectively. However, length and angle variations occur in time scales of months and LISA is interested in length variations in time scales of hours, hence, LISA can surely detect GWs in the submilli-Hertz frequency range, albeit the distance between spacecraft is not constant over long time scales.

LISA works, basically, as a giant Michelson interferometer with an extra arm added to give independent information on the GW polarisations and for redundancy. In LISA, the arm-length of the interferometer ($5 \cdot 10^6$ km) determines the frequency range in which observations can be made [the arm-length needs to be close to $\lambda_{\text{GW}}/2$ —see Eq. (1.2)] and it has been chosen to allow observations of most of interesting sources of gravitational radiation. In LISA each of the three spacecraft contains two optical assemblies. The two assemblies on one spacecraft are each pointing towards an identical assembly on each of the other two spacecraft to form a pseudo-Michelson interferometer —see Figure 1.5 (right). To achieve the desired sensitivity the interferometric system must keep the noise (shot noise, mainly) in measuring the differences in the round-trip path length between two arms below ~ 40 pm Hz $^{-1/2}$ (or an equivalent GW strain of $\sim 10^{-20}$ Hz $^{-1/2}$) in the milli-Hertz frequency range. Each spacecraft contains two vacuum enclosures housing a platinum-gold cube, 46 mm in size, in nominally perfect *free fall* (or geodesic motion), known as the test mass (TM), which serves as an optical reference or mirror for the light beams of the interferometer. A passing GW will change the length of the optical path between the test masses of one arm relative to the other arms.

The spacecraft is used to isolate the test masses from the *environment*, specially from the solar radiation pressure and solar wind, to maintain them in perfect geodesic motion or free fall. Consequently, the spacecraft will not be able to maintain its movement along the geodesic whereas the tests masses do. The spacecraft position, thus, does not directly translate into the GW signal, however, it is totally necessary to keep the spacecraft well centred on their respective test masses to reduce spurious local noise forces and, obviously, to avoid a spacecraft-test mass crash. To do this, the relative motion of the spacecraft with respect to the TMs can be measured precisely by means of a capacitive sensor that measures the change in the electrical capacitance between the TM and a set of electrodes surrounding it, fixed to the spacecraft. This measurement is then converted into a force-command which activates a set of micro-thrusters⁶ which exert forces on the spacecraft. This technique is known as *drag-free control* [77]. The required resolution of the capacitive sensors

⁶The needed force is micro-Newton. The used thrusters are field emission electric propulsion (FEEP) and they operate by accelerating ions in an electric field, and ejecting them to thrust.

is $\sim 10 \text{ nm Hz}^{-1/2}$ and the disturbing accelerations induced by the sensor back-action and by the parasitic forces on the test mass must be lower than $3 \text{ fm s}^{-2} \text{ Hz}^{-1/2}$ in the frequency range of 0.1 mHz to few milli-Hertz [14].

The sensitivity of LISA is determined by the response of the interferometer to a GW of strain h compared with the effects of various noise sources that fake the GW. A Michelson type interferometer measures the phase difference between the two beams after they have returned from the two arms of length L , i.e., $2L$ plus noise effects (δL_n). The transfer function of the antenna is⁷ —cf. Eq. (1.2) and see Figure 1.6—,

$$H(\omega_{\text{GW}}) = \text{sinc} \frac{\omega_{\text{GW}} \tau}{2} \quad (1.3)$$

where ω_{GW} is the frequency of the incoming GW and τ is the round-trip time for the light beam in each arm of the interferometer.

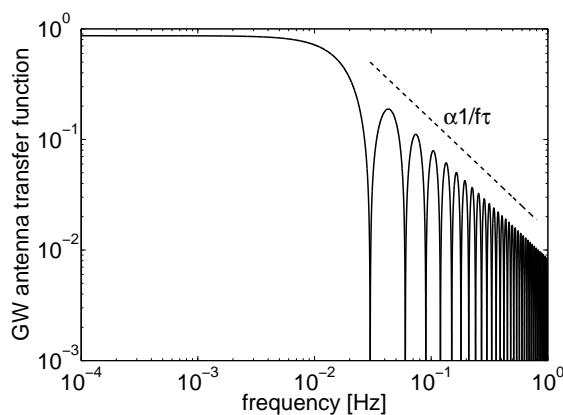


Figure 1.6: Magnitude of the LISA transfer function assuming $L = 5 \cdot 10^6$ km and a passing GW perpendicular to the LISA plane.

However, LISA interferometry is considerably different from the classical Michelson interferometer. In such interferometers a single light source is split and recombined after travelling similar pathlengths. Therefore, when they are combined and measured by the photodetector the noise is rejected since it is common to both laser beams. On the contrary, LISA uses six different light sources: one per test mass —see Figure 1.5 (right). The noise from the light sources is uncorrelated and the time for a photon to travel from one spacecraft to another is ~ 15 s. The uncorrelated noise of the lasers will dominate the measurement of the distance between the test masses, hampering the detection of GWs. However, it is possible to form combinations of different phasemeter outputs from different optical benches (there is one optical bench per test mass) with suitable time delays that cancel the laser phase noise and meet the requirements to detect GWs. This technique is known as time-delay interferometry (TDI) and requires accurate knowledge of the distance between the spacecraft and generation of time-delayed copies of the phasemeter signals [139, 31].

The sensitivity limiting noise effects in LISA can be summarised in [14, 33, 126]:

- *Shot noise* The effect is a spurious path difference δL_n inversely proportional to the square root of the received laser power. Due to the low level of light power received by the interferometer telescopes, the shot noise plays a major role in the total noise budget of spurious displacements. This noise defines the flat centre band of the LISA sensitivity curve,

⁷In the case of LISA, the two arms do not form a right angle, but one of 60° , thus, decreasing the response of the antenna. A factor $\sin 60^\circ = 0.866$ appears in the transfer function.

- *Antenna transfer function* The antenna response rolls off as $(f\tau)^{-1}$ at frequencies above the inverse of the round-trip time τ —see Eq. (1.3) and Figure 1.6. Thus, at these frequencies the sensitivity decreases proportionally to ω ,
- *Acceleration noise* At frequencies below 1 mHz the noise is dominated by the acceleration of the test mass that cannot be shielded by the drag-free control, i.e., internal forces due to phenomena related to temperature fluctuations, magnetic forces, charging of the test mass due to cosmic and solar radiation, microgravity effects, back actions related to the drag-free control, etc. Residual noise accelerations have a rather white spectral distribution, which results in position errors rolling off approximately as ω^{-2} , since

$$S_{\Delta x}^{1/2} = \frac{S_{\Delta F}^{1/2}}{m_{\text{TM}}\omega^2} \quad (1.4)$$

where m_{TM} is the mass of each test mass.

Considering these noise sources and the frequency dependence of the interferometer response, the LISA typical sensitivity curve is the one shown in Figure 1.7.

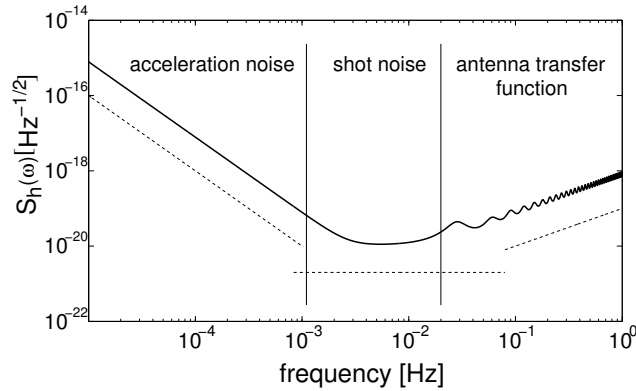


Figure 1.7: Sensitivity of LISA. Noise related to disturbances acting on the test masses such as temperature fluctuations are proportional to ω^{-2} . The shot noise defines the noise in the centre of the band. The high frequency noise is due to the antenna transfer function and increases proportionally to ω .

At this moment, the *permitted* noise in the low frequency range, < 2 mHz, must be defined. The noise at such frequencies is determined by the acceleration noise, leading to a decrease in sensitivity towards lower frequencies proportional to ω^{-2} . Above ~ 2 mHz the noise is dominated by the shot noise of the laser, whereby the decline of the antenna transfer function above 10 mHz causes a decrease in sensitivity proportional to ω .

Low frequency stray forces inside the spacecraft tend to move the test masses away from their geodesics and, therefore, they prevent to put them in *perfect* free fall. A residual noisy acceleration can be converted to *strain noise* as

$$S_{\Delta F}^{1/2}(\omega) \xrightarrow{\frac{1}{m}} S_{\Delta a}^{1/2}(\omega) \xrightarrow{\frac{1}{\omega^2}} S_{\Delta x}^{1/2}(\omega) \xrightarrow{\frac{2}{L}} S_h^{1/2}(\omega), \quad (1.5)$$

i.e.,

$$S_h^{1/2}(\omega) = \frac{2}{m_{\text{TM}}L} \frac{1}{\omega^2} S_{\Delta F}^{1/2}(\omega). \quad (1.6)$$

As the effect decays with ω^2 , above ~ 3 mHz the performance of LISA is expected to be set by the nearly shot noise limited displacement sensitivity of the laser interferometer of ~ 40 pm $\text{Hz}^{-1/2}$.

This is true only if stray forces have a power spectral density of

$$S_{\Delta a}^{1/2}(\omega) = \frac{S_{\Delta F}^{1/2}(\omega)}{m_{\text{TM}}} \leq 3 \cdot 10^{-15} \left[1 + \left(\frac{\omega/2\pi}{3 \text{ mHz}} \right)^2 \right] \text{ m s}^{-2} \text{ Hz}^{-1/2} \quad (1.7)$$

down to a frequency of 0.1 mHz. This residual noise is shown in Figure 1.8 and it determines the free fall accuracy level required.

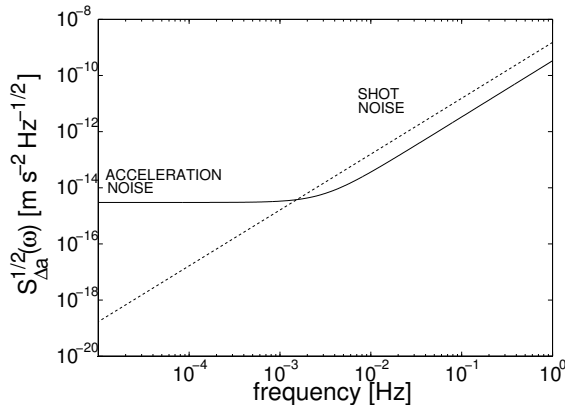


Figure 1.8: Power spectral density of the residual noise acceleration allowed for LISA to achieve the sensitivity curve shown in Figure 1.7. Shot noise stands for the noise in the relative position measurement of the interferometer (assumed to be flat and of $\sim 40 \text{ pm Hz}^{-1/2}$). From this figure we can infer the permitted noise levels (in terms of acceleration) due to thermal fluctuations, magnetic fields, etc. and that they become important at frequencies below the milli-Hertz.

Up to now the difficulties and the great challenges to detect GWs have been exposed. These difficulties arise from the fact that the interaction between GWs and the measuring apparatus is exceedingly small.

1.4 LISA Pathfinder mission overview

During the various studies for LISA, the need for a technological mission demonstration was recognised: the so-called LISA Pathfinder (LPF) mission. It includes the European Space Agency (ESA) science module LISA Technology Package (LTP) [145] plus parts of its National Aeronautics and Space Administration (NASA) counterpart, the Disturbance Reduction System (DRS) [47]. The main goal of LPF is to check if the residual acceleration in Eq. (1.7) can be achieved, i.e., it must verify the ability to set a test mass in purely gravitational free fall to the level required by Eq. (1.7), although in the LPF mission the requirements have been relaxed one order of magnitude both in amplitude and in frequency, i.e.,

$$S_a^{1/2}(\omega) = \frac{S_F^{1/2}(\omega)}{m_{\text{TM}}} \leq 3 \cdot 10^{-14} \left[1 + \left(\frac{\omega/2\pi}{3 \text{ mHz}} \right)^2 \right] \text{ m s}^{-2} \text{ Hz}^{-1/2}, \quad 1 \text{ mHz} \leq \omega/2\pi \leq 30 \text{ mHz} \quad (1.8)$$

The basic idea of the LTP is to squeeze one LISA arm from $5 \cdot 10^6 \text{ km}$ to 30 cm and place it aboard a single spacecraft —see Figure 1.9. This scheme, thus, prevents LPF from detecting GWs due to the short arm-length, 30 cm , and converts it into a test bench for the different technologies to be used in LISA⁸. The whole instrument is designed to contain the essence of the construction

⁸Specially, the two main concepts: the GRS (and drag-free and low-frequency control) and the interferometric system.

procedure needed for LISA and, thus, demonstrate its feasibility. This demonstration requires two steps [7, 5]:

- Based on a noise model, the mission is designed so that any differential residual acceleration noise of the test masses is kept below the requirements. This level of performance cannot be verified on the ground due to the impossibility of setting TMs in accurate free fall for long periods of time (in the order of hours).
- Once in orbit, the residual acceleration noise of the test masses is measured. The noise model predicts that the contributions to the total power spectral density fall into three broad categories:
 - Noise sources whose effect can be identified and suppressed by a proper adjustment of selected instrument parameters. For instance, the force due to residual coupling of test masses to the spacecraft.
 - Noise forces related to measurable fluctuations of some physical parameter. Typical examples are forces due to thermal gradients or to magnetic fields. The transfer functions between these fluctuations and the corresponding proof-mass acceleration fluctuations will be measured by enhancing the variation of the physical parameter under investigation and by measuring the induced acceleration in the TM. For instance, the LTP includes heaters to induce thermal gradients, and magnetic coils to apply large magnetic field signals. Moreover, the LTP also includes sensors to measure the fluctuation of the above physical disturbances [86]. A system identification problem needs to be solved for different subsystems of the LTP. After the system is well characterised and accurate transfer functions are estimated, one can generate an expected acceleration noise data stream to identify critical systems of the mission. Alternatively, the expected acceleration noise data stream can be subtracted from the main differential data stream. This way the contributions of these noise sources are suppressed and the residual acceleration power spectral density decreased.
 - Noise sources that cannot be removed by any of the above methods such as the charged particle flux due to cosmic rays and solar radiation. These noise source will be also measured in order to compare them with the predicted noise models.

The result of the above procedure is the validation of the noise model for LISA and, hopefully, the demonstration that no unforeseen sources of disturbance are present.

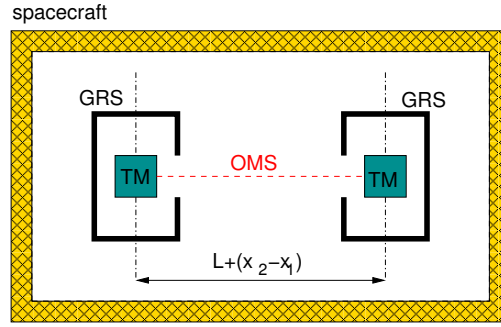


Figure 1.9: LTP scheme: two gravitational reference sensors (GRS) and a laser interferometer (OMS) mounted on an ultra-stable optical bench that measures the relative distance of one TM with respect to the other. The capacitive sensor measures the distance of one of the TMs with respect to the spacecraft (in the three axis) and sends the signals to the thrusters which correct the position of the spacecraft to maintain the TM centred. In the science mode, the other TM is forced to follow the other TM by means of the low frequency suspension control which applies forces to the TM by means of electrostatic forces generated by the GRS.

The basic scheme of the LTP is shown in Figure 1.9: two free-floating test masses (cubes made of gold-platinum of mass 1.96 kg and size 46 mm) separated by 376 mm are hosted within a single spacecraft. The relative motion along a common sensitive axis, the x -axis, is measured by means of a laser interferometer. The two test masses are surrounded by their position sensing electrodes which provides the information to the drag-free control that commands the micro-Newton thrusters to keep the spacecraft centred with respect to some point⁹. The residual acceleration of a single-mass/single-axis system is [145, 67] —see Figure 1.10,

$$a_n = \frac{f_{\text{str}}}{m_{\text{TM}}} + \omega_p^2 \left(x_n + \frac{F_{\text{ext}}}{M_{\text{SC}}\omega_{\text{DF}}^2} \right) \quad (1.9)$$

where

- f_{str} are the stray forces acting on the test mass due to phenomena such as temperature fluctuations, magnetic fields, etc.
- ω_p^2 ($\equiv k_p/m_{\text{TM}}$) is the parasitic springlike stiffness per unit mass that couples the test mass to the spacecraft due to the capacitive sensor itself,
- x_n is the capacitive sensor displacement noise,
- F_{ext} is the noise force acting on the spacecraft,
- and $M_{\text{SC}}\omega_{\text{DF}}^2$ is the drag-free feedback open-loop gain.

To ensure compliance with Eq. (1.8), it is then necessary to minimise the position independent stray forces, f_{str} , but also the contributions from the product of the parasitic coupling, ω_p^2 , with the residual relative motion coming from the sensor noise, x_n , and from the external forces on the spacecraft, F_{ext} .

⁹In the science mode the spacecraft is centred with respect to one of the test masses while the other test mass is forced to follow the former by means of the low frequency suspension [145].

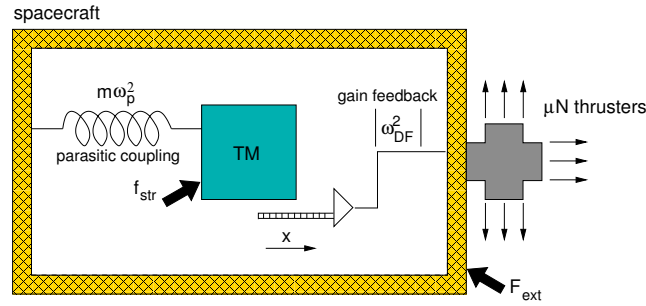


Figure 1.10: Single-mass/single-axis system. The TM/SC position is kept constant by means of the drag-free control. The measurement of the position between the TM and the SC is used to move the latter by means of the micro-Newton thrusters. The drag-free accuracy is determined by Eq. (1.9).

The basic elements of the LTP are [7, 5]:

- *Gravitational reference sensor* (GRS) [39, 67, 18, 23]. Each test mass is surrounded by a set of electrodes that read out the test mass position and orientation with respect to the spacecraft¹⁰. Measurements are obtained by measuring the change of the capacitance between the electrodes and the test mass. Each test mass is enclosed in a high vacuum chamber (10^{-5} Pa) —see Figure 1.13. The system formed by one proof mass and its electrode housing (capacitive sensor and actuator) inside the vacuum enclosure is the GRS itself. The sensitivity of the GRS for the x -axis is better than $1.8 \text{ nm Hz}^{-1/2}$ for displacement at 1 mHz and better than $200 \text{ nrad Hz}^{-1/2}$ for angular sensitivity at 1 mHz too. The measurement obtained by means of the GRS is used to centre the spacecraft on one of the test masses by applying electrostatic forces to the test masses (low-frequency suspension control or electrostatic suspension) and/or by commanding the micron-Newton thrusters (drag-free control) of the spacecraft —see Figures 1.9 and 1.10.
- *Optical Metrology System* (OMS) [61, 62, 112, 58]. In the LTP, the interferometer is a diagnostic tool for the GRS and, therefore, is a key system to verify the performance of the GRS by monitoring the distance between the TMs. The sensitivity required for the interferometric system is $\sim 10 \text{ pm Hz}^{-1/2}$ between 3 mHz and 30 mHz, relaxing as $1/f^2$ towards 1 mHz. The system designed to do this is a heterodyne Mach-Zehnder interferometer. The laser interferometer light passes through the vacuum chamber wall through an optical window (OW) to reach the TMs. The interferometer system is based on an optical bench (OB) which contains four separate interferometers —see Figure 1.11: (i) the $x_1 - x_2$ interferometer which provides the distance between the two TMs and their differential alignment. This measurement is the one needed to assess the performance of the GRS; (ii) the x_1 interferometer which provides the distance and alignment between one TM and the optical bench (fixed to the spacecraft); (iii) the *reference* interferometer. It provides the reference phase for the two previous measurements; and (iv) the *frequency* interferometer which measures the laser frequency fluctuations.
- *Data and diagnostics subsystem* (DDS) [86, 6, 83, 82]. The DDS consists of two main parts: the data management unit (DMU) and the diagnostic elements —see Figure 1.12. The DMU is the LTP computer and it is responsible for driving and control of the diagnostics items, and of the acquisition and on-board processing of phasemeter data. The DMU also interfaces with other systems, in particular with the on board computer (OBC), the main mission computer. The DMU has three main components, all of them duplicated as a resource against failure or

¹⁰In the six degrees of freedom: x, y, z and ϕ, θ, η .

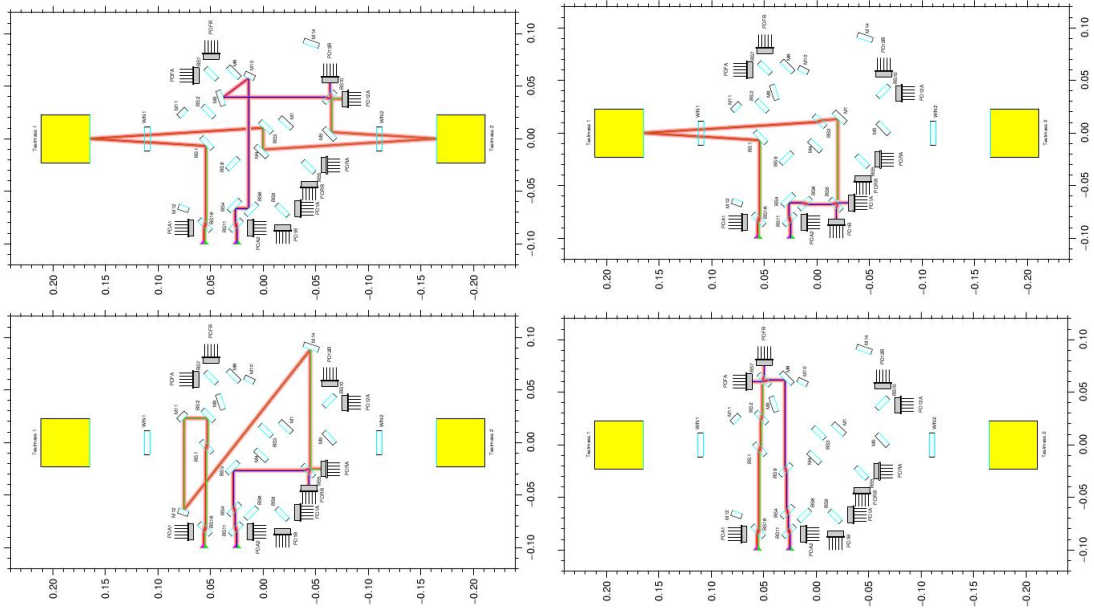


Figure 1.11: Top left: $x_1 - x_2$ interferometer. Top right: x_1 interferometer. Bottom left: *reference* interferometer. Bottom right: *frequency* interferometer.

malfunction. They are: (i) the power distribution unit (PDU), (ii) the data acquisition unit (DAU) [20] and (iii) the data processing unit (DPU). The other main part of the DDS is the *diagnostic elements*. These are number of sensors and actuators which are intended to monitor various disturbances happening inside the LTP and generate controlled disturbances. They are: (i) temperature sensors and heaters; (ii) magnetometers and coils; and (iii) radiation monitor.

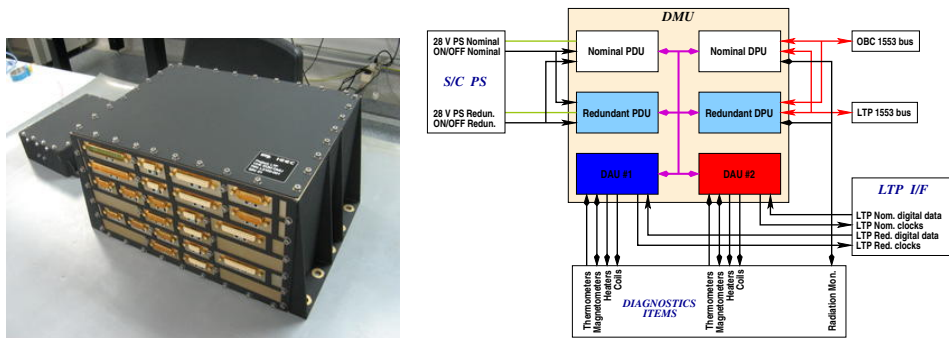


Figure 1.12: Left: flight model of the DMU. Right: DMU electrical interface global structure.

Figure 1.13 shows a general view of the LTP and its main subsystems. The core of the mission is the LTP core assembly (LCA) which is formed by two parts: the GRS and the OB between them. The LCA is fixed to the satellite structure by means of struts of carbon fiber reinforced plastic (CFRP) and is surrounded by a thermal shield which guarantees a thermal stability of $10^{-4} \text{ KHz}^{-1/2}$ in the MBW and the temperature to be between 10°C and 30°C [145].

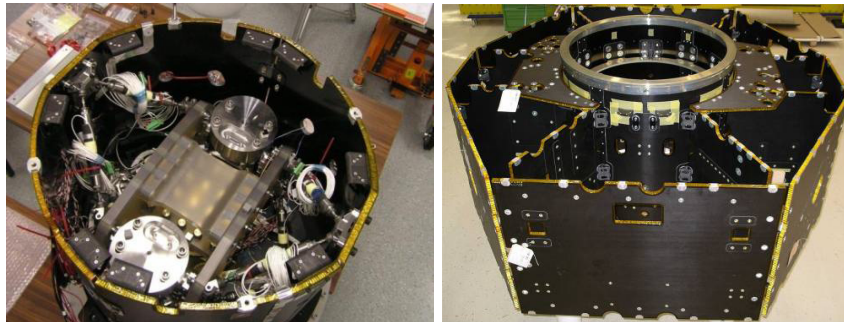
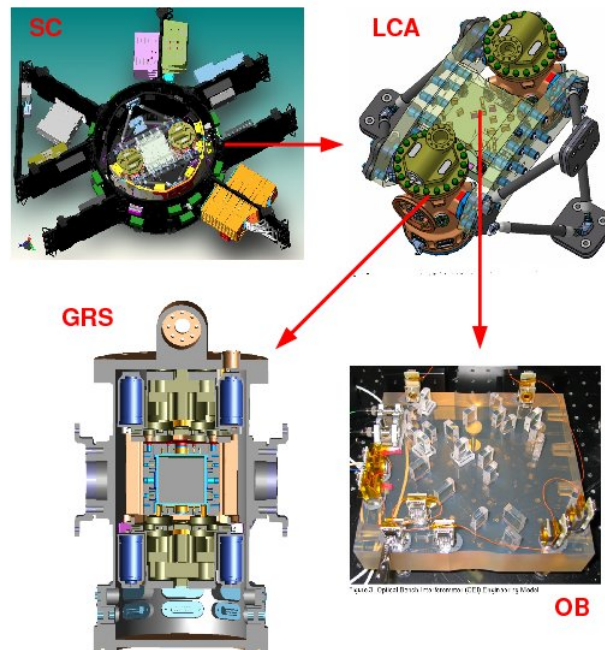


Figure 1.13: The “SC” picture represents the spacecraft which contains the LCA and all the electronics (boxes of different colours). The “LCA” picture is the LTP core assembly which is the payload of the mission. It is placed inside the thermal shield which should maintain the temperature fluctuations at $10^{-4} \text{ KHz}^{-1/2}$ in the MBW and the absolute temperature between 10°C and 30°C . The LCA main subsystems are the OMS and the GRS. The former includes the optical bench (OB) of the interferometric system which measures the distance between the TMs and between one of the TMs and the spacecraft. The GRSs are the two cylinders at the extremes of the optical bench. Each of them contains a TM surrounded by an EH that incorporates a capacitive sensor and electrical actuators. The influence of the temperature in these subsystems (OMS and GRS) can degrade their performance. For this reason, the thermal diagnostic subsystem is necessary: on the one hand, to measure the temperature fluctuations in the subsystems and, on the other hand, to estimate the actual coupling between temperature and the systems performance by proper thermal excitations. The photos in the bottom are the LCA with the payload and a general view of the SC.

The LTP will fly on LISA Pathfinder and it will operate in a Lissajous orbit around the Lagrange point L1 of the Sun-Earth system, an environment similar to that where the LISA constellation will operate.

In summary, LISA Pathfinder will demonstrate the possibility of building an inertial frame in a spacecraft orbiting the Sun on a scale of a metre in space and of a few hours in time at the level of residual acceleration of Eq. (1.8). As exposed previously, LISA's drag-free system cannot be tested on Earth for long periods of time due to *gravity noise*. Figure 1.14 shows the required drag-free for LPF and LISA. With this in mind, and in order to reduce the risks of a direct launch of LISA, ESA has decided to first launch a precursor mission demonstration to put all the LISA technologies to test.

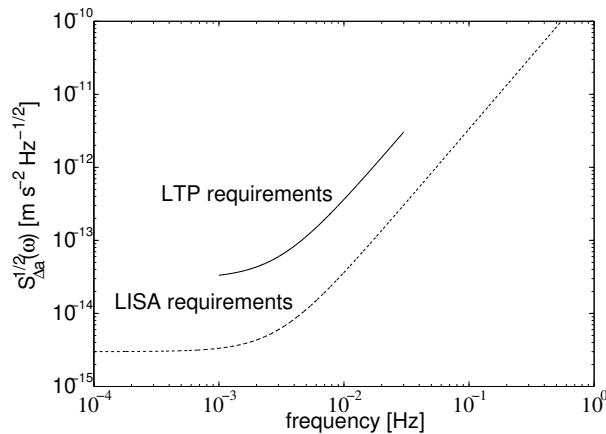


Figure 1.14: LTP and LISA residual noise acceleration requirements.

The following sections review on the diagnostics in the LTP and, specially, on the thermal diagnostics, which are the leitmotif of this thesis. The need for this system is justified altogether with the derivation of its requirements.

1.5 Diagnostics in the LTP

Different disturbances have been identified which need to be diagnosed in the LTP. The ones that will be monitored by the DDS are: temperature fluctuations, magnetic fluctuations and incident fluxes of charged particles [6, 145]. A quantitative assessment of the actual contribution of each of these items to the system noise requires knowledge of the transfer functions relating the disturbance and the effect on the displacement of the test masses. Such transfer functions will be determined on the basis of in-flight experiments, which will consist in measuring (by means of thermometers and magnetometers) the effect of induced perturbations (by means of heaters and coils) on the system response.

Once the transfer functions are determined, we project the different noisy sources to the total measured acceleration noise in nominal conditions, i.e., in absence of induced perturbations. This will permit to identify critical systems and/or unforeseen effects in the systems. In the following sections we focus on the aspects related to the thermal effects in the LTP which set the requirements of the thermal diagnostic subsystem.

1.5.1 Thermal disturbances in the LTP

Equation (1.8) gives the total noise budget permitted for residual acceleration in the LTP. This total noise is made up of contributions from different perturbing physical phenomena, both of in-

strumental and environmental origin. One of these perturbing elements is *temperature fluctuations*, for which a stability requirement for the LTP experiment has been set to [86, 145, 84]

$$S_T^{1/2}(\omega) \leq 10^{-4} \text{ K Hz}^{-1/2}, \quad 1 \text{ mHz} \leq \omega/2\pi \leq 30 \text{ mHz} \quad (1.10)$$

in the absolute temperature range of 10°C to 30°C.

Because temperature stability is important, high precision temperature thermometers will be placed in different strategic points over the LTP. Such measurements will be useful to identify the fraction of the total system noise which is due to temperature fluctuations only, and this will in turn provide important debugging information to assess the performance of the LTP. In addition, by applying controlled temperature signals and measuring their effect on the system read out, the transfer function between temperature fluctuations and displacement (real or faked¹¹) in the test masses will be estimated. In this manner we want to assess whether or not the modeling of the thermal effects in the subsystems of the LTP are accurate.

In the following the temperature stability requirement expressed in Eq. (1.10) is analysed. The sources of temperature fluctuations that contribute to the total noise budget of Eq. (1.8) are identified and quantified. Afterwards we discuss how the temperature stability requirement results in the definition of the temperature measurement subsystem performance.

Random temperature fluctuations in the LTP introduce noise in the system through different mechanisms. Proper characterisation of these effects will set the limits of temperature fluctuations compatible with the LTP requirements. As a rule of thumb, the total contribution of temperature fluctuation noise to the total acceleration noise —Eq. (1.8)— should not exceed 10%. Thus, it is required that

$$S_{a,T}^{1/2}(\omega) \leq 3 \cdot 10^{-15} \left[1 + \left(\frac{\omega/2\pi}{3 \text{ mHz}} \right)^2 \right] \text{ m s}^{-2} \text{ Hz}^{-1/2} \quad (1.11)$$

within the LTP MBW. This assumption is in fact somewhat conservative, as it has been estimated that more than twice this value is actually compliant with the overall LTP noise budget [155]. However, here Eq. (1.11) is adopted as reference to ensure that we are on the safe side.

The influence of the temperature in the whole LTP experiment has been separated into two subsystems: the GRS and the OMS.

1.5.1.1 Noise effects inside the GRS

Temperature differences between the walls of the electrode housing inside the GRS cause differential pressures on opposite faces of the test masses, which in turn result in net forces on them, and real motion of the test masses. Three different mechanisms have been identified: radiation pressure, radiometer effect and asymmetric outgassing [145, 84, 26].

Radiation pressure A body at any (absolute) temperature T emits thermal radiation. This exerts pressure on any surface the radiation hits —see Figure 1.15. According to electromagnetic theory, such pressure is given by

$$p_{\text{e.m.}} = \frac{4}{3} \frac{\sigma}{c} T^4 \quad (1.12)$$

where $\sigma=5.67 \cdot 10^{-8} \text{ W m}^{-2} \text{ K}^{-4}$ is the Stefan-Boltzmann constant, and c is the speed of light. Consequently, if there are temperature fluctuations around the test mass, a noisy net force will appear on it —see Figure 1.15. The pressure gradient through x is easily inferred from Eq. (1.12) as:

$$\frac{dp_{\text{e.m.}}}{dx} = \frac{dp_{\text{e.m.}}}{dT} \frac{dT}{dx} = \frac{16\sigma}{3c} T^3 \frac{dT}{dx}, \quad (1.13)$$

¹¹For instance local temperature fluctuations in different components of the OMS cause errors in the measurement susceptible of being confused with actual test masses' displacement.

hence

$$\Delta p_{e.m.} = \frac{16\sigma}{3c} T^3 \Delta T \quad (1.14)$$

where Δp and ΔT are the differences of pressure and temperature between the sides of the test masses, respectively. Associated acceleration noise is easily obtained multiplying Eq. (1.14) by the TM surface area, ℓ_{TM}^2 , and dividing by its mass¹², m_{TM} , i.e.,

$$a_{e.m.} = \frac{16\ell_{TM}^2\sigma}{3m_{TM}c} T^3 \Delta T. \quad (1.15)$$

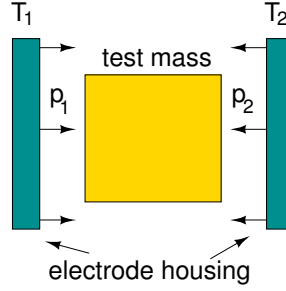


Figure 1.15: Effect of the different pressure on opposite faces of a test mass due to differences of temperature in the walls of the EH.

Radiometer effect [96] This effect happens in rarefied gas atmospheres. In low pressure atmospheres, where the gas particles have a mean free path well in excess of the dimensions of the containing vessel, equilibrium conditions do not happen when pressure is uniform, but rather when the ratios of pressure to square root of temperature equal each other. Let A and B be the two sides

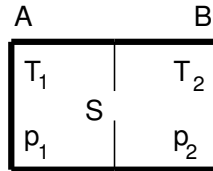


Figure 1.16: Receptacle with different temperature and pressures.

of a receptacle with temperatures T_1 and T_2 , separated by a wall with a hole S —see Figure 1.16. The equilibrium condition between both sides occurs when the number of molecules per time unit passing from A to B and from B to A is the same, i.e.,

$$n_1 \bar{c}_1 = n_2 \bar{c}_2 \quad (1.16)$$

where n_1 and n_2 are the number of particles per unit volume of both receptacle sides, and \bar{c}_1 and \bar{c}_2 are the average speeds of the particles. They can be expressed as

$$n_i = \frac{p_i}{k_B T_i}, \quad (1.17a)$$

$$\bar{c}_i = \sqrt{\frac{8RT_i}{\pi M}} \quad (1.17b)$$

¹²In [26] the radiation pressure factor is modelled as $(8\sigma/3c)T^3\Delta T$.

where $k_B = 1.38 \cdot 10^{-23} \text{ JK}^{-1}$ is Boltzmann's constant, $R = 8.314 \text{ JK}^{-1} \text{ mol}^{-1}$ is the ideal gas constant and M is the molar mass of the gas.

Substituting Eqs. (1.17a) and (1.17b) into Eq. (1.16) the equilibrium condition is obtained:

$$\frac{p_1}{\sqrt{T_1}} = \frac{p_2}{\sqrt{T_2}}. \quad (1.18)$$

Equation (1.18) can be expressed in the form of

$$p(T) = p_0 \sqrt{\frac{T}{T_0}} \quad (1.19)$$

and its gradient through x is easily derived from Eq. (1.19), i.e.,

$$\frac{dp(T)}{dx} = \frac{dp(T)}{dT} \frac{dT}{dx} = \frac{1}{2} p(T) \frac{1}{T} \frac{dT}{dx}. \quad (1.20)$$

Re-arranging we obtain

$$\frac{\Delta p_{r.m.}}{p(T)} = \frac{1}{2} \frac{\Delta T}{T} \quad (1.21)$$

and considering $\Delta p_{r.m.} = (m_{TM} a_{r.m.}) / \ell_{TM}^2$ we arrive to¹³

$$a_{r.m.} = \frac{1}{2} \frac{p(T) \ell_{TM}^2}{m_{TM}} \frac{\Delta T}{T}. \quad (1.22)$$

Outgassing Outgassing is one of the causes of the presence of gas within the walls of the GRS. In the present context, outgassing problems actually derive from *temporal fluctuations* in rate, which once more result in pressure fluctuations, thence in noise. Partial evidence has been gathered that outgassing might be in practise a small effect in the LTP [25, 26]. Moreover, a baking process to the GRS will be done in order to reduce the potential effects of this issue. Therefore this effect will be omitted in further analysis.

Total temperature fluctuation noise in the GRS Radiometer and radiation pressure acceleration fluctuations are of course totally correlated since they have the same noisy source, ΔT . If we neglect outgassing then Eqs. (1.15) and (1.22) are linearly added, and hence the spectral densities of acceleration and temperature in the GRS are related by

$$S_{a,GRS}^{1/2}(\omega) = \left[\frac{16 \ell_{TM}^2 \sigma}{3 m_{TM} c} T^3 + \frac{p \ell_{TM}^2}{2 m_{TM}} T^{-1} \right] S_{\Delta T,GRS}^{1/2}(\omega) \quad (1.23)$$

Nominal conditions in the GRS are as follows,

$$\begin{aligned} \ell_{TM} &= 46 \cdot 10^{-3} \text{ m}, \\ m_{TM} &= 1.96 \text{ kg}, \\ T &= 293 \text{ K}, \\ p &= 10^{-5} \text{ Pa} \end{aligned}$$

which yield

$$S_{\Delta T,GRS}^{1/2}(\omega) = [2.2 \cdot 10^{10} \text{ K (ms}^{-2}\text{)}^{-1}] \cdot S_{a,TFGRS}^{1/2}(\omega) \quad (1.24)$$

with 60% coming from the radiation pressure term, and 40% from the radiometer effect term in Eq. (1.23). Equation (1.24) gives $70 \mu\text{K Hz}^{-1/2}$ as the permitted fluctuations in the worst case that all the thermal acceleration budget, Eq. (1.11), is allocated to temperature fluctuations in the GRS.

¹³In [26] this effect is modelled as $(1/4)p(T)\ell_{TM}^2 m_{TM}^{-1} \Delta T/T$.

1.5.1.2 Noise effects inside the OMS

The optical metrology system is affected by temperature fluctuations basically through two distinct effects [145, 84, 97]:

- the index of refraction of optical components depends on the temperature and,
- temperature changes cause dilatation (and contractions) of optical elements, which in turn cause light's optical path to change accordingly.

It is not difficult to characterise how individual components are influenced by the above effects. For instance a set of on-ground tests in the optical window (OW) and the optical bench (OB) of the OMS have been done in order to estimate the relationship between temperature and interferometer performance when this thermally disturbed. In the case of the OW it has been estimated $\sim 6.5 \text{ nm K}^{-1}$, which allows a maximum temperature fluctuations in the OW of $\sim 10^{-4} \text{ K Hz}^{-1/2}$ not to exceed the noise budget allocated for the interferometer [98, 58].

However, the assessment of the behaviour of the fully integrated optical metrology is a complicated task. Significant progress has been made since the early design proposals, and improved materials and designs more immune to temperature fluctuations are now available. Altogether, it appears that

$$S_{T,\text{OMS}}^{1/2}(\omega) \lesssim 10^{-4} \text{ K Hz}^{-1/2} \quad (1.25)$$

in the LTP MBW is a requirement which should guarantee the performance of the OMS against temperature fluctuations in flight. Again, the noise level in Eq. (1.25) has been estimated for about 10% of the total LTP acceleration noise.

1.5.2 Temperature measurement subsystem sensitivity requirement

Estimates so far indicate that both GRS and OMS noise must be in the order of $10^{-4} \text{ K Hz}^{-1/2}$, as shown in the requirement in Eq. (1.10). Noise in the GRS should be, in principle, uncorrelated with the noise in the OMS since they are of different nature: temperature gradient fluctuations across the test masses cause noise in the GRS, local temperature fluctuations affect the OMS read out. Then, the zero-correlation hypothesis implies that both kinds of noise add quadratically:

$$S_{\Delta T,T}^{1/2}(\omega) = [S_{\Delta T,\text{GRS}}(\omega) + S_{T,\text{OMS}}(\omega)]^{1/2} \leq 10^{-4} \text{ K Hz}^{-1/2} \quad (1.26)$$

Equation (1.26) sets the maximum temperature fluctuations permitted in the LTP to respect the requirement given in Eq. (1.11). We are thus reassured that Eq. (1.10) is a sensible requirement for the temperature fluctuations which can be tolerated in the LTP, and this will be designed to ensure such temperature stability. Nevertheless, it is necessary to know if the stability is actually met during the mission. For this reason it is required to monitor the temperature across different places in the LTP by means of temperature sensors able to detect small temperature fluctuations: $10^{-4} \text{ K Hz}^{-1/2}$ in the frequency range of 1 mHz to 30 mHz. The temperature measurement subsystem (TMS) should be one order of magnitude less noisy than the maximum noise level that has to be measured in the temperature range from 10°C to 30°C [83, 119], or

$$S_{T,\text{TMS}}^{1/2}(\omega) \leq 10^{-5} \text{ K Hz}^{-1/2}, \quad 1 \text{ mHz} \leq \omega/2\pi \leq 30 \text{ mHz}, \\ 10^\circ\text{C} \leq T \leq 30^\circ\text{C} \quad (1.27)$$

which, in fact, becomes a mission top level requirement [146]. There are mainly two reasons which support this decision: (i) Eq. (1.10) defines the maximum acceptable level of temperature fluctuations in the LTP. This, of course, must be satisfied by proper satellite design. Hence, actual fluctuations will be, in principle, less than that. Requirement (1.27) sets a 10% minimum discrimination capability for the measuring system, a standard approach which is compatible with better

performance and (ii) LISA is more demanding than LPF as regards thermal stability (by one order of magnitude [145, 14, 126]). If we require (1.27) for LTP then we are in a position where analysis of thermal sources of noise of relevance for LISA can be identified and tagged for improvement. This prospect is in line with the very concept of LPF as a precursor mission.

1.6 Structure of the thesis

Temperature fluctuations are an important physical phenomena to take into account for LISA and for LPF. In §1.5.1 we have presented the different mechanisms whereby temperature fluctuations cause forces in a macroscopic body and thus, challenge the free fall of the body. For this reason in LISA and LPF temperature fluctuations must be kept within certain limits. The required temperature stability is based on calculations (and on ground experiments) assuming certain feedthrough factors¹⁴.

In view of this, the role of the thermal diagnostic subsystem in the LTP on-board LPF is twofold: on the one hand it is used to excite thermally different subsystems of the LTP (mainly, the GRS and the OMS) to estimate the transfer functions between temperature and TMs acceleration and OMS performance. On the other hand, it must monitor the temperature stability in the LCA which is ensured by a suitable thermal shield that keeps the fluctuations at the level of $\sim 10^{-4} \text{ K Hz}^{-1/2}$ in the milli-Hertz range —see §1.5.1. With this information the purpose of the thermal diagnostic subsystem is to provide information to identify the fraction of noise in the test masses motion caused by thermal effects, with the goal of diagnosing the LTP performance, and guiding the search for the final sensitivity leap from Eq. (1.8) to (1.7). This is the reason why the LTP diagnostics in general is such an important subsystem: it would surely be less relevant should LPF be the ultimate mission, i.e., with no further projection into LISA.

The following chapters focus on aspects of the thermal diagnostics on-board LISA Pathfinder, specially, on the temperature measurement subsystem (TMS). They are organised as follows:

- In chapter 2 we describe the TMS designed for the LTP. The system must reach a noise equivalent temperature of $10^{-5} \text{ K Hz}^{-1/2}$ in the LTP measurement bandwidth. Aspects related to the positioning and connections of the items forming the LTP TMS are also discussed.
- Chapter 3 focuses on potential problems of placing temperature sensors in the GRS. First, we analyse the compatibility of the sensors with the required magnetic cleanliness in the GRS. Temperature sensors in the LTP are thermistors which exhibit a tiny ferromagnetic behaviour. Second, we take into account the capacitive coupling between the cables of the thermistors and the high frequency signals present in the capacitive sensor since they can degrade the TMS performance.
- In chapter 4 we describe the test bed designed in order to validate the LTP TMS. The validation requires to place the temperature sensors in an environment where fluctuations are kept below $10^{-5} \text{ K Hz}^{-1/2}$ for $f \geq 1 \text{ mHz}$. Another test bed to validate the noise performance of the sensors in the LISA band ($f \geq 0.1 \text{ mHz}$) is also described.
- Chapter 5 presents the results of the different test campaigns for the validation of the TMS. The results belong to the prototype validation campaign, to the engineering model (EM) campaign and to the flight model (FM) campaign. In addition, results of the noise investigations of the TMS in the LISA band are presented.
- Chapter 6 focuses on the improvement of the LTP TMS in view of the LISA mission which is more demanding in terms of bandwidth and sensitivity. Effects related to the analog-to-digital converters that limit the sensitivity at low frequency are discussed. The reduction of the floor noise of the TMS is also analysed.

¹⁴Feedthrough factors stand for the coefficients relating thermal effects with TM motion (radiation pressure, radiometer effect, etc.) or error read out in the OMS, e.g., the index of refraction temperature dependence, etc.

- Chapter 7 deals with the issues related to the thermal experiments to be performed in the GRS in order to estimate the feedthrough factors relating temperature and forces induced in the test masses. An analysis of the suitable signals to extract the maximum information of the thermal experiments is presented altogether with simulations.
- Finally, in chapter 8 we present the conclusion of this work.
- A few appendices are added to expand technical details.

Chapter 2

The LTP temperature measurement subsystem

In this chapter we describe in detail the LTP temperature measurement subsystem (TMS). Once the noise requirement of the measurement has been defined the design of the system can be addressed. The TMS must comply with the noise requirement given in Eq. (1.27) —cf. §1.5. We write it down again

$$S_{T,\text{req}}^{1/2}(\omega) \leq 10^{-5} \text{ K Hz}^{-1/2}, \quad 1 \text{ mHz} \leq \omega/2\pi \leq 30 \text{ mHz} \quad (2.1)$$

in the temperature range of 10 °C to 30 °C. This means a root-mean-square (rms) noise of $\sim 0.3 \mu\text{K}$ in a bandwidth of 1 mHz.

The chapter is organised as follows: first, we review the state of the art in low noise temperature measurements. Second, the LTP TMS is described: in §2.2 the temperature sensor itself and in §2.3 the analog and the digital signal processing chains [119]. The last section of the chapter deals with the positioning and the connections of the thermal diagnostic devices in the LTP.

2.1 State of the art

A variety of techniques are available to detect temperature variations [28]. Our interest lies in the detection of temperature fluctuations of small amplitude ($< 10^{-4} \text{ K Hz}^{-1/2}$) at the frequency of the milli-Hertz and at room temperature. Different techniques, configurations and temperature sensors have been designed for this purpose [28, 111, 159, 54, 161, 60]. Considerable efforts have been done in the development of bolometers for applications such as infrared astronomy and microcalometry. Basically, all these designs are based on an ac bridge and the subsequent signal demodulation at the bias frequency. This configuration allows measurements of temperature fluctuations of $\sim \mu\text{K Hz}^{-1/2}$ at low frequencies (tens of milli-Hertz). However, most of these designs have been used at low temperature. Table 2.1 summarises the main results reported in the literature.

Low noise temperature measurements are also required in microdegree temperature controllers which are important devices in many areas of research and applications (investigations in pure fluids, laser heterodyne research [45], study of weak teleseismic signals [40], microgravity experiments on fluids, etc.) [144]. Most of the designs described in the literature use ac techniques altogether with lock-in amplifiers and thermistors as the sensing element. Attempts with dc techniques are also done, however, the temperature stability achieved is worse due to problems related to offset drifts, thermally induced voltages, $1/f$ electronic noise, etc. The results reported of controllers at room temperature are of tens of micro-Kelvin during a few hours¹ [144, 40, 45].

¹However they are not usually expressed in terms of power spectral density.

Ref.	T [K]	NET [K Hz ^{-1/2}]	f [Hz]	Technique
[29]	2.17	$\lesssim 10^{-10}$	$\gtrsim 0.01$	SQUID
[35]	2.17	$\gtrsim 5 \times 10^{-11}$	(not specified)	SQUID
[53]	2.17	$\gtrsim 5 \times 10^{-10}$	(not specified)	SQUID
[158]	3.31	$\lesssim 10^{-9}$	$\gtrsim 0.1$	SQUID (for low temperature experiment in Earth orbit)
[159]	0.3	$6 \cdot 10^{-8}$	0.01	NTC (Ge:Ga)+ac bridge
[37]	0.3	10^{-6}	0.035	NTC (Ge:Ga)+ac bridge
[110]	87.4	$8 \cdot 10^{-6}$	10	YBCO thermometers
[54]	0.1	—	0.1	thermistor+capacitive load in ac bridge
[60]	90	10^{-4}	0.001	YBCO+ac bridge
[161]	300	$6 \cdot 10^{-7}$	10	LSMO thermometers

Table 2.1: Summary of high-sensitivity temperature measurement system designs reported. The ones in the first rows use SQUIDs (superconducting quantum interference device) in conjunction with materials that change their magnetisation with temperature.

All in all temperature fluctuations measurements at the micro-Kelvin level and at the milli-Hertz range at room temperature have been hardly done. Results for uncooled (at room temperature) bolometric detectors have been reported in [161], where noise levels of $0.6 \mu\text{K Hz}^{-1/2}$ at 10 Hz and dissipating 10 mW in the sensor are shown. Another design is reported for an active cavity radiometer where platinum resistance thermometers and yttrium barium cuprate (YBCO) superconducting thermometers were tested at room temperature exhibiting noise levels of $10 \mu\text{K Hz}^{-1/2}$ at 0.1 Hz [60]. In view of this, dedicated investigations in the design of a system able to meet the requirement set in Eq. (2.1) are mandatory. Furthermore, the design of the system is subject to space missions constraints such as availability of space qualified components, power constraints or room.

2.2 Temperature sensors

Two different temperature sensors are commonly used for sensing small temperature variations, although both are based on the same principle: the change of a resistive element under temperature changes. The two available types are resistance temperature detectors (RTDs) and negative temperature coefficient (NTC) thermistors. Their characteristics are summarised in Table 2.2.

	RTD (Pt)	Thermistor
Temperature span	-250 to 900 °C	-100 to 450 °C
Sensitivity	0.00385 K^{-1}	$\simeq 0.04 \text{ K}^{-1}$
Accuracy	$\pm 0.01 \text{ K}$	$\pm 0.1 \text{ K}$
$R - T$ curve	Linear	Exponential
Excitation	Current or voltage source	Current or voltage source
Typical size	6 mm × 6 mm	3 mm × 3 mm

Table 2.2: Typical properties of platinum RTD sensors and NTC thermistors.

Usually in low-noise temperature measurements thermistors are the preferred option because their high sensitivity. In the following we consider thermistors and platinum resistance temperature detectors.

2.2.1 Resistance temperature detectors (RTDs)

RTDs are resistive elements manufactured with different metals such as platinum, nickel or copper. These metals exhibit a known change in their resistance with changes in their temperature. The change of the resistance in these materials is large enough to detect small temperature variations [101]. Commercial RTDs are, however, manufactured mainly with platinum, hence, we only describe these ones here. The relationship between resistance and temperature can be expressed, in general, as

$$R(T) = R_o[1 + \alpha_1(T - T_o) + \alpha_2(T - T_o)^2 + \dots + \alpha_n(T - T_o)^n] \quad (2.2)$$

where T is the temperature, $\alpha_1, \alpha_2, \dots, \alpha_n$ are constant coefficients and R_o is the resistance at a reference temperature, T_o , usually, 273 K. In the linear region (which extends from -250°C to 850°C) Eq. (2.2) reduces to [28]

$$R(T) = R_o[1 + \alpha_{\text{Pt}}(T - T_o)] \quad (2.3)$$

where α_{Pt} is the sensitivity of the sensor defined as

$$\alpha_{\text{Pt}} = \frac{1}{R_o} \frac{dR(T)}{dT} \quad (2.4)$$

which for platinum RTD is 0.00385 K^{-1} . The value of R_o varies from $25\ \Omega$ to $10\ \text{k}\Omega$, however, the use of large values of R_o does not produce better results in the noise performance of the system as one could expect —see §2.3.2.1—, but does reduce the errors due to the 2-wire measurement set up —see appendix §A.4. Two important features of the platinum sensor are [72, 28]: (i) its long-term stability (manufacturers specify values around $0.05\ \text{K yr}^{-1}$) and (ii) its excellent repeatability. However, as it will be shown in §2.3.2.1 the sensitivity of the platinum RTD is not enough to reach the demanding requirements of the measurement under certain power limitations.

2.2.2 NTC thermistors

NTC thermistors are also resistive elements that change their resistance with temperature. NTC thermistors are manufactured mixing and synthesising oxides doped with metals. The usual oxides used are of manganese, nickel, cobalt, iron, copper or aluminium. The oxide proportion determines the resistance and the temperature coefficient of the sensor [123, 101]. Thermistors are characterised by (i) exhibiting a large change in their resistance under small temperature variations, (ii) a negative temperature coefficient and (iii) an exponential relationship between temperature and resistance, which implies a non-constant, but high sensitivity —see Figure 2.1.

The resistance-temperature relationship of a thermistor can be expressed by means of the Steinhart-Hart equation [133],

$$T^{-1} = A + B \ln R(T) + C \ln^3 R(T) \quad (2.5)$$

where T is the temperature in Kelvin units and A, B and C are constant coefficients that depend on the thermistor type and are given by the manufacturer. Nevertheless, Eq. (2.5) can be simplified, if the working temperature range is small ($\Delta T \simeq 50\ \text{K}$) to [123, 28, 101]

$$R(T) = R_o e^{\beta(T^{-1} - T_o^{-1})} \quad (2.6)$$

where β is the temperature characteristic of the material and is constant for small temperature ranges and R_o is the resistance of the thermistor at a given reference temperature, T_o , usually 298 K. The values of R_o for space qualified thermistors are in the $\text{k}\Omega$ range ($2\ \text{k}\Omega$ to $20\ \text{k}\Omega$ [16]), thus, appropriate for the 2-wire measurement configuration [75, 101, 28] —see appendix §A.4. The value of β depends on the thermistor and the typical values are around $3500\ \text{K}$ [16].

The sensitivity of the thermistor can be calculated for small temperature intervals by making use of the definition given in Eq. (2.4). The resultant sensitivity is

$$\alpha_{\text{NTC}} = -\frac{\beta}{T^2} \quad (2.7)$$

which is $\sim 0.04 \text{ K}^{-1}$ at 298 K. The sensitivity is the most important parameter of the sensor for our purposes since its value appears in the expression that sets the noise performance of the system: the higher the sensitivity the lower the noise in the measurement —see §2.3.2. For this reason the thermistor appears, in principle, as the baseline for the temperature measurement subsystem (TMS). Figure 2.1 shows the change in the resistance as a function of the temperature for platinum RTDs and for NTC thermistors: the higher sensitivity of the thermistor with respect to the platinum RTD is clearly seen.

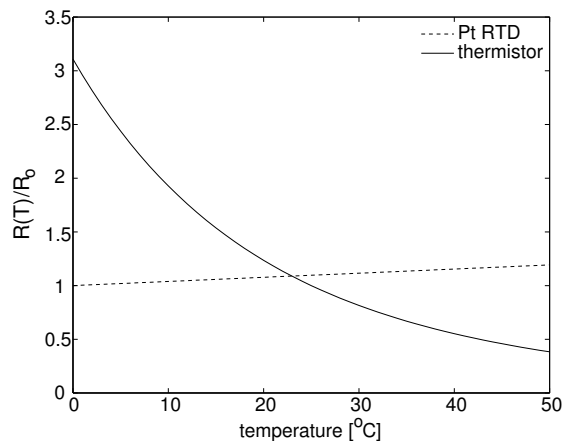


Figure 2.1: Normalised resistance vs. temperature for a NTC thermistor and a Pt RTD.

Thermistors, however, present different concerns that must be taken into account:

- thermistors are, in fact, semiconductors and, thus, some $1/f$ excess noise might appear in the measurement [90, 56],
- thermistors are manufactured with tiny amounts of ferromagnetic materials (nickel, cobalt or iron) [123, 160, 101]. The severe magnetic cleanliness requirement in the test masses location might be incompatible with the magnetic properties of the NTCs,
- the long-term stability might not be as good as in the platinum sensors. Different studies on this subject, however, appear reassuring [79, 80, 41],
- the repeatability of the thermistors might not be good enough, i.e., sensors from the same batch actually exhibit different performance. This implies the need of a screening process to select those sensors which work properly.

These concerns are analysed in this thesis in order to validate the use of NTC thermistors as the sensors for the LTP TMS. Platinum RTD sensors have been discarded because the requirement given in Eq. (2.1) cannot be met with the power limitations of the system —see §2.3.2.

The NTC thermistors selected (which obviously have to be space qualified) are BetaTherm, specifically, the G10K4 surface type model. They are matched glass coated² NTC thermistor beads, mounted on aluminium housing and pot with Sty cast 2850 ft epoxy —see Figure 2.2. The nominal resistance is 10 k Ω and β is 3694 K [16].

²Glass encapsulation of the thermistor chip provides better long-term stability.



Figure 2.2: NTC thermistor: G10K4 surface type model of BetaTherm.

2.3 Signal processing chain

The signal processing is composed of two blocks: the analog signal processing and the digital signal processing. Both are described in the following sections. Prior to that a short explanation on the principle of measurement is presented.

2.3.1 Principle of measurement

The designed system must be capable of measuring very small amplitude signals in the milli-Hertz range. The maximum permitted noise is in the order of tens of $\text{nV Hz}^{-1/2}$ at 1 mHz for the LTP. The signal from the sensor must be amplified to be properly quantised by the analog-to-digital converter (ADC). However, even precision instrumentation amplifiers (IAs) are unable to perform amplification with such low noise in the milli-Hertz range due to their inherent $1/f$ noise —see §2.3.2.4. Consequently, the only possible way to reach the desired performance is the use of the lock-in amplification technique [128, 102, 43]. This method has been widely used in high sensitivity temperature measurements, however, it has not been assessed in the milli-Hertz region [159, 54, 111, 131, 60, 38] —cf. §2.1.

The principle of operation of this method is based on: (i) the modulation of the signal of interest to a frequency away from the $1/f$ noise of the amplifier; (ii) the amplification of the modulated signal and, (iii) the demodulation of the signal coming out from the IA and the proper low-pass filtering. This process is schematically represented in Figure 2.3.

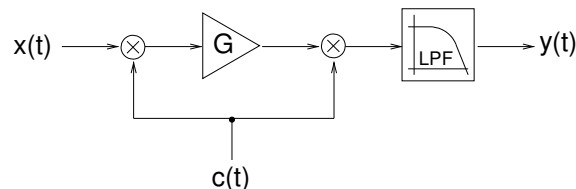


Figure 2.3: Principle of measurement used in the TMS which is based on the lock-in amplification technique. The temperature signal is $x(t)$ while the carrier signal is $c(t)$.

The low frequency signal of interest is $x(t)$ and the modulating signal is $c(t)$ which, obviously, must be an ac signal (sine wave, square wave, triangular wave, etc.). Figure 2.4 shows the signals involved during the process (in the frequency domain), with $c(t)$ a sine wave —see the caption of the figure for details.

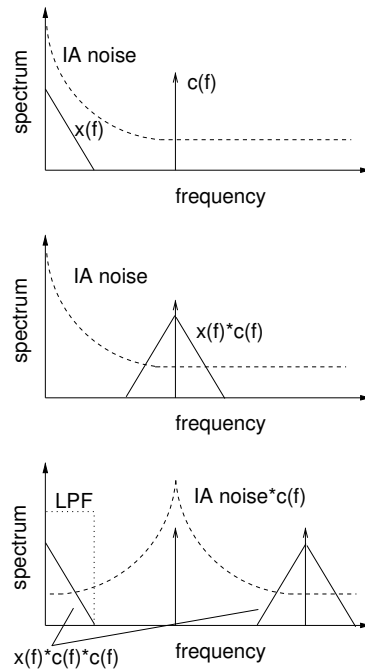


Figure 2.4: Top: the spectrum of the signals are given: $x(f)$ stands for the power spectral density of the low frequency and low amplitude signal, $x(t)$. $c(f)$ stands for the Fourier transform of the carrier (modulating signal), in this example, a sine wave. The noise of the IA is also shown. It is clear that the noise of the amplifier masks the signal of interest if the latter is directly amplified. Middle: the signal of interest is modulated by the carrier signal, i.e., $x(t)c(t)$ [or $x(f) * c(f)$]. The noise of the IA remains unaltered. Bottom: the signal of interest is amplified (consider gain unity for simplicity) and demodulated by $c(t)$. Consequently, the signal of interest is shifted back to the original frequency band [and a replica at the double frequency of $c(t)$] and the IA noise is now modulated, i.e., the $1/f$ is shifted to the frequency of the carrier signal and the noise of the IA at the carrier frequency (white noise) is shifted to the dc band. Afterwards a simple low-pass filter is used to eliminate the *high* frequency components and, thus, recover the signal of interest, $x(t)$. Frequency bands not to scale.

The TMS designed for the LTP is based on this principle of operation. The modulating signal is, though, a square wave and the demodulation is done digitally³. The following sections describe how this method has been implemented.

³The square wave has been chosen since is very easy to generate and the same applies to the digital demodulation. However, the ac square wave modulation/demodulation process reduces slightly the signal-to-noise ratio with respect to a sine wave.

2.3.2 Analog signal processing

The analog signal conditioning circuit can be divided into three main blocks: (i) the Wheatstone bridge circuit, (ii) the multiplexing, amplification and low-pass filter circuits and (iii) the ADC circuit. These blocks are shown in Figure 2.5 where $c(t)$, $n(t)$ and $n_{\text{ADC}}(t)$ are the square wave modulating signal, the noise sources of the Wheatstone bridge and the amplification stage, and the noise of the analog-to-digital conversion stage, respectively. These stages are discussed in the following sections.

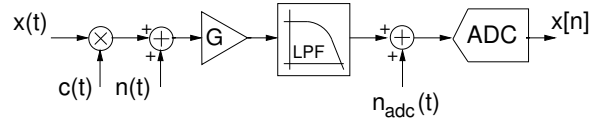


Figure 2.5: Analog signal processing block diagram. The demodulation of $x[n]$ is done digitally —see §2.3.3.

2.3.2.1 Wheatstone bridge circuit

The Wheatstone bridge is used to measure the resistance of the sensor by means of the deflection method [101], i.e., by measuring the difference of the drop voltage between the two arms of the bridge. The bridge circuit is shown in Figure 2.6.

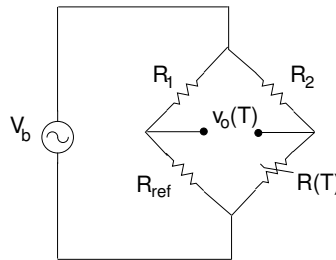


Figure 2.6: Wheatstone bridge circuit scheme. $R(T)$ is the sensor and R_{ref} determines the centre of the temperature scale in the absolute measurements. When differential measurements are needed R_{ref} is substituted by another temperature sensor.

The resultant output voltage of the Wheatstone bridge is

$$v_o(T) = V_b \left[\frac{R_{\text{ref}}}{R_{\text{ref}} + R_1} - \frac{R(T)}{R(T) + R_2} \right] \quad (2.8)$$

where

- V_b is the voltage supply of the bridge,
- R_1 and R_2 are fixed resistors,
- R_{ref} is an array of resistors that allows to centre the temperature scales to some specific values,
- $R(T)$ is the resistance of the temperature sensor.

The Wheatstone bridge circuit allows centring the zero output for different temperature scales by only changing the resistor R_{ref} and, also, permits to perform differential measurements by simply substituting R_{ref} by another temperature sensor. The value of R_2 is calculated by substituting Eq. (2.6) into Eq. (2.8) and looking for the value of R_2 that maximises the sensitivity of the bridge. This leads to

$$R_2(T) = R(T) \frac{\beta - 2T}{\beta + 2T}. \quad (2.9)$$

Assuming a sensor of nominal resistance of 10 k Ω and $\beta=3694$ K, the value of R_2 ($\equiv R_1$) is set to 10 k Ω in order to simplify the design⁴. The value of R_{ref} depends on the temperature scale chosen and it can be selected by means of the multiplexers placed at the output of the bridge. Six scales have been defined with centre temperatures: 12, 15, 20, 22.5, 25 and 27.5 $^{\circ}\text{C}$ —see Table 2.3 and §2.3.6. This solution has been adopted due to the high sensitivity and resolution needed in a temperature span of 20 $^{\circ}\text{C}$ (from 10 $^{\circ}\text{C}$ to 30 $^{\circ}\text{C}$ —cf. §1.5.2) and to maintain the output of the bridge as close to zero as possible and, thus, minimise the effect of the gain errors and gain temperature coefficient along the measurement chain —see Figure 2.17 and appendix §A.

Another important parameter that must be considered is the dissipated power in the sensor, which is limited to a maximum of 10 μW not to disturb other nearby LTP subsystems such as the GRS and the OMS [83] (an estimation of the effect of the power dissipated in the thermistors in the temperature stability of the GRS is given in §6.2.2) and to minimise the errors due to the self-heating effect in the sensor [71] —see §2.3.2.3 and appendix §B. This limits the bridge voltage excitation, V_b , to

$$V_b = (4R_2 P_{\text{max}})^{1/2} \stackrel{P_{\text{max}}=10 \mu\text{W}}{\Rightarrow} V_b = 0.632 \text{ V}. \quad (2.10)$$

The sensitivity of the Wheatstone bridge is defined as

$$s_b(T) = \frac{dv_o(T)}{dT} [\text{V K}^{-1}]. \quad (2.11)$$

By substituting Eqs. (2.3), (2.6) and (2.8) into Eq. (2.11) we obtain an expression for the sensitivity of the bridge for each of the sensor types, i.e.,

$$s_{b,\text{NTC}}(T) = V_b \frac{R_2}{[R_2 + R(T)]^2} \frac{R(T)}{T^2} \beta, \quad (2.12a)$$

$$s_{b,\text{RTD}}(T) = \frac{R_2 R_o}{R_2 + R(T)} \left[\frac{P_{\text{max}}}{R(T)} \right]^{1/2} \alpha_{\text{Pt}}. \quad (2.12b)$$

These expressions are plotted in Figure 2.7 for $V_b=0.632$ V ($P=10 \mu\text{W}$). Figure 2.7 is useful to compare both sensors under the same conditions: with the same nominal resistance ($R_o=10$ k Ω) and the same dissipated power. The value of R_2 ($=10$ k Ω) for the thermistor bridge has been chosen using Eq. (2.9) in order to have a maximum sensitivity around 20 $^{\circ}\text{C}$. For the case of the platinum RTD, the sensitivity of the bridge increases with the value of R_2 to an asymptotic value for $R_2 \simeq 100R_o$. However, such solution entails an increase of the common mode voltage [102] at the output of the bridge which translates into an error at the output of the amplification stage due to the finite common-mode rejection ratio (CMRR) and its temperature dependence. Anyway, we have used also $R_2=10$ k Ω .

⁴Actually for each T there is an optimum value of R_2 , for instance, for $T=283$ K is 14 k Ω and for $T=303$ K is 6 k Ω .

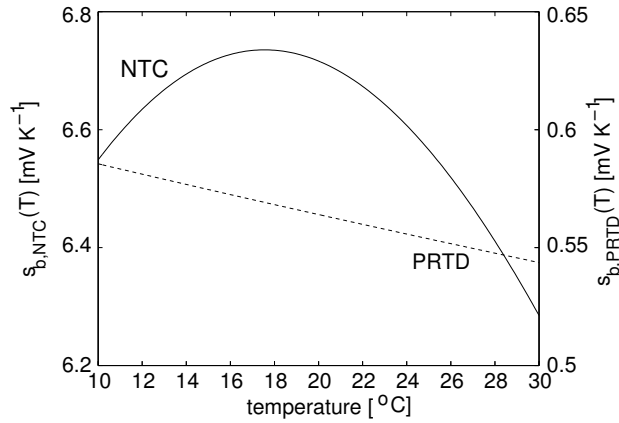


Figure 2.7: Wheatstone bridge sensitivity for NTC thermistors (solid trace) and for platinum RTD sensors (dashed trace). Dissipated power is $10 \mu\text{W}$ and both sensors have a nominal resistance of $10 \text{ k}\Omega$. Note that the scale of the thermistor is one order of magnitude higher than the RTD one. The resistor R_2 in the Wheatstone bridge is $10 \text{ k}\Omega$ which implies a maximum sensitivity at $\simeq 18^\circ\text{C}$ when using thermistors —see Eq. (2.9). In the case of the platinum sensors if R_2 is set to $100 \text{ k}\Omega$ instead of $10 \text{ k}\Omega$ the sensitivity is $\simeq 1 \text{ mV K}^{-1}$, still a factor of 6 lower than the thermistor one. The sensitivity shown is, though, with $R_2=10 \text{ k}\Omega$ [106].

The NTC thermistor bridge sensitivity is about one order of magnitude larger than the platinum RTD one, as expected since a thermistor has a typical sensitivity of $\simeq -0.04 \text{ K}^{-1}$ while the platinum sensor one is 0.00385 K^{-1} —see §2.2.

The bridge circuit is the first element of the measuring chain. Therefore, the noise introduced by this stage contributes to the overall system performance. In order to estimate the levels of noise introduced by this stage we consider the Johnson noise model for the three resistors (R_1 , R_2 and R_{ref}) and the same for the sensors⁵. The expression of the noise power spectral density (in units of $\text{V}^2 \text{ Hz}^{-1}$) introduced by the bridge is (assuming $T = T_{\text{NTC}} \simeq T_{\text{FEE}}$ ⁶)

$$S_{V,b}(T, \omega) = 4k_{\text{B}}T \left[\frac{R_1 R_{\text{ref}}}{R_1 + R_{\text{ref}}} + \frac{R_2 R(T)}{R_2 + R(T)} \right] \quad (2.13)$$

where $k_{\text{B}} = 1.38 \cdot 10^{-23} \text{ J K}^{-1}$ is Boltzmann's constant. A more convenient way to deal with this expression for our purposes is to express it in terms of noise equivalent temperature ($\text{K}^2 \text{ Hz}^{-1}$). This is readily done by dividing Eq. (2.13) by the bridge sensitivity, i.e.,

$$S_{T,b}(T, \omega) = \frac{S_{V,b}(T, \omega)}{[s_b(T)]^2}. \quad (2.14)$$

Manipulating Eq. (2.14) we obtain a useful generic equation for the equivalent temperature noise bridge contribution to the system,

$$S_{T,b}^{1/2}(T, \omega) = \frac{S_{V,b}^{1/2}(T, \omega)}{\frac{R_2}{R_2 + R(T)} \alpha [PR(T)]^{1/2}} \quad (2.15)$$

where α (the relative sensitivity of the sensor) is 0.04 K^{-1} and 0.00385 K^{-1} for the NTC thermistor and the platinum sensor, respectively. Equation (2.15) leads to important conclusions:

⁵The hypothesis of modelling the sensors as Johnson noise sources even at frequencies around the milli-Hertz region has been confirmed by experimental results —see §5.

⁶FEE stands for the front-end electronics of the temperature measurement subsystem.

- the greater the dissipated power in the sensor, P , the lower the noise,
- the greater the relative sensitivity, α , the lower the noise,
- the value of the nominal sensor resistance, R_o , does not reduce or increase the noise,
- in the case of the platinum sensors the increase of R_2 translates into a lower noise, although the noise is not further reduced for a relationship of $R_2/R_o > 100$.

Evaluation of Eq. (2.15) for both sensors is shown in Figure 2.8. The results confirm that the noise levels when using a thermistor are one order of magnitude lower than those of the platinum RTD. Furthermore, the noise levels of the latter are non-compliant with the requirement. The thermistor noise levels are five times lower than the requirement. Consequently, at this point, platinum RTDs were discarded as an option capable of achieving the requirements and the NTC thermistor was the option chosen for the LTP TMS although some concerns had first to be cleared —see §2.2.2.

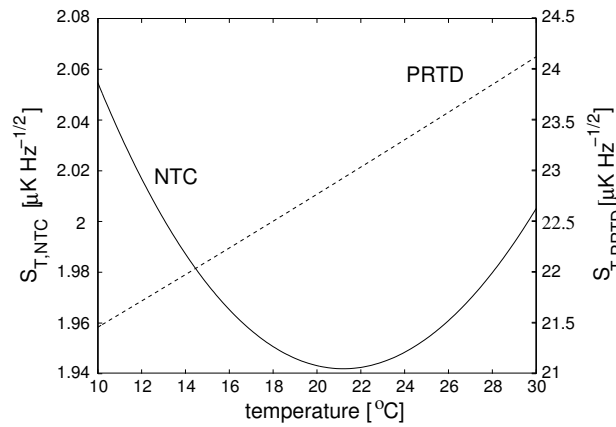


Figure 2.8: Wheatstone bridge noise equivalent temperature when using a thermistor and a platinum RTD. The latter is already above the requirement —see Eq. (2.1)— and, therefore, it is discarded. This noise figure is valid for all the frequency range since Johnson noise, i.e., white noise, is considered. The dissipated power in the sensor is $10 \mu\text{W}$. The noise of the bridge when using a platinum sensor can be slightly reduced by using a higher value of R_2 . For $R_2=100 \text{ k}\Omega$ the noise goes down a factor of $\simeq 2$, still not meeting the requirements. The noise of the bridge when using thermistors is five times lower than the requirement.

Another important issue to take into account with respect to the Wheatstone bridge is its temperature coefficient (TC), α_b . Temperature fluctuations in the resistors forming the bridge show up as an error in the measurement. The coefficient for the whole bridge is (in V K^{-1}) —see appendix §A.3,

$$\alpha_b(T) = V_b R \left[\frac{2R_{\text{ref}}}{(R_{\text{ref}} + R)^2} + \frac{R_{\text{NTC}}(T)}{(R_{\text{NTC}} + R)^2} \right] \alpha_R \quad (2.16)$$

where $R = R_1 = R_2 = 10 \text{ k}\Omega$ and α_R is the temperature coefficient of the resistors. The maximum bridge resistors' TC, α_R , permitted in the MBW can be calculated by using the following expression

$$\frac{\alpha_b(T)}{s_{b,NTC}} S_{T,FEE}^{1/2}(\omega) \leq S_{T,req}^{1/2}(\omega) \quad (2.17)$$

where $S_{T,FEE}^{1/2}$ stands for the temperature fluctuations in the electronics, i.e., in the Wheatstone bridge and $S_{T,req}^{1/2} = 10^{-5} \text{ K Hz}^{-1/2}$. Thus, the maximum permitted resistors' TC, α_R , depends

on the temperature fluctuations of the electronics on board the satellite. In the design we have assumed to be less than $0.1 \text{ K Hz}^{-1/2}$ which appears to be comfortably met in the satellite. This leads to a maximum value of α_R of 2 ppm K^{-1} . The resistors of the bridge (R_1 , R_2 and R_{ref}) used in the system have a lower temperature coefficient (Vishay Metal Foil resistors of 0.6 ppm K^{-1}) in order to be on the safe side.

In summary, the Wheatstone bridge designed consists of two high stability resistors ($R_1 = R_2 = 10 \text{ k}\Omega$), six high-stability reference resistors ($R_{\text{ref}0}$ to $R_{\text{ref}5}$) to centre the output of the bridge at different temperatures and a NTC thermistor as the sensing element. Table 2.3 summarises the references used and the associated centre for each of the scales and their temperature span considering a gain of 200 in the amplification stage —see §2.3.2.4.

reference label	resistance [$\text{k}\Omega$]	centre of scale [$^\circ\text{C}$]	$T_{\text{min}} - T_{\text{max}}$ [$^\circ\text{C}$]
0	17.5	12	8.28—15.87
1	15	15	11.79—19.29
2	12.5	20	15.99—23.41
3	11	22.65	18.97—26.54
4	10	25	21.21—28.89
5	9.1	27.5	23.47—31.29

Table 2.3: References used and their corresponding centres of scale in the Wheatstone bridge circuit. All the resistors have very low temperature coefficient (0.6 ppm K^{-1}). The selection of the references is done by means of multiplexers —see Figure 2.10. T_{min} and T_{max} are calculated assuming the gain of the amplification stage is 200. The temperature expected in the LCA of the LTP is from 10°C to 30°C .

The bridge exhibits a sensitivity of $\simeq 6.5 \text{ mV K}^{-1}$ in the temperature range from 10°C to 30°C with $P \simeq 10 \mu\text{W}$. In terms of noise equivalent temperature the Wheatstone bridge contributes with white noise⁷ of amplitude $\simeq 2 \mu\text{K Hz}^{-1/2}$ (20% of the requirement). Finally, we calculate the needed number of bits of the ADC by using the dynamical range (DR) definition [102], i.e.,

$$\text{DR} = 20 \log \frac{\text{temperature span}}{\text{resolution}} \simeq 6N_{\text{bit}} \quad (2.18)$$

where the temperature span is $T_{\text{max}} - T_{\text{min}} \simeq 7 \text{ K}$ and the resolution is set to 10^{-6} K . These numbers yield a needed number of bits, N_{bit} , of $\simeq 22$ —see §2.3.2.5.

2.3.2.2 Drive bridge circuit

As explained in §2.3.1 and shown in §2.3.2.4 the $1/f$ noise introduced by the amplification stage prevents achieving the requirement given in Eq. (2.1). For this reason and also to reduce dc errors (thermoelectric voltages, offset voltages, and bias current), the Wheatstone bridge circuit is powered with an ac square signal which keeps *quasiconstant* the electrical power dissipated in the thermistor⁸. With this technique the bridge signal is modulated at a specific frequency while the noise introduced by the amplification stage is not. Thus, when demodulating, the signal returns to the baseband while the $1/f$ noise of the amplification stage is modulated and kept away from the baseband —see §2.3.1 and §2.3.4.

In this section we describe the circuit designed for the ac square wave voltage generation which modulates the temperature signal of the bridge. The demodulation of the signal is done digitally and is described in §2.3.3. The drive bridge circuit is a circuit based on two operational amplifiers (OAs) and two analog switches controlled by digital signals —see Figure 2.9.

⁷The noise is white since Johnson noise is assumed as the noise model for all the discrete elements of bridge, including the sensors.

⁸This reduces non-linear effects due to the non-linear relationship between the dissipated power in the sensor and the self-heating effect —see 2.3.2.3. Moreover the generation of a square wave is simple and, usually, exhibits higher stability than a sine wave.

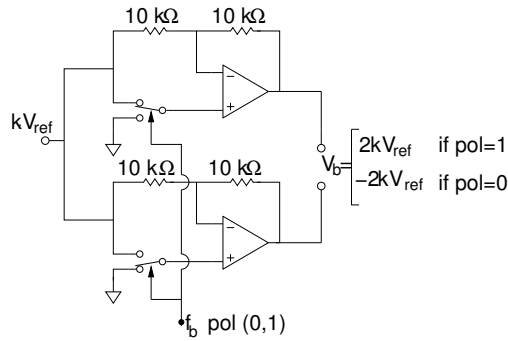


Figure 2.9: Drive bridge circuit scheme for the square wave bridge voltage supply.

The switches in Figure 2.9 permit reversing the output voltage of the bridge: for one polarity the output of the bridge is V_b and for the other is $-V_b$. The polarity is reversed each 90 ms, thus, the frequency of the square wave is $(180\text{ ms})^{-1}=5.55\text{ Hz}$, which minimises the $1/f$ noise of the amplification stage —see §2.3.2.4.

Another important feature of this circuit is that the bridge voltage supply is the ADC voltage reference ($V_{ADC}=2.5\text{ V}$) with a scale factor, k ($=0.25$), to adjust the power in the sensor. This technique permits a voltage reference-independent conversion and, thus, highly accurate conversions using voltage references of modest quality are performed. The voltage reference-independent conversion can be expressed, in general, as [49]

$$D = \frac{2^{N_{\text{bit}}} - 1}{V_{\text{ADC}}} v_o = \frac{2^{N_{\text{bit}}} - 1}{V_{\text{ADC}}} \alpha V_{\text{ADC}} = (2^{N_{\text{bit}}} - 1)\alpha \quad (2.19)$$

where D is the digital code output and αV_{ADC} is the output of the bridge.

The temperature coefficient (TC) of the resistors of the drive bridge circuit (the $10\text{ k}\Omega$ resistors in Figure 2.9) also affects the performance of the measuring system —see appendix §A.1.2. The value must be below 30 ppm K^{-1} (assuming ambient temperature fluctuations lower than $0.1\text{ K Hz}^{-1/2}$). The resistors used are of 0.6 ppm K^{-1} (the same type of the ones used in the Wheatstone bridge). Moreover, the offset, the bias current, the open-loop gain, and the common-mode rejection ratio (CMRR) of the OAs introduce a gain error and their dependence with temperature can cause fluctuating errors in the measurement. These effects are, in principle, tiny (tens of μK), specially, if the temperature of the environment is stable —see appendix §A.1.

2.3.2.3 Self-heating effect error considerations

The self-heating effect (SHE) introduces an error in the measurement due to the non-zero thermal contact resistance [71, 16], θ , between the thermistor chip and the temperature of the sensed body⁹. In terms of power spectral density it can be expressed as¹⁰

$$S_{T_{\text{SHE}}}^{1/2}(\omega) = \theta S_P^{1/2}(\omega) \quad (2.20)$$

where $S_P^{1/2}$ stands for the power fluctuations in the thermistor.

⁹Experimental tests have shown that $\theta < 100\text{ K W}^{-1}$ when attaching the sensors to an aluminium block surrounded by polyurethane foam. This value might be different in the satellite since it depends on the environmental conditions, however, it must be taken into account that an intrinsic thermal resistance of $\sim 50\text{ K W}^{-1}$ is always present —see appendix §B.

¹⁰The thermal mass of the thermistor is very small and we are interested in the milli-Hertz region. For this reason we can consider the transfer function between power and temperature as a constant, i.e., the bandwidth of the transfer function is much larger than the frequency of interest. Thus, we omit the frequency dependence of θ .

Power fluctuations, $S_P^{1/2}$, come in two different ways: (i) bridge voltage fluctuations that in the end result in voltage fluctuations in the thermistor, $S_V^{1/2}$, and (ii) NTC resistance fluctuations due to actual temperature fluctuations. Manipulation of Eq. (2.20) leads to the error introduced by both mechanisms,

$$S_{T_{\text{SHE}},1}^{1/2}(\omega) = \theta \frac{2V}{R} S_V^{1/2}(\omega) \quad (2.21a)$$

$$S_{T_{\text{SHE}},2}^{1/2}(\omega) = \theta V^2 \frac{\beta}{R_o T_o^2} S_T^{1/2}(\omega) \quad (2.21b)$$

where V ($= V_b/2$) is the voltage in the NTC, R is the resistance of the NTC, $S_V^{1/2}$ are the voltage fluctuations in the thermistor, and $S_T^{1/2}$ are the temperature fluctuations in the thermistor. Equations (2.21a) and (2.21b) are used to calculate the maximum voltage fluctuations permitted in the NTC and the maximum temperature fluctuations. Both contributions must be lower than $10^{-6} \text{ K Hz}^{-1/2}$ in order to keep this effect one order of magnitude below the requirement. The values obtained are (assuming $P=10 \mu\text{W}$, $T=293 \text{ K}$ and $\theta=100 \text{ K W}^{-1}$)

$$S_V^{1/2}(\omega) \lesssim 0.15 \text{ mV Hz}^{-1/2}, \quad \omega/2\pi \geq 1 \text{ mHz}, \quad (2.22a)$$

$$S_T^{1/2}(\omega) \lesssim 0.025 \text{ K Hz}^{-1/2}, \quad \omega/2\pi \geq 1 \text{ mHz}, \quad (2.22b)$$

Voltage fluctuations are about $2 \mu\text{V Hz}^{-1/2}$ at 1 mHz, i.e., they met comfortably the requirement given in Eq. (2.22a); and, obviously, the temperature fluctuations condition is also met — Eq. (2.22b)— since the fluctuations to measure are of $0.1 \text{ mK Hz}^{-1/2}$. In conclusion, self-heating effect does not affect the measurement due to the low power dissipated in the thermistor. In chapter 6.2 we show the effect of dissipating higher power in the thermistors.

2.3.2.4 Multiplexers, amplification and low-pass filter

The blocks described in this section are placed at the output of the Wheatstone bridge. They are:

- the multiplexers (MUX),
- the instrumentation amplifier (IA) and,
- the low-pass filter.

A total of 24 channels (and 36 measurements —see §2.4) are needed to monitor temperature at different places of interest of the LTP [113, 83] —see §1.5 and §2.4. Weight, size and power limitations prevent a single conditioning chain for each temperature sensor¹¹. For this reason six independent boards have been used to perform all the needed measurements. Each electronic board must allow measurements of four channels with respect to six reference temperatures (defined by R_{ref}) and one differential measurements between two sensors —see §2.4.3. The circuit designed to deal with this requirement is shown in Figure 2.10.

The arms of the bridge are selected by two one-to-eight channel solid state MUXs (Maxim DG408 in the prototype; Intersil HI-508 in the FM design). Each half of the bridge is selected by the MUXs with digital signals and connected to the non-inverting and inverting inputs of the IA. The MUXs contribution to the whole noise system performance is negligible¹².

The following block is the instrumentation amplifier. The IA is used to amplify the Wheatstone bridge output, v_o —see Eq. (2.8). The output voltage of the bridge when measuring at the level

¹¹This would imply a bridge circuit with six references and a drive bridge circuit for each of the 24 sensors. Also an amplification stage, a low-pass filter and a dedicated ADC for each sensor. This, clearly, appears unfeasible.

¹²The MUXs can be modelled as a simple resistance, R_{ON} , which is in the order of 400Ω as maximum, which, assuming Johnson noise results on a equivalent noise of $\simeq 0.4 \mu\text{K Hz}^{-1/2}$, well below the noise of the Wheatstone bridge itself.

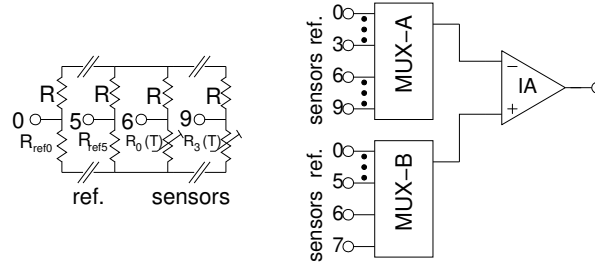


Figure 2.10: Wheatstone bridge and multiplexer connections. This scheme permits absolute measurements (using different scales: from $R_{\text{ref}0}$ to $R_{\text{ref}5}$) and differential measurements. Also a measurement to check the electronics itself independent of the sensors is possible by measuring one reference against another one.

of the micro-Kelvin is very weak (tens of nV), thus, amplification is mandatory before the digital conversion is done by the ADC (16-bit) — see §2.3.2.5. The noise introduced by the 16-bit ADC to the system (referred to the input) is¹³

$$S_{T, \text{ADC}}^{1/2}(T, \omega) = \frac{\sigma_{\text{ADC}}}{2^{16}} V_{\text{FS}} \frac{1}{\sqrt{f_s/2}} \frac{1}{G_{\text{IA}} s_b(T)} \quad (2.23)$$

where $\sigma_{\text{ADC}}=1$ LSB (least significant bit) is the noise specified by the manufacturer, $V_{\text{FS}}=10$ V is the full-scale voltage, f_s is the sampling frequency (38.4 kHz in the prototype, 50 kHz in the FM design), G_{IA} is the gain of the IA and s_b is the sensitivity of the bridge ($\simeq 6.5$ mV K⁻¹). Now we calculate the needed gain of the IA in order to keep this noise below $1 \mu\text{K Hz}^{-1/2}$, i.e.,

$$\frac{\sigma_{\text{ADC}}}{2^{16}} V_{\text{FS}} \frac{1}{\sqrt{f_s/2}} \frac{1}{G_{\text{IA}} s_b(T)} \leq 10^{-6} \rightarrow G_{\text{IA}} \geq 170. \quad (2.24)$$

The IA used in the prototype is the AD624 of Analog Devices (the one used in the FM design is very similar, the AD620 from Analog Devices). This solution reduces the use of discrete resistors, eliminates in some cases the necessity of external trims, and maintains a low temperature coefficient of the amplifier, specially for the gain. The gain of the IA, G_{IA} , is set to 200 which is easily configured in the AD624 (and in the AD620) and is slightly larger than the minimum required calculated in Eq. (2.24). Therefore, the sensitivity of the system at the output of the IA is

$$s_{\text{IA}} = s_b G_{\text{IA}} \simeq 1.35 \text{ V K}^{-1} \quad (2.25)$$

around 20°C. The IA also introduces noise in the measurement due to its inherent voltage and current noise sources. In order to analyse the contribution of the IA to the total noise, the bridge output impedance (the MUX impedance can be neglected) has to be taken into account. Figure 2.11 shows the noise sources coming from the IA.

The equivalent spectral voltage density referred to the input (RTI) is

$$e_{\text{IA, RTI}}^2(T, \omega) = e_n^2(\omega) + i_n^2(\omega) \left[\left(\frac{RR_{\text{ref}}}{R + R_{\text{ref}}} \right)^2 + \left(\frac{RR_{\text{NTC}}(T)}{R + R_{\text{NTC}}(T)} \right)^2 \right] \quad (2.26)$$

where e_n^2 and i_n^2 can be modelled as [102]

$$e_n^2(\omega) = e_{\text{ni}}^2 + \frac{e_{\text{no}}^2}{G_{\text{IA}}^2} = K_v^2 \left(1 + \frac{\omega_{\text{cv}}}{\omega} \right), \quad (2.27)$$

$$i_n^2(\omega) = K_i^2 \left(1 + \frac{\omega_{\text{ci}}}{\omega} \right). \quad (2.28)$$

¹³Note this is not the quantisation noise. This is known as the transition noise in ADC data-sheets. The quantisation noise is considered later on.

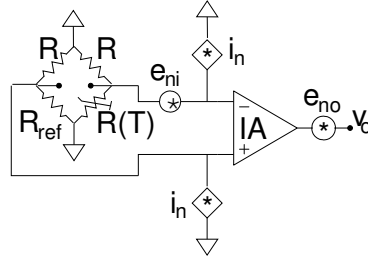


Figure 2.11: IA + Wheatstone bridge noise equivalent circuit.

The noise parameters of the IA AD624 are $K_v=4\text{ nV Hz}^{-1/2}$, $\omega_{cv}/2\pi=3\text{ Hz}$, $K_i=0.3\text{ pA Hz}^{-1/2}$, and $\omega_{ci}/2\pi=100\text{ Hz}$. The noise levels introduced by the IA can be converted into noise equivalent temperature dividing Eq. (2.26) by the sensitivity of the bridge, i.e.,

$$S_{T, \text{IA (RTI)}}^{1/2}(T, \omega) = \frac{e_{\text{IA, RTI}}(T, \omega)}{s_b(T)}. \quad (2.29)$$

Evaluation of Eq. (2.29) leads to the results given in Figure 2.12.

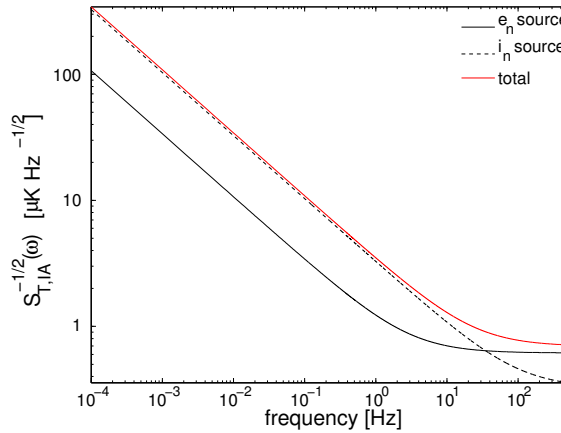


Figure 2.12: Noise introduced by the amplification stage. The noise in the measurement corresponds to that at the modulating frequency ($=5.55\text{ Hz}$) —see §2.3.1. The modulating frequency cannot be set arbitrarily high due to the settling time of the anti-alias filter.

Two important aspects must be noted from Figure 2.12: (i) the dominating noise source comes from the noisy current sources of the IA [which translates into noise voltage when coupling with the Wheatstone bridge impedance —see Eq. (2.26)] and, (ii) the noise in the MBW, i.e. at the milli-Hertz region exceeds the requirement of $10^{-5}\text{ K Hz}^{-1/2}$ if no lock-in amplification is used. Actually, the noise at 1 mHz is one order of magnitude higher than that. However, we have to keep in mind that the the noise of the IA is modulated by the demodulation of the Wheatstone bridge signal, thus, the $1/f$ noise of the IA is shifted to the modulating frequency, ω_b , and the IA noise present at the modulating frequency is shifted to the baseband —see §2.3.1. This means that the noise introduced in the MBW during the amplification stage must be calculated at $f = \omega_b/2\pi$, i.e., at 5.55 Hz . Figure 2.13 shows the actual noise introduced by the IA as a function of the measured temperature. The discontinuities are caused by the change of scale —see Table 2.3.

Other sources of error that might affect the performance of the system are the common-mode voltage error and the gain temperature coefficient of the IA. The common-mode voltage at the input

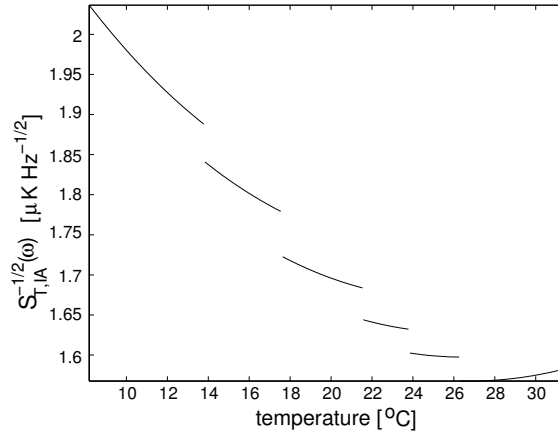


Figure 2.13: Noise introduced by the IA after the demodulation process. This is the noise at $f = \omega_b/2\pi = 5.55$ Hz.

of the IA is not cancelled by the modulation/demodulation process, hence, this error appears at the output of the IA attenuated by the IA CMRR. The errors can be up to $140 \mu\text{K}$ in a very worst case. However, we are not interested in absolute temperature values but in their relative changes, thus, the common-mode voltage can only be a problem if the temperature coefficient of the CMRR of the IA is high —see appendix §A.6. The other important parameter to take into account is the temperature coefficient of the IA gain, $\alpha_{G_{IA}}$. The temperature coefficient of the amplification stage is

$$\alpha_{IA}(T) = v_o(T)\alpha_{G_{IA}}. \quad (2.30)$$

The maximum permitted TC of the IA gain is readily calculated by

$$\frac{v_o(T)\alpha_{G_{IA}}}{s_b(T)} S_{T,\text{FEE}}^{1/2}(\omega) \leq S_{T,\text{req}}^{1/2}(\omega) \quad (2.31)$$

where the value obtained for $\alpha_{G_{IA}}$, assuming $S_{T,\text{FEE}}^{1/2}$ lower than $0.1 \text{ K Hz}^{-1/2}$, is 3.5 ppm K^{-1} . The value for the AD624 is 3.5 ppm K^{-1} (the FM model IA, the AD620, is slightly higher, 10 ppm K^{-1}).

The low-pass filter stage is included to limit the signal bandwidth before sampling and, thus, reduce as much as possible the effect of the aliasing due to high frequency noise and interference signals. The cut-off frequency of the filter cannot be reduced arbitrarily: there is a compromise between the settling time of the filter and the aliasing errors. The low-pass filter implemented is a second order Sallen-Key Butterworth —see Figure 2.14— with $R_1=2.84 \text{ k}\Omega$, $R_2=10.7 \text{ k}\Omega$, $C_1=100 \text{ nF}$ and $C_2=33 \text{ nF}$. This results in a cut-off frequency of 500 Hz .

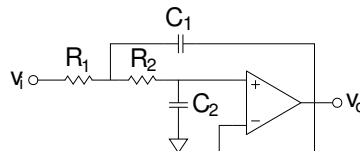


Figure 2.14: Second order Sallen-Key Butterworth low-pass filter.

Each time the polarity of the bridge is reversed or another channel is selected, the filter has to settle to the new value. Thus, it is necessary to introduce a delay after a change in the input before

acquiring the signal with the ADC. For this reason the data from the first 10 ms are discarded after a change in the bridge polarity or in the channel selected. This dead-time reduces the error of this effect at the level of the pico-Kelvin —see appendix §A.7.

2.3.2.5 Analog-to-digital conversion stage

The analog-to-digital conversion circuit has been implemented using a complete integrated complementary metal oxide semiconductor (CMOS) sampling ADC (AD977 of Analog Devices for the prototype and ADS7809 of Texas Instruments for the FM design)¹⁴. This stage contains a 16-bit capacitive-based successive approximation register (SAR) ADC with sample-and-hold, reference voltage, clock and serial data interface. This implementation reduces the external components to a minimum. As mentioned in §2.3.2.2, the voltage reference of the ADC is also used to feed the Wheatstone bridge to obtain a voltage reference-independent conversion —see Eq. (2.19). Two different sources of noise appear during the analog-to-digital conversion: (i) the noise (transition noise) calculated in Eq. (2.23) which for $G_{IA} = 200$ is (at most) $\simeq 0.8 \mu\text{K Hz}^{-1/2}$ and, (ii) the quantisation noise, which for an ideal ADC is¹⁵

$$S_q(\omega) = \frac{\Delta^2}{12} \frac{1}{f_s/2} \quad (2.32)$$

where $\Delta = V_{FS}/2^{N_{\text{bit}}}$ is the quantisation step or least significant bit (LSB). The quantisation noise with $f_s=38.4 \text{ kHz}$, $N_{\text{bit}}=16$ and $V_{FS}=10 \text{ V}$ is $\simeq 0.2 \mu\text{K Hz}^{-1/2}$ from dc to $f_s/2$. Thus, the noise introduced by the ADC to the system is within the requirements, i.e., below $10 \mu\text{K Hz}^{-1/2}$.

Finally, the full-scale error drift due to the temperature affects the measurement. The temperature coefficient of this stage is

$$\alpha_{\text{ADC}}(T) = v_o(T) \alpha_{G_{\text{ADC}}} \quad (2.33)$$

where $\alpha_{G_{\text{ADC}}}$ is the temperature coefficient of the ADC gain. The following expression permits to calculate its maximum permitted value,

$$\frac{v_o(T) \alpha_{G_{\text{ADC}}}}{s_b(T)} S_{T, \text{FEE}}^{1/2}(\omega) \leq S_{T, \text{req}}^{1/2}(\omega). \quad (2.34)$$

The value obtained for $\alpha_{G_{\text{ADC}}}$, assuming $S_{T, \text{FEE}}^{1/2}$ lower than $0.1 \text{ K Hz}^{-1/2}$, is 35 ppm K^{-1} . The AD977 gain temperature coefficient is around 7 ppm K^{-1} (the FM ADC, ADS7809, has the same TC).

2.3.3 Digital signal processing

The digital signal processing consists, basically, in the digital demodulation of the signal v_o . The process is the following: during one polarity N points of M points are averaged (the first 10 ms are discarded to avoid errors due to the low-pass filter settling time —see §2.3.2.4). When the polarity of the bridge is reversed the same process is done and then the two averaged samples are subtracted and divided by 2 to obtain the final value.

The digital processing chain extends from the ADC output to the final temperature value. In the prototype design, it has been implemented in the firmware of the electronics [using a 16F877 PIC of Microchip] and in a computer running a Labview application software [in the FM design it is implemented in a field programmable gate array (FPGA) in the DAUs of the DMU and in the DPU —see Figure 1.12]. The digital demodulation described above is shown in the block diagram of Figure 2.15, which is an alternative representation of the typical demodulation scheme —see Figure 2.3— that permits to easily analyse the noise in the system.

¹⁴Space qualified constraints force to use 16-bit ADC [44]. Furthermore, ADCs with higher number of bits are Delta-Sigma which, in general, are not suitable for multiplexed systems nor for signals with steep changes (such as a square wave) due to *long* stabilisation times.

¹⁵Problems with the non-ideality of the quantisation transfer curve of the ADC are discussed in §6.

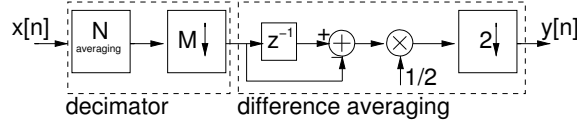


Figure 2.15: Digital demodulation block diagram. $d[n]$ is the signal quantised by the ADC. The analog signal processing block is shown in Figure 2.5.

The digital output from the ADC, $x[n]$, consists of M samples ($=3456$, or 90 ms), however, only N samples ($=3072$, or 80 ms) are averaged —see Table 2.4. This is equivalent to a low-pass filter and a subsequent downsampling by M . This process results on an equivalent resolution of¹⁶ [74, 22, 70]

$$N_{\text{eq bit}} = N_{\text{bit ADC}} + \frac{1}{2} \log_2 N \simeq 22 \text{ bit} \quad (2.35)$$

which meets the required resolution in Eq. (2.18) —see §2.3.2.1. The equivalent transfer function of the digital averaging is

$$|H_N(\omega)| = \frac{\sin \pi N \omega / \omega_s}{N \sin \pi \omega / \omega_s} \quad (2.36)$$

where N is the number of averaged points and $\omega_s/2\pi$ is the ADC sampling frequency. The power spectral density of the downsampled (by M) signal is [100]

$$S_{M\downarrow}(\omega) = \sum_{k=0}^{M-1} S_N \left(\omega - k \frac{\omega_s}{M} \right) \quad (2.37)$$

where S_N is the spectrum of the digitised data after the averaging, i.e.,

$$S_N(\omega) = |H_N(\omega)|^2 S_d(\omega) \quad (2.38)$$

with S_d the spectrum of the digitised analog signal, i.e.,

$$S_d(\omega) = \sum_{k=-\infty}^{\infty} S_{T,\text{analog}}(\omega - k\omega_s). \quad (2.39)$$

The spectrum of the discrete signal is essentially free of aliasing since the sampling frequency —see Table 2.4— is well above the cut-off frequency of the anti-alias filter (500 Hz). Therefore, $S_d(\omega) = S_{T,\text{analog}}(\omega)$ from dc to $f_s/2$, or

$$S_d(\omega) = S_{T,\text{analog}}(\omega) = S_{T,\text{b}}(\omega) + S_{T,\text{IA}}(\omega) + S_{T,\text{ADC}}(\omega) \quad (2.40)$$

where $S_{T,\text{b}}$, $S_{T,\text{IA}}$ and $S_{T,\text{ADC}}$ are the noise of the Wheatstone bridge, the noise of the IA and the noise of the ADC¹⁷, respectively.

The actual temperature value is obtained by taking the average difference of two consecutive samples. This is equivalent to an average difference and a subsequent downsampling by 2. The transfer function of the average difference is

$$H_{\text{diff}}(\omega) = \frac{e^{-i\omega/\omega_s M} - 1}{2} \rightarrow |H_{\text{diff}}(\omega)| = |\sin \pi M \omega / \omega_s| \quad (2.41)$$

¹⁶Due to the oversampling and considering white noise greater than the quantisation noise at the input of the ADC.

¹⁷The high frequency transition noise of the ADC is aliased because is not low pass filtered.

and the power spectral density of the signal downsampled by 2, i.e., the output temperature measurement, is

$$S_{2\downarrow}(\omega) = \sum_{k=0}^1 S_{\text{diff}}\left(\omega - k\frac{\omega_s}{2M}\right) \quad (2.42)$$

where

$$S_{\text{diff}}(\omega) = |H_{\text{diff}}(\omega)|^2 S_{M\downarrow}(\omega). \quad (2.43)$$

The parameters involved in the digital processing are summarised in Table 2.4.

Parameter	Value	Description
N	3072	Number of averaged samples
M	3456	Number of samples per polarity
$\omega_s/2\pi$	38.4 kHz	ADC sampling frequency
$\omega_b/2\pi$	5.55 Hz	Frequency of the square wave

Table 2.4: Parameters and their values involved in the digital signal processing of the prototype TMS.

The resultant total noise after the analog and signal processing chain is given in next section.

2.3.4 Theoretical noise equivalent temperature

Once all the signal processing chain (analog and digital) has been described we proceed to the evaluation of the theoretical expected noise of the system. It is calculated by using Eqs. (2.36) to (2.43). Results are shown in Figure 2.16.

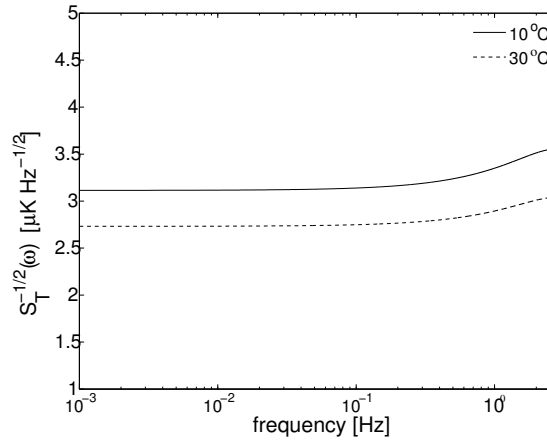


Figure 2.16: Theoretical noise for the TMS at $T=10\text{ }^\circ\text{C}$ and $T=30\text{ }^\circ\text{C}$ after the analog and digital signal processing. The noise is slightly higher when measuring *low* temperature since the equivalent resistance of the bridge is higher at low temperatures.

The $1/f$ noise of the IA vanishes after the digital demodulation, and the resulting power spectral density is flat with a small increase at *high* frequencies due to the differentiation process. The noise figure is $\simeq 3 \mu\text{K Hz}^{-1/2}$ in the MBW, thus, within the requirement given in Eq. (2.1). Table 2.5 summarises the sources of noise of the complete signal conditioning chain.

Noise source	$S_T^{1/2} [\mu\text{K Hz}^{-1/2}]$
Bridge	2
IA	2
ADC	1
Total	3

Table 2.5: Main noise sources of the measurement system. The total noise is obtained by the quadratic sum of the noise figures.

The noise power spectral density shown in Figure 2.16 corresponds for a single channel measurement. Nevertheless, a multiplexing system is used in order to perform the required measurements —see §2.3.2.4 and §2.4.3. For this reason each independent temperature subsystem multiplexes six measurements¹⁸. This is equivalent to a raw downsampling by 6, i.e. with no previous anti-alias filtering. Consequently, all the energy above the frequency $f_b/(2 \cdot 6)$ will be aliased into the 0 to $f_b/(2M \cdot 6)$ band, or,

$$S_T(\omega) = \sum_{k=0}^5 S_{2\downarrow} \left(\omega - k \frac{\omega_b}{6} \right) \quad (2.44)$$

where $S_{2\downarrow}$ is the function plotted in Figure 2.16 and $\omega_b/2\pi$ is the main frequency of the square wave. Since $S_{2\downarrow}$ is almost constant, Eq. (2.44) reduces to

$$S_{T,\text{sys}}(\omega) \simeq 6S_{2\downarrow}(\omega), \quad 0 \leq \omega \leq \omega_b/2 \quad (2.45)$$

or, in words, the increase of the noise in the system due to the multiplexing scheme is proportional (in units of power spectral density) to the ratio f_1/f_2 where f_1 is the frequency of the square wave (or the final sampling frequency after the digital processing). This implies that, ideally, the expected noise of the temperature measurement system on-board the LTP is $\sqrt{6} \cdot 3 \mu\text{K Hz}^{-1/2} = 7.35 \mu\text{K Hz}^{-1/2}$, still within the requirements.

2.3.5 Temperature coefficient and uncertainty

During the analog signal processing chain it has been shown that the temperature coefficient of the electronic components plays an important role in the performance of the system. Figure 2.17 (left) shows the estimated temperature coefficient for the whole TMS —see appendix §A for details.

The highest value of the temperature coefficient is $60 \mu\text{K K}^{-1}$ (when measuring temperatures near 30°C). This value limits the maximum temperature fluctuations permitted in the electronics to

$$\alpha_{\text{FEE}}(T) S_{T,\text{FEE}}^{1/2}(\omega) \leq 10^{-5} \rightarrow S_{T,\text{FEE}}^{1/2}(\omega) \leq 0.16 \text{ K Hz}^{-1/2} \quad (2.46)$$

within the MBW. These temperature fluctuation levels are reasonable both in the on-ground test conditions —see §5— and in the spacecraft.

Finally, for completeness the uncertainty in the measurement chain is given in Figure 2.17 (right) —see appendix §A for details. This uncertainty, in principle, should not pose a problem in the measurement since we are interested in relative changes. The uncertainty is in the order of tens of milli-Kelvin if only the electronics is considered, however, the uncertainty of the thermistors is in the order of $\pm 0.5 \text{ K}$ and, thus, it dominates the global uncertainty.

¹⁸4 absolute and 1 differential measurements and 1 measurement between two references to check the electronics itself.

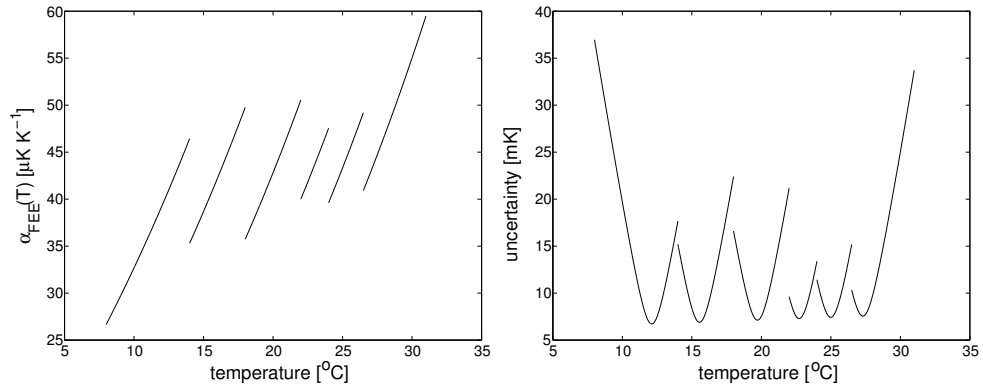


Figure 2.17: Left: theoretical global temperature coefficient of the system (worst-case analysis). Right: uncertainty of the system considering worst-case conditions. The tolerance of the thermistor is not considered which is ± 0.5 K and dominates the uncertainty of the measurement.

2.3.6 Scales changing scheme

As shown in the previous sections, six different scales are present in the system to deal with the temperature range in the LTP core assembly (LCA), i.e., from 10°C to 30°C . As shown in Table 2.3, the temperature range is split into six overlapping scales with a temperature span of $\simeq 7$ K. As explained in §2.3.2.1 and §2.3.2.4 the different scales are readily chosen by simply changing R_{ref} in the Wheatstone bridge by means of the MUXs commanded by digital signals.

The scheme implemented, though, does not coincide with the values of T_{min} and T_{max} given in Table 2.3. The scale changing scheme has been designed to maintain the Wheatstone bridge as close to zero as possible to minimise gain errors and their temperature dependence. The voltage values for the scale changing have been calculated as

$$v_{\text{o,IA}}^i(T) = -v_{\text{o,IA}}^{i+1}(T) \quad (2.47)$$

where $v_{\text{o,IA}}^i$ stands for the output voltage of the instrumentation amplifier when measuring with the reference scale i ($i=0, 1, \dots, 5$). Nevertheless, in order to avoid *chattering* due to the noise when changing the scale, a hysteresis scheme has been implemented. The width of the hysteresis is $\Delta T_{\text{h}} = T_{\text{u}} - T_{\text{d}} = 0.2$ K which is sufficiently large considering the small temperature changes expected in the measurements. This scheme is depicted in Figure 2.18.

The values of the scale changing are given in Table 2.6 in different units.

ref.	T_{min}	T_{max}	$V(T_{\text{min}})$	$V(T_{\text{max}})$	$C(T_{\text{min}})$	$C(T_{\text{max}})$
0	8.28	13.94	5	-2.43	32768	-15944
1	13.74	17.74	2.43	-2.94	15944	-19300
2	17.54	21.32	2.94	-2.14	19300	-14031
3	21.12	23.96	2.14	-1.64	14031	-10734
4	23.76	26.25	1.64	-1.64	10734	-10721
5	26.05	31.47	1.64	-5	10721	-32768

Table 2.6: References and their temperature range. The equivalent values in volts and in ADC counts are also given. The values differ from the ones given in Table 2.3 since the scale changing scheme has been defined in order to keep the Wheatstone bridge as close to zero as possible.

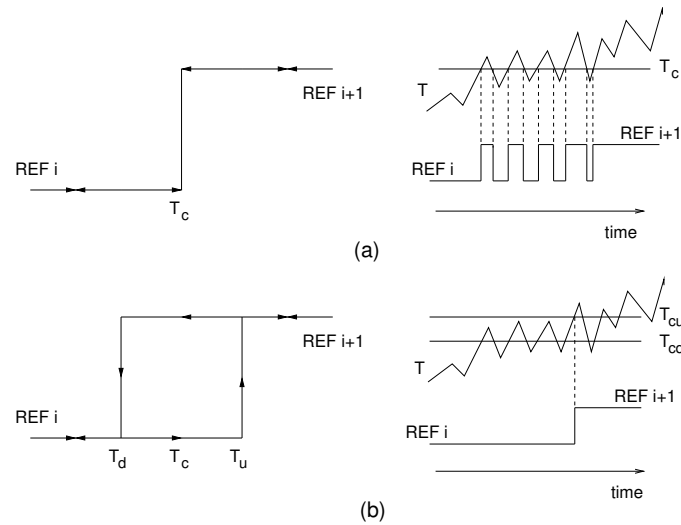


Figure 2.18: (a) Scale changing scheme with no hysteresis. Note that *chattering* appears during the change of the scale. (b) Scale changing scheme with hysteresis to avoid *chattering*.

2.4 Thermal diagnostic items positioning and connections

The data diagnostic subsystem (DDS) of the DMU is composed of two sets of three identical printed circuit boards (PCBs) [81] —see §1.4:

- the PDU (power distribution unit),
- the DPU (data processing unit) and,
- the DAU (data acquisition unit) —see Figure 2.19.

The two PDUs and DPUs operate in full hot/cold redundancy, i.e., only one PDU and one DPU operate at a time. Instead, the two DAUs [20] are both operative at the same time, and are not redundant from the diagnostics items point of view —see Figure 2.19. This means that if one of the DAUs fails, half of the diagnostic devices will become inoperative. The number of connectors in each DAU is less than the number of required diagnostics items connections, so the diagnostics items must be distributed between the two DAUs. An adequate connection distribution must be chosen to minimise losses in case of problems in one of the DAUs [113].

In the following sections we describe the location and the connections in the DAUs of the thermal diagnostic items: temperature sensors and heater devices.

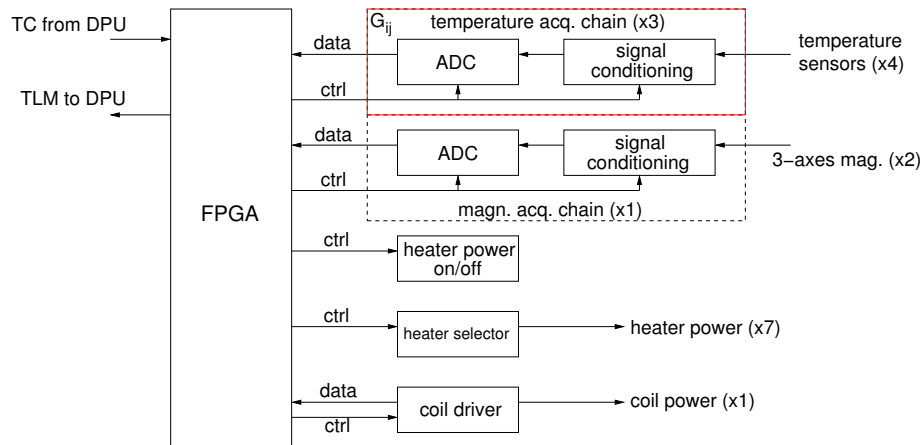


Figure 2.19: Scheme of the DAU functional blocks. Each DAU contains connections for 12 sensors. The number of sensors in the LTP is 24.

2.4.1 Temperature sensors location

The locations where temperature measurements are of interest are shown in Figure 2.20. They are the GRS, the OMS and the struts.

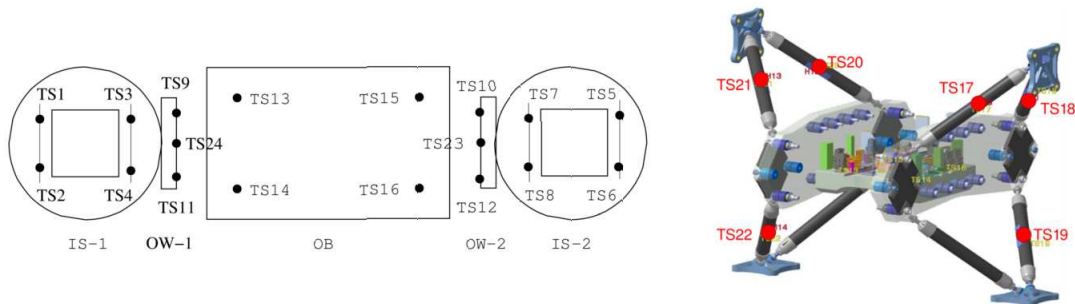


Figure 2.20: Temperature sensors (TS) distribution across the LTP.

A total of 24 sensors must be connected to the DAUs. The available connections in each of the DAUs are 12. The chosen connections are shown in Table 2.7. The connection configuration adopted has been based on the following criteria:

- *Gravitational reference sensor* Temperature gradients across the test mass are the most important measurement in this location, thus, pairs of sensors in the same GRS brought face to face must be connected to the same DAU¹⁹. For this reason TS1 and TS3 and TS5 and TS7 are connected to DAU-1 and TS2 and TS4 and TS6 and TS8 to DAU-2.
- *Optical bench* The configuration proposed is intended to keep acquiring OB data in case one of the DAUs fails.

¹⁹Differential measurements must be performed by sensors placed in the same DAU, even in the same group of each DAU —see Table 2.9.

- *Optical window* In principle, absolute and differential measurements are meaningful in this location [98]. Thus, TS9 and TS11 have been connected to DAU-1 and TS10 and TS12 to DAU-2. However if one of the DAUs fails no OW temperature read out would be available in one of the OWs. In order to avoid this limitation two sensors (TS23 and TS24) are added in each OW.
- *Struts* The configuration is based on the criteria to keep acquiring temperature data of the struts even if one of the DAUs fails.

location	DAU-1 sensor	DAU-2 sensor
GRS-1	TS1, TS3	TS2, TS4
GRS-2	TS5, TS7	TS6, TS8
OW-1	TS9, TS11	TS24
OW-2	TS23	TS10, TS12
OB	TS13, TS15	TS14, TS16
struts	TS17, TS19, TS21	TS18, TS20, TS22

Table 2.7: Temperature sensors: location and DAUs connections.

2.4.2 Heaters location

Heaters must be placed in different locations of the LTP to generate controlled thermal perturbations —see §1.6 and §7. Figure 2.21 shows the heaters distribution across the LTP chosen in order to accomplish their final purpose, i.e., to determine different thermal couplings in the LTP subsystems, together with the sensors information.

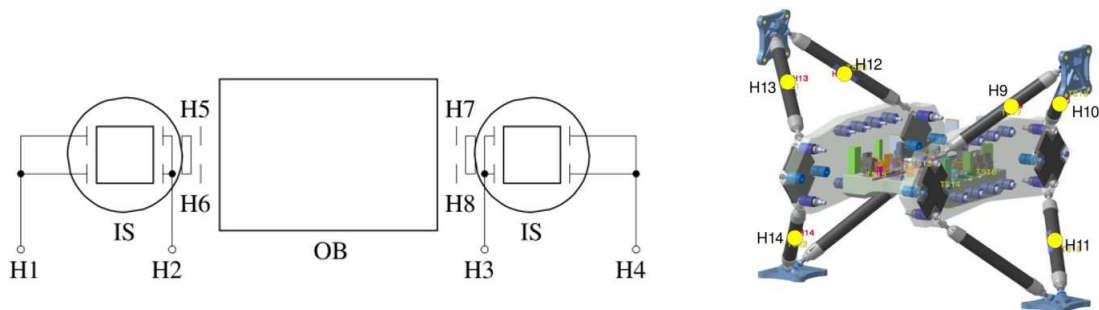


Figure 2.21: Heaters (H) distribution across the LTP.

The total number of *physical* heaters is 18. However, since the heaters placed in the same face of the same EH are connected together and they use the same connector, we can consider them as a single heater, we call them *logical* heaters. This is shown in Figure 2.21 where H1, H2, H3 and H4 are logical heaters although in fact each of them is formed of two physical devices. Thus, the number of *logical* heaters is 14. The number of available heaters connections in each DAU is 7, thus, as done with the sensors, we have to distribute the 14 heaters into the two DAUs. Table 2.8 summarises the heaters-DAUs connections which have been chosen based on the following criteria:

- heaters and temperature sensors must be somehow correlated, i.e., sensors and heaters placed close to each other must be connected to the same DAU,

- H1 and H2 must be connected to different DAUs (the same applies for heaters H3 and H4) since, if one of the DAUs fails, one heater will still remain operative in each IS,
- H5 and H6 are connected to different DAUs (the same for H7 and H8), hence, it will be possible to apply heat perturbations to both OWs even if one DDU fails.

location	DAU-1	DAU-2
	sensor	sensor
GRS-1	H1	H2
GRS-2	H3	H4
OW-1	H5	H6
OW-2	H7	H8
struts	H9, H11, H13	H10, H12, H14

Table 2.8: Heaters: location and DAUs connections.

Another issue to take into account is that the heaters in the GRS are NTC thermistors. The *standard* heaters placed in the OW and the struts were discarded to be used in the GRS for reasons such as outgassing constraints and potential magnetic incompatibilities. The idea of using thermistors as heaters in the GRS arose once the circuitry to control *standard* heaters was designed. Thermistors are compatible with the magnetic cleanliness requirements —see chapter §3— and their levels of outgassing are also compliant with the requirements [122]. The circuit to feed the heaters is a voltage source commanded by a digital-to-analog converter (DAC). This circuit is not the best option to feed thermistors when using them as heaters because, due to the self-heating effect, their resistance decreases and consequently, the current through them increases. Nevertheless, the power dissipated in the heaters of the GRS is tens of milli-Watt —see §7— which will not pose a problem even though we use a voltage source. In appendix B the use of thermistors instead of standard heaters to generate heat pulses in the GRS is discussed.

2.4.3 Summary of sensors and heaters location

Figure 2.22 summarises the location and the connections (to DAU-1 and DAU-2) of all the thermal diagnostic devices.

However, temperature sensors-DAUs connections need to be further specified. Each DDU consists of three identical independent electronic boards (G_{ij} —see Table 2.9 and Figure 2.19), each capable of performing four absolute temperature measurements, one differential measurement and one *check* measurement. Low noise differential measurements must be performed by sensors connected to the same group of one DDU. In view of this, the sensor connections and the measurement flow chart of both DAUs have been defined as shown in Table 2.9.

G_{11}	DAU-1		G_{12}	DAU-2	
	G_{12}	G_{13}		G_{22}	G_{23}
TS1 (IS-1)	TS5 (IS-2)	TS9 (OW-1)	TS2 (IS-1)	TS6 (IS-2)	TS10 (OW-2)
TS13 (OB)	TS17 (S)	TS19 (S)	TS14 (OB)	TS18 (S)	TS20 (S)
TS3 (IS-1)	TS7 (IS-2)	TS11 (OW-1)	TS4 (IS-1)	TS8 (IS-2)	TS12 (OW-2)
TS15 (OB)	TS21 (S)	TS23 (OW-2)	TS16 (OB)	TS22 (S)	TS24 (OW-1)
ref	ref	ref	ref	ref	ref
TS3–TS1	TS7–TS5	TS11–TS9	TS4–TS2	TS8–TS6	TS12–TS10

Table 2.9: Temperature measurements performed for each independent board on each of the two DAUs.

From Table 2.9 we see that the number of measurements is 36 and the sampling frequency is $1/1.2=0.833$ Hz (each measurement takes 200 ms and there are six measurements per group). This

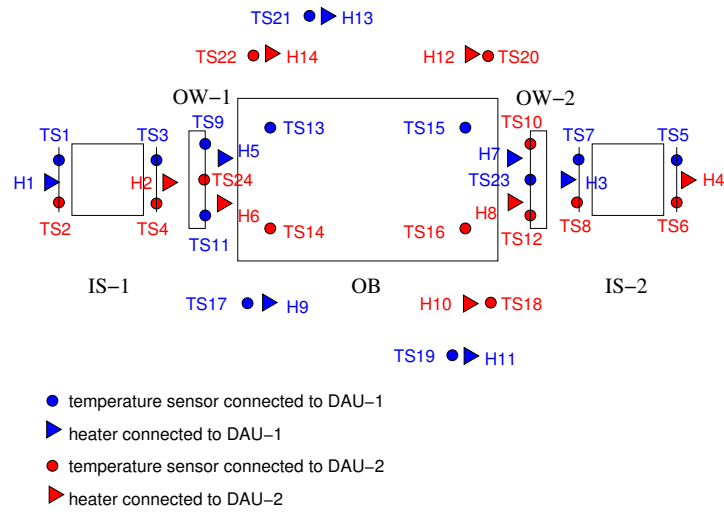


Figure 2.22: Summary of thermal diagnostics location and connections.

implies a bit rate of 1386.67 bps, which is considered too high. The bit rate has been reduced by a factor of four by means of a digital downsampling. This process is described in appendix C.

Chapter 3

Interactions with LTP subsystems

The interaction of the temperature measurement subsystem with the other subsystems on board the LTP is another issue that needs to be analysed. The thermal diagnostic subsystem might perturb other subsystems nearby and vice versa, i.e., some subsystems might degrade the measurement of temperature. We focus on the potential problems in the gravity reference sensor (GRS), since it is the most sensitive subsystem of the LTP with diagnostics devices in it. Two basic potential problems have been identified. On the one hand, the magnetic polarisation of the thermistors might be incompatible with the magnetic cleanliness requirements of the GRS and thus, they could cause an excess force noise in the test mass (TM) [120]. On the other hand, the capacitive coupling through stray capacitance between the electrodes of the capacitive sensor in the GRS (or other unforeseen interferences) and the temperature sensors might degrade the temperature measurement. Both problems are discussed in the following sections.

3.1 Thermistors magnetic polarisation

Four thermistors are attached to the outer face of the electrode housing (EH) surrounding the TMs. More specifically, two acting as sensors ($R_o=10\text{ k}\Omega$) and two acting as heaters ($R_o=2\text{ k}\Omega$) —see §2.4 and appendix §B— on each of the two EH face perpendicular to the LTP sensitive axis. All in all, eight devices are laid down around each of the TMs at a distance of only ~ 13 millimetres —see Figure 3.1.

NTCs however, as previously stated, are manufactured by mixing and synthesising oxides doped with metals such as manganese, nickel, cobalt, iron and copper [123, 160, 101]. Except manganese and copper, which show paramagnetic and diamagnetic behaviours, respectively, these materials show ferromagnetic behaviour. In spite of their tiny size, NTC magnetic properties can jeopardise the performance of the LTP, as they are placed quite near the TMs.

Magnetic cleanliness in the LTP must comply with the requirements that limit the acceptable values of magnetic field and magnetic field gradient in the region occupied by the TMs. These requirements are set both on dc values and fluctuations of these quantities —see §3.1.1. Previous missions such as the Advanced Composition Explorer (ACE)¹ currently measuring the magnetic field in the Lagrange point L1 (where LPF will operate) have shown that the interplanetary magnetic field will not pose a problem in this sense since its dc values and fluctuations are orders of magnitude below the LTP magnetic cleanliness requirements —see Figure 3.2 and Table 3.2.

¹Data extracted from www.srl.caltech.edu/ACE/ASC/level2/1v12DATA_MAG.html.

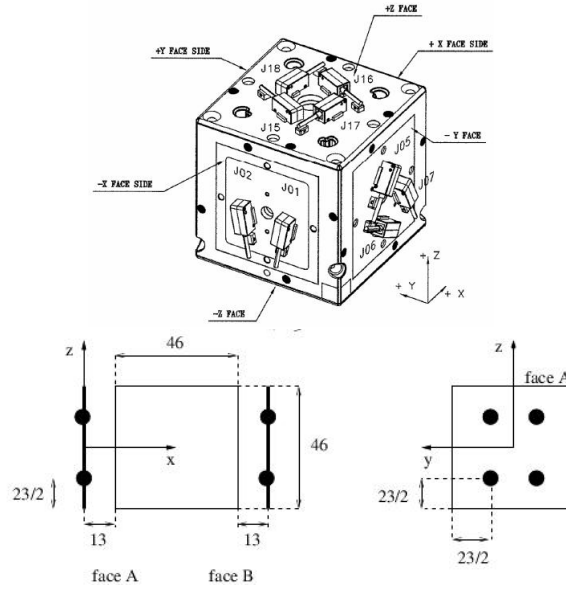


Figure 3.1: Top: EH perspective (thermistors are not drawn). Bottom: layout of the eight NTCs in the EH around one TM. Axes are labelled with distances in millimetres. The approximate distance of each thermistor to the TM is 13 mm.

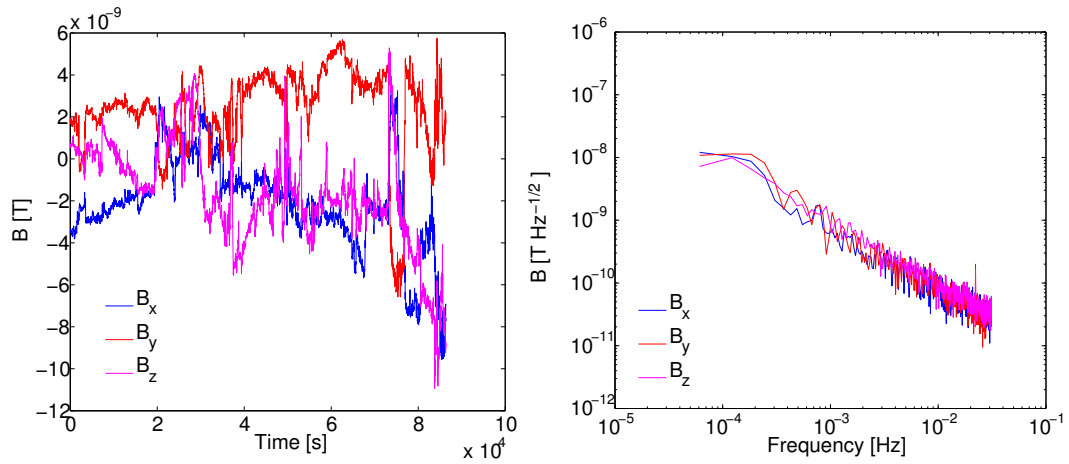


Figure 3.2: ACE mission data. Left: magnetic field in the Lagrange point L1. Right: magnetic field power spectral density in the Lagrange point L1. The requirement of the background dc value in the LTP is $10 \mu\text{T}$, at L1 the values are around the nano-Tesla. The fluctuations in L1 are also two orders of magnitude lower than the expected inside the LTP due to electronic systems [141] —see Table 3.2.

We thus only need to consider the magnetic field generated by the sources *inside* the LTP spacecraft and, among these, specially those that are close to the TMs, i.e., the thermistors. All magnetic sources will be outside the LTP core assembly (LCA) and are designed not to exceed the magnetic requirements in the TM location. Inside the LCA, only thermal diagnostic items will be close enough to perturb the magnetic cleanliness, in case of being magnetically active. The noise

acceleration budget assigned to magnetic effects has been set to [146]

$$S_{a, \text{magn}}^{1/2}(\omega) \leq 12 \text{ fm s}^{-2} \text{ Hz}^{-1/2} \quad (3.1)$$

in the LTP MBW.

The following sections address the problem of the potential excess noise caused by the magnetic behaviour of the thermistors. First we review the mechanism whereby magnetic fields induce forces on the TM. Second, we present the measurements performed to characterise magnetically the NTCs and the relationship between their magnetic moment and the created magnetic field and magnetic field gradient in the TM location. Finally, we estimate the effect of the thermistors on the TM noise, and suggest actions to minimise the risk of possible excess noise of this nature [120].

3.1.1 Force fluctuations in the TM due to magnetic field and magnetic field gradient

If a magnetic field \mathbf{B} acts on a small volume d^3x of magnetic material with low magnetic susceptibility χ and density of magnetic moment \mathbf{M} then the force on that small volume is given by [73]

$$\frac{d\mathbf{F}}{d^3x} = \nabla \left[\left(\mathbf{M} + \frac{\chi}{2\mu_0} \mathbf{B} \right) \cdot \mathbf{B} \right] = \left[\left(\mathbf{M} + \frac{\chi}{\mu_0} \mathbf{B} \right) \cdot \nabla \right] \mathbf{B} \quad (3.2)$$

where $\mu_0 = 4\pi \times 10^{-7} \text{ m kg s}^{-2} \text{ A}^{-2}$ is the magnetic constant. The second equality follows from the first as a consequence of Maxwell's equation $\nabla \times \mathbf{B} = 0$.

To calculate the total force on the TM, Eq. (3.2) must be integrated to its volume, $V = (46 \text{ mm})^3$. It is expedient to express the integral in terms of averaged quantities, defined by

$$\langle f \rangle \equiv V^{-1} \int_V f(x) d^3x \quad (3.3)$$

where f is any function, scalar, vector or tensor. We are mostly interested in the x -component of the force, as it is the relevant one for the mission science. With this notation,

$$F_x = V \langle \mathbf{M} \cdot \nabla B_x \rangle + \frac{\chi V}{\mu_0} \langle \mathbf{B} \cdot \nabla B_x \rangle. \quad (3.4)$$

The *fluctuations* of the force are, from Eq. (3.4), given by

$$\delta F_x = V \langle \delta \mathbf{M} \cdot \nabla B_x \rangle + V \langle \mathbf{M} \cdot \delta(\nabla B_x) \rangle + \frac{\chi V}{\mu_0} \langle \delta \mathbf{B} \cdot \nabla B_x \rangle + \frac{\chi V}{\mu_0} \langle \mathbf{B} \cdot \delta(\nabla B_x) \rangle \quad (3.5)$$

where δ refers to *temporal fluctuations*, and provided second order terms are neglected².

The magnetic field \mathbf{B} in Eq. (3.5) is the sum of the background field, \mathbf{B}_{bg} , and the field created by the thermistors (if any) \mathbf{B}_{NTC} :

$$\mathbf{B} = \mathbf{B}_{\text{bg}} + \mathbf{B}_{\text{NTC}} \quad (3.6)$$

Fluctuations of the density of magnetic moment of the TM, $\delta \mathbf{M}$, can be neglected since the environmental temperature is very stable [84], and the same applies to the magnetic field and magnetic field gradient fluctuations created by the NTCs. Consequently, Eq. (3.5) can be simplified to

$$\delta F_x = V \langle \mathbf{M} \cdot \delta(\nabla B_x) \rangle + \frac{\chi V}{\mu_0} \langle \delta \mathbf{B} \cdot \nabla B_x \rangle + \frac{\chi V}{\mu_0} \langle \mathbf{B} \cdot \delta(\nabla B_x) \rangle \quad (3.7)$$

² Terms of the form $\delta \mathbf{B} \cdot \delta(\nabla B_x)$, etc. These may be relevant in the presence of high frequency fields which, due to the quadratic coupling, can generate low frequency fluctuations. We do not consider this possibility here.

where $\delta\mathbf{B}$ and $\delta(\nabla B_x)$ refer only to the background magnetic field. A worst case estimate of the force fluctuations in the TM (in terms of spectral density) due to the magnetic properties of the TM and the magnetic field and magnetic field gradient in it is —see appendix §D,

$$S_{\delta F_x}(\omega) = V^2 |\langle \mathbf{M} \rangle|^2 S_{\nabla B_x}(\omega) + \left(\frac{\chi V}{\mu_0} \right)^2 |\langle \nabla B_x \rangle|^2 S_{\mathbf{B}}(\omega) + \left(\frac{\chi V}{\mu_0} \right)^2 |\langle \mathbf{B} \rangle|^2 S_{\nabla B_x}(\omega) \quad (3.8)$$

where $S(\omega)$ refer to power spectral densities. The values of $S_{\mathbf{B}}$ and $S_{\nabla B_x}$ are assumed uniform throughout the TM volume. This approach is, again, based on the assumption that fluctuations come only from the background field which can be considered *homogeneous* in the TM volume. The same applies to its fluctuations —see Table 3.2.

From Eq. (3.8) we note that the potential *excess* noise due to the presence of the NTCs surrounding the TM will only come from the last two terms, since the first term is only affected by the magnetic field gradient background fluctuations, $S_{\nabla B_x}$, and the density of magnetic moment of the TM, \mathbf{M} . Numerical evaluation of Eq. (3.8) depends on the values of the fluctuations of the environmental magnetic field and gradient, as dc magnetic fields couple to fluctuating fields to generate *noise*, due to non-null magnetic susceptibility, χ , of the TMs. The magnetic nominal properties of the TM are given in Table 3.1. The measurement and estimation of the averaged values in Eq. (3.8) caused by the presence of the NTCs, $|\langle \mathbf{B}_{\text{NTC}} \rangle|$ and $|\langle \nabla B_{\text{NTC}} \rangle|$, are detailed in §3.1.2, while the dc requirements for \mathbf{B}_{bg} and $\nabla B_{\text{bg},x}$ are given in Table 3.2.

$$\frac{|\chi|}{2 \cdot 10^{-5}} \quad \frac{|\mathbf{M}|}{2 \cdot 10^{-4} \text{ A m}^{-1}} \quad \frac{S_{\mathbf{M}}(\omega)}{\sim 0}$$

Table 3.1: TM magnetic properties [34, 124, 141, 146].

dc Req.	PSD est. $\forall \mathbf{x}$
$ \mathbf{B}_{\text{bg}} \leq 10 \mu\text{T}$	$S_{\mathbf{B}}^{1/2}(\omega) \leq 100 \text{ nT Hz}^{-1/2}$
$ \nabla B_{\text{bg},x} \leq 5\sqrt{3} \mu\text{T m}^{-1}$	$S_{\nabla B_x}^{1/2}(\omega) \leq 50\sqrt{3} \text{ nT m}^{-1} \text{ Hz}^{-1/2}$

Table 3.2: Magnetic dc requirements in the TMs [146] and estimated magnetic fluctuations in the TMs location [141, 145]. Note that $S_{\mathbf{B}}^{1/2} = S_{\mathbf{B}_{\text{bg}}}^{1/2}$ and $S_{\nabla B_x}^{1/2} = S_{\nabla B_{\text{bg},x}}^{1/2}$, since the magnetic field background and its gradient are the only time dependent terms.

The numbers shown in Tables 3.1 and 3.2 yield a *nominal* acceleration noise due to magnetic effects in the TM in absence of thermistors, i.e., for $\mathbf{B} = \mathbf{B}_{\text{bg}}$ and $\nabla B_x = \nabla B_{\text{bg},x}$. The values are given in Table 3.3, which will be the noise reference when considering the force noise added by the magnetisation of the thermistors. It is thus clear that the requirement set by Eq. (3.1) is comfortably satisfied in the absence of thermistors. The last row in Table 3.3 is the total magnetic noise spectral density, and is evaluated by the expression

$$S_{\text{total mag}}^{1/2}(\omega) = V \left[\left(\frac{\chi}{\mu_0} |\langle \nabla B_x \rangle| \right)^2 S_{\mathbf{B}}(\omega) + \left(|\langle \mathbf{M} \rangle| + \frac{\chi}{\mu_0} |\langle \mathbf{B} \rangle| \right)^2 S_{\nabla B_x}(\omega) \right]^{1/2} \quad (3.9)$$

where we have assumed that $S_{\mathbf{B}}$ and $S_{\nabla B_x}$ are uncorrelated.

Term	S_{F_x} [fN Hz ^{-1/2}]	S_{a_x} [fm s ⁻² Hz ^{-1/2}]
$V \langle \mathbf{M} \rangle S_{\nabla B_x}^{1/2}(\omega)$	1.68	0.86
$(\chi V/\mu_0) \langle \nabla B_x \rangle S_{\mathbf{B}}^{1/2}(\omega)$	1.67	0.85
$(\chi V/\mu_0) \langle \mathbf{B} \rangle S_{\nabla B_x}^{1/2}(\omega)$	1.67	0.85
$S_{\text{total mag}}^{1/2}(\omega)$	3.74	1.91

Table 3.3: Nominal (in absence of NTCs) noise values in terms of force and acceleration ($m_{\text{TM}}=1.96$ kg) within the MBW.

3.1.2 Magnetic field and magnetic field gradient in the TM due to NTCs. Measurement of the magnetic properties of the NTCs

G10K4D and G2K7D BetaTherm NTCs are small devices, 6 mm in diameter, and 2 mm thick [16]. Eight NTCs are surrounding each of the TMs at a distance of $\simeq 13$ mm as shown in Figure 3.1.

In the following, in order to estimate the magnetic field and magnetic field gradient caused by the thermistors in the TM, we shall make the assumption that the NTCs behave like magnetic dipoles of remanent magnetic moments, \mathbf{m}_a , $a=1, \dots, 8$. Given their small size, corrections to this hypothesis may only be tiny. Under this assumption, the magnetic field created by these dipoles will be given by [73]

$$\mathbf{B}_{\text{NTC}}(\mathbf{x}) = \frac{\mu_0}{4\pi} \sum_{a=1}^8 \frac{3(\mathbf{m}_a \cdot \mathbf{n}_a)\mathbf{n}_a - \mathbf{m}_a}{|\mathbf{x} - \mathbf{x}_a|^3} \quad (3.10)$$

and its gradient by

$$\frac{\partial B_{\text{NTC},i}}{\partial x_j} = \frac{\mu_0}{4\pi} \sum_{a=1}^8 \frac{3}{|\mathbf{x} - \mathbf{x}_a|^4} [(m_{a,i}n_{a,j} + m_{a,j}n_{a,i}) + (\mathbf{m}_a \cdot \mathbf{n}_a)(\delta_{ij} - 5n_{a,i}n_{a,j})] \quad (3.11)$$

where \mathbf{x}_a is the position of the a -th NTC, and \mathbf{n}_a is the unit vector in the direction from the a -th NTC to the field point \mathbf{x} , or $\mathbf{n}_a = (\mathbf{x} - \mathbf{x}_a)/|\mathbf{x} - \mathbf{x}_a|$. δ_{ij} is the usual Kronecker symbol. In order to evaluate Eqs. (3.10) and (3.11) and, thus, be able to calculate $|\langle \mathbf{B}_{\text{NTC}} \rangle|$ and $|\langle \nabla B_{\text{NTC},x} \rangle|$ we need to know the magnetic moments of the NTCs, \mathbf{m}_a . In the following sections we describe the measurements done to characterise magnetically the NTCs.

3.1.3 NTCs magnetic characterisation

The instrument used to characterise the magnetic properties of the thermistors is a Quantum Design MPMS XL SQUID of the Serveis Científic-tècnics of the Universitat de Barcelona. The tests consisted in measuring the magnetic moment, \mathbf{m} , of the NTCs when subjected to an external varying magnetic field, \mathbf{H} , and thus obtain the hysteresis cycle of the device. In order to fully characterise the thermistor, the hysteresis curve was measured in two different orientations of the NTCs relative to the direction of the external field (configurations parallel and orthogonal) —see Figure 3.3.

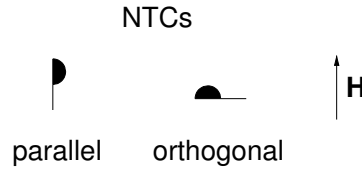


Figure 3.3: Orientation configurations of the NTCs inside the SQUID with respect to the applied external magnetic field, \mathbf{H} , for the NTC magnetic moment measurement.

We first characterised a BetaTherm 10 k Ω NTC (intended to be used as temperature sensor) and a BetaTherm 2 k Ω NTC (intended to be used as heater in the EH). The results are shown in Figure 3.4. All the measurements were done at 300 K since is the expected temperature at the TM location.

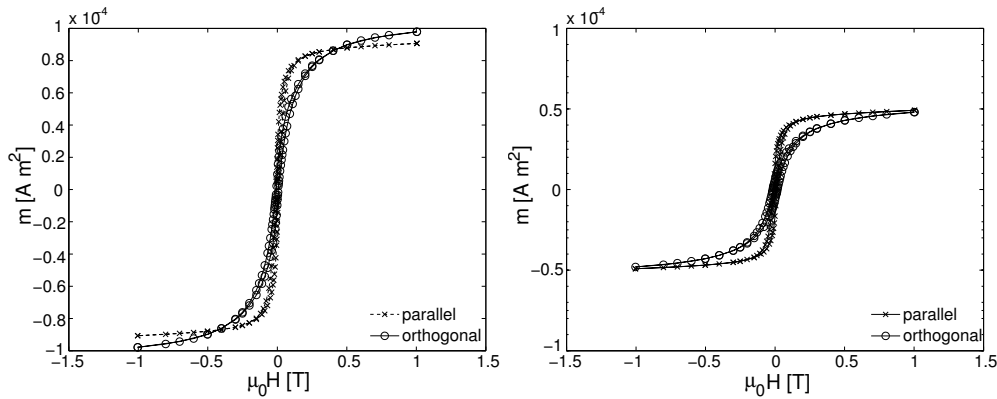


Figure 3.4: Hysteresis curve at 300 K for the 10 k Ω BetaTherm NTC thermistor (left) and the same for the 2 k Ω thermistor (right).

Results given in Figure 3.4 show that both items exhibit a ferromagnetic behaviour (coercive field, $\mu_0 |\mathbf{H}_{\text{coer}}|$, is about 10 mT), and that the remanent magnetic moment, \mathbf{m}_r , of the 10 k Ω NTC is slightly higher than that of the 2 k Ω one. Table 3.4 summarises these results.

Conf.	2 k Ω		10 k Ω	
	$ \mathbf{m}_r $	$ \mathbf{m}_{\text{sat}} $	$ \mathbf{m}_r $	$ \mathbf{m}_{\text{sat}} $
Par.	16 $\mu\text{A m}^2$	50 $\mu\text{A m}^2$	26 $\mu\text{A m}^2$	90 $\mu\text{A m}^2$
Orth.	7 $\mu\text{A m}^2$	50 $\mu\text{A m}^2$	9.4 $\mu\text{A m}^2$	100 $\mu\text{A m}^2$

Table 3.4: BetaTherm (2 k Ω and 10 k Ω) NTCs magnetic properties. Coercive field, $|\mu_0 \mathbf{H}_{\text{coer}}|$, for both sensors and configurations is 10 mT.

The values of the remanent magnetic moment, \mathbf{m}_r , are indicative of the very worst case since they reflect the magnetisation of the sensor after being saturated. The saturating magnetic field is around 500 mT, a considerably large one.

The assessment of the effect of NTCs on the LTP acceleration noise depends on the quality of the determination of the magnetic properties of the thermistors, specially the remanent magnetic moment parameter, \mathbf{m}_r . In view of this, measurements of a set of BetaTherm NTC thermistors (four samples) and another type of thermistor, YSI NTC (five samples of the YSI 44031 bead type

model), were performed to ratify the parameters given in Table 3.4 and to compare them with another type of thermistor (the YSI one). Thermistors tested were all of 10 k Ω . NTCs of 2 k Ω were not tested because they are less *magnetic* than the 10 k Ω ones —see Table 3.4. Moreover, the magnetic moment of the BetaTherm thermistor was measured only for the parallel configuration since this corresponds to the worst case —see Table 3.4. The orientation in the YSI thermistors was irrelevant due to its spherical symmetry. Hysteresis curves for both sets of thermistors are shown in Figure 3.5.

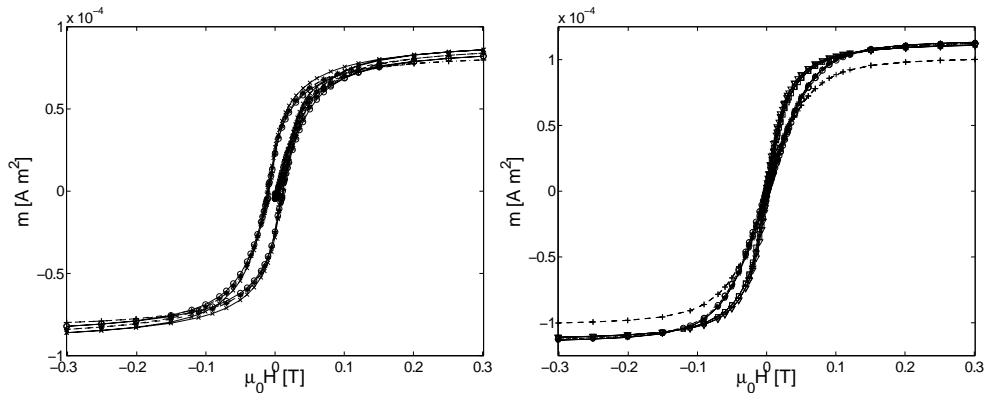


Figure 3.5: Left: hysteresis curve at 300 K for the set (four samples) of 10 k Ω NTC thermistors of BetaTherm and parallel configuration. Right: *idem* for the set of YSI thermistors.

Figure 3.5 (left) confirms the behaviour observed in the measurements done previously with the BetaTherm NTCs, i.e., ferromagnetism. However, Figure 3.5 (right) shows that YSI thermistors get easily demagnetised after removing the external magnetic field, i.e., they have a comparatively small coercive field ($\simeq 1$ mT) and a small susceptibility, too. Finally, Figure 3.5 shows that the results for each set of thermistors are consistent with one another (small standard deviation values). Results are summarised in Table 3.5.

Sensor	$ \mathbf{m}_r $	$ \mathbf{m}_{\text{sat.}} $	$\mu_0 \mathbf{H}_{\text{coer.}} $
BetaTherm	$24 \pm 2 \mu\text{A m}^2$	$83 \pm 2.5 \mu\text{A m}^2$	10 mT
YSI	$1.8 \pm 0.5 \mu\text{A m}^2$	$110 \pm 5 \mu\text{A m}^2$	1 mT

Table 3.5: Magnetic properties for the two sets of thermistors tested. BetaTherm values are for the parallel configuration (see Figure 3.3) and for the 10 k Ω of nominal resistance only. Four BetaTherm samples and five YSI samples were measured.

3.1.4 Numerical calculations

In order to evaluate Eq. (3.8) we first calculate the averaged values of the magnetic field and magnetic field gradient created by the NTCs —Eqs. (3.10) and (3.11). We make the simplifying assumption that all 8 NTCs are 10 k Ω , even if only 4 are. We accordingly overestimate the magnetic effect, which gets us on the safe side.

The evaluation of the averaged values has been done by means of numerical methods. More specifically, by a finite element method (FEM) approach: the volume of the TM, $(46 \text{ mm})^3$, has been divided into N volume elements, $\Delta V (=V/N)$, and for each ΔV Eqs. (3.10) and (3.11) have

been used, then the average value and modulus calculated, i.e.,

$$\langle \mathbf{B}_{\text{NTC}} \rangle \simeq N^{-1} \sum_{k=1}^N \mathbf{B}_{\text{NTC}}(\mathbf{x}_k) \quad (3.12)$$

$$\langle \nabla B_{\text{NTC},x} \rangle \simeq N^{-1} \sum_{k=1}^N \nabla B_{\text{NTC},x}(\mathbf{x}_k) \quad (3.13)$$

where \mathbf{x}_k is the position of the k -th volume element. This has been chosen of 8 mm^3 , which corresponds to $N=12167$. Decreasing the size of the volume elements did not improve the results of the computations. Calculations considering different orientations of the eight magnetic moments of the NTCs allow us to know the worst possible magnetic moment orientation combinations for each axis. These are summarised in the four configurations shown in Figure 3.6. In terms of magnetic field, configurations B and D give the highest mean magnetic field value. However, the magnetic field gradient is zero. On the contrary, configurations A and C yield the highest mean value of the magnetic field gradient, but the mean magnetic field is zero. Intermediate configurations have been seen to produce milder effects.

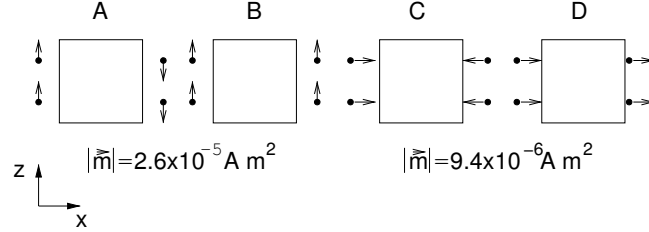


Figure 3.6: Configurations analysed for the evaluation of Eqs. (3.10) and (3.11). Configurations A and B assume the magnetic moments of all NTCs are oriented along the z -axis. However, in configuration A magnetic moments take opposite directions, while in B all the orientations are equal. Configurations C and D assume all the NTCs are oriented along the x -axis. In configuration C magnetic moment orientations are antiparallel, while in configuration D all the orientations coincide. This four configurations cover the worst cases. The magnetic moment values used are extracted from Table 3.4.

The results obtained for the configurations given in Figure 3.6 are summarised in Table 3.6, and they can be seen graphically for configurations A and B in Figure 3.7.

Conf.	$\langle \mathbf{B} \rangle$; $ \langle \mathbf{B} \rangle $ [μT]	$\langle \nabla B_x \rangle$; $ \langle \nabla B_x \rangle $ [$\mu\text{T m}^{-1}$]
A	(0,0,0); 0	(0,0,15.5); 15.5
B	(0,0,-0.25); 0.25	(0,0,0); 0
C	(0,0,0); 0	(-11.3,0,0); 11.3
D	(0.18,0,0); 0.18	(0,0,0); 0

Table 3.6: Mean values and modulus for the magnetic field and magnetic field gradient caused by the eight NTCs in the TM. The magnetic moment used in configurations A and B is $|\mathbf{m}_r| = 26 \mu\text{A m}^2$, and $|\mathbf{m}_r| = 9.4 \mu\text{A m}^2$ for configurations C and D —see Table 3.4 and Figure 3.6.

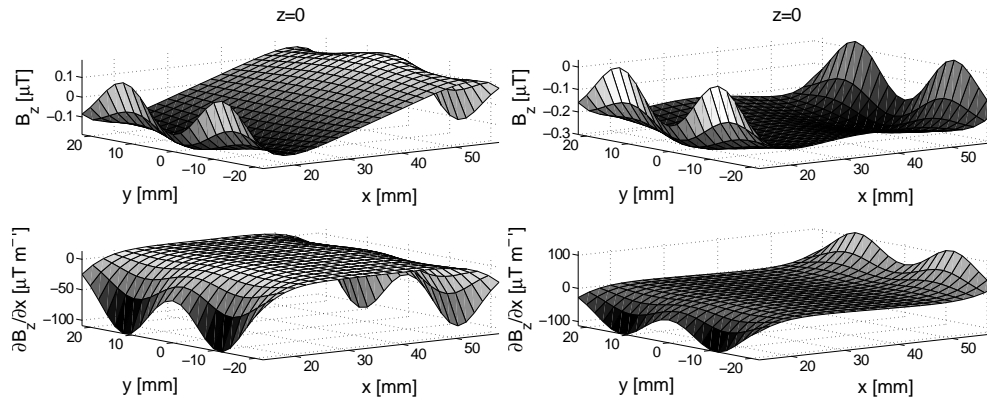


Figure 3.7: Left: configuration A (see Fig. 3.6) and $|\mathbf{m}_r|=26 \mu\text{A m}^2$. Top: Representation of the z -component of the magnetic field in the equatorial plane of the TM, i.e., xy -plane for $z=0$ —see Figure 3.1. The parity symmetries of field and gradient, $B_z(x, y) = B_z(x, -y) = -B_z(-x, y)$, and $\partial_x B_z(x, y) = \partial_x B_z(x, -y) = \partial_x B_z(-x, y)$, respectively, are clearly visible in the plots. In view of these symmetries, the field at the top averages to zero, while the gradient at the bottom does not. Right: configuration B (see Figure 3.6) and $|\mathbf{m}_r|=26 \mu\text{A m}^2$. In this case the parity symmetries of field and gradient are slightly different: $B_z(x, y) = B_z(x, -y) = B_z(-x, y)$, and $\partial_x B_z(x, y) = \partial_x B_z(x, -y) = -\partial_x B_z(-x, y)$, and are also reflected in the plots. In view of these symmetries, the gradient at the bottom averages to zero, while the field at the top does not. See Table 3.6 for numerical results.

3.1.5 NTCs first magnetisation curve

The magnetic moments used in the calculations of the previous section are remanent magnetic moments *after* saturating the NTCs. However, it must be realised that the magnetic fields the LTP will go through, from the launch pad to the operation orbit, are orders of magnitude below the saturation field of the thermistor $\mu_0 H_{\text{sat}} \sim 500 \text{ mT}$. For instance, the Earth magnetic field is in the order of $50 \mu\text{T}$, the magnetic field in the van Allen belts is of the same order of magnitude³, and the interplanetary magnetic field is in the order of $10\text{-}100 \text{ nT}$ [21] —see Figure 3.2. These values suggest that we are heavily overestimating the effect of the NTCs on the TM when using the remanent magnetic moment after saturation, which fully magnetises the device⁴.

To fine-tune the previous estimates, we proceeded to analyse the first magnetisation curve (FMC) of the NTCs. The FMC is obtained by means of a two step procedure [129]: (i) an alternate magnetic field with decreasing amplitude is applied to the sample in order to demagnetise it to the level of the instrument resolution, and (ii) an external magnetic field which slowly increases in small steps ($\sim 0.1 \text{ mT}$ in our case) is applied to the sample.

With this method, we first *erase* the magnetic moment of the NTC to then evaluate the *magnetic response* of the thermistor. We thus obtain the first response to the magnetic field, which will be lower than the response after applying a strong magnetic field. The FMC has been measured for the two sets of $10 \text{ k}\Omega$ NTC thermistors studied previously, the BetaTherm and the YSI ones. However, the demagnetisation was only meaningful for the BetaTherm NTCs due to its ferromagnetic behaviour, though not so for the YSI NTCs due to their narrow hysteresis curve —cf. §3.1.3. Results are shown in Figure 3.8 and summarised in Table 3.7.

³Data extracted from the mission Champ, www.gfz-postdam.de/pb1/op/champ/results/index_RESULTS.html.

⁴The highest risk of exposition to stronger fields actually resides in the *transport* phases of the LTP on-ground, when stronger magnetic fields in transporting vehicle machinery may cause problems.

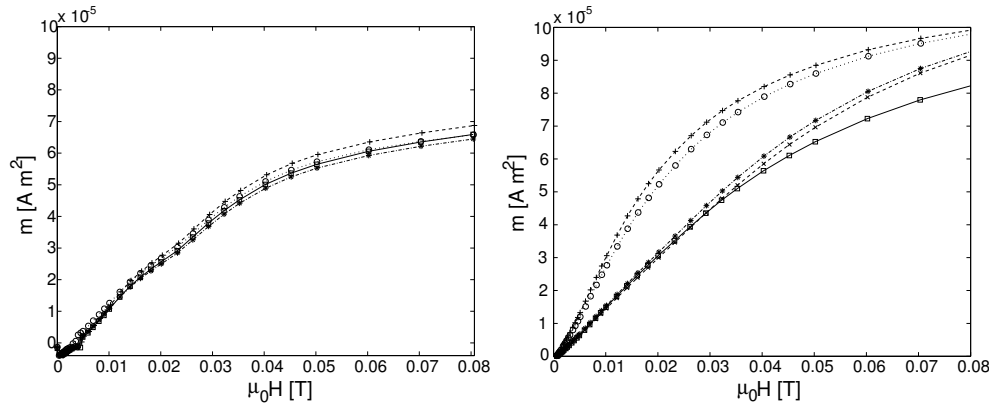


Figure 3.8: Measured FMC. Left: set of four BetaTherm samples (10 k Ω and parallel configuration). Right: set of five YSI samples.

Sensor	$ \mathbf{m}_{\text{demag}} $ [$\mu\text{A m}^2$]
BetaTherm	1.4 ± 0.2
YSI	0.75 ± 0.06

Table 3.7: Remanent magnetic moment after demagnetisation, $\mathbf{m}_{\text{demag}}$.

The FMC for the BetaTherm NTCs can be linearised near the full demagnetisation zone. We find

$$|\mathbf{m}_{\text{FMC}}| \simeq 1.45 \times 10^{-3} \mu_0 |\mathbf{H}_{\text{FMC}}| \quad (3.14)$$

where international system units are used. This is very accurate up to magnetic fields of about 40 mT. However, because magnetisation is not a reversible process, the above approximation cannot be used when it comes to estimating the remanent magnetisation *after* the field which magnetised the NTC is switched off. It does however provide an *upper limit* of the magnetisation remaining in the device, which corresponds to that reached when the field was on —see Figure 3.9. Equation (3.14) will be useful to determine the maximum external magnetic field which the BetaTherm NTCs can tolerate, once the largest magnetic moment compatible with the TM magnetic acceleration noise budget is determined —see §3.1.6.

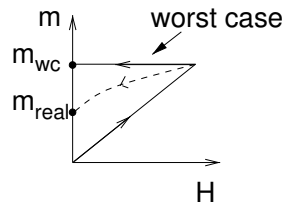


Figure 3.9: Magnetic moment vs. external magnetic field. After applying an external magnetic field the remanent magnetic moment is \mathbf{m}_{wc} in the very worst case assumption. \mathbf{m}_{real} is a somewhat more realistic value.

Now we re-calculate Table 3.6 with the magnetic moment after demagnetisation. The values obtained are given in Table 3.8.

Conf.	$\langle \mathbf{B} \rangle; \langle \mathbf{B} \rangle $ [μT]	$\langle \nabla B_x \rangle; \langle \nabla B_x \rangle $ [$\mu\text{T m}^{-1}$]
A	(0,0,0); 0	(0,0,0.84); 0.84
B	(0,0,0.01); 0.01	(0,0,0); 0

Table 3.8: dc values after demagnetisation ($|\mathbf{m}_{\text{demag}}|=1.4 \mu\text{A m}^2$) for the 10 k Ω BetaTherm NTCs for the configurations A and B (worst-cases).

Values shown in Table 3.8 are all within the requirements given in Table 3.2. Actually, the mean values of magnetic field and magnetic field gradient have been reduced by a factor of 20 due to the magnetic moment reduction by a factor of 20 achieved with the demagnetisation process.

3.1.6 Excess TM noise calculations

The results obtained in §3.1.4 and §3.1.5 can now be used to calculate the force/acceleration *excess* noise in the TM due to the presence of the thermistors. We only have to substitute the mean values of the magnetic field and magnetic field gradient into Eq. (3.8). Calculations are given in Table 3.9 for the BetaTherm and YSI thermistors and using the magnetic moment for the worst case (NTCs fully magnetised) and for the best case (NTCs fully demagnetised) for both thermistor sets.

Term	No NTCs	BetaTherm		YSI	
		$ \mathbf{m}_r =$ $24 \mu\text{A m}^2$	$ \mathbf{m}_{\text{demag}} =$ $1.4 \mu\text{A m}^2$	$ \mathbf{m}_r =$ $1.8 \mu\text{A m}^2$	$ \mathbf{m}_{\text{demag}} =$ $0.75 \mu\text{A m}^2$
$V \langle \mathbf{M} \rangle S_{\nabla B_{\text{bg},x}}^{1/2}(\omega)$	1.68	1.68	1.68	1.68	1.68
$\frac{\chi V}{\mu_0} \langle \nabla B_x \rangle S_{B_{\text{bg}}}^{1/2}(\omega)$	1.67	4.77	1.84	1.91	1.75
$\frac{\chi V}{\mu_0} \langle \mathbf{B} \rangle S_{\nabla B_{\text{bg}}}^{1/2}(\omega)$	1.67	1.67	1.67	1.67	1.67
$S_{\text{total mag}}^{1/2}(\omega)$	3.74	5.82	3.82	3.86	3.78
Δ	—	55.6%	2.14%	3.21%	1.07%

Table 3.9: Force noise values for the BetaTherm and YSI sensors. Both in configuration A (worst case) —see Figure 3.6. Units in $\text{fN Hz}^{-1/2}$.

The excess noise, Δ , is defined by

$$\Delta \doteq \frac{S_{\text{total mag,NTCs}}^{1/2} - S_{\text{total mag,no NTCs}}^{1/2}}{S_{\text{total mag,no NTCs}}^{1/2}} \quad (3.15)$$

and $S_{\text{total mag}}^{1/2}$ has been calculated using Eq. (3.9).

From Table 3.9 we notice that in any case the total required magnetic cleanliness is reached —see Eq. (3.1)— since the maximum acceleration noise (BetaTherm NTC in configuration A and $|\mathbf{m}_r| = 24 \mu\text{A m}^2$) is $5.82/1.96=2.97 \text{ fm s}^{-2} \text{ Hz}^{-1/2}$. BetaTherm thermistors in the very worst case increase the *excess* noise by 55%, whereas the YSI NTCs in the very worst case add a mere 3% *excess* noise. When demagnetising the thermistors, a clear improvement can be observed in the BetaTherm NTCs. Such large improvement is not observed in the YSI ones, as previously stated.

If the noise added by BetaTherm thermistors is required not to exceed 10% of the nominal one then we can calculate the background magnetic field to which they can be exposed. A 10% increase of the nominal noise is (in the MBW)

$$S_{F_x,10\% \text{ increase}}^{1/2}(\omega) \leq 4.1 \text{ fN Hz}^{-1/2} \quad (3.16)$$

which means that

$$|\langle \nabla B_{\text{NTC},x} \rangle| \leq 12 \mu\text{T m}^{-1} \quad (3.17)$$

From Eq. (3.17) we can now calculate the maximum magnetic moment permitted assuming configuration A (worst case scenario). This results in

$$|\mathbf{m}|_{\max} \leq 18.5 \mu\text{A m}^2 \quad (3.18)$$

which, using Eq. (3.14), leads to

$$\mu_0 |\mathbf{H}|_{\max} \leq 13 \text{ mT} \quad (3.19)$$

Consequently, in order to minimise the contribution of the NTCs to acceleration noise in the TMs, they should not be exposed to magnetic fields higher than 13 mT after having been demagnetised.

In conclusion, the work reported in this section originated from the observation that NTC thermistors, due to the materials they are made of, might constitute a problem potentially able to compromise the achievement of LISA Pathfinder's science output. The reason is that such materials have ferromagnetic properties, whereby they become sources of magnetic field which contribute to increase the acceleration noise of the LTP proof masses. The proximity of some of the NTCs to the TMs was an additional element of risk for the optimum performance of the LTP. A quantitative study of the effects of the NTCs on the TMs was therefore mandatory.

The study has revealed that, under the most unfavourable conditions, very unlikely to be met in practise, the magnetic properties of the NTCs selected to fly in LPF can degrade the performance of the LTP, increasing the magnetic noise by $\sim 55\%$ relative to the background. Even in such extreme conditions the budgeted magnetic noise, $12 \text{ fm s}^{-2} \text{ Hz}^{-1/2}$ (or $23.5 \text{ fN Hz}^{-1/2}$), is not reached —see Table 3.9.

It also appears from the present study that *demagnetisation* of the NTCs produces very good results: the magnetic noise they induce can be reduced by about an order of magnitude, which makes it mostly negligible. In addition, the strong fields required for magnetic saturation are as high as a fraction of a Tesla, an extremely high field intensity which makes re-magnetisation a very unlikely process in any LTP circumstances [142].

For completeness, and as a backup, two families of NTC thermistors were subjected to the same analysis: one was manufactured by BetaTherm, the other by YSI. The first had been chosen for flight before the magnetic issues were spotted, while the second had been considered less convenient, on the basis of prior laboratory research work. It appears that the YSIs are significantly less magnetic than the BetaTherm's, and this translates into a milder contribution to the total noise when the former are used *without demagnetising* them first. However, the differences when the NTCs are demagnetised basically disappear. The presumed stability of the demagnetised state in the BetaTherm's —see previous paragraph— thus confirms that the initial choice to fly this NTC brand should be maintained.

3.2 Interferences in the thermistors in the GRS

Thermistors in the GRS are attached to the outer surfaces of the electrode housing (EH). A potential problem arises due to the different *location* of the ground connections of the GRS front-end electronics and the data management unit (DMU), which contains the data acquisition and processing units. The outer surface of the EH (a plate of molybdenum) is grounded, but this ground might fluctuate with respect to the ground of the DMU since the latter is connected at another physical point. Depending on the value of the impedance between the two grounds the fluctuations might be *large* and, thus, due to a stray capacitance, C_p , between the EH molybdenum surface and the thermistors, these fluctuations can disturb the temperature read out —see Figures 3.10 and 3.11. Another potential interference comes from the 100 kHz signal of amplitude ~ 1 V used in the electrodes of the capacitive sensor intended to measure the position of the TMs —see §1.4. Any stray capacitance between the cables of the thermistor and the cables of the sensing electrodes causes the 100 kHz signal to appear in one of the arms of the Wheatstone bridge and, consequently, perturb the temperature measurement —see Figure 3.10. Both problems exist because the thermistors' cables inside the GRS cannot be shielded due to harness constraints.

Next sections describe this problem and quantify the potential impact in the measurement. First we analyse the analog signal chain, then we focus on the demodulation process. Finally, upper limits are given for the potential interferences/ground fluctuations.

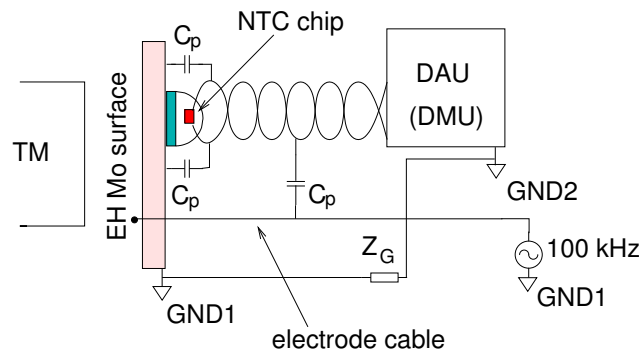


Figure 3.10: Scheme of the capacitive coupling between the EH walls and the TMS and between the electrode of the capacitive sensor and the TMS. The stray capacitances are a fair path to high frequency signals to appear in the temperature measurement.

3.2.1 Analog signal processing chain

The measurement of the resistance of the thermistors is based on the measurement of the difference voltage between the two arms of a Wheatstone bridge —cf. §2.3.2.1. The stray capacitance, C_{pi} —see Figure 3.10 and Figure 3.11— together with the fluctuations of the ground of the molybdenum plate with respect to the ground of the DMU, or the 100 kHz signal in the cables of the electrodes of the capacitive sensor can degrade the measurement of the thermistor resistance. The equivalent circuit to analyse this problem is shown in Figure 3.11 where v_i stands for the interference.

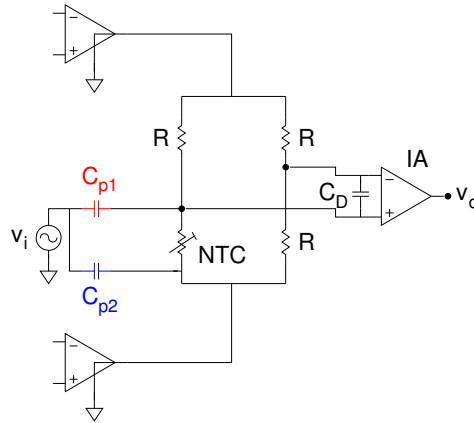


Figure 3.11: Schematic of the problem shown in Figure 3.10. v_i is the interference signal and $C_{p,i}$ the stray capacitances.

The stray capacitance at the output of the operational amplifier (OA), C_{p2} , will not affect the measurement due to the OA low-impedance output⁵. However, the stray capacitance at one of the inputs of the instrumentation amplifier (IA) will do. Figure 3.12 shows the equivalent circuit assuming the OA output impedance is zero, i.e., neglecting the effect of C_{p2} .

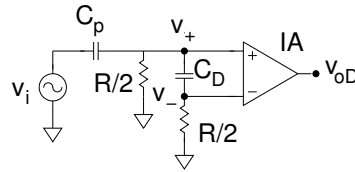


Figure 3.12: Equivalent circuit of the one given in Figure 3.11. C_{p2} is neglected since it does not perturb the measurement. It is also assumed that all the resistances of the bridge are R , i.e., 10 k Ω . The capacitor C_D is a 1 nF capacitor that acts as a differential low-pass filter.

From Figure 3.12 we find that the signal at the output of the IA due to an interference, v_i , is

$$v_o(s) = \frac{Z_x(s)}{Z_x(s) + Z_p(s)} \left[G_{IA} \left(1 - \frac{R/2}{R/2 + Z_D(s)} \right) + \frac{1}{2CMRR(s)} \left(1 + \frac{R/2}{R/2 + Z_D(s)} \right) \right] v_i(s) \quad (3.20)$$

where

$$Z_x = \frac{(R/2)(Z_D + R/2)}{Z_D + R}, \quad (3.21a)$$

$$Z_p = \frac{1}{sC_p}, \quad (3.21b)$$

$$Z_D = \frac{1}{sC_D}. \quad (3.21c)$$

The output of the IA, v_o , is low-pass filtered by the second-order Butterworth filter —see §2.3.2.4. A potential interference, v_i , will appear at the input of the analog-to-digital converter (ADC) in

⁵This OA is one of the OAs used for the ac square wave generation to feed the bridge —see §2.3.2.2.

the following manner:

$$v(s) = H_{\text{BW}}(s)v_o(s) \quad (3.22)$$

where v_o is given in Eq. (3.20) and H_{BW} is the transfer function of the Butterworth filter. The transfer function of the whole analog signal processing chain is plotted in Figure 3.13 with the following parameters: $R=10\text{ k}\Omega$, $C_{\text{D}}=1\text{ nF}$, $G_{\text{IA}}(s)=200(5 \cdot 10^4/s/2\pi+5 \cdot 10^4)$ and $CMRR(s)=3.1 \cdot 10^6(10/s/2\pi+10)$. The stray capacitance of the sensor was measured⁶: the value obtained was $C_{\text{p}} \simeq 3\text{ pF}$.

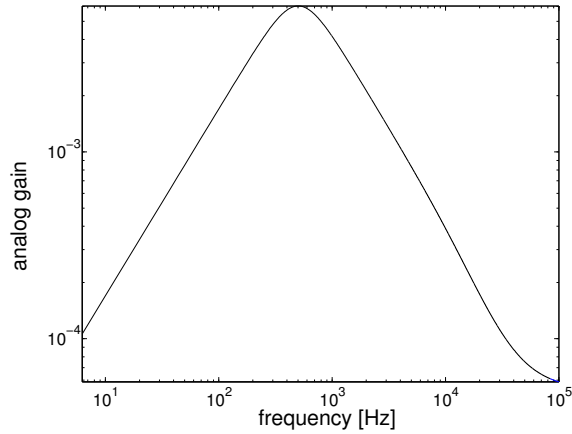


Figure 3.13: *Gain* of the interference signal at the input of the ADC after the analog signal conditioning circuit. The stages involved are three: the capacitive coupling, the IA and the low-pass filter.

3.2.2 Signal demodulation process

In this section we analyse how an interference signal appears in the temperature measurement after the digital signal processing, i.e., after the demodulation by the square wave signal. The interference signal —see Figure 3.11— is not modulated by the ac square wave bridge excitation. Thus, when the temperature signal coming from the bridge is demodulated, the interference signal is actually modulated —see §2.3.1. The problem analysed herein is reduced to the one shown in Figure 3.14 where $v(t)$ is the interference at the output of the ADC —see Eq. (3.22)— and $c(t)$ is the square wave used in the demodulation. For simplicity, we first assume $v(t)$ and $c(t)$ are continuous time-domain signals. The digitisation of the signals will be considered afterwards. In this section the analog signal processing chain is not considered. The whole chain (analog processing + digital processing) is analysed in §3.2.5 where it is compared with experimental results.

⁶The stray capacitance measured corresponds to that between the small aluminium plate of the thermistor and one of the cables of the thermistor.

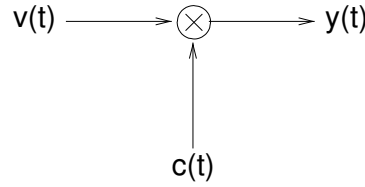


Figure 3.14: Signal demodulation. The interference, $v(t)$, is not modulated by the square wave excitation but it is *modulated* by the digital signal processing. This process consists in multiplying the interference, $v(t)$, by the square wave, $c(t)$.

The square wave signal, $c(t)$, is not a perfect square wave since dead times are incorporated to avoid errors due to the settling time of the anti-alias Butterworth filter —see appendix §A.7. The square wave signal is shown in Figure 3.15 where a is the dead-time, b is the integration time (for each polarity) and T ($= 2a + b$) is the period.

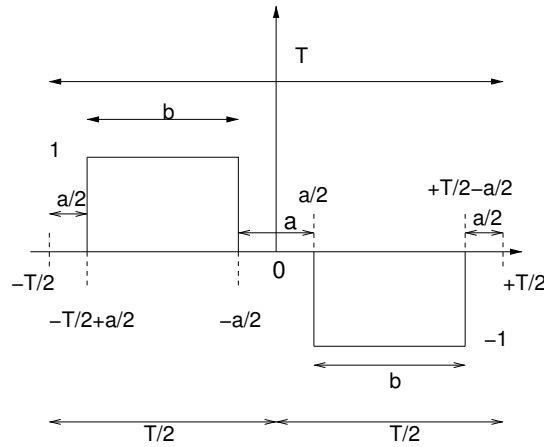


Figure 3.15: Square wave signal, $c(t)$, used in the demodulation process.

It is convenient to convert the signals, $v(t)$ and $c(t)$, to the frequency domain. To do this we first calculate the Fourier series of $c(t)$,

$$c(t) = \sum_{n=1}^{\infty} b_n \sin n \frac{2\pi}{T} t \quad (3.23)$$

where b_n is

$$b_n = \frac{1}{T/2} \int_{-T/2}^{T/2} c(t) \sin \left(\frac{n2\pi}{T} t \right) dt = -\frac{4}{n\pi} \sin \frac{n\pi}{2} \sin \frac{n\pi}{2T} (T - 2a). \quad (3.24)$$

Substituting Eq. (3.24) into Eq. (3.23) yields

$$c(t) = -\frac{4C_o}{\pi} \sum_{n=1}^{\infty} \frac{K(n)}{n} \sin n \frac{2\pi}{T} t \quad (3.25)$$

where, for clarity, we define $K(n)$ as

$$K(n) = \sin \frac{n\pi}{2} \sin \left[\frac{n\pi}{2T} (T - 2a) \right] \quad (3.26)$$

which is zero for n even.

The other signal involved in the process is the interference, $v(t)$. We assume the interference is a sine wave of frequency Ω , phase ϕ , and amplitude V , i.e.,

$$v(t) = V \sin(\Omega t + \phi). \quad (3.27)$$

We have the two waves of interest, $c(t)$ and $v(t)$, defined in the time domain. The latter is given in Eq. (3.27) and the former is given in Eq. (3.25). We write it down again with $C_o = 1$ —see Figure 3.15—,

$$c(t) = -\frac{4}{\pi} \sum_{n=1}^{\infty} \frac{K(n)}{n} \sin(n\omega_c t) \quad (3.28)$$

where $\omega_c/2\pi$ is the fundamental frequency of the square wave, i.e., $1/T$. The Fourier transforms of both signals are now readily obtained. They are:

$$\tilde{v}(\omega) = -i\pi V [e^{i\phi}\delta(\omega - \Omega) - e^{-i\phi}\delta(\omega + \Omega)], \quad (3.29a)$$

$$\tilde{c}(\omega) = i4 \sum_{n=1}^{\infty} \frac{K(n)}{n} \{\delta(\omega - n\omega_c) - \delta(\omega + n\omega_c)\}. \quad (3.29b)$$

These two signals are multiplied during the demodulation process in the time domain —see Figure 3.14—, which in the frequency domain is equivalent to the convolution,

$$y(t) = v(t)c(t) \rightarrow \tilde{y}(\omega) = \frac{1}{2\pi} \tilde{v}(\omega) * \tilde{c}(\omega). \quad (3.30)$$

The result of the convolution, \tilde{y} , is

$$\begin{aligned} \tilde{y}(\omega) &= \frac{1}{2\pi} \int_{-\infty}^{\infty} \tilde{v}(\omega') \tilde{c}(\omega - \omega') d\omega' \\ &= 2V \left[\sum_{n=1}^{\infty} \frac{K(n)}{n} \{e^{i\phi}\delta(\omega - \Omega - n\omega_c) - e^{i\phi}\delta(\omega - \Omega + n\omega_c) - \right. \\ &\quad \left. - e^{-i\phi}\delta(\omega + \Omega - n\omega_c) + e^{-i\phi}\delta(\omega + \Omega + n\omega_c)\} \right]. \end{aligned} \quad (3.31)$$

Two cases of interest as a result of the obtained output, \tilde{y} , are presented below: (i) when the interference signal is an even multiple of ω_c and (ii) when it is an odd multiple of ω_c . For the first case ($\Omega = n_\Omega \omega_c$ with n_{Omega} even), the interference, \tilde{v} , will appear at the output, \tilde{y} , at the following frequencies

$$\omega = \pm(n_\Omega + n)\omega_c, \quad (3.32a)$$

$$\omega = \pm(n_\Omega - n)\omega_c \quad (3.32b)$$

which implies that for $\omega = 0$ the output is zero [$K(n) = 0$ for n even]. Moreover all the frequency lines are multiples of ω_c . This is important because they will be killed by the posterior averaging —see §3.2.3. For the second case, i.e., when $\Omega = n_\Omega \omega_c$ with n_Ω odd Eq. (3.31) becomes

$$\begin{aligned} \tilde{y}(\omega) &= \tilde{y}(0) \Big|_{n=n_\Omega} + 2V \left[\sum_{\substack{n=1 \\ n \neq n_\Omega}}^{\infty} \frac{K(n)}{n} [e^{i\phi}\delta(\omega - (n_\Omega + n)\omega_c) + e^{-i\phi}\delta(\omega + (n_\Omega + n)\omega_c)] \right. \\ &\quad \left. + \sum_{\substack{n=1 \\ n \neq n_\Omega}}^{\infty} \frac{K(n)}{n} [-e^{i\phi}\delta(\omega + (-n_\Omega + n)\omega_c) - e^{-i\phi}\delta(\omega + (n_\Omega - n)\omega_c)] \right] \end{aligned} \quad (3.33)$$

where $\tilde{y}(0)|_{n=n_\Omega}$ stands for the signal at $\omega = 0$, i.e., the gain at dc, or

$$\tilde{y}(0)\Big|_{n=n_\Omega} = -4V \frac{K(n_\Omega)}{n_\Omega} \cos \phi. \quad (3.34)$$

All the terms in Eq. (3.33) will be killed by the digital filtering (since they are located at multiples of ω_c) —see §3.2.3— except the term $\tilde{y}(0)\Big|_{n=n_\Omega}$.

3.2.3 Digital filtering and downsampling

The digital filter consists of an average of N samples, with $N = (2b+2a)f_s$. We keep the continuous time analysis for simplicity, however, it must be noticed that $\tilde{y}(\omega)$ is repeated at multiples of f_s (the sampling frequency of the ADC, 38.4 kHz in the prototype and 50 kHz in the FM). The filter, in the continuous time domain, is

$$H(\omega) = \frac{T \sin \omega T/2}{2b \omega T/2} \quad (3.35)$$

where the factor $T/2b$ appears because the sum of all the samples is divided by $2b$ instead of T , i.e., the points within the dead times ($2a$) are not averaged. The filter is zero at integer multiples of ω_c .

After the filtering, the outputs for the two cases mentioned in the previous section are

$$\tilde{y}_F(\omega = 0) = -\frac{T}{2b} 4V \frac{K(n_\Omega)}{n_\Omega} \cos \phi, \quad (3.36)$$

and $\tilde{y}_F = 0$ for $\omega \neq 0$. Note that $\tilde{y}(0)$ is zero for n_Ω even since $K(n) = 0$. When n_Ω is odd the gain at dc depends on the phase, ϕ , of the interference, $v(t)$. Once the signal is filtered a downsampling by N is performed. The process of downsampling consists in

$$\tilde{y}_{DS}(\omega) = \sum_{\ell=0}^{N-1} \tilde{y}_F(\omega - \ell \frac{\omega_s}{N}) = \sum_{\ell=0}^{N-1} \tilde{y}_F(\omega - \ell \omega_c) \quad (3.37)$$

where $\omega_c/2\pi$ is the fundamental frequency of the square wave. The output of the downsampled signal is exactly the same of the one obtained after the filtering if the interference is a multiple of ω_c since the filter has zeroes at all the harmonics (a generalisation for any frequency is given in §3.2.4), i.e., $\tilde{y}_{DS}(\omega) = \tilde{y}_F(\omega)$. At this moment we have assumed that the interference complies with the Nyquist requirement, i.e., $\Omega < \omega_s/2$ and, thus, aliasing is not present. Later on this is taken into account.

Figure 3.16 shows the gain at dc as a function of the phase, ϕ , and the frequency of the interference, $n_\Omega \omega_c$. The plot in the right represents the worst-case, i.e., only the maximum value for each n_Ω bin (this occurs at $\phi = 0$ and $\phi = \pi$). Different vales of dead times, a , are shown to observe their effect on the interference signal. The gain at dc of the shifted component is calculated by evaluating the ratio between $\tilde{y}(0)$ and $\tilde{v}(\omega)$, or⁷

$$H_{dc} = \frac{\tilde{y}_{DS}(0)}{2\tilde{v}(n_x \omega_c)} = \frac{2}{\pi} \frac{K(n_\Omega)}{n_\Omega} \cos \phi \quad (3.38)$$

⁷The factor of 2 in the denominator is present because at dc the negative and the positive frequencies coincide.

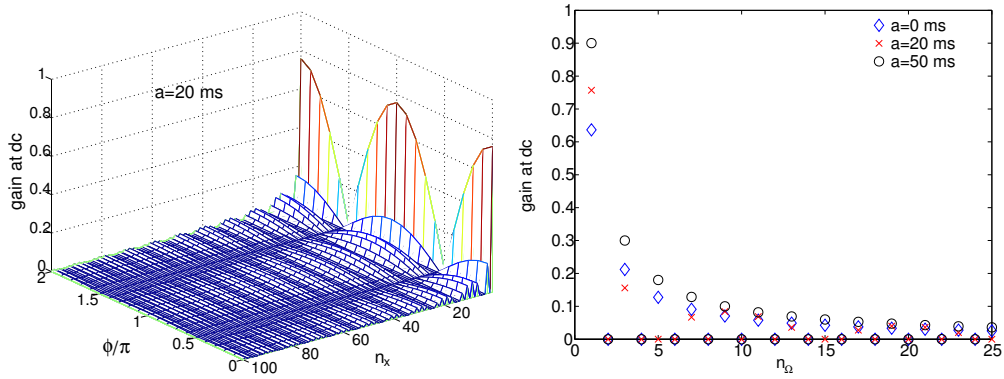


Figure 3.16: Left: gain at dc as a function of the frequency and the phase of the interference [Eq. (3.36)] with a dead time $a=20$ ms. Right: maximum gain for each frequency bin and different dead times (0 ms, 20 ms and 50 ms). If the interference is an even multiple of ω_c no signal is present at dc (nor at any other frequency) after the demodulation and the digital filter. However, if the frequency is an odd multiple of ω_c a signal at dc will appear due to the demodulation. The gain depends on the value of a . For instance for $a=50$ ms the gain of a sine wave interference $\Omega = \omega_c$ is 0.9, for $a=20$ ms is 0.75 and for $a=0$ ms is 0.63. This occurs because a square wave with dead times is more similar to a sine wave than an ideal square wave is.

3.2.4 Generalisation for any frequency

So far we have analysed the problem considering the interference signals are at multiples of the frequency of the square wave. In this section we give an expression for an interference signal at any frequency Ω . The downsampled output signal is

$$\tilde{y}_{DS}(\omega) = \sum_{\ell=0}^{N-1} \tilde{y}_F(\omega - \ell \frac{\omega_s}{N}) = \sum_{\ell=0}^{N-1} \tilde{y}_F(\omega - \ell \omega_c) \quad (3.39)$$

with

$$\tilde{y}_F(\omega - \ell \omega_c) = H(\omega - \ell \omega_c) \tilde{y}(\omega - \ell \omega_c) \quad (3.40)$$

where $H(\omega)$ is the filter given in Eq. (3.35). It can be shown that an interference at Ω will appear at a frequency within 0 and $\omega_c/2$ given by

$$\omega_o = |\Omega - n_\Omega \omega_c| \quad (3.41)$$

where

$$n_\Omega = \text{round} \left[\frac{\Omega}{\omega_c} \right]. \quad (3.42)$$

The signal that appears at ω_o is⁸

$$|\tilde{y}_{DS}(\omega_o)| = \begin{cases} 4V \frac{T}{2b} \left| \frac{K(n_\Omega)}{n_\Omega} \cos \phi \right|, & \omega_o = 0 \\ V \left| \sum_{k=1,3,5}^{N-1-n_\Omega} \frac{K(k)}{k} H(-\Omega - k\omega_c) - \sum_{k=1,3,5}^{N-1+n_\Omega} \frac{K(k)}{k} H(-\Omega + k\omega_c) \right|, & \omega_o \neq 0 \end{cases} \quad (3.43)$$

⁸The spectra of the modulated signal, \tilde{y} , is repeated at $m f_s / 2\pi$ (the ADC sampling frequency) for $m = \pm 1, \pm 2, \dots$. In order to obtain a *simple* expression we have assumed that it is only repeated at $\pm f_s$. If $f_s \gg f_c$ the assumption is accurate enough since we are only discarding the high frequency components of the signal that are weighted by $K(n)/n$.

and the gain is calculated as in Eq. (3.38), i.e.,

$$|\tilde{H}_{\text{DS}}(\omega_o)| = \begin{cases} \frac{2}{\pi} \frac{T}{2b} \left| \frac{K(n_\Omega)}{n_\Omega} \cos \phi \right|, & \omega_o = 0 \\ \frac{1}{\pi} \left| \sum_{k=1,3,5}^{N-1-n_\Omega} \frac{K(k)}{k} H(-\Omega - k\omega_c) - \sum_{k=1,3,5}^{N-1+n_\Omega} \frac{K(k)}{k} H(-\Omega + k\omega_c) \right|, & \omega_o \neq 0 \end{cases} \quad (3.44)$$

Figure 3.17 represents the *gain function* given in Eq. (3.44). The peaks (at ω_c , $3\omega_c$, $5\omega_c$, etc.) are gains at dc where the negative and positive frequency coincide. The rest of the signals are originated by intermediate frequencies and the frequency bin at which they will appear is calculated using Eq. (3.41).

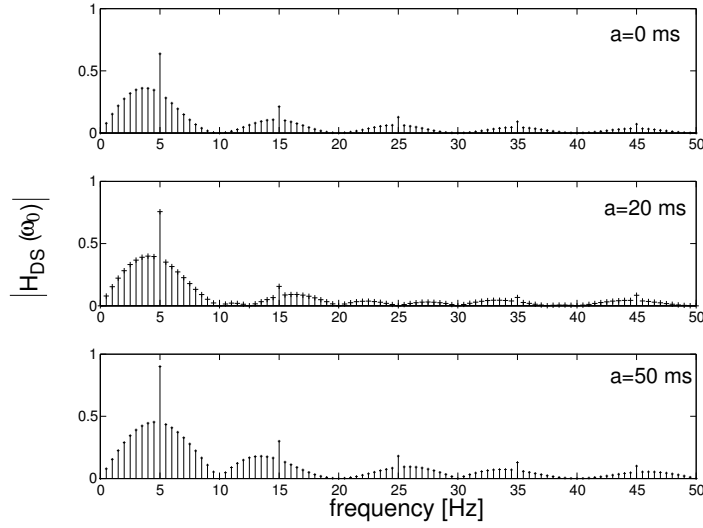


Figure 3.17: Gain after the digital demodulation and the digital filtering. Top: $a=0$ ms. Centre: $a=20$ ms. Bottom: $a=50$ ms. The frequency where the interferences will appear in $\tilde{y}(\omega)$ is calculated using Eq. (3.41). For instance, an interference at 24 Hz appears at 1 Hz with a certain attenuation depending on the the dead time value.

The gain pattern shown in Figures 3.16 and 3.17 is repeated at multiples of the sampling frequency of the ADC, f_s (38.4 kHz in the prototype and 50 kHz in the FM version), due to the aliasing introduced by the sampling of the ADC. For instance, a signal at $f_s + f_c$ will appear at f_c and then when demodulating will appear as a signal at dc —see Figure 3.18.

3.2.5 Experimental results

A test to verify the analysis was performed. The test included the whole measurement chain, i.e., the analog and digital signal processing, thus, the final output is the combination of the analog acquisition chain plus the digital demodulation. The test consisted in applying a sine wave of different frequencies and then measuring the output to estimate the gain of the whole system. The sine wave was injected as v_i in Figure 3.11 with $C_p=3$ pF which represents the worst-case scenario⁹. The experimental results and the theoretical values are shown in Figure 3.18. The agreement

⁹The 3 pF stray capacitance is the one between the small aluminium plate of the thermistor and its cables. In the case of the ground fluctuations the stray capacitance will not differ too much from this value, however, in the case of the interference coming from the electrodes of the capacitive sensor it can be much smaller. This depends on the harness configuration. The higher the distance between both cables (thermistors and electrodes) the lower the stray capacitance between them.

between the experimental and theoretical gain is good. It can be seen that high frequency signals appear in the MBW. For instance, an interference at $f_s + f_c$ (38 400 Hz+5 Hz) and another at f_c (5 Hz) have approximately the same effect in the MBW.

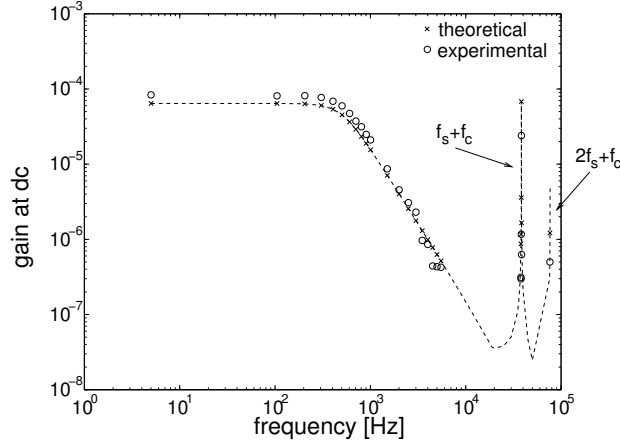


Figure 3.18: Experimental and theoretical results for the effect of a sine wave interference at one of the arms of the Wheatstone bridge. The plot represents the gain at dc, i.e., how a signal at high frequency appears in the measurement of temperature at dc (or at low frequency). The agreement between theoretical calculations and experimental results is good (the dashed trace is the envelope of the actual gain curve). The interferences used were at frequencies of 5 Hz, 105 Hz, 205 Hz, ..., etc. Note that due to aliasing an interference at 38 400 Hz+5 Hz ($f_s + f_c$) exhibits a gain similar to an interference at 5 Hz. f_s is the ADC sampling frequency and f_c is the frequency of the square wave.

3.2.6 Permitted amplitudes of the interferences

Once the transfer function between the effect of an interference signal and the temperature measurement has been found, we can set upper limits of the permitted amplitudes of the interference and of the ground fluctuations. Tentative numbers are given in the following sections which are split into two independent scenarios: ground fluctuations and sine wave interferences.

3.2.6.1 Sine wave interferences

We first consider the case of a pure sine wave as the interference at the input of the system. The fact that the capacitive sensor uses a signal of 100 kHz with an amplitude of 1 V makes relevant the analysis. By taking into account the gain curve shown in Figure 3.18 we can calculate the maximum permitted amplitude of the interference which does not affect the temperature measurement in a very worst-case, i.e., with $C_p=3$ pF.

The power spectral density of the temperature read out is estimated as [13]

$$\widehat{S}(\omega) = \frac{1}{t_m} \left| \int_0^{t_{tot}} x(t) e^{-i\omega t} dt \right|^2 \quad (3.45)$$

where t_m is the time of the measurement. In the case of the presence of an interference signal, $x(t)$ is

$$x(t) = v(t) + n(t) \quad (3.46)$$

where $v(t)$ is the interference and $n(t)$ is the nominal noise of the measurement. Substituting Eq. (3.46) into Eq. (3.45) yields

$$\widehat{S}(\omega) = \widehat{S}_n(\omega) + \frac{1}{t_m} |\tilde{v}(\omega)|^2 + \frac{1}{t_m} [\tilde{n}(\omega)\tilde{v}^*(\omega) + \tilde{n}^*(\omega)\tilde{v}(\omega)] \quad (3.47)$$

where \widehat{S}_n is the power spectral density of the noise. \tilde{v} and \tilde{n} are the Fourier transform of the interference and the noise signals, respectively. We want to find the maximum amplitude of the interference not to degrade the measurement, i.e., $\widehat{S}(\omega) \cong \widehat{S}_n(\omega)$ in Eq. (3.47). The “ \cong ” symbol in our case means that $\widehat{S}(\omega) < \widehat{S}_n(\omega)/10$, or

$$\frac{1}{t_m} |\tilde{v}(\omega)|^2 + \frac{1}{t_m} [\tilde{n}(\omega)\tilde{v}^*(\omega) + \tilde{n}^*(\omega)\tilde{v}(\omega)] < \frac{\widehat{S}_n(\omega)}{10} \quad (3.48)$$

where if we consider that¹⁰

$$|\tilde{v}(\omega)|^2 \gg \tilde{n}(\omega)\tilde{v}^*(\omega) + \tilde{n}^*(\omega)\tilde{v}(\omega) \quad (3.49)$$

we obtain

$$\frac{1}{t_m} |\tilde{v}(\omega)|^2 < \frac{\widehat{S}_n(\omega)}{10}. \quad (3.50)$$

The Fourier Transform of $v(t)$ (a sine wave of amplitude V and angular frequency Ω) during an integration time, t_m , is

$$\tilde{v}(\omega) = \frac{Vt_m}{2i} [\text{sinc}(\omega - \Omega)t_m/2 - \text{sinc}(\omega + \Omega)t_m/2] \quad (3.51)$$

thus, the maximum permitted amplitude of the interference for a given measurement time, t_m , is

$$V(\omega) < \frac{1}{\sqrt{5t_m/2}} \frac{1}{|H(\omega)|} \widehat{S}_n^{1/2}(\omega) \quad (3.52)$$

where $|H(\omega)|$ is the transfer function shown in Figure 3.18, i.e., the gain of the whole measurement chain for an interference signal assuming a stray capacitance of 3 pF. Equation (3.52) is plotted in Figure 3.19. The measurement time, t_m , considered is 10 ks. Theoretically, a signal of 100 kHz should not affect the measurement: the ADC (in the EM and the FM system) samples at 50 kHz, thus, a 100 kHz signal appears at dc due to aliasing, however, when demodulating by the 5 Hz square wave signal the interference is shifted to the 5 Hz frequency bin. Nevertheless, in practise the frequency of the interference will fluctuate around 100 kHz, and therefore the noise introduced in the MBW will not be exactly zero as it should ideally be.

The maximum amplitude for an interference at 100 kHz \pm 5 Hz considering a stray capacitance of 3 pF and an integration time of 10 ks is \sim 10 mV. However, the stray capacitance between the cables of the capacitive sensor and the thermistors' cables will be much lower than 3 pF, thus the maximum amplitude of the 100 kHz can be much higher than 10 mV. Moreover, if the frequency of the 100 kHz signal is stable, its effect on the TMS will be negligible.

3.2.6.2 Electrical ground fluctuations

For the ground fluctuations case we consider them as white noise. The noise introduced in the measurement bandwidth due to this effect is

$$\widehat{S}_n(\omega) = S_{n, \text{GND}}(\omega) 1 \sum_{n=0}^{\infty} \frac{|H(n\omega_c)|^2}{(2n+1)^2}. \quad (3.53)$$

¹⁰For long time measurements and assuming $v(t)$ is a sine wave, this is true since $|\tilde{v}(\omega)|^2$ is proportional to t_m^2 whereas $\tilde{v}(\omega)$ is proportional to t_m and $\tilde{n}(\omega)$ is white noise which its amplitude is constant independently of the measurement time.

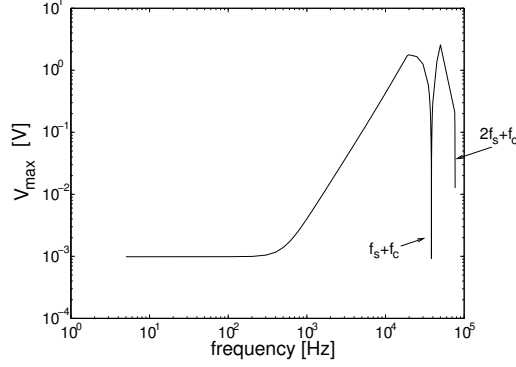


Figure 3.19: Maximum amplitude permitted for a sine wave interference not to affect the temperature measurement performance. The sampling frequency of the ADC is 38.4 kHz (in the FM is 50 kHz). The measurement time is 10 ks and the stray capacitance considered is 3 pF. The concern about ac interference signals comes, mainly, from the 100 kHz signal of the electrodes. The values shown in this figure are a very-worst case: actually, C_p should be much lower than 3 pF and the signal is at 100 kHz ($2f_s$), not 100 kHz+5 Hz ($2f_s + f_c$) which alleviates the risk of this problem.

The maximum permitted fluctuations between both grounds are readily obtained by considering that

$$S_{n, \text{GND}}(\omega) \sum_{n=0}^{\infty} \frac{|H(n\omega_c)|^2}{(2n+1)^2} < \frac{\hat{S}_n(\omega)}{10}. \quad (3.54)$$

If we truncate n to the 100 kHz range the term of the summatory is $\simeq 2 \cdot 10^{-10}$ and, therefore, the noise levels permitted are readily calculated: $S_{n, \text{GND}}(\omega) < 200 \text{ mV Hz}^{-1/2}$ (from zero to 100 kHz) which seems comfortable.

The analysis presented in this section describes a potential problem in the TMS due to the capacitive coupling between different systems in the GRS. Such problem mainly depends on the harness configuration of the subsystems in the LTP. One may not predict whether this problem will affect the temperature measurements or not until the test of the TMS within the assembled satellite will be performed, but at least the analysis presented here can provide a clue in case extra noise or anomalous behaviours are observed during such tests. The tests performed on ground to validate the TMS showed that it is very sensitive to capacitive couplings. In view of this, during such tests all the *metallic bodies* were always connected to the same ground of the electronics and, in addition, the cables were shielded —see chapter §5. Any missconfiguration led to noticeable interferences in the measurement, specially in long runs. For this reason capacitive coupling is an important issue to take into account in the performance of the TMS. Once more, such fears cannot be discarded until tests with the entire satellite will be performed.

Chapter 4

Test bed design for the TMS validation

This chapter describes the test bed designed to perform a meaningful test to determine the noise of the temperature measurement subsystem described in §2. Two configurations are discussed. The first one is intended to assess whether or not the requirements for the LTP TMS are met. The second configuration focuses on noise investigations in the thermistor and the electronics in the frequency range of LISA going one order of magnitude below that of LISA Pathfinder. The results obtained during the investigations in the MBW of LISA are, obviously, also useful for the temperature measurements of the LTP.

Both test bed configurations are based on the reduction of all possible environmental disturbances, mainly the temperature fluctuations at the location of the thermistors. If we ensure that the thermistors are placed in a sufficiently stable environment, we can ascribe all the fluctuations in the measurement to noise coming from the sensor or the electronics, not to temperature fluctuations. Consequently, the limits in the temperature measurements in the LTP can be established.

4.1 Test bed for the LTP requirements

A specific on-ground test to confirm whether or not the theoretical noise levels of the TMS given in §2.3 are accurate is absolutely necessary [84]. The sensors and the associated electronics must be able to make measurements capable of discerning temperature fluctuations at the level of $10^{-4} \text{ K Hz}^{-1/2}$ —cf. §1.5—, which implies a maximum equivalent temperature noise level in the sensor and electronics one order of magnitude lower, i.e., $10^{-5} \text{ K Hz}^{-1/2}$ —see §1.5 and §2. In order to do a meaningful test a stable thermal environment must be guaranteed for the sensors not to confuse real temperature fluctuations with sensor and/or electronic noise. In other words, real temperature fluctuations in the sensors must be at least one order of magnitude smaller than the limit imposed in Eq. (2.1), or

$$S_{\text{test bed}}^{1/2}(\omega) \leq 10^{-6} \text{ K Hz}^{-1/2}, \quad 1 \text{ mHz} \leq \omega/2\pi \leq 30 \text{ mHz}. \quad (4.1)$$

The required stability figure of Eq. (4.1) is not available in standard climatic chambers. The analysis and design of a special thermal insulator jig to guarantee the levels required by Eq. (4.1) have been necessary. The concept idea of the insulator is shown in Figure 4.1 [84, 97]: a block of aluminium inside a layer of polyurethane (or another insulating material) of suitable dimensions. The aluminium block ensures the temperature stability of the sensors attached to it, while the surrounding polyurethane shields them from external temperature fluctuations in the laboratory. The thermal insulator must be designed taking into account the necessity of placing and removing

different thermistors for test without damaging them —see Appendix E. In this section the design of such insulator is described.

4.1.1 Insulator design: theoretical analysis

A passive insulator capable of attenuating temperature fluctuations around five orders of magnitude needs to be designed. In order to do this we have found the theoretical transfer function of a multilayer insulator. The basic assumption for this analysis is that heat exchange between the interior of the jig and the laboratory ambient is only due to thermal conduction. For simplicity, the insulator is considered spherical in this analysis¹. Under these hypotheses, $T(r, t)$ satisfies Fourier's partial differential equation² [27]

$$\rho c \frac{\partial T(r, t)}{\partial t} = \kappa \nabla^2 T(r, t) \quad (4.2)$$

where ρ , c , and κ are the density, the specific heat and the thermal conductivity, respectively, of the substrate. They can be represented as discontinuous functions if we consider three layers³, i.e.,

$$\rho, c_p, \kappa(r) = \begin{cases} \rho_1, c_{p1}, \kappa_1, & \text{if } 0 \leq r \leq a_1, \\ \rho_2, c_{p2}, \kappa_2, & \text{if } a_1 \leq r \leq a_2, \\ \rho_3, c_{p3}, \kappa_3, & \text{if } a_2 \leq r \leq a_3. \end{cases} \quad (4.3)$$

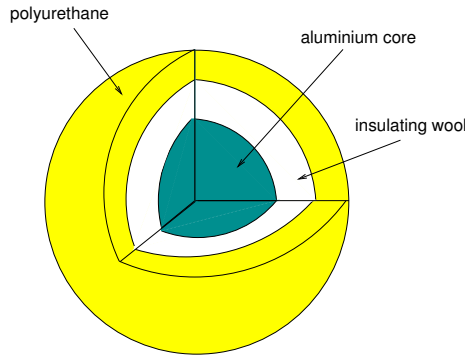


Figure 4.1: Insulator spherical shape used for the theoretical analysis. Three layers are considered since the physical insulator was constructed in this manner —see appendix §E.

We reasonably assume the insulator as well as the boundary conditions are isotropic. By the change of variable $u(r, t) = rT(r, t)$ Eq. (4.2) simplifies to⁴

$$\frac{\partial u_i(r, t)}{\partial t} = K_i \frac{\partial^2 u_i(r, t)}{\partial r^2}, \quad \text{for } i = 1, 2 \text{ and } 3 \quad (4.4)$$

where we have identified u_i with u in each of the regions in Figure 4.1 and $K_i = \kappa_i / (\rho_i c_{pi})$ which stands for the thermal diffusivity.

We are interested in the transfer function in the frequency domain of the insulator, i.e., the relationship between the ambient temperature and the temperature in the centre of the aluminium

¹Physical implementation is a cube due to construction simplicity criteria.

²In spherical coordinates and assuming radial dependence only, i.e., homogeneity.

³The constructed insulator contains three layer —see appendix E.

⁴Problems on radial flow in the sphere are reduced to problems on linear flow.

block. The transfer function can be found by using the Laplace transform of the equations above, which results in a differential equation of second order [27, 84, 97], i.e.,

$$s\tilde{u}_i(r, s) - u_i(r, 0) = K_i \frac{d^2 \tilde{u}_i(r, s)}{dr^2}, \quad \text{for } i = 1, 2 \text{ and } 3 \quad (4.5)$$

where $\tilde{u}(r, s) \equiv \mathcal{L}[u(r, t)]$. Initial conditions are defined as $\tilde{u}_i(r, 0) = 0$ (for $i=1,2$ and 3), hence, substituting them into Eq. (4.5) we obtain

$$\frac{d^2 \tilde{u}_i(r, s)}{dr^2} - q_i^2 \tilde{u}_i(r, s) = 0, \quad \text{for } i = 1, 2 \text{ and } 3 \quad (4.6)$$

with $q_i^2 = s/K_i$. The solution of the differential equation is

$$\tilde{u}_1(r, s) = A \sinh q_1 r + B \cosh q_1 r, \quad (4.7a)$$

$$\tilde{u}_2(r, s) = C \sinh q_2 r + D \cosh q_2 r, \quad (4.7b)$$

$$\tilde{u}_3(r, s) = E \sinh q_3 r + F \cosh q_3 r \quad (4.7c)$$

where we must take $B=0$ in order to have \tilde{T} finite as $r \rightarrow 0$.

The functions u_i satisfy matching conditions at the interface between the insulator's layers. These are conditions of continuity of the temperature and the heat flux across the layer boundaries. They are easily seen to be given by the system of equations

$$\tilde{u}_1(a_1, s) = \tilde{u}_2(a_1, s), \quad (4.8a)$$

$$\tilde{u}_2(a_2, s) = \tilde{u}_3(a_2, s), \quad (4.8b)$$

$$\tilde{u}_3(a_3, s) = a_3 \tilde{T}_{\text{amb}}(s), \quad (4.8c)$$

$$\kappa_1 \left[a_1 \frac{\partial \tilde{u}_1(r, s)}{\partial r} - \tilde{u}_1(r, s) \right] = \kappa_2 \left[a_1 \frac{\partial \tilde{u}_2(r, s)}{\partial r} - \tilde{u}_2(r, s) \right], \quad (4.8d)$$

$$\kappa_2 \left[a_2 \frac{\partial \tilde{u}_2(r, s)}{\partial r} - \tilde{u}_2(r, s) \right] = \kappa_3 \left[a_2 \frac{\partial \tilde{u}_3(r, s)}{\partial r} - \tilde{u}_3(r, s) \right] \quad (4.8e)$$

where \tilde{T}_{amb} is the ambient temperature. From Eqs. (4.8) the parameters A , C , D , E and F in Eqs. (4.7) can be determined. Once these parameters are identified the transfer function at the centre of the block is defined as

$$\lim_{r \rightarrow 0} H_{\text{ins}}(r, s) = \frac{\lim_{r \rightarrow 0} [\tilde{u}_1(r, s)/r]}{\tilde{T}_{\text{amb}}(s)}. \quad (4.9)$$

This transfer function has been evaluated for different materials and dimensions. Those actually used in the construction are given in Tables 4.1 and 4.2.

4.1.2 Insulator sizing

The requirement imposed for the temperature fluctuations inside the thermal insulator is —see §4.1,

$$S_{T, \text{testbed}}^{1/2}(\omega) \leq 10^{-6} \text{ K Hz}^{-1/2}, \quad 1 \text{ mHz} \leq \omega/2\pi \leq 30 \text{ mHz}. \quad (4.10)$$

Ambient temperature fluctuations have been determined in the laboratory to be $\sim 0.1 \text{ K Hz}^{-1/2}$ at 1 mHz and decreasing as $\sim f^{-1}$ at higher frequencies. Hence, the requirement on the insulator jig transfer function is readily set, i.e.,

$$|H_{\text{ins}}(\omega)| \leq 10^{-5}, \quad \omega/2\pi \geq 1 \text{ mHz} \quad (4.11)$$

where H_{ins} is the transfer function of the insulator for $r \rightarrow 0$ —see Eq. (4.9). The insulator is composed of three layers —see Table 4.2: a metal core (aluminium) of high thermal inertia surrounded by a layer of poorly conductive material (insulating wool⁵ and polyurethane foam). The dimensions of each layer are given in Table 4.1 and the properties of the materials in Table 4.2.

⁵Superwool 607 of Thermal Ceramics.

a_1 [cm]	a_2 [cm]	a_3 [cm]
7.5	9.5	25

Table 4.1: Dimensions chosen for the thermal insulator.

	Density ρ [kg m ⁻³]	Specific heat c_p [J kg ⁻¹ K ⁻¹]	Thermal conductivity κ [W m ⁻¹ K ⁻¹]
Aluminium	2700	900	250
Wool	300	1000	0.08
Polyurethane slab	35	1000	0.024

Table 4.2: Properties of the materials chosen for the insulator.

The theoretical transfer function is shown in Figure 4.2 (left panel, solid trace). It is clear that, theoretically, the ambient temperature fluctuations are sufficiently screened by the insulator. The required attenuation at 1 mHz is 10^{-5} . The gain at 1 mHz is, ideally, $\sim 10^{-8}$. The transfer function of the insulator has been also determined experimentally. The results are also shown in Figure 4.2 and compared with the theoretical calculations. At low frequencies ($f < 0.1$ mHz) the experimental and theoretical transfer functions match. However, at higher frequencies the experimental results differ significantly from the ideal response. The experimental gain at 1 mHz is $\simeq 10^{-5}$ while the theoretical one is orders of magnitudes lower, 10^{-8} —see Figure 4.2 (right panel).

On the one hand, the construction of the insulator is obviously not ideal, and at such level of attenuation any small *leak* path degrades the performance of the insulator. On the other hand, cables connecting thermistors to the electronics constitute a *free* path for temperature fluctuations from outside to show up in the thermistor —see §4.1.3. Altogether, the attenuation of the real insulator at 1 mHz is $\sim 10^{-5}$. The test will be meaningful if the laboratory temperature fluctuations are below $0.1 \text{ K Hz}^{-1/2}$ in the MBW. Otherwise, we would be measuring temperature fluctuations and not only electronic and sensor noise.

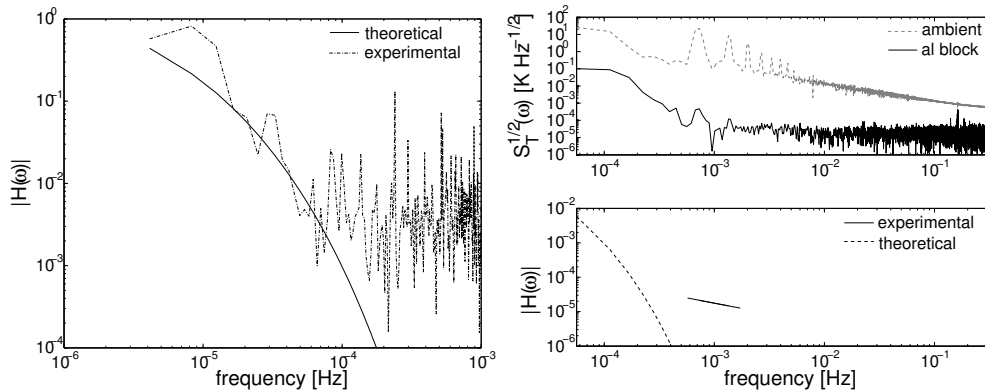


Figure 4.2: Left panel: theoretical and experimental transfer function for the designed and constructed insulator. The transfer function at frequencies higher than 0.1 mHz is not well estimated due to the low signal-to-noise ratio. Right panel: test performed in order to estimate the attenuation of the insulator at 1 mHz. The plot at the top shows the thermal excitation and the measured temperature inside the insulator (in PSD). The bottom plot shows the estimated gain at ~ 1 mHz which is $\sim 10^{-5}$.

4.1.3 Heat leakage through thermistors' cables

The sensors, attached to the centre of the aluminium block, are connected to the electronics by means of cables. The electronics is placed out of the insulator. Consequently, the cables of the sensors are exposed to ambient temperature fluctuations like the rest of the electronics. Obviously, cables are electrically and thermally conductive, therefore they constitute a fair path for the ambient fluctuations to appear in the thermistors due to the non-zero thermal contact between the sensor and the aluminium block. This section focuses on the analysis of such effect.

Figure 4.3 shows a thermistor representation [16]. The material sensitive to temperature is, actually, a tiny electronic chip —Figure 4.3, right— placed into an epoxy encapsulation —Figure 4.3, left. When attaching the sensor to a certain body, even if the thermal contact is ideal, there is always a thermal resistance due to the sensor structure itself which corresponds to the thermal resistance between the thermistor material and the small aluminium plate which is the outer element of the sensor, and the one in direct contact with the body. The *internal* thermal resistance is $\sim 50 \text{ K W}^{-1}$ —see appendix §B— and it is present in any measurement, independently of the thermal contact between the aluminium surface and the body. As shown later, the presence of such thermal resistance causes that ambient temperature fluctuations in the cables appear in the thermistor.

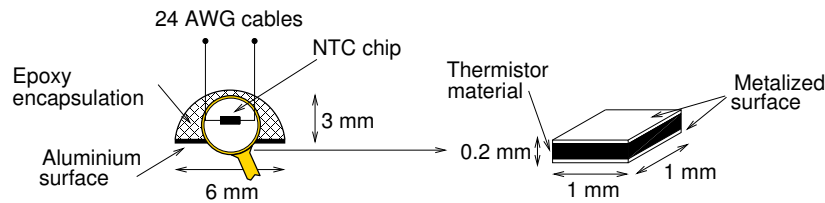


Figure 4.3: Left: general scheme of the thermistor. The temperature sensitive chip is encapsulated in epoxy. Right: *zoom* of the thermistor chip [16].

An electrical analogy is used to better understand and analyse the problem —see Figure 4.4. The parts drawn are: (i) the cables; (ii) the thermal capacitance of the NTC chip, C_1 , and the thermal resistance between the chip and the outer part of the sensor, θ_1 ; (iii) the thermal resistance, θ_2 , and thermal capacitance, C_2 , of the contact; (iv) the thermal capacitance of the aluminium block, C_{Al} , and (v) two terms representing the radial heat leakage through the cables before the thermistor chip, θ_w and C_x . It is important to note that the temperature of the NTC chip, T_{NTC} , is the one that is measured. For this reason if the cables have good thermal conductivity and the thermal resistances (of the sensor and of the contact) are large, then T_{amb} might appear at T_{NTC} only slightly attenuated.

The thermal model shown in Figure 4.4 is used to find the transfer function of the effect of the cables. The thermistor, the thermal contact, the aluminium block and the thermal impedance modeling the radial leakage are packaged in a single entity, Z —see Eq. (4.16), which represents the equivalent thermal impedance [71]. The aim of the analysis is to obtain the transfer function relating the ambient temperature, T_{amb} , to the temperature at the end of the cable, T_{NTC} .

In order to solve the problem in Figure 4.4 we consider the Fourier heat equation in one dimension, x , for the cables and, a lumped model for the sensor, the thermal contact and the aluminium block. The heat equation for the cables is

$$\rho_w c_w \frac{\partial T(x, t)}{\partial t} = \kappa_w \frac{\partial^2 T(x, t)}{\partial x^2} \quad (4.12)$$

where ρ_w , c_w and κ_w are the density, the specific heat and the thermal conductivity of the cables, respectively, and T is their temperature, which at $x = 0$ corresponds to the temperature of the thermistor.

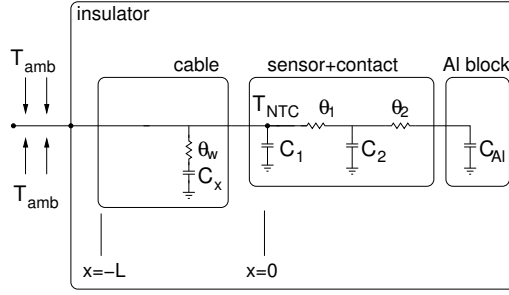


Figure 4.4: Equivalent circuit to analyse the heat leakage through the cables. In the frequency range of interest C_1 and C_2 can be omitted and C_{Al} can be considered as a *thermal short* due to its large value.

The solution to the problem is obtained by using the method described in §4.1.1. We Laplace transform Eq. (4.12) with the initial condition $\tilde{T}(x, s = 0) = 0$, i.e.,

$$\frac{d^2 \tilde{T}(x, s)}{dx^2} - q_w^2 \tilde{T}(x, s) = 0 \quad (4.13)$$

where

$$q_w^2 = \frac{\rho_w c_w}{\kappa_w} s = \frac{s}{K_w}. \quad (4.14)$$

The boundary conditions of the system are defined based on: (i) the temperature at $x = -\ell$ of the cable is the ambient temperature, and (ii) the condition of continuity of the heat flux across the cable and thermistor interface —see Figure 4.4,

$$\tilde{T}(-\ell, s) = \tilde{T}_{\text{amb}}(s), \quad (4.15a)$$

$$-\kappa_w \left. \frac{\partial \tilde{T}(x, s)}{\partial x} \right|_{x=0} = \frac{\tilde{T}(x=0, s)}{A_w} \frac{1}{Z(s)} \quad (4.15b)$$

where A_w is the cross section of the cable and Z is the thermal impedance. By inspection of Figure 4.4 and considering C_{Al} large and C_1 and C_2 small, we have that

$$Z(s) \simeq \frac{\theta_w(\theta_1 + \theta_2)C_x s + (\theta_1 + \theta_2)}{\theta_w(\theta_1 + \theta_2)C_x s + 1} \quad (4.16)$$

which is independent of the aluminium block and of the thermal capacitance of the sensor and of the contact since they are very small —see appendix §B.

As stated before the temperature of the NTC corresponds to that at $x = 0$. The solution of Eq. (4.13) for $x = 0$ with the boundary conditions given in Eqs. (4.15a) and (4.15b) is⁶

$$H_w(x = 0, s) = \frac{\tilde{T}(x = 0, s)}{\tilde{T}_{\text{amb}}(s)} = \sqrt{2} \frac{\kappa_w A_w Z q_w}{\kappa_w A_w Z q_w \cosh q_w \ell + \sinh q_w \ell}. \quad (4.17)$$

In order to evaluate Eq. (4.17) we need to know the properties of the cable and the thermal properties of the sensor. The properties of the former are well known and the properties of the

⁶A factor of $\sqrt{2}$ is added since two cables are used to connect the thermistors, i.e., $S_T(\omega) = 2|H_w(\omega)|^2 S_{T,\text{amb}}(\omega)$.

latter are estimated in appendix §B. The cables used are of copper and 24AWG⁷ size, i.e.,

$$\begin{aligned} c_w &= 385 \text{ J kg}^{-1} \text{ K}^{-1}, \\ \rho_w &= 8700 \text{ kg m}^{-3}, \\ \kappa_w &= 400 \text{ W m K}^{-1}, \\ A_w &= 2 \cdot 10^{-7} \text{ m}^2 \quad (r_w = 0.255 \text{ mm}) \text{ [24AWG]}, \\ \ell_w &= 1 \text{ m} \end{aligned}$$

and $\theta_1 \sim 50 \text{ K W}^{-1}$ and $\theta_2 \sim 30 \text{ K W}^{-1}$ —see appendix §B. The theoretical transfer function H_w considering the above properties is shown in Figure 4.5 for different values of θ_w . The thermal capacitance value used is the one of the aluminium block ($=8000 \text{ J K}^{-1}$). The transfer function, in the very worst case ($\theta_w = \infty$, i.e., assuming no radial heat transfer) is quasi-flat from the micro-Hertz to the milli-Hertz range. The gain at 1 mHz is $\simeq 8 \cdot 10^{-4}$, and thus in this case the attenuation of the insulator would be useless since the cables would degrade the performance of the system. The very best case is the one where $\theta_w = 0$, i.e., the leaking temperature fluctuations due to the cables are filtered by the aluminium core before they reach the thermistor head. The gain in such scenario at 1 mHz is $\simeq 10^{-7}$. In this case the effect of the cables would be negligible. The transfer functions for intermediate values of θ_w are also plotted. In a practical case θ_w should be small ($<1 \text{ K W}^{-1}$) due to the length of the cables, their very tiny insulating sheath and because they are wounded to the aluminium block.

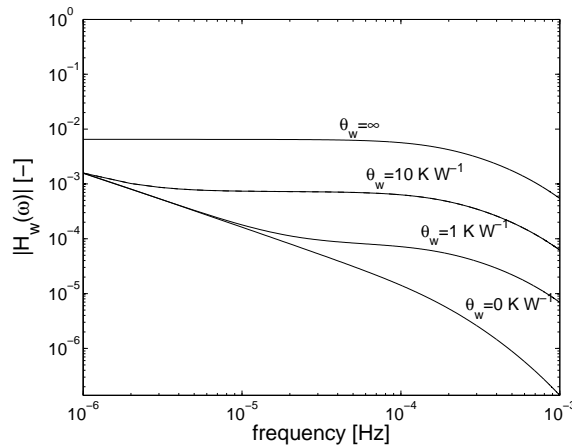


Figure 4.5: Transfer function relating the ambient temperature fluctuations and the fluctuations in the thermistor chip due to the heat leakage through the cables —see Eq. (4.17). $\theta_w \rightarrow \infty$ represents the very worst case since in that case radial heat transfer is not considered. The best case is for $\theta_w = 0$ (perfect contact between the cables and the aluminium block) which means that temperature fluctuations coming from outside through the cables are attenuated before reaching the thermistor head.

The transfer function attenuation increases (a) with the length of the cables, ℓ_w , and decreases (b) with the radius of the cables, r_w , (c) with the thermal resistance, θ_1 and θ_2 , and (d) with the thermal resistance between the cables and the aluminium core, θ_w .

Tests have been performed in order to estimate the actual transfer function. The tests have consisted in exciting thermally the outer end of the cables, observing the temperature response of the thermistor and then comparing the thermal excitation with that. The results of these experiments were, however, hardly conclusive since the heat leakage through the cables when using

⁷American wire gauge. 24AWG cables have a radius of 0.255 mm.

different configurations to enhance the effect on one of the sensors and to mitigate it on another one were similar. Figure 4.6 shows the response of a thermistor when exciting the end of the cables. The cables used are described above. The increase of temperature in the thermistors is clear. The input signal was a triangular wave of 0.6 mHz and peak-to-peak amplitude 2 K. The increase of temperature in the thermistor was $\simeq 20 \mu\text{K}$ which corresponds to a gain of $\simeq 10^{-5}$.

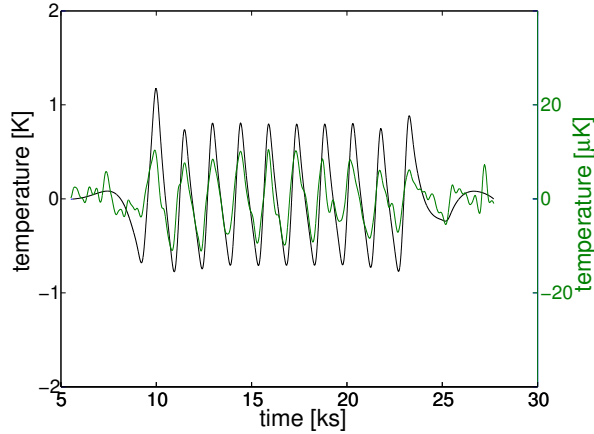


Figure 4.6: Thermal excitation of the cables (blue trace) and the response of the thermistor placed inside the insulator (green trace). The input signal has a peak-to-peak amplitude of 2 K and frequency 0.6 mHz. The response is a similar waveform of amplitude peak-to-peak $20 \mu\text{K}$. The attenuation is $\sim 10^{-5}$ at 0.6 mHz. This test was done with cables of different radii, however, not significant differences were observed.

In summary, the capability of screening the laboratory temperature fluctuations by the insulator considering non-idealities and heat leakage through the cables is $\simeq 10^{-5}$ at 1 mHz. Therefore, the insulator system is compliant with the requirements to perform meaningful tests —see Eq. (4.11). In order to fully overcome the potential effect of the cables a precaution was taken: the use of long and thin cables⁸ wound a few turns around the aluminium block [40] —see Figure 4.7.

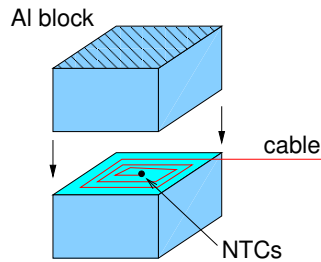


Figure 4.7: Thermal trap concept. The ambient temperature fluctuations are attenuated in the aluminium block prior to reach the sensing head of the thermistor.

⁸Length of the cables was $\sim 2\text{m}$ and the radius was of 0.1 mm instead of 0.255 mm.

4.2 Test bed for the LISA MBW

Investigations of the behaviour of the TMS in the LISA measurement bandwidth have been also done. The LISA frequency range goes down to 0.1 mHz, i.e., one order of magnitude lower than LTP. In principle, the electronic noise should remain flat due to the measurement method used —see §2.3. However, unexpected noise might appear at these very low frequencies, specially, due to the sensor itself. Thermistors are of semiconductor nature —see §2.2.2—, therefore susceptible to exhibit $1/f$ noise. The test bed designed to assess whether or not the system is compliant with the requirements in the LTP band has been described in §4.1. However, the test bed design in the submilli-Hertz region is considerably more complicated. In this section we describe the problems that appear when measuring at 0.1 mHz and the methods adopted to overcome them. We have to keep in mind that the main concerns of excess noise in the system come from the thermistor itself, thus the aim of the following investigations is the study of potential $1/f$ noise in the thermistors. We remark that $10^{-5} \text{ K Hz}^{-1/2}$ at 0.1 mHz is equivalent to temperature variations of $\sim 10^{-7} \text{ K}$ in time scales of hours⁹.

First, we consider the possibility of using the same concept of test described in §4.1, although re-scaling the size of the insulator. It was soon discovered that this option is not practical. At 0.1 mHz the ambient temperature fluctuations become much larger than those at 1 mHz and, in addition, the passive insulator attenuation appears to be poor¹⁰, unless a prohibitively large one is built. The *nominal* laboratory temperature fluctuations and those required inside the insulator are, at 0.1 mHz,

$$S_{T, \text{amb}}^{1/2}(0.1 \text{ mHz}) \sim 1 \text{ to } 10 \text{ K Hz}^{-1/2}, \quad (4.18a)$$

$$S_{T, \text{ins}}^{1/2}(0.1 \text{ mHz}) \sim 10^{-5} \text{ K Hz}^{-1/2}. \quad (4.18b)$$

From Eqs. (4.18a) and (4.18b) the needed attenuation at 0.1 mHz is readily calculated, i.e.,

$$|H_{\text{ins}}(0.1 \text{ mHz})| \leq 10^{-5} \text{ to } 10^{-6}. \quad (4.19)$$

In order to obtain such attenuation the needed passive insulator would consist in a aluminium sphere of 0.4 m diameter surrounded by a 2 m diameter polyurethane foam layer which appears inconvenient. However, the strongest reason to discard using a passive insulator is its time constant which is about 10 days. Therefore, temperature stabilisation down to $10^{-5} \text{ K Hz}^{-1/2}$ at 0.1 mHz by using a mere passive insulator appears rather problematic.

4.2.1 Solution: differential measurements

A straightforward solution to avoid the need of a giant insulator is the use of differential measurements instead of absolute measurements¹¹. For differential measurements we have

$$S_{T_1}(\omega) = |H_{\text{ins}}(\omega)|^2 S_{T, \text{amb}}(\omega) + n_{T_1}(\omega), \quad (4.20a)$$

$$S_{T_2}(\omega) = |H_{\text{ins}}(\omega)|^2 S_{T, \text{amb}}(\omega) + n_{T_2}(\omega) \quad (4.20b)$$

where n_{T_1} and n_{T_2} are the noise (in power spectral density) of each of the thermistors, plus the electronic noise. Thus, the differential measurement fluctuations are¹²

$$S_{\Delta T}(\omega) = n_{T_1}(\omega) + n_{T_2}(\omega). \quad (4.21)$$

⁹Or voltage fluctuations in the Wheatstone bridge of $\sim 5 \cdot 10^{-10} \text{ V}$ in time scale of hours.

¹⁰The insulator designed for the LTP tests exhibits a gain of $\sim 10^{-3}$ at 0.1 mHz —cf. Figure 4.2.

¹¹“Differential measurements” stands for measuring the temperature difference between two thermistors very close to one another in a more or less thermally stable environment while “absolute measurements” stands for measuring the temperature of individual thermistors.

¹²Assuming the noise of the two thermistors is uncorrelated.

Ideally, when differential measurements are considered, only noise from the thermistors and the electronics is measured, the common ambient temperature fluctuations cancel out. Therefore, a less demanding passive insulator would be enough for our purposes. However, different non-idealities arise in the practical implementation. These are discussed in next section.

4.2.2 Test bed non-idealities

Different non-idealities preclude a repetition of the test proposed in §4.2.1 at 0.1 mHz. The main limitations of the test set up are:

- power fluctuations in the thermistor (k_V),
- temperature coefficient of the electronics (α_{FEE}),
- cables connecting the thermistors to the electronics (k_c),
- intrinsic differences between thermistors (k_{NTC}).

All these effects couple into the measurement and disturb the $1/f$ thermistor noise investigations. The apportioning of these effects appears in the differential measurements as follows:

$$S_{\Delta T}(\omega) \simeq n_{T_1}(\omega) + n_{T_2}(\omega) + k_V^2 S_{V,\text{ref}}(\omega) + \alpha_{\text{FEE}}^2 S_{T,\text{FEE}}(\omega) + k_c^2 S_{T,\text{amb}}(\omega) + k_{\text{NTC}}^2 S_{T,\text{ins}}(\omega) \quad (4.22)$$

where $S_{V,\text{ref}}$, $S_{T,\text{FEE}}$, $S_{T,\text{amb}}$ and $S_{T,\text{ins}}$ stand for the voltage reference fluctuations of the Wheatstone bridge, the temperature fluctuations in the electronics, in the laboratory and inside the insulator, respectively. The main objective is to determine $n_{T_1} + n_{T_2}$, hence, all the other contributions must be minimised. More specifically, we assign $\simeq 5 \mu\text{K Hz}^{-1/2}$ to each of the four disturbing terms¹³. In the following we detail these non-idealities and the solutions adopted to overcome them.

Reference voltage fluctuations (k_V) Fluctuations in the voltage supply of the thermistor cause temperature fluctuations in the sensors by the self-heating effect —see §2.3.2.3. When differential measurements are considered, the temperature fluctuations in the measurement are (assuming both sensors are exactly at the same temperature)

$$S_{\Delta T}(\omega) = \left| \frac{2V_{\text{NTC}}}{R_{\text{NTC}}} \Delta\theta \right|^2 S_{V_{\text{NTC}}}(\omega) \quad (4.23)$$

where $\Delta\theta$ is the difference between the thermal resistances of the two thermistors (the voltage feeding both thermistors is, in principle, correlated), V_{NTC} is the voltage applied to the thermistors, $S_{V_{\text{NTC}}}$ are the voltage fluctuations and R_{NTC} is the resistance of the thermistor (the same for both thermistors since they are at the same temperature). The term within brackets is k_V in Eq. (4.22). Using Eq. (4.23), an upper limit for the voltage fluctuations, $S_{V_{\text{NTC}}}$, can be calculated. The numbers involved are $V_{\text{NTC}} \simeq 0.3 \text{ V}$, $R_{\text{NTC}} \simeq 10 \text{ k}\Omega$, $\theta \simeq 50 \text{ K W}^{-1}$ (we use θ instead of $\Delta\theta$ to be in a worst-case, i.e., assuming the voltage fluctuations in both thermistors are not correlated) —see appendix §B— and $S_{\Delta T}^{1/2} \leq 5 \cdot 10^{-6} \text{ K Hz}^{-1/2}$. The required stability for the reference voltage stability, $S_{V_{\text{NTC}}}^{1/2}$, results in $1.5 \text{ mV Hz}^{-1/2}$ for $f \geq 0.1 \text{ mHz}$. The measured stability at 0.1 mHz is $\sim 0.1 \text{ mV Hz}^{-1/2}$. With these numbers the contribution of this effect at 0.1 mHz is $\simeq 0.3 \mu\text{K Hz}^{-1/2}$, thus negligible.

¹³This results in a total noise of $\sqrt{4(5 \cdot 10^{-6})^2} = 10^{-5} \text{ K Hz}^{-1/2}$.

Temperature coefficient of the measurement system (k_{FEE}) The electronics temperature coefficient causes read out errors —see §2.3.4:

$$S_{\Delta T}(\omega) = \alpha_{\text{FEE}}^2 S_{T,\text{FEE}}(\omega) \quad (4.24)$$

where $S_{T,\text{FEE}}$ are the temperature fluctuations of the electronics, α_{FEE} is the temperature coefficient of the system, and $S_{\Delta T}$ are the fluctuations in the differential temperature measurement due to this effect.

The theoretical estimation of α_{FEE} is given in §2.3.4. However, in order to determine it more precisely a simple test has been done. The test consisted in connecting a high-stability resistor¹⁴, instead of a thermistor to the measurement system. The high-stability resistor acts as a thermistor at a constant temperature of 25 °C. The FEE was thermally excited by using a heater and the temperature of the electronics and the equivalent temperature of a 10 k Ω resistor were measured. Using these two measurements the value of the electronics temperature coefficient is readily estimated. A scheme of the test set up and the obtained measurements are shown in Figure 4.8.

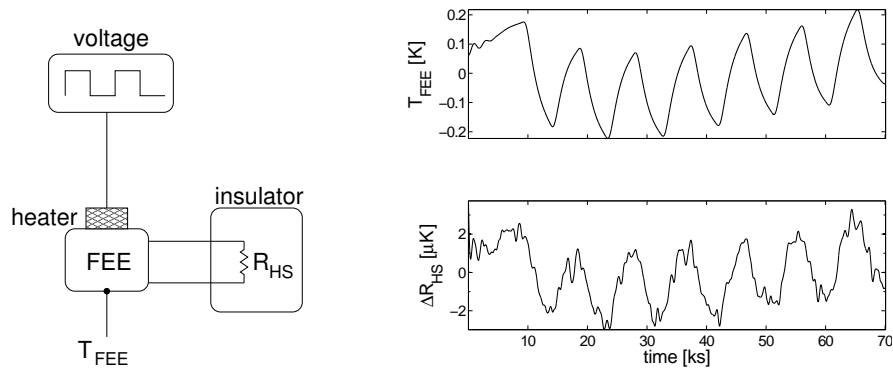


Figure 4.8: Electronics temperature coefficient estimation. The resistance of a high-stability resistor is measured while applying a thermal excitation to the electronics. The change in the high-stability resistor is attributed to the TC of the electronics. The panel in the right shows the temperature of the electronics when being thermally excited and the measurement of the resistance (low-pass filtered to reject the high frequency noise of the measurement).

From the measurements shown in Figure 4.8 (right) the estimation of the parameter α_{FEE} is

$$\hat{\alpha}_{\text{FEE}} = 13.5 \mu\text{K K}^{-1} \quad (4.25)$$

which is in good agreement with the theoretical prediction —cf. §2.3.4 (in the very worst-case scenario at 25 °C it is 40 $\mu\text{K K}^{-1}$). This value limits the maximum temperature fluctuations of the electronics. The budget for this effect is $\simeq 5 \mu\text{K Hz}^{-1/2}$, thus, the fluctuations in the electronic must be $\lesssim 0.35 \text{K Hz}^{-1/2}$ at 0.1 mHz. The fluctuations in the electronics are approximately the same as those in the ambient, which at 0.1 mHz are $\sim 1 \text{K Hz}^{-1/2}$ —see Eq. (4.18a). In order to overcome this problem, the temperature of the electronics was controlled by means of a feedback control (a proportional control) that maintained the temperature stable by controlling a heater attached to the electronics.

Cables connecting the thermistors to the electronics (k_c) Cables are a fair path for the ambient temperature fluctuations to show up in the thermistors' readings. In the case of the

¹⁴10 k Ω Vishay resistor with of $0.6 \cdot 10^{-6} \text{K}^{-1}$ placed inside the insulator

differential measurements the effect of the cables is very attenuated because the ambient temperature fluctuations are exactly the same for both. The only fluctuations that can appear are due to *asymmetries* in the cables (for instance, if they are of different length) and in the thermistors themselves. In the case of absolute temperature measurements the effect of the cables does not affect the performance of the insulator provided long cables and a good thermal contact is ensured. In the case of the differential measurements, this effect is even milder.

A test to assess whether or not the differential measurement rejects the common-mode temperature fluctuations was performed. A thermal excitation (triangular wave of peak-to-peak amplitude 0.2 K) was applied to the cables of both sensors while measuring the differential temperature. The results are shown in Figure 4.9 where no signal correlated with the excitation is observed. The thermal excitation main frequency component was at 2 mHz. In the test in the LISA MBW we are interested at 0.1 mHz, however, the response at 2 mHz and 0.1 mHz should be similar since the transfer function describing the heat leakage through the cables does not differ too much between 1 mHz and 0.1 mHz —see Figure 4.5. Thus, the effect of the cables should not pose a problem for the test.

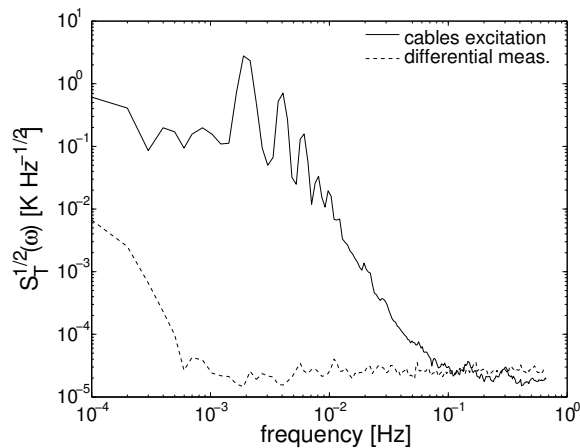


Figure 4.9: Thermal excitation at the cables of both thermistors during differential measurements. The solid trace shows the excitation at the cable’s end, and the dashed line is the differential measurement which is free of the effect of the heat leakage.

Intrinsic differences between thermistors (k_{NTC}) The inherent mismatch between thermistors, causes an error in the differential temperature due to differences in the response of each thermistor. The apportioning of this effect is:

$$S_{\Delta T}(\omega) = |H_1(\omega) - H_2(\omega)|^2 S_{T,\text{ins}}(\omega) \quad (4.26)$$

where here $H_1 - H_2$ is¹⁵

$$H_1(\omega) - H_2(\omega) = \frac{q_1(\omega)}{\sinh a q_1(\omega)} - \frac{q_2(\omega)}{\sinh a q_2(\omega)} \quad (4.27)$$

with a the radius of the thermistor head and

$$q_i = \frac{\rho_i c_i}{\kappa_i} i \omega \quad (4.28)$$

¹⁵Assuming the head of the thermistor is spherical [27].

where ρ_i , c_i and κ_i are the density, the specific heat and the conductivity of the thermistors, respectively. Equation (4.27) is difficult to evaluate due to not well-known characteristics of the thermistors. However, it can be seen that Eq. (4.27) is actually a high-pass filter, i.e.

$$H_1(\omega) - H_2(\omega) \simeq k_{\text{NTC}}i\omega. \quad (4.29)$$

The experiments to estimate k_{NTC} consisted of exciting thermally the aluminium block and measuring the absolute and the differential temperature. These measurements allow us to find the relationship between the absolute temperature in the centre of the aluminium block and the differential measurement between two thermistors very close to one another¹⁶, also in the centre of the block. The thermal excitation consisted in dissipating a constant power in a heater placed in one of the faces of the block. The evolution of the absolute temperature is shown in Figure 4.10 (top left panel), and the differential measurement is shown in the top right panel. The estimation of k_{NTC} is done by calculating the time derivative of the absolute temperature measurement and then fitting it to the measured differential data. The estimated parameter is $\hat{k}_{\text{NTC}} \simeq 6$ s. Figure 4.10 (bottom) shows the measured differential temperature (solid trace) and the fit with $k_{\text{NTC}} = 6$ s. The agreement is good, thus confirming the behaviour predicted by Eq. (4.29).

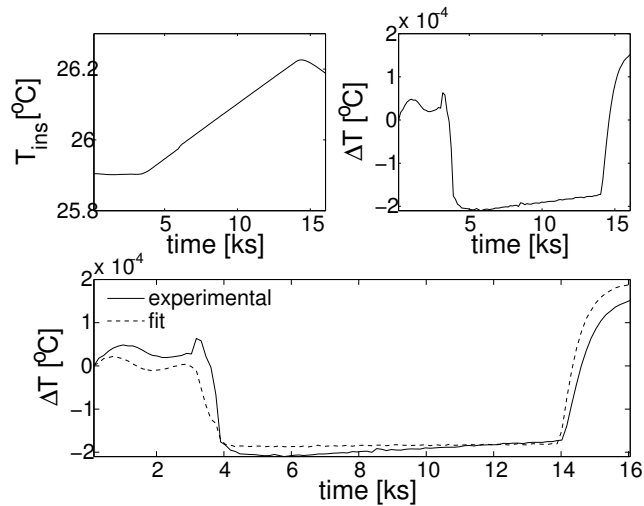


Figure 4.10: Top left: absolute temperature measurement in the aluminium block. Top right: differential temperature measurement between two thermistors very close one to each other in the aluminium block. Bottom: differential temperature measurement (solid trace) and that obtained by the time derivative of the absolute temperature and adjusting the parameter to $k_{\text{NTC}}=6$ s (dashed trace).

This effect implies that the temperature fluctuations of the aluminium block at 0.1 mHz must be less than $5 \cdot 10^{-3} \text{ K Hz}^{-1/2}$ not to perturb the test. This figure is used to calculate the attenuation required for the the thermal insulator, i.e.,

$$|H_{\text{ins}}(\omega)| = \frac{S_{T,\text{Al}}^{1/2}(\omega)}{S_{T,\text{amb}}^{1/2}(\omega)} \Big|_{0.1 \text{ mHz}} \sim 10^{-4} \quad (4.30)$$

The insulator constructed for the LTP test exhibits a gain of 10^{-3} at 0.1 mHz —see Figure 4.2. Instead of designing another insulator with such attenuation, a combination of the built insulator in conjunction with an active temperature control in the aluminium block was implemented.

¹⁶For this reason, the temperature difference between the two sensors is interpreted as a mismatch between them.

Finally, another source of error is the difference between the temperature characteristic of the thermistors, β . The tolerance specified by the manufacturer is $\pm 0.3\%$ [16]. This represents a coefficient of $\sim 10^{-3} \text{ K K}^{-1}$ in the differential measurements. If a temperature stability of $5 \cdot 10^{-3} \text{ K Hz}^{-1/2}$ is required in the aluminium block, the contribution of this effect is negligible.

4.2.3 Temperature control design

The implementation of an active system to control the temperature [48, 60, 65, 78, 144, 42, 40] of the aluminium block inside the insulator appears as the only feasible option to deal with the investigation of the $1/f$ noise in the thermistors in the submilli-Hertz frequency band. In this section we describe the design and different aspects of the implementation.

An active temperature control based on a feedback-feedforward (FB-FF) scheme¹⁷ [104, 12] —see Figure 4.11— has been used to keep the temperature fluctuations of the insulator less than $\sim 5 \cdot 10^{-3} \text{ K Hz}^{-1/2}$ at 0.1 mHz —see §4.2.2. The active controller attenuates the fluctuations in the submilli-Hertz region (and at lower frequencies) while the passive insulator screens out the fluctuations in the milli-Hertz region (and at higher frequencies) —see Figure 4.16. Our main concern is the rejection of ambient temperature fluctuations in the aluminium block. The effect of the disturbance (the ambient temperature) on the system, in principle, can be highly reduced by using the feedforward compensation shown in Figure 4.11, which can be implemented provided the disturbance signal can be measured and good knowledge of the transfer functions involved in the system are available. The former condition is possible, we only have to place a thermistor outside the insulator; the latter condition is also met with reasonable accuracy. The control system works as follows: a reference temperature for the aluminium block, T_{ref} (a few degrees over the ambient temperature), is set; the control tries to maintain this temperature by dissipating power through a heater attached to the aluminium block. The required power is calculated by a computer using the data coming from the ambient temperature (feedforward) and from the aluminium block temperature (feedback). The needed power is converted to units of Volt and sent to a programmable power supply connected to a heater placed onto one of the aluminium block faces. The block diagram of the control system is given in Figure 4.11.

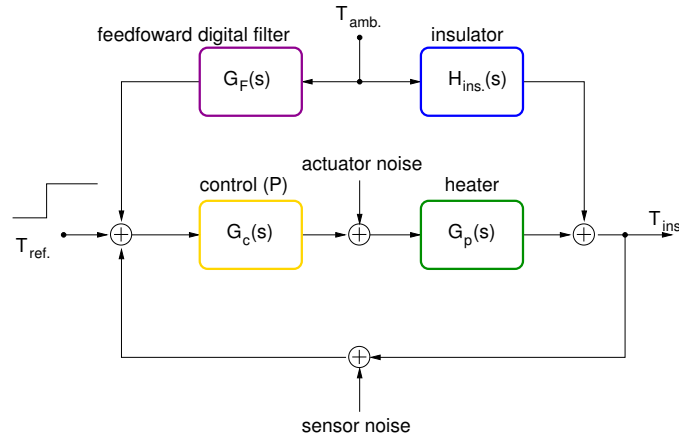


Figure 4.11: Feedback-feedforward temperature control system block diagram.

The closed-loop response of the FB-FF system is (in the s -domain, we omit the s dependence

¹⁷With only a proportional feedback control an attenuation of four orders of magnitude is difficult to attain. The needed gain of the controller, G_c , has to be large and the system is of very high order. This combination results in an under-damped system that spoils the purpose of the test.

argument in the rest of the section for notation simplicity)

$$\tilde{T}_{\text{ins}} = \frac{G_c H_h}{1 + G_c H_h} \tilde{T}_{\text{ref}} + \frac{H_{\text{ins}} - G_c H_h G_{\text{FF}}}{1 + G_c H_h} \tilde{T}_{\text{amb}} + \frac{H_h}{1 + G_c H_h} \tilde{n}_{\text{act}} + \frac{G_c H_h}{1 + G_c H_h} \tilde{n}_{\text{sens}} \quad (4.31)$$

where:

- H_h is the heater transfer function, i.e., the transfer function that relates the power dissipated in the heater to the increase of temperature in the aluminium block. The units are K W^{-1} . The estimation of this transfer function is presented in §4.2.3.1,
- H_{ins} is the passive insulator transfer function. This transfer function is accurately known for $f \leq 0.1$ mHz —see §4.1 and Figure 4.2,
- G_c is the controller transfer function, in our case a mere constant, K_p [W K^{-1}],
- G_{FF} is the feedforward filter. The main purpose of this filter is to fully reject ambient temperature fluctuations from the aluminium block. By inspection of Eq. (4.31) we notice that the term multiplying \tilde{T}_{amb} can be nulled if the feedforward filter is

$$G_{\text{FF}} = \frac{1}{G_c} \frac{H_{\text{ins}}}{H_h} \quad (4.32)$$

where all the transfer functions in the right hand side of the equation are known to a certain accuracy. The filter design and implementation is described in §4.2.3.1,

- \tilde{T}_{ref} , \tilde{T}_{ins} and \tilde{T}_{amb} are the set point temperature for the aluminium block, the measured temperature of the aluminium block and the laboratory temperature, respectively,
- \tilde{n}_{act} and \tilde{n}_{sens} are the noise introduced by the programmable power supply and the noise of the absolute temperature sensor. They are negligible for the measurement of interest (the differential measurement).

4.2.3.1 Feedforward filter design

In this section the different steps needed to design and implement the feedforward filter are described. The filter is defined in Eq. (4.32) where it is clear that the transfer functions of the passive insulator, H_{ins} , and of the heater, H_h , are needed. The former has been described in §4.1.1 and §4.1.2. In the following the heater transfer function is estimated and then the feedforward filter design is described.

Heater transfer function (H_h) This transfer functions relates the power dissipated in the heater to the increase of temperature in the aluminium block. In order to obtain an analytical transfer function we consider the problem as shown in Figure 4.12: all the faces of the aluminium block are considered adiabatic except the one with the heater attached to it. The insulating material is modelled by a lumped thermal resistance, θ , and a lumped capacitance, C . Therefore, the power dissipated in the heater heats up the aluminium block, but, also the insulating material. Our interest is in the temperature increase at $x = \ell/2$ (where the sensors are placed) due to the power dissipated in the heater, P .

The transfer function of the system is —see appendix F—,

$$\tilde{H}(x, s) = \frac{\tilde{T}(x, s)}{\tilde{P}(s)} = \theta \frac{\cosh q(\ell - x)}{A\kappa\theta q \sinh q\ell + \cosh q\ell(q^2 K\theta C + 1)} \quad (4.33)$$

where, as usual, $K = \kappa/(\rho c)$, $q^2 = s/K$ and θ and C are the lumped thermal parameters of the insulating layer —see Table 4.2. A is the contact area of the heater with the aluminium block. In

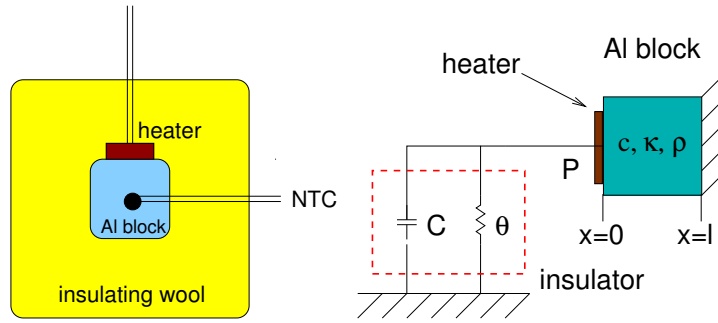


Figure 4.12: System to heat up the temperature of the aluminium block. We are interested in the transfer function between the electrical power dissipated in the heater and the increase of temperature at $x = \ell/2$ (at the centre of the block). The figure in the left is the actual system whereas the figure in the right is the model used for the analysis.

order to assess whether the model is accurate or not we have to compare it to experimental data. A simple way to obtain the response of the system is to apply a power step to the system and observe the temperature evolution at $x = \ell/2$. However, the expression given in Eq. (4.33) is in the frequency domain, therefore it must be transformed to the time domain to compare it with the experimental data. The input signal, P , is the Heaviside function. The response of the system in the time domain to the Heaviside function can be obtained by using Eq. (4.33) and the Inversion theorem. The resultant expression is [27] —see appendix §F for details—,

$$T(t) = P\theta \left[1 - 2 \sum_{n=1}^{\infty} \frac{e^{-K\alpha_n^2 t}}{\alpha_n} \frac{\cos \alpha_n(\ell - x)}{\theta \alpha_n (A\kappa\ell + 2KC) \cos \alpha_n \ell + (\ell + A\kappa\theta - \ell\theta K\alpha_n^2 C) \sin \alpha_n \ell} \right] \quad (4.34)$$

where α_n are the solutions of

$$\alpha_n \tan \alpha_n \ell = \frac{1 - \alpha_n^2 \theta K C}{A\kappa\theta}. \quad (4.35)$$

The experimental temperature and analytical responses for $P = 0.095 \text{ W}$ are shown in Figure 4.13 (left panel). The expression given in Eq. (4.34) has been fitted to the experimental response with θ and C as free parameters. The values found are given in Table 4.3. Figure 4.13 (right panel) shows the transfer function in the frequency domain which is the one needed in the design of the feedforward filter.

parameter	value
K	$\rho c / \kappa \simeq 10^{-4} \text{ s m}^{-2}$
A	0.005 m^2
θ	7.5 K W^{-1}
C	10 kJ K^{-1}
ℓ	0.15 m

Table 4.3: Parameters used for the evaluation of Eqs. (4.33) and (4.34) —see Figure 4.13. θ and C represent the properties of the insulating material surrounding the aluminium block. Their values have been found by fitting Eq. (4.34) to the experimental temperature response. However, a rough estimation of them leads to similar values: for the case of the thermal resistance, if we calculate θ considering a hollow sphere, the obtained value is $\sim 9 \text{ K W}^{-1}$ and the heat capacity is $\sim 12 \text{ kJ K}^{-1}$.

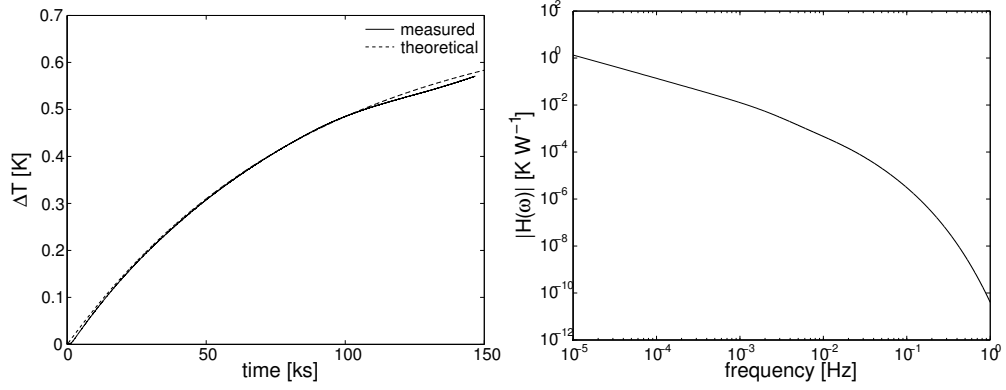


Figure 4.13: Left: temperature response to a power step of 0.095 W. Solid trace represents the experimentally measured response, while the dashed trace is the one estimated by means of Eq. (4.34). Right: The transfer function in the frequency domain (at $x = \ell/2$). The parameters used for both plots are those shown in Table 4.3.

Feedforward filter (G_{FF}) The feedforward filter is —see Eq. (4.32),

$$G_{\text{FF}} = \frac{1}{K_p} \frac{H_{\text{ins}}}{H_h} \quad (4.36)$$

where H_h and H_{ins} are the heater transfer function and the insulator transfer function, respectively, which have been characterised before. The term K_p is the gain of the proportional control, and is a mere constant to be set later on—see §4.2.3.2. The feedforward filter is implemented digitally in a computer. To do so, we first approximate it to a pole-zero filter (still in the s -domain) to then convert it into a discrete filter. The term H_{ins}/H_h is approximated by the following pole-zero expression¹⁸:

$$\frac{H_{\text{ins}}(s)}{H_h(s)} = \frac{1}{\theta} \underbrace{\frac{1}{(as+1)^7(bs+1)^3}}_{\text{low pass filter}} \underbrace{\frac{(-cs+1)^2(-ds+1)(-es+1)}{(cs+1)^2(ds+1)(es+1)}}_{\text{all pass filter}} \quad (4.37)$$

with $a=320$, $b=3800$, $c=185$, $d=100$ and $e=50$. Equation (4.37) is formed by two parts, the first is a low-pass filter of 10-th order and is used to adjust the gain, and the second is an all-pass filter which adjusts the phase —see Figure (4.14). The approximation is good but they do not quite match, although the errors at 0.1 mHz are small. At higher frequencies the needed accuracy of the feedforward filter, G_{FF} , is relaxed since the passive insulator is the one which screens the temperature fluctuations.

¹⁸The pole-zero model chosen was obtained by minimising the error of the gain and the phase at the region of 0.1 mHz with a filter of reasonable order.

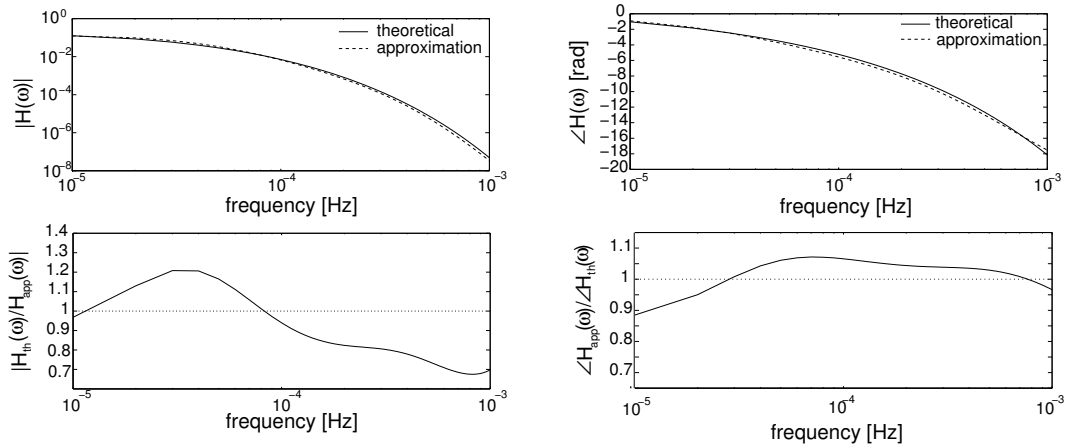


Figure 4.14: Left: gain of the theoretical feedforward filter (solid trace) and gain of the approximate feedforward filter (dashed trace). The quotient between the theoretical and the approximate filter is shown in the bottom. Right: *idem* as the plots in the left panel for the phase.

Equation. (4.37) corresponds to an infinite impulse response (IIR) filter in the discrete time domain. The digital filter has been designed by the mapping from the s -plane to z -plane by means of the bilinear transform [105], i.e.,

$$s = \frac{2}{t_s} \left(\frac{1 - z^{-1}}{1 + z^{-1}} \right) \quad (4.38)$$

where t_s is the sampling period and z is the shift operator. The filter has been implemented in a cascade-form structure, otherwise the filter becomes unstable due to finite numerical precision in the implementation and the high order of the filter. Therefore, prior to the bilinear transform, the system has been factored into a cascade of second order subsystems, i.e.,

$$G_{\text{FF}}(s) = \prod_{k=1}^7 G_{k,\text{FF}}(s) \quad (4.39)$$

The digital implementation is done using the regular direct form II [105], i.e.,

$$y[n] = \frac{1}{m_0} (n_0 w[n] + n_1 w[n-1] + n_2 w[n-2]) \quad (4.40)$$

with

$$w[n] = x[n] - \frac{1}{m_0} (m_1 w[n-1] + m_2 w[n-2]) \quad (4.41)$$

where m_i are the coefficients of the z^{-i} in the denominator and n_i are the coefficients of z^{-i} in the numerator. This implementation is schemed in Figure 4.15 for a single stage.

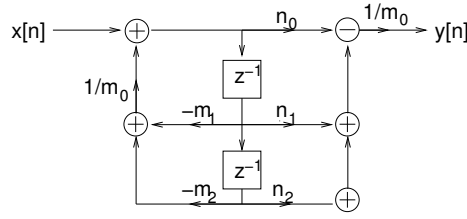


Figure 4.15: Second order IIR filter implementation [105].

4.2.3.2 Feedback-feedforward control

Our goal is to design an insulator able to attenuate ambient temperature fluctuations at 0.1 mHz by four orders of magnitude. The figure of merit of the control loop is thus the transfer function relating the ambient temperature to the aluminium block temperature —see Eq. (4.31), i.e.,

$$\tilde{T}_{\text{ins}} = \frac{H_{\text{ins}} - K_p H_h G_{\text{FF}}}{1 + K_p H_h} \tilde{T}_{\text{amb}} \quad (4.42)$$

The value of K_p is set to 30 to obtain a gain of $\sim 10^{-4}$ at 0.1 mHz —see Eq. (4.30). Higher gains lead to an oscillating temperature response since the poles of the transfer function related to T_{ref} become complex and close to the unity boundary (see footnote 16).

Equation (4.42) is plotted in Figure 4.16 for different values of K_p . Ideally, the solid traces in Figure 4.16 should all be zero. However, the digital implementation of the feedforward filter is only an approximation to the desired one, therefore the differences between the approximate and the desired filter lead to a non-zero numerator in Eq. (4.42). All in all, the gain at 0.1 mHz using the FB-FF control with $K_p=30 \text{ W K}^{-1}$ is 10^{-4} which should be enough for the investigation of excess noise in the thermistors. The test implementation and the results are given in chapter §5.2.

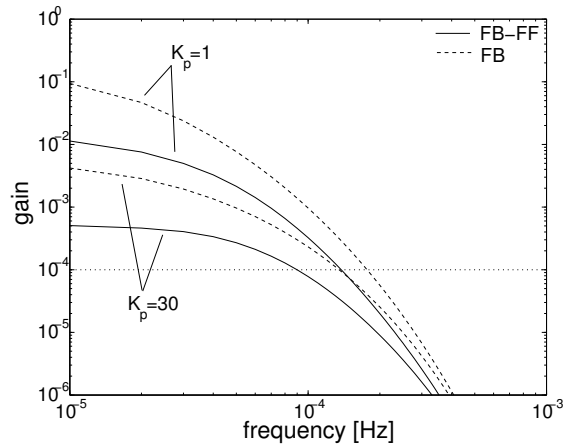


Figure 4.16: Ambient temperature fluctuations attenuation inside the insulator. Solid traces represent the FB-FF system for different gains, and dashed traces are plotted for comparison when using a FB scheme. The gain implemented in the final design is $K_p=30 \text{ W K}^{-1}$.

Chapter 5

TMS performance tests

In this chapter we describe the tests performed in order to assess whether or not the TMS achieves the required performance for the LTP mission. We restate the requirement for the noise of the system, i.e.,

$$S_{T,\text{req}}^{1/2}(\omega) \leq 10^{-5} \text{ K Hz}^{-1/2}, \quad 1 \text{ mHz} \leq \omega/2\pi \leq 30 \text{ mHz} \quad (5.1)$$

The test bed for such measurements has been described in §4.1 and, thus, in this chapter we only present and discuss the results. The test was done using three *systems*: first, the test was carried out using the prototype measurement system [107, 119]; then, the replica of the prototype implemented in the engineering model (EM) of the DMU was tested [115] and, finally, the flight model (FM)¹ system was also put to test [116]. Results for the three test campaigns are discussed since all of them were of interest for some specific reasons.

The second part of the chapter shows the results of the test campaign dedicated to investigations on the performance of the TMS at frequencies of 0.1 mHz. This campaign was done in view of the LISA requirements which are defined in the frequency band from 0.1 mHz to 0.1 Hz, and also to know the limits of the designed measurement system [118].

5.1 Tests in the LTP measurement bandwidth

The results of the test campaigns to validate the temperature measurement subsystem are shown in the following sections.

5.1.1 Prototype TMS test

First, dedicated measurements to determine the inherent noise of the prototype electronics (without considering the thermistors) were done. In order to do this, a high-stability (HS) resistor of 10 k Ω instead of a thermistor was connected to the electronics. In addition, a measurement with the two inputs of the instrumentation amplifier (IA) short-circuited was done. The former measurement permits setting the floor noise levels of the system when measuring at an equivalent temperature of 25 °C. The performance obtained in this measurement is used as the reference floor noise and it establishes the minimum levels of noise achievable by the system. Therefore if when measuring with the thermistor the noise levels are the same, the hypothesis suggested in §2.3.2 where the noise source corresponding to the thermistor was modelled as Johnson noise is validated. The measurement with the inputs of the IA short-circuited indicates the noise that must be attributed only to the voltage noise source of the IA and the noise related with the analog-to-digital conversion stage. This measurement does not contain the Johnson noise of the Wheatstone bridge, nor the noise introduced

¹The FM is the subsystem which will fly aboard the LTP mission. The EM is an *exact* replica of the FM used for testing.

by the current noise sources of the IA in conjunction with the equivalent resistance of the bridge —see §2.3.2.4. Figure 5.1 shows the power spectral density² (PSD) of these measurements. The test was carried out at the laboratory with no temperature control³. The temperature fluctuations of the chamber are also given.

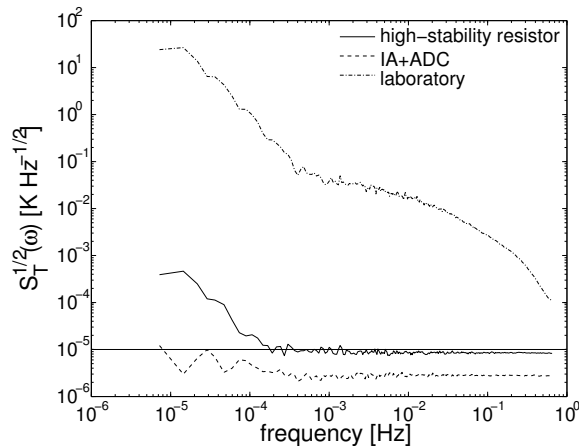


Figure 5.1: Measurement system prototype electronics test results. The solid trace stands for the measurement of a HS resistor of 10 k Ω and sets the lower noise limits of the measurement when sampling four channels ($f_s=1.38$ Hz). The dashed trace is the measurement with the two inputs of the IA short-circuited. The upper trace (dash-dotted trace) stands for the temperature fluctuations in the laboratory.

Several figures of interest can be extracted from the results shown in Figure 5.1. The $1/f$ noise of the IA is not present in the measurements due to the lock-in amplification technique —see §2.3.1. The increase of the noise at frequencies below 0.1 mHz is due to the temperature coefficient (TC) of the electronics which was measured previously —see §4.2.2. The value obtained was $15 \mu\text{K K}^{-1}$, which is exactly the ratio of the ambient temperature fluctuations to the HS resistor measurement noise at low frequencies, i.e.,

$$\left. \frac{S_{T,\text{HS}}^{1/2}(\omega)}{S_{T,\text{amb}}^{1/2}(\omega)} \right|_{\frac{\omega}{2\pi} \leq 0.1 \text{ mHz}} \simeq \alpha_{\text{FEE}}. \quad (5.2)$$

Moreover, the temperature dependence of the electronics is mainly due to the TC of the resistors of the bridge as was foreseen by the theoretical analysis in appendix A —see Table A.1. This is also readily inferred by comparison of the 10 k Ω measurement and that with the inputs of the IA short-circuited. The temperature dependence is hardly observed in the latter while it is clear seen in the 10 k Ω resistor measurement. As a consequence of these results we also conclude that $1/f$ noise in the high-stability resistors of the bridge is not present⁴.

The floor noise of the system when measuring 25 $^{\circ}\text{C}$ (10 k Ω) is $\simeq 8 \mu\text{K Hz}^{-1/2}$ (when multiplexing four measurements, i.e., with a sampling frequency of 1.38 Hz instead of the 5.55 Hz). The theoretical estimation in §2.3.4 was of $3 \mu\text{K Hz}^{-1/2}$ with no multiplexing, thus, if four channels are sampled the theoretical noise becomes $6 \mu\text{K Hz}^{-1/2}$ which agrees with the ones obtained experimentally⁵.

²The power spectral densities have been estimated using the LPSD (logarithmic frequency axis power spectral density) [140]. The same method has been used for the rest of chapters.

³Actually, temperature control in test chambers hampers the measurements since they usually have frequency components of large amplitude in the MBW.

⁴The ac excitation of the bridge does not avoid the potential $1/f$ noise of the resistors, if present [94].

⁵The small discrepancies between the theoretical and the experimental data come from a small amount of aliasing. The sampling frequency is 38.4 kHz and the cut-off frequency of the second-order anti-alias filter is 500 Hz, however,

Therefore, the analysis presented in §2.3 is confirmed by the experimental results, at least when using a HS resistor instead of a thermistor. As with the temperature coefficient, the Wheatstone bridge is the stage that contributes the higher fraction to the total noise in the system. The noise of the IA (decoupled from the Wheatstone bridge) plus the analog-to-digital converter (ADC) is $\simeq 3 \mu\text{K Hz}^{-1/2}$, hence, by using Eq. (2.40) we can estimate the noise contribution of the bridge: $S_{T,b}^{1/2} \simeq 7.4 \mu\text{K Hz}^{-1/2}$, which represents 85% of the total noise (in terms of power). The Wheatstone bridge noise, in turn, is split into the Johnson noise of the bridge itself and the noise coming from the IA current noise together with the equivalent resistor of the bridge. The former contributes 30% of the total noise (in terms of power), while the latter is 70%. The noise of the Wheatstone bridge itself cannot be reduced by using lower resistance resistors since the noise equivalent temperature of the bridge is independent of the nominal resistance of the bridge —see §2.3.2.1. The latter cannot be further reduced either since the optimum resistance taking into account the instrumentation amplifier used (AD624) is $8 \text{ k}\Omega$ (very close to the $10 \text{ k}\Omega$ of the design) —see §6.2.

All in all, the electronics of the system worked as expected and no excess noise of any nature was detected. The next step was the assessment of the noise performance of the system when using thermistors, i.e., when measuring temperature. The test set up has been described in detail in §4.1. The concept is very simple if we keep in mind that we are interested in determining the noise model of the thermistor. The test consisted in maintaining the temperature fluctuations of the thermistor lower than the electronic floor noise of the system, i.e., we had to ensure that the thermistor was placed in a location where temperature fluctuations were lower than $\simeq 1 \mu\text{K Hz}^{-1/2}$ at $f \geq 1 \text{ mHz}$ —see Eq. (4.10) [84]. The test set up is shown in Figure 5.3 and consisted in attaching three thermistors to the aluminium block plus another thermistor placed outside the insulator in order to measure the temperature of the environment. The aluminium block was surrounded by the insulating material and thoroughly closed. The tests for the LTP bandwidth did not require any active temperature control since the passive insulator was, in principle, able to screen the laboratory temperature fluctuations to the required level at the milli-Hertz —see §4.1. Moreover, the set up was placed in an anechoic chamber at Universitat Politècnica de Catalunya (UPC) premises —see Figure 5.2— where the temperature stability is $\sim 0.1 \text{ K Hz}^{-1/2}$ at 1 mHz . The attenuation of the insulator at 1 mHz is $\simeq 2 \cdot 10^{-5}$, the aluminium block fluctuations should therefore not exceed $\simeq 2 \mu\text{K Hz}^{-1/2}$ for $f \geq 1 \text{ mHz}$.

Once everything was in place, a certain time for temperature stabilisation was required. The time constant of the insulator, τ_{ins} , is $\simeq 80 \text{ ks}$ ($\simeq 1 \text{ day}$). After waiting for 2-3 time constants the temperature of the aluminium block was stable enough for our purposes.

The data used to estimate the noise levels of the system when using thermistors is shown in Figure 5.4 (left) and the obtained power spectral density of all the measurements is given in Figure 5.4 (right). The floor noise when measuring a HS resistor of $10 \text{ k}\Omega$ is also plotted for comparison since this measurement is used as the reference noise level.

the filter is, obviously, not ideal and the attenuation at high-frequency ($f > 100 \text{ kHz}$) is not better than 60 dB. Also the transition noise of the ADC is not low pass filtered, and thus introduces aliasing.



Figure 5.2: Anechoic chamber at UPC premises. This chamber was used due to its good temperature stability and to avoid disturbances during the test (such as people passing by, interferences, etc.).

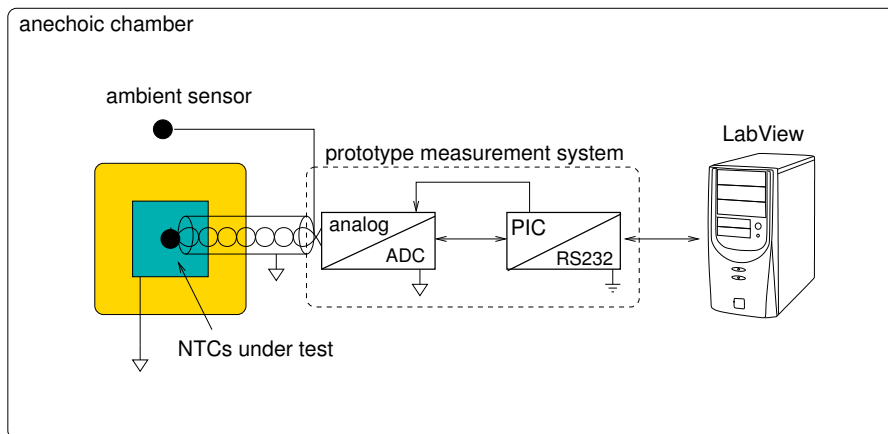


Figure 5.3: Set up for the TMS prototype test. Three thermistors are attached to the aluminium block which, in turn, is surrounded by the insulating material. The cables connecting the thermistors to the electronics are twisted and shielded to avoid interferences. The aluminium block, the cable shields and the electronic boxes are all connected to the same ground also to avoid interferences. The digital signal processing is done by a PIC that sends out data via serial interface to a computer running a LabView application. The ground of the serial interface and the ground of the electronics are kept separated to avoid interferences related with the ground of the computer. Opto-isolators are used for this purpose. This set up is placed into an anechoic chamber at Universitat Politècnica de Catalunya (UPC) premises to work in a quiet environment.

The results in Figure 5.4 show that the system exhibited the same noise levels when using thermistors as when measuring HS resistors, for frequencies higher than 1 mHz. Therefore, excess noise is not observed in the thermistors in the LTP MBW [119]. These results show that the temperature measurement noise levels required for the LTP mission are met. However, at frequencies below

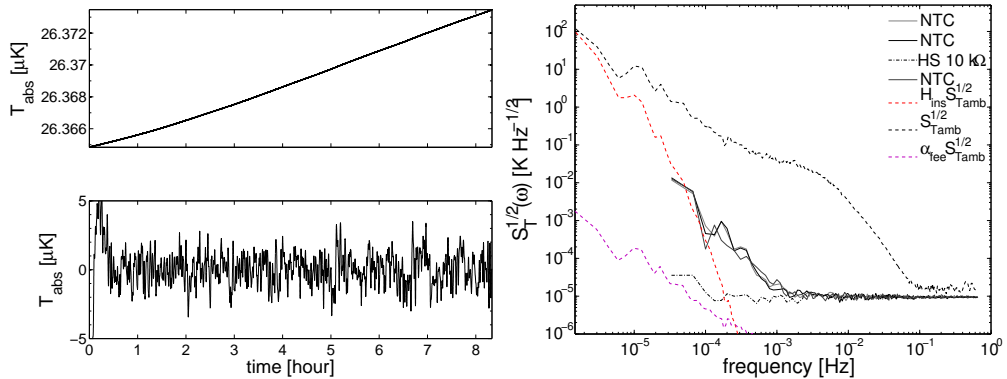


Figure 5.4: Left panel: the plot in the top shows the temperature evolution of one of the measurements. The bottom plot shows the same data band-pass filtered (between 0.5 mHz and 10 mHz) to remove the trend. The rms noise is $\sim 10^{-6}$ K in the bandwidth between 0.5 mHz and 10 mHz. Right panel: power spectral density for different measurements are shown. The upper dashed trace stands for the temperature fluctuations in the anechoic chamber. The three superimposed black traces are the measurements with the thermistors inside the insulator and the lowest dash-dotted trace is the measurement with a 10 k Ω high-stability resistor. The red dashed trace stands for the ambient temperature fluctuations projection in the aluminium block. The magenta dashed trace is the noise projection of the temperature fluctuations caused by the TC of the electronics together with ambient temperature fluctuations. The power spectral density in the MBW is within the requirement, i.e., 10^{-5} K Hz $^{-1/2}$.

1 mHz the fluctuations in the thermistor are higher than the expected ones. The excess noise for $f < 1$ mHz could be, in principle, ascribed to different sources. One of them is the temperature coefficient of the electronics together with ambient temperature fluctuations. This is immediately discarded since the ambient temperature was stable enough not to degrade the measurement —see dashed magenta trace, or

$$\alpha_{\text{FEE}} S_{T,\text{amb}}^{1/2}(\omega) < 10^{-5} \text{ K Hz}^{-1/2}, \quad \omega/2\pi > 0.1 \text{ mHz.} \quad (5.3)$$

Another possible source of *noise* is real temperature fluctuations of the aluminium block, however, this possibility can be also discarded: the projection of the laboratory temperature fluctuations in the aluminium block considering the insulator described in §4.1 does not agree with the experimental results —see the dashed red trace in Figure 5.4. They only match at very low frequency (< 0.1 mHz). Moreover the excess noise in the thermistors presents peaks (in the PSD) which are not observed in the ambient temperature fluctuations. After having discarded the previous possible explanations, there is still one possibility: the excess noise at frequencies below 1 mHz could have been caused by some unforeseen noise coming from the electronics. This hypothesis is, in principle, difficult to maintain since when measuring with high-stability resistors the performance of the system is the expected one. Nevertheless, there is an important difference between both measurements: the value of the high-stability resistor remains constant, i.e., the system is always measuring 10 k Ω (or 25 $^{\circ}\text{C}$ in equivalent temperature); on the contrary, when measuring temperature with the thermistor its resistance is drifting with time. In other words, the slope of the input signal when measuring the high-stability resistor is *zero*, while when measuring with thermistors it can be of micro-Kelvin per second. Drifting signals at the input of the ADC add noise to the signal due to non-idealities of the ADC. Different tests have confirmed this hypothesis. An example of this is shown in Figure 5.5 where it is clear that the power spectral density increases with the slope of the input signal and

that this effect spreads over the MBW. The PSD of the solid trace in Figure 5.5 (right) has been estimated using the data shown in the left panel of Figure 5.5. The slope (in absolute value) of such data varies from 15 to $8 \mu\text{K s}^{-1}$. The PSD of the dashed trace has been estimated using data where the temperature slope is lower than $0.5 \mu\text{K s}^{-1}$. It is clear that, under the latter conditions, most of the excess noise in the LTP MBW vanishes. For this reason the maximum slope permitted in the input signal not to degrade the system performance in the frequency range of the LTP is $\simeq 0.5 \mu\text{K s}^{-1}$ (this value depends on each specific ADC, however, it should not differ significantly when using another ADC of the same kind). Higher slopes result in an increase of the noise at frequencies around the milli-Hertz⁶. Temperature slopes of $\simeq 0.5 \mu\text{K s}^{-1}$ are not foreseen in nominal conditions⁷ in the locations where the sensors are attached to. Moreover, it is also important to note that differential measurements are, in principle, free of this problem since these measurements should exhibit very low slopes. Consequently, the problem of the non-ideal quantisation of the temperature signal must not pose a problem in the LTP MBW. Although in views of LISA this effect must be minimised since the measurement bandwidth goes down to 0.1 mHz and any small slope in the signal can degrade the measurement at that frequency. Further results on this issue are shown in §5.1.2 and a dedicated chapter describing the identification and minimisation of this problem is presented in §6.1.

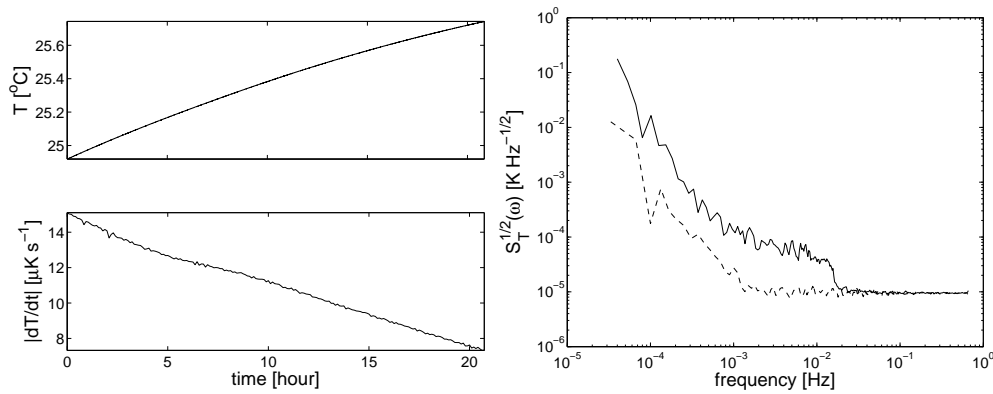


Figure 5.5: Left panel: absolute temperature measurement and its temperature slope (in absolute value). Right panel: Power spectral density of two measurements. The solid trace corresponds to the data shown in the left panel where the slope varied from $14 \mu\text{K s}^{-1}$ to $8 \mu\text{K s}^{-1}$. The dashed trace is the noise curve of an absolute measurement where the slope did not exceed $0.5 \mu\text{K s}^{-1}$. The former exhibits noise levels one order of magnitude higher than those obtained with the measurement with lower slopes. It is thus clear that in order to stick to the TMS requirements of the LTP, the slopes of the measured temperature must be less than $\simeq 0.5 \mu\text{K s}^{-1}$.

5.1.2 Engineering model test

The TMS in the engineering model (EM) of the data management unit (DMU) was also tested [115] —see Figure 5.7. The system design is exactly the same of the prototype with minor changes in some parts due to space qualified component constraints. The test was performed with *half* DMU, i.e.,

⁶Roughly speaking the frequency at which this effect appears is proportional to the slope of the input signal.

⁷The worst-case rate change of temperature at the LCA strut interface is $0.4 \mu\text{K s}^{-1}$. Since the thermal noise requirements within the LCA are more stringent than those at the interface, it is likely that they will be better within the LCA [154]. High slopes are, however, foreseen during the thermal experiments to be performed on-board the LTP —see chapter §7. However, in those experiments the temperature signal is also very strong and this effect becomes negligible.

only one of the data acquisition units (DAU) was tested —see Figure 1.12. Twelve EM thermistors were tested since each DAU permits connections for 12 sensors. The test set up was very similar to that used for the prototype qualification campaign —see Figure 5.3—, however, this time the anechoic chamber used was the one at the Centre Tecnològic de Telecomunicacions de Catalunya (CTTC) —see Figure 5.7. A significant difference from the prototype tests was that during this test the 12 thermistors were attached to the aluminium block by means of the *glue* (CV-2496 Nusil Tech.) intended to be used for the final attachment of the sensors at the specific locations of the LTP. The attachment process consisted in gluing each thermistor onto the aluminium block surface. The glue needs a cure time of about one week at ambient temperature. In order to keep the sensor securely attached during the curing time, a lid of methacrylate was used to exert pressure over them —see Figure 5.6— and, thus, ensure a good thermal contact between the sensors and the aluminium block.

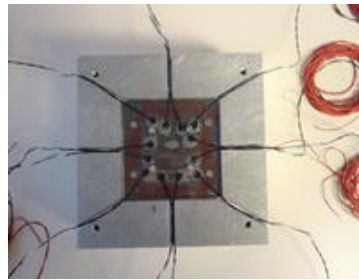


Figure 5.6: 12 thermistors attached onto the aluminium block surface. A small lid of methacrylate is used to exert pressure in the thermistors to keep them tightly fixed during the curing time of the glue.

The measurement flow chart is the one shown in Table 2.9: 12 absolute temperature measurements (four in each of the three boards in the DAU), 3 differential measurements (one in each of the three boards in the DAU) and 3 reference measurements (one in each of the three boards in the DAU). As stated in §5.1.1 the input temperature slope must be below a certain limit to ensure the performance of the measurement due to problems related with the ADC. The limit of such slope was set, initially, to $|dT/dt| \lesssim 0.5 \mu\text{K s}^{-1}$. However, the ADC of the EM (ADS7809 of Texas Instruments) TMS performed slightly worse than the model used in the prototype design (AD977 of Analog Devices). The former was more sensitive to drifting input temperatures than the latter. For this reason, the maximum temperature slope of the input signal not to degrade the EM (and FM) TMS performance in the MBW is $0.4 \mu\text{K s}^{-1}$ instead of $0.5 \mu\text{K s}^{-1}$.

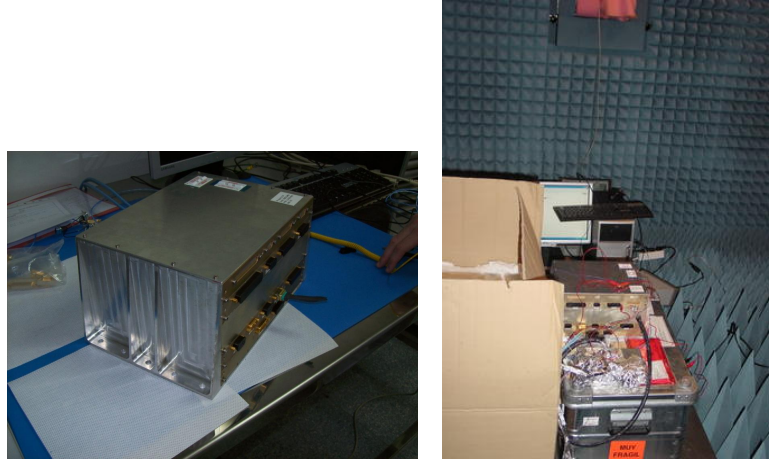


Figure 5.7: Left: engineering model of the DMU. Right: CTTC anechoic chamber.

Figures from 5.8 to 5.10 show the results for the 12 absolute temperature measurements. The results for the three independent electronic boards in the DAU are given separately. The plots in the left display the temperature and the temperature slope evolution with time. The plots in the right are the power spectral density estimated from the data where the temperature slope was lower than $0.4 \mu\text{K s}^{-1}$.

The noise level of the sensors attached to the first independent board (G_{11} in Table 2.9) of the DAU are within the expectations. The floor noise is $\approx 7.5 \mu\text{K Hz}^{-1/2}$, and stays flat for $f \geq 1$ mHz. The floor noise of the EM system is slightly lower than the prototype one. The reason is the higher sampling frequency (in the ADC) of the EM system with respect to the prototype. The EM sampling frequency is 50 kHz while the one of the prototype is 38.4 kHz: the higher the sampling frequency the higher the immunity to aliasing. The noise levels of the four sensors are essentially the same, except for one which presents a tiny increase in the milli-Hertz region.

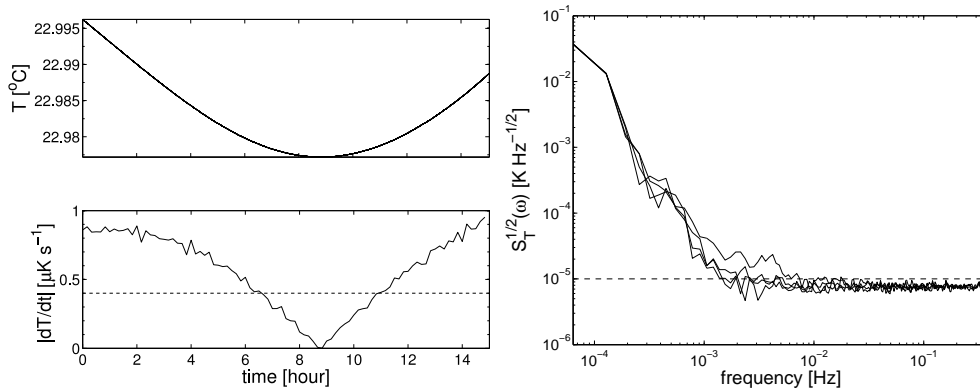


Figure 5.8: Measurements of the first group of the EM DAU, G_{11} . The left panel shows one absolute temperature measurement (top) and its slope (bottom). The data segment used for the PSD estimation shown in the right panel (for all four sensors) is that where the slope is less than $0.4 \mu\text{K s}^{-1}$ (dashed horizontal line in the plot on the left).

Figure 5.9 shows the results for the absolute temperature measurements of the second board of the DAU, G_{12} , where an unexpected behaviour in one of the sensors is observed.

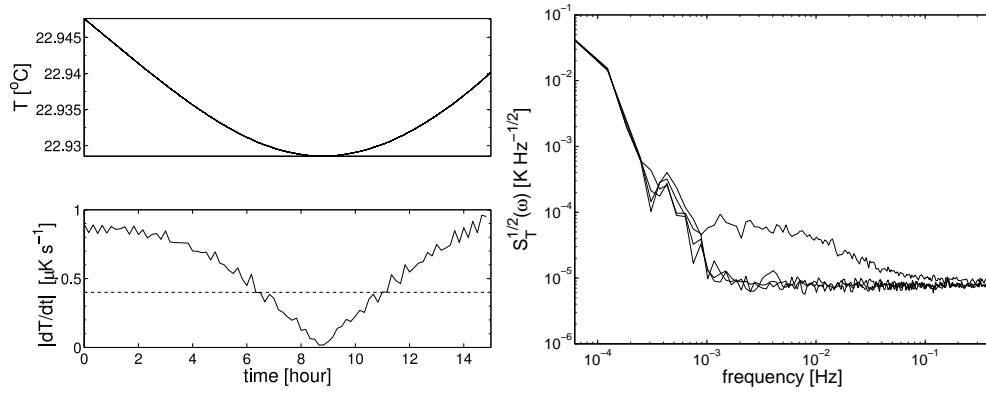


Figure 5.9: *Idem* as Figure 5.8 for the four sensors connected to the second board of the DAU, G_{21} .

The results for the measurements of the third independent board in the DAU, G_{31} , are given in Figure 5.10. Again, one of the sensors exhibits an anomalous behaviour which translates into unacceptable noise levels. The analysis of such behaviour and the possible causes of it are detailed in §5.1.2.2. Like in the previous measurements, the noise performance of the system is obtained using data with temperature slope lower than $0.4 \mu\text{K s}^{-1}$. The rest of the sensors performed properly within the MBW.

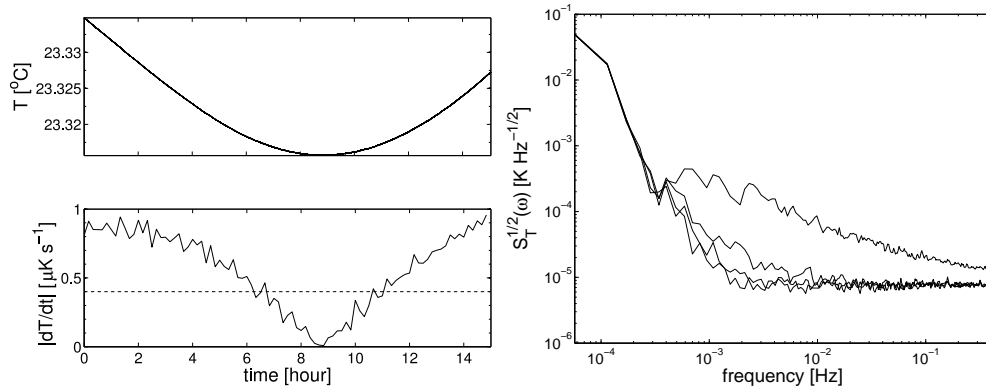


Figure 5.10: *Idem* as Figure 5.8 for the four sensors connected to the third board of the DAU, G_{31} .

Figures 5.11 and 5.12 show the differential and the reference measurements of the three boards, respectively. The former corresponds to the measurement between two thermistors in the aluminium block. Two of the measurements (those in G_{21} and G_{31}) are very noisy because one of the thermistors involved in the differential measurements was not working properly, as it can be seen in Figures 5.9 and 5.10. The differential measurement of G_{11} performs as expected⁸. This

⁸The differential measurements are intended to be done between locations with similar temperatures, therefore, the differential measurement should exhibit small drifts with time since the *common mode temperature* is rejected. During the on-ground tests the differential measurements were performed between two sensors attached to the

measurement presents noise levels of $\simeq 7 \mu\text{K Hz}^{-1/2}$ at frequencies close to 0.1 mHz.

The reference measurement consists in measuring two high-stability resistors forming the Wheatstone bridge. This measurement permits to observe any anomaly in the performance of the electronics independently of the sensors. This measurement will be also done in flight in order to identify any malfunctioning of the electronics. The results of the reference measurements during the EM test showed that the electronics were working properly. The noise is flat at frequencies close to 0.1 mHz with an amplitude of $\simeq 7 \mu\text{K Hz}^{-1/2}$. The anechoic chamber temperature fluctuations did not perturb the measurement since the temperature was very stable during the tests⁹ (for this reason the reference and differential measurements are almost flat at frequencies close to 0.1 mHz). In addition, the DMU metallic box also acts as a thermal insulator and screens out ambient temperature fluctuations from the electronics.

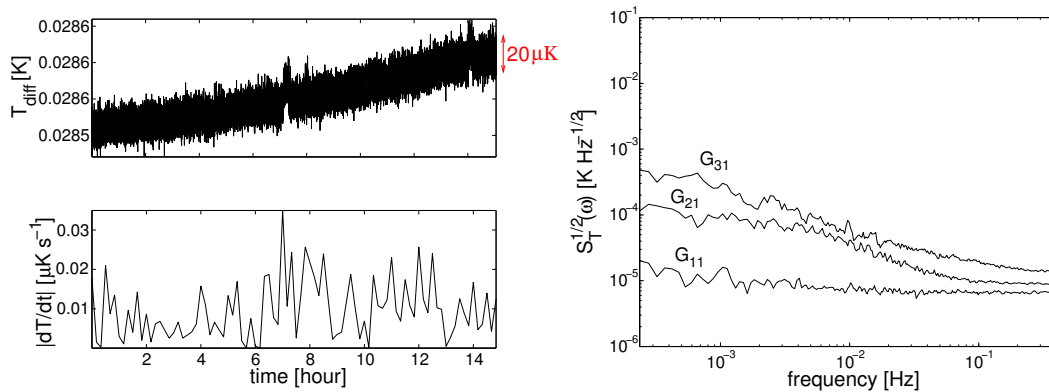


Figure 5.11: *Idem* as Figure 5.8 for the three differential measurements (one per group in the DAU). Two measurements are much noisier than the *nominal* floor noise. This is so because the sensors in the differential measurements were the malfunctioning sensors detected in the absolute measurements. The differential measurement of the first group, G_{11} , is performing correctly and it is free of the non-ideal quantisation excess noise since the two sensors are measuring similar temperatures, i.e., the slope of the differential signal is small, e.g., $0.02 \mu\text{K s}^{-1}$. The time domain data shown here is not filtered, thus the band goes from 0.1 mHz to 0.5 Hz. The rms noise in such band is $\simeq 3 \mu\text{K}$.

aluminium block, hence, at the *same* temperature.

⁹At 1 mHz fluctuations were $\simeq 0.05 \text{ K Hz}^{-1/2}$.

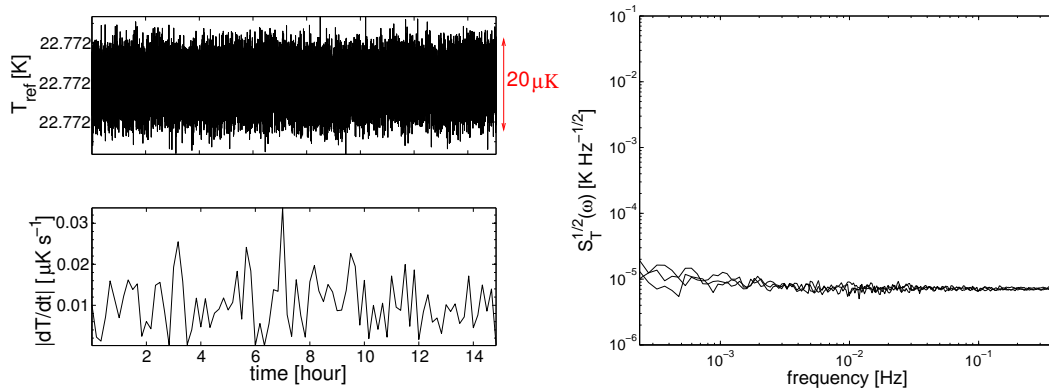


Figure 5.12: *Idem* of Figure 5.8 for the three reference measurements (one per group in the DAU). The three boards worked perfectly. The electronic noise is equivalent to a rms noise of $20\ \mu\text{K}$ in a band of $0.1\ \text{mHz}$ to $0.5\ \text{Hz}$.

Two important conclusions emerge from the EM test. On the one hand, the effect of the analog-to-digital conversion when measuring signals drifting with time was confirmed, although it should not be a problem in the LTP measurement bandwidth, as previously stated. On the other hand, and more worrying, is the fact that two sensors out of 12 were not performing properly for unknown reasons. The following sections deal with these two issues.

5.1.2.1 Excess noise due to non-ideal analog-to-digital conversion

As discussed in §5.1.1 the noise in the absolute temperature measurements is affected by the slope of the measured temperature. In this section we present more examples confirming this effect in the EM. These examples are intended to help understand the nature of this effect. However, the problem is described and investigated at length in §6.1.

Figure 5.13 (top left) shows the temperature slope for the data used in the PSD estimation of the EM test, i.e., data with a slope lower than $0.4\ \mu\text{K s}^{-1}$ —see Figures 5.8, 5.9 and 5.10. The bottom left plot shows the temperature band-pass filtered¹⁰. The correlation between both plots is clear: when the slope is close to zero (from $t=1.5\ \text{h}$ to $t=3\ \text{h}$) random noise with a peak-to-peak amplitude of $\simeq 2\ \mu\text{K}$ is present. On the contrary, as the temperature slope grows (from $t=0\ \text{h}$ to $t=1.5\ \text{h}$ and from $t=3\ \text{h}$ to the end), the noise in the measurement becomes *periodic* with a peak-to-peak amplitude of $\simeq 8\ \mu\text{K}$. This effect is thus responsible for the increasing noise at frequencies around the milli-Hertz (and lower) observed in Figures 5.8, 5.9 and 5.10. For comparison, the same plots for a differential measurement are given in Figure 5.13 (right): the slope of the signal is almost zero during the whole measurement, and the extra noise does not show up but it is rather kept with a peak-to-peak noise amplitude of $\simeq 2\ \mu\text{K}$, which further confirms the correlation between temperature slope and noise.

¹⁰The filter used is a Butterworth of second order with cut-off frequencies at $0.5\ \text{mHz}$ and $10\ \text{mHz}$. The filter is applied forward and backward in order obtain a zero-phase filter.

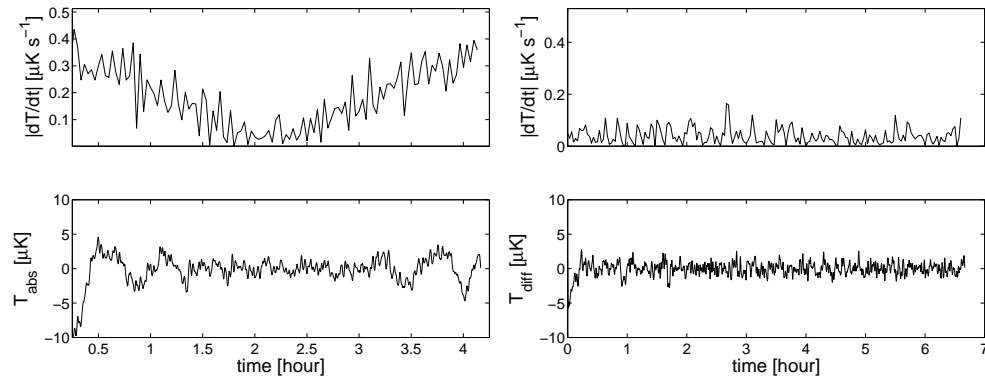


Figure 5.13: The plots in the left show the slope of an absolute temperature measurement (top) and the band-pass filtered absolute temperature measurement. The plots on the right are the same, but for a differential measurement. Higher noise is observed in the absolute measurement due to the increasing slopes at the beginning and at the end of the data segment.

Figure 5.14 shows another example of the quantisation problem when sampling signals of *high slope*. In this case the temperature slope varies from $\simeq 2 \mu\text{K s}^{-1}$ to $\simeq 1 \mu\text{K s}^{-1}$. The performance of the measurement is drastically reduced, i.e., the noise is about one order of magnitude higher than that under *nominal* conditions for $f < 5 \text{ mHz}$. The time evolution of the measurement when different slopes are present is shown in Figure 5.14 (left panel). The noise is somehow modulated by the slope of the measured temperature, i.e., the frequency of the *periodic noise* signal decreases as the temperature slope decreases, and vice versa. Consequently, if the temperature slope is changing with time the noise due to this effect is spread over the measurement bandwidth. For this reason, the power spectral density of this measurement presents a *plateau* at frequencies below 5 mHz. If for instance, the temperature slope is constant, the noise in the spectrum appears as peaks and is not spread over the band. The theoretical analysis, more experimental evidences and methods to overcome this problem are given in §6.1.

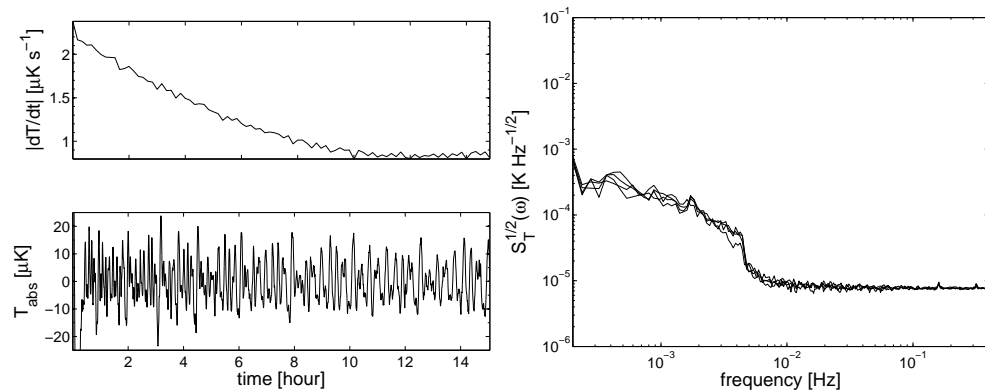


Figure 5.14: Left panel: the plot in the top shows the temperature slope. The plot in the bottom shows the temperature band-pass filtered. The relationship between the slope and the noise is clear. The higher the slope the higher the frequency of the *periodic* components of the noise. Right: power spectral density. The noise is clearly higher than usual in the MBW.

5.1.2.2 Excess noise in the thermistors

During the engineering model test an unexpected behaviour in 2 of the 12 sensors was detected. The noise in these two measurements was about one order of magnitude higher than the expected one in the measurement bandwidth. The measured data in the time domain are shown in Figure 5.15. The plot in the top corresponds to a correct thermistor. The plots in the middle and in the bottom correspond to the measurements of the two *malfunctioning* sensors connected to the boards G_{21} and G_{31} . Spurious steps appear in the measurement which translate into high noise levels when estimating the PSD —see Figures 5.9 and 5.10.

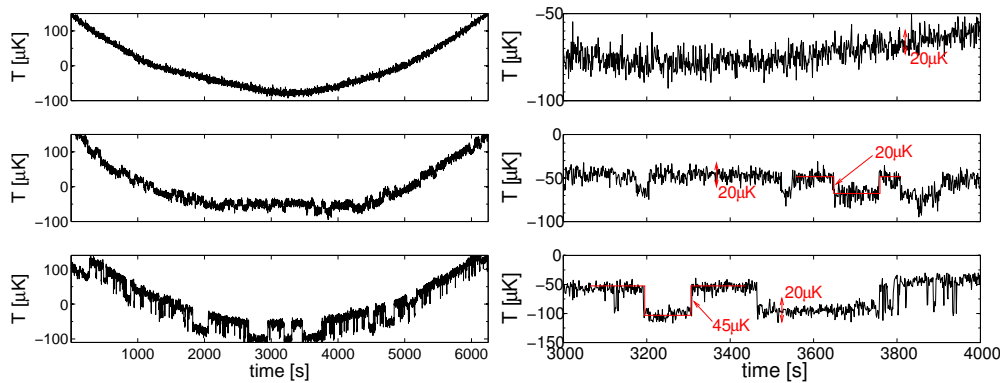


Figure 5.15: Top: absolute temperature measurement of a thermistor working properly. Middle: *idem* for the malfunctioning thermistor of the second board of the DAU, G_{21} . Bottom: *idem* for the malfunctioning thermistor of the third board of the DAU, G_{31} . Data is detrended for clearer visualisation. The plot in the right is a zoom.

Different potential sources were investigated in order to discern the actual reason of such behaviour. The causes considered were: (i) electronics of the DAU, (ii) bad soldering, (iii) poor thermal contact and, (iv) mechanical stress.

Electronics of the DAU This cause was very unlikely since all the other measurements were working properly, and the reference measurements were also correct. However, in order to fully discard this possibility, the two sensors exhibiting extra noise were connected to other channels of the DAU which were working OK with other thermistors, and vice versa. The results obtained were exactly the same, i.e., the sensors working correctly continued to work properly and the malfunctioning ones failed in the same manner as when they were connected to their original channels. Therefore, the excess noise was definitely ascribed to the thermistors themselves.

Bad soldering The cables of the EM sensors were not long enough to connect them directly to the DAU connections. For this reason, they had to be soldered to other longer cables. A possible bad soldering could have caused the behaviour observed in the two sensors. In order to discard this possibility, a visual inspection of the soldering was first done; no sign of bad soldering was detected. Another test consisted in measuring two high-stability resistors using the cables and solders of the two malfunctioning sensors. The obtained measurements did not exhibit anomalies, either. Consequently, the soldering was discarded as the source of the problems in the measurement.

Poor thermal contact The third possible cause considered was a possible poor thermal contact between the sensors and the aluminium block, this also was very unlikely since the thermal resistance should be about one order of magnitude higher than the usual ones to provoke such noise. The thermal resistances for the two malfunctioning sensors were $\simeq 60 \text{ K W}^{-1}$, which are typical values

—see appendix §B. Consequently, the unexpected noise in the two malfunctioning sensors could not be attributed to the thermal contact.

Mechanical stress Mechanical stress induced in the NTCs during the mounting onto the aluminium block was also considered. Thermistors were glued to the aluminium block and then a lid of methacrylate was screwed covering them in order to ensure a good attachment —see Figure 5.6. A test in order to check whether or not mechanical stress could have provoked an anomalous behaviour in the sensors was done [115]. A thermistor working properly was subjected to different levels of pressure while measuring its performance. The screwing torque was quantified by using a torque wrench. The torques applied are summarised in Table 5.1.

Test name	Torque applied at each screw
ST0	0.0 N m
ST1	0.3 N m
ST2	0.5 N m
ST3	0.7 N m
ST4	1.0 N m

Table 5.1: Screwing torques.

After each new torque applied, the aluminium block (with the two NTCs) was placed inside the insulator and measurements were performed. Results of the estimated PSDs are given in Figure 5.16 (left).

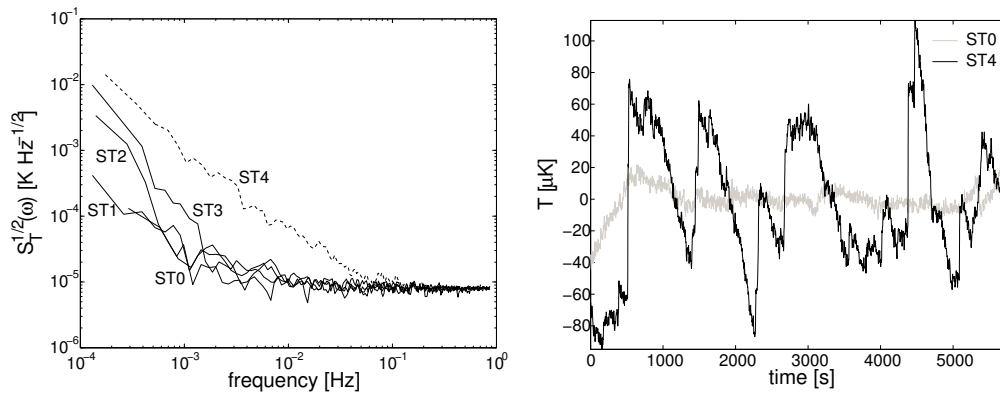


Figure 5.16: Left: noise equivalent temperature for the thermistor under different pressure conditions. Right: time-domain data for a thermistor under normal conditions (grey trace) and for a thermistor with the screws at 1 N m (black trace, ST4), which corresponds to the dashed trace in the plot on the left. The malfunctioning behaviour was detected when the torque applied to the sensor was 1 N m.

From Figure 5.16 we notice that the thermistor started exhibiting an anomalous behaviour at a screwing torque of 1 N m (ST4) and, actually, after 20-hour measurement it broke down¹¹. The plot in the right in Figure 5.16 shows (in time domain) the comparison between the measurement done with a sensor without any pressure applied to it and the ones obtained when measuring the sensor subjected to a torque of 1 N m at each screw. Clearly, the compressed sensor was not performing correctly. Somehow, a similar behaviour is observed in the time domain plots between the sensor

¹¹The torque of 1 N m in each of the screws is very high and even physical damage was naked eye observed in the sensor.

subjected to the torque of 1 N m and the sensors that failed in the EM test, even though the results of the former are much noisier than those exhibited by the latter. For this reason, at that moment the hypothesis of some damage in the NTCs during the attachment procedure in the EM test was temporarily accepted, although in a sceptical manner¹². The test of the TMS flight model discarded this explanation —see §5.1.3.

5.1.3 Flight model test

The test for the flight model (FM) —see Figure 5.17— was exactly the same as the one described for the EM test, although this time it was carried out at the anechoic chamber in UPC premises [116]. In this test, though, both DAUs were present in the DMU. However, again, only 12 FM thermistors were available. For this reason, two independent runs were performed during this test. In the first run, thermistors were connected to DAU-1 while a set of high-stability resistors of different values¹³ were connected to DAU-2. During the second run, the connections were swapped, i.e., thermistors were connected to DAU-2 and the high-stability resistors to DAU-1. During the FM test a simple feedback control was implemented in the insulator jig in order to reduce the duration of the test: by using a temperature control, the temperature slope of the aluminium block was maintained within the required values to avoid ADC errors, i.e., $0.4 \mu\text{K s}^{-1}$. Otherwise, we would have to wait for the stabilisation of the system, and then wait for a suitable segment of data where the slope was low enough, which depended on the environmental conditions.

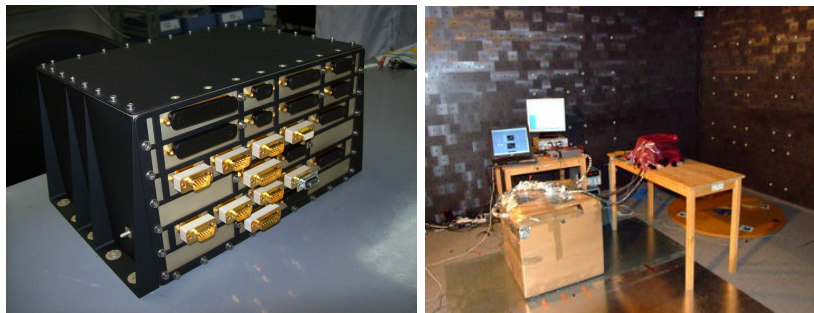


Figure 5.17: Left: Flight model of the DMU. Right: Anechoic chamber of the UPC with the set up for the test.

The results of the test were again not fully satisfactory since two thermistors were also exhibiting an anomalous behaviour as explained in the EM test —see §5.1.2. The electronics and the rest of the thermistors (ten) were performing correctly. The explanation of the excess noise in the EM test related to the mechanical stress induced during the attachment of the sensors to the aluminium block was discarded. This time, the torque applied in each of the screws when attaching the FM thermistors to the aluminium block was controlled and it was never larger than 0.5 N m, which should not be harmful for the sensors —see §5.1.2.2. Therefore, after testing 24 thermistors (12 for the EM test and 12 for the FM test), a total of four sensors were not performing correctly due to noticeable excess noise in their measurements.

An important consequence of these results is that not all space qualified thermistors exhibit the same performance. Four sensors out of 24 have shown an anomalous behaviour. This fact might occur since thermistors prior to be delivered by the manufacturer are subjected to a set of tests related with space qualification constraints. The tests involve thermal shock, burn-in, etc. [? 95]. Consequently, it is possible that the qualification process damages the performance of some of the

¹²The pressure in the thermistor needed to observe an anomalous behaviour was much higher than the one applied in the mounting of the EM test.

¹³In order to have a measurement in each temperature scale.

thermistors at the sensitivity levels we are interested in (micro-Kelvin)¹⁴ or it is just an effect of the manufacturing process.

In view of this problem, a screening process is mandatory in order to select those thermistors working properly, otherwise defective sensors could be flown with the LTP. The rest of the system worked as expected, and the requirement for the LTP was fully attained: the noise of the system is $10^{-5} \text{ K Hz}^{-1/2}$ in the frequency band of 1 mHz to 30 mHz.

5.2 Tests in the LISA MBW

Once the requirements for the LTP have been accomplished the next question, with an eye on LISA, but also of importance for the LTP, is: do we have the same noise levels at 0.1 mHz? In principle, the electronic noise of the system should remain flat in the MBW due to the measurement technique used —see §2.3.1. However, excess noise might appear at very low frequency (0.1 mHz), specially, due to the semiconductor nature of the thermistor —cf. §2.2.2.

A dedicated test in order to assess whether or not extra noise is present in the LISA frequency band has been done [118]. The test bed is more complicated than that needed for the LTP MBW and it has been presented in §4.2. The scheme of the whole set up is shown in Figure 5.18. During the test, four measurements were taken: laboratory temperature (needed for the feedforward control scheme), electronics temperature (needed for the temperature control of the electronics), aluminium block temperature (needed for the feedback control) and the temperature difference between two sensors very close one to each other attached onto the aluminium block, which is the measurement of interest for the noise analysis. The sampling frequency, though, differed from the *nominal* one when sampling four channels (1.3875 Hz) due to the control loops implemented in the system. The sampling frequency went down to 0.68 Hz which implies a higher floor noise due to aliasing —cf. §2.3.4. A Labview application was used to control the temperature of the aluminium block —see §4.2.3, and also to control the temperature of the electronics. Both controls were commanding a programmable power supply (E3631A of Agilent) by means of the feedback-feedforward control described in §4.2. The Labview application was also in charge of selecting the channels of the multiplexers in order to choose the adequate measurements. Altogether, these actions were done in series, and, thus, the sampling frequency was reduced, specially due to the time needed to command the programmable power supply.

¹⁴Defective for us means that the noise is higher than $\sim 10^{-5} \text{ K Hz}^{-1/2}$ although they perform correctly from the point of view of the manufacturer specifications.

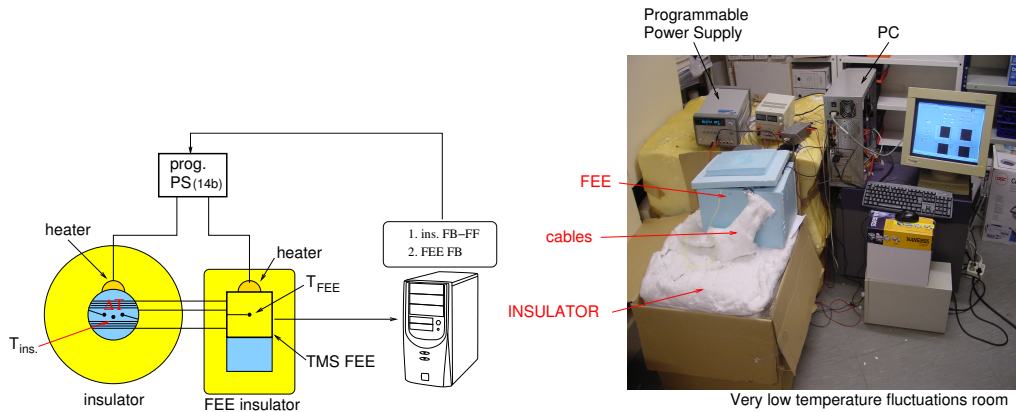


Figure 5.18: Left: simplified scheme of the test set up for the test at the LISA measurement bandwidth. Details are given in §4.2. Right: implementation of the system in a thermally stable and isolated room. The test was only done with prototype system.

The power spectral densities of the measurements are shown in Figure 5.19. The temperature control achieved an attenuation of $\simeq 5 \cdot 10^{-4}$ at 0.1 mHz which result in a temperature fluctuations in the aluminium block, “ T_{ins} ”, of $\simeq 2 \cdot 10^{-4} \text{ K Hz}^{-1/2}$ at 0.1 mHz. The required stability for a meaningful test was $5 \cdot 10^{-3} \text{ K Hz}^{-1/2}$ —see §4.2.3.

The red solid trace labelled as “ ΔT ” is the differential measurement noise levels. The differential measurement did not exhibit $1/f$ noise at frequencies down to 0.1 mHz. The floor noise in this measurement was slightly higher than the usual one, it was $\simeq 12 \mu\text{K Hz}^{-1/2}$ instead of $\simeq 8 \mu\text{K Hz}^{-1/2}$ since the sampling frequency went down from 1.375 Hz to 0.68 Hz. Thus the floor noise increased by a factor of $\sqrt{1.375/0.68}$.

The conclusion of the noise investigations presented in this section is that $1/f$ noise is not present in the thermistors and the associated electronics designed for the LTP, i.e., the noise remains flat down to 0.1 mHz. The thermistor was the critical component of the measurement chain susceptible of exhibiting $1/f$ noise. This test has discarded such hypothesis. The electronic noise is kept white in the measurement bandwidth thanks to lock-in amplification technique which avoids the $1/f$ noise of the instrumentation amplifier —see §2.3. It is also important to note that the resistors forming the Wheatstone bridge did not exhibit any $1/f$ noise, as also could be expected [94]. This means that the thermal environment of the LTP can be measured with a limiting noise of $\simeq 8 \mu\text{K Hz}^{-1/2}$ for $f \geq 0.1 \text{ mHz}$ or, in other words, a rms noise of $0.1 \mu\text{K}$ in a bandwidth of 0.1 mHz. In view of LISA, we have shown that the designed system for the LTP is also suitable for the LISA measurement bandwidth and, as shown in §6.2, the floor noise can be still further reduced to $\simeq 1 \mu\text{K Hz}^{-1/2}$.

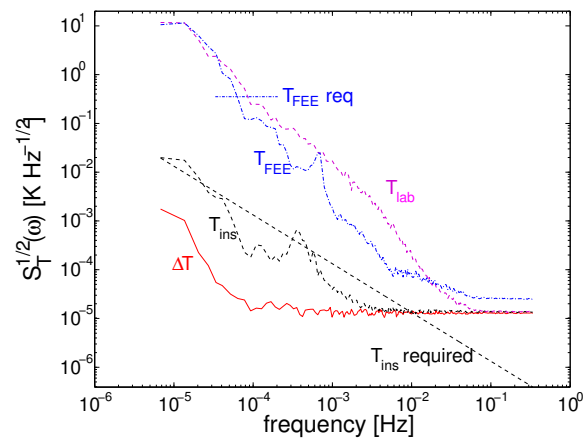


Figure 5.19: Test results: “ T_{lab} ” magenta trace: ambient temperature fluctuations. “ T_{FEE} ” blue trace shows the temperature fluctuations of the electronics, while “ T_{FEE} required” sets the maximum permitted value for a successful test. The electronics temperature was controlled by a feedback control to maintain the temperature fluctuations below $0.35 \text{ K Hz}^{-1/2}$ at 0.1 mHz . “ T_{ins} ” black trace shows the aluminium temperature fluctuations and the dashed black trace is the maximum permitted. The peak in the PSD in “ T_{ins} ” appears due to the control loop that maintains the fluctuations of the aluminium block below $10^{-3} \text{ K Hz}^{-1/2}$ at 0.1 mHz . “ ΔT ” red trace: differential measurement temperature fluctuations, where we notice that excess noise is not present in the measurement for $f \geq 0.1 \text{ mHz}$.

Chapter 6

Performance improvements of the TMS

This chapter describes some aspects that have been discussed qualitatively in the previous sections and, basically, are a consequence of the results obtained during the different test campaigns. They are related to improvements in the design to achieve a more sensitive measurement system in view of LISA. We first discuss the problem stated in chapter §5 related to the quantisation of the signal with a non-ideal ADC [117]. This problem arises in the LTP measurement bandwidth when signals with slopes higher than $\simeq 0.5 \mu\text{K s}^{-1}$ are sampled. Although in the LTP this should not pose a problem¹, the LISA mission works at a frequency one order of magnitude lower than LPF, thus this effect could limit the system performance. The second part of the chapter deals with another issue: the temperature stability required in LISA is still not defined, but it will likely be one order of magnitude more demanding than in the LTP. Therefore, a TMS one order of magnitude more sensitive will be needed.

6.1 ADC non-linear errors correction

In §5.2 we have shown that the designed system exhibits noise levels in terms of temperature of

$$S_T^{1/2}(\omega) \leq 10^{-5} \text{ K Hz}^{-1/2}, \quad \omega/2\pi \geq 0.1 \text{ mHz} \quad (6.1)$$

However, excess noise has been detected when the measured temperature drifts. The following sections focus on the identification and reduction of such noise. First, we state the problem of the non-ideality in the ADCs² which has been identified as the source of the problem. Second, different ways to overcome this problem are exposed and, finally, experimental results assessing this possibility are shown.

6.1.1 Non-ideal quantisation noise

In this section we analyse the ADC non-linearity error and how it perturbs the temperature measurements. Quantisation is inherently a non-linear process. In an ideal ADC this error is bounded to the quantisation step which is defined as [74]

$$\Delta = \frac{1}{2^N} V_{\text{FS}} \quad (6.2)$$

¹The expected slopes are lower than $0.5 \mu\text{K s}^{-1}$ in nominal conditions in the LCA. See footnote 6 in chapter §5.

²Only one ADC suitable for this purpose has been certified for use in space applications. This device uses a 16-bit capacitor based successive approximation register (SAR).

where N is the number of bits, V_{FS} is the full-scale voltage of the ADC and Δ is the least-significant bit (LSB) or quantisation step. The error introduced by the quantisation step can be treated as an independent random variable with uniform probability density function (pdf) and uniform spectral density when a large number of bits is present [74]:

$$S_q(\omega) = \frac{\Delta^2}{12} \frac{1}{f_s/2}, \quad 0 \leq \omega/2\pi \leq f_s/2 \quad (6.3)$$

where f_s is the sampling frequency.

Nevertheless, in a non-ideal ADC the quantisation steps are not uniform due to mismatches in its internal topology, specifically, due to tolerances in the capacitors [66, 76, 8, 150]. This non-uniformity is specified in two parameters: differential non-linearity (DNL) and integral non-linearity (INL). The DNL error is defined as the deviation between the actual difference between midpoints and a least significant bit (LSB) for adjacent codes. The additional noise related to this effect can be bounded by proper dithering [24, 59, 125, 149, 151, 152, 11, 153, 19]. The inherent *analog noise* of our system can be considered as a dither source, enough to make this effect negligible—see §6.1.1.3. On the other hand, the INL error is defined as the discrete integration of the DNL and can be understood as the difference between the non-ideal and the ideal (uniform quantisation steps) ADC transfer curves—see Figure 6.1. The noise introduced by this error is usually less noticeable, although much more difficult to reduce. The DNL and INL are expressed as [92, 89]

$$DNL(i) = K_{i+1} - K_i - \Delta \quad i = 0, 1, 2, \dots, 2^N - 1 \quad (6.4a)$$

$$INL(i) = \sum_{j=0}^i DNL(j) \quad i = 0, 1, 2, \dots, 2^N - 1 \quad (6.4b)$$

where K_i is the i -th transition voltage of the ADC. The left panel of Figure 6.1 shows the transfer curves of an ideal 8-bit ADC and a simulated non-ideal 8-bit ADC. The difference between both results in the error signal is shown in the bottom plot. The panel in the right shows the DNL and the INL of the non-ideal 8-bit ADC. Such curves are different for each individual ADC and they appear due to non-uniform quantisation steps.

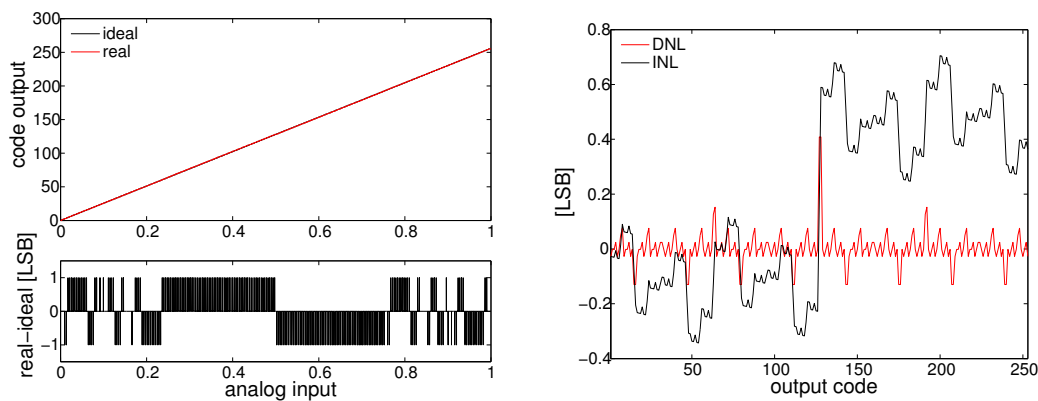


Figure 6.1: Left: ideal and non-ideal (simulated) 8-bit ADC transfer curves. The difference between both is shown in the plot in the bottom. Right: DNL and INL of the non-ideal ADC. The non-idealities of the ADC have been simulated considering a 1% tolerance in the capacitors of the ADC.

We focus on the INL error since it is the one limiting the performance of the measurement when slow rate input signals, i.e., with slopes of $\mu\text{V s}^{-1}$, are considered, which is a common situation in

temperature measurements. The sensitivity of the TMS is 1.35 K V^{-1} , therefore, drifts of $\mu\text{K s}^{-1}$ are equivalent to drifts of $\mu\text{V s}^{-1}$ at the input of the ADC.

6.1.1.1 ADC bit error description

In this section we describe the effect of a faulty bit in a SAR ADC. Afterwards, we will apply these results to actual measurements to validate whether or not the origin of the extra noise is due to ADC non-linearities. To do so, a simple model for the ADC is considered. The analog-to-digital conversion is done (in SAR ADCs) by comparing the sampled signal with an analog voltage generated by a digital-to-analog converter (DAC) and a SAR³ [66]. The topology of the DAC is based on a switching capacitor bank composed of 16 capacitors, scaled from $2^{16}C$ to C , where $2^{16}C$ is the most-significant bit (MSB) and C is the LSB. A *faulty bit* is that with a capacitance value different from the ideal one. The transition voltage of the ADC, i.e., the DAC output voltage is [74]

$$V_{\text{DAC}} = \frac{\sum_{k=0}^{N-1} b_k 2^k C}{\sum_{k=0}^{N-1} 2^k C} V_{\text{FS}} = \frac{\sum_{k=0}^{N-1} b_k 2^k C}{(2^N - 1)C} V_{\text{FS}} \quad (6.5)$$

where b_k is the binary digit ($k = 0$ stands for the LSB and $k = N - 1$ for the MSB); it is set to 0 or 1 depending on the sampled voltage⁴, and N is the number of bits. An error $\delta C_k = C_{k,\text{real}} - 2^k C$ in the k -th capacitor results in an error in the DAC output when the corresponding bit is 1, i.e., the transition voltage is slightly different from the ideal one. The error for a faulty bit is

$$\begin{aligned} \epsilon_k &\doteq V_{\text{DAC,real}}(k) - V_{\text{DAC,ideal}}(k) \\ &\simeq \frac{b_k \delta C_k}{(2^N - 1)C} V_{\text{FS}} = b_k \frac{\delta C_k}{C} \Delta \end{aligned} \quad (6.6)$$

The erroneous bit produces a superimposed periodic pattern in the quantisation error of the ADC with 1 LSB of amplitude when the input voltage varies between zero and V_{FS} , and exhibits a periodicity of $2^{k+1}\Delta$. An example of this is shown in Figure 6.2 where it can be seen how a faulty bit introduces low frequency components superimposed on the typical sawtooth error function of an ideal ADC (red trace). In the left panel of Figure 6.2 the effect of a faulty bit in the transfer curve is clearly seen. The transition voltages in the ideal ADC (red trace) and the non-ideal ADC (black trace) are different.

³Successive approximation register (SAR) uses the algorithm put forth Tartaglia in 1556 to determine an unknown weight by a minimal sequence of weighting operations [76]. The algorithm is the following: for instance, we assume $x=7$. Then, is $x \geq 2^3$? no, the bit is set to zero and we do not retain 2^3 . Is $x \geq 2^2$? Yes, the bit is set to 1 and we retain 2^2 . Is $x \geq (2^2 + 2^1)$? Yes, the bit is set to 1 and we retain 2^1 . Is $x \geq (2^2 + 2^1 + 2^0)$? Yes, the bit is set to 1. The result is 0111_2 .

⁴The values of b_k are the ones obtained by means of the SAR algorithm. In the example of footnote 3, $b_k=(1 \ 1 \ 1 \ 0)$.

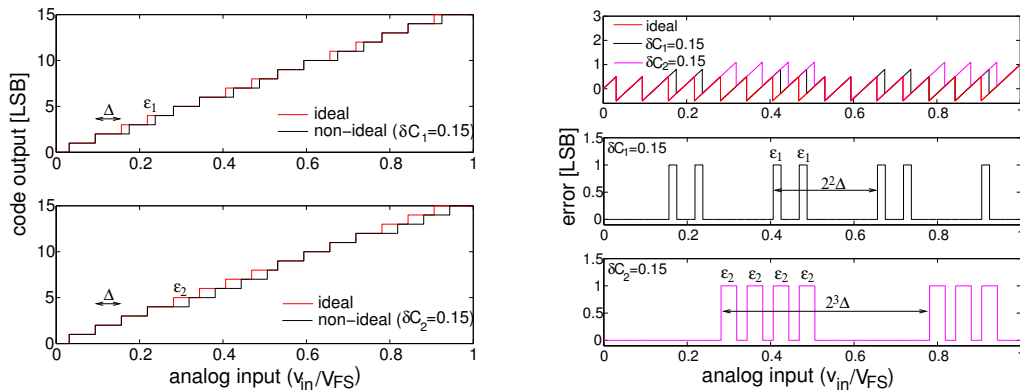


Figure 6.2: Three simulated 4-bit ADC: ideal, $\epsilon_1 = 0.3\Delta$ and $\epsilon_2 = 0.6\Delta$. Left: transfer curves. Right: in the top we show the quantisation error functions. The plot in the centre and in the bottom show the differences between the ideal and the non-ideal transfer curves. Note the low frequency components superimposed (black and magenta traces) to the ideal ADC transfer curve (red trace). The differences between the ideal ADC transfer curve and the real ADC ones are also shown and represent the *extra* noise due to the non-idealities of the ADC.

Another example is shown in Figure 6.3. The Fourier transforms of the quantisation error functions of an ideal 8-bit ADC and an 8-bit ADC with a faulty bit in the fourth LSB ($k=3$) are shown — see §6.1.1.2 and §6.1.1.3. It is clear the extra components introduced by the non-idealities of the ADC.

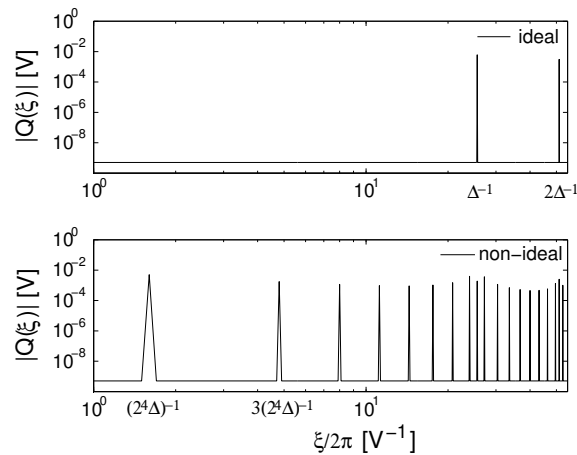


Figure 6.3: 8-bit ADC. Top: Fourier transform of the ideal quantisation noise. Bottom: *idem* as the plot in the top for a non-ideal ADC: $\epsilon_3=0.4\Delta$. The components of the non-ideal ADC are the ones of the ideal quantiser plus the ones due to ϵ_k .

6.1.1.2 Dither signal effect in ideal quantisers

When a dither voltage, d , with a certain probability density function (pdf), $p(d)$, is added to the input signal of the ADC, v , the average of the quantisation error observed at the ADC output,

$\langle q(v) \rangle$, is given by [149]

$$\langle q(v) \rangle = \int_{-\infty}^{\infty} q(v+z)p(z)dz \quad (6.7)$$

where $q(v)$ stands for the quantisation error of an ideal ADC. If we define the Fourier transform in voltage domain by⁵

$$\mathcal{Q}(\xi) = \int_{-\infty}^{\infty} q(v)e^{-i\xi v} dv \quad (6.8)$$

and apply it to Eq. (6.7), the following ensues:

$$\langle \mathcal{Q}(\xi) \rangle = \mathcal{Q}(\xi)\mathcal{P}^*(\xi) \quad (6.9)$$

The quantisation error for an ideal ADC (a sawtooth waveform of amplitude $\Delta/2$ —see Figure 6.2) is a periodic function of v with period Δ . It can be expanded in Fourier series:

$$q(v) = \frac{\Delta}{\pi} \sum_{n=1}^{\infty} \frac{(-1)^{n+1}}{n} \sin \frac{2\pi n v}{\Delta} \quad (6.10)$$

and its Fourier transform is

$$\mathcal{Q}(\xi) = -i\Delta \sum_{\substack{n=-\infty \\ (n \neq 0)}}^{\infty} \frac{(-1)^{n+1}}{n} \delta \left(\xi - \frac{2\pi n}{\Delta} \right) \quad (6.11)$$

where $\delta(\cdot)$ is Dirac's delta function.

If we consider zero-mean Gaussian noise as the dither voltage, its pdf and Fourier transform are, respectively,

$$p(d) = \frac{1}{(2\pi)^{1/2}\sigma} e^{-\frac{d^2}{2\sigma^2}} \quad (6.12)$$

$$\mathcal{P}(\xi) = e^{-\xi^2\sigma^2/2} \quad (6.13)$$

where σ^2 is the variance of the noise. Substituting Eqs. (6.11) and (6.13) into Eq. (6.9) and taking the modulus we obtain

$$|\langle \mathcal{Q}(\xi) \rangle| = \Delta e^{-\xi^2\sigma^2/2} \sum_{\substack{n=-\infty \\ (n \neq 0)}}^{\infty} \frac{1}{n} \delta \left(\xi - \frac{2\pi n}{\Delta} \right), \quad (6.14)$$

From Eq. (6.14) we note that the Gaussian dither signal, d , low-pass filters the quantisation error —see Figure 6.6. For instance, for $\sigma = \Delta$ the attenuation of the first term in the series is $2.7 \cdot 10^{-9}$. In our case, we have a 16-bit ADC with $V_{\text{FS}}=10$ V, *quasi*-white noise at the input of the ADC $S_V^{1/2} \simeq 7 \mu\text{V Hz}^{-1/2}$ and a noise equivalent bandwidth (NEBW) of $\Delta f \simeq 1.2 f_{\text{cut-off}}=600$ Hz where $f_{\text{cut-off}}$ is the cut-off frequency of the anti-alias filter —see §2.3.2.4. Thus, Δ and σ can be readily calculated, i.e.,

$$\Delta = \frac{1}{2^N - 1} V_{\text{FS}} = 0.15 \text{ mV}, \quad (6.15)$$

$$\sigma = S_V^{1/2}(\omega) \cdot f_{\text{cut-off}}^{1/2} \simeq 0.17 \text{ mV}. \quad (6.16)$$

In our case $\sigma \simeq \Delta$, thus the quantisation noise from the ideal ADC is suppressed by the inherent noise of the analog processing chain.

In Figure 6.4 an example of this effect is shown. We have added white Gaussian noise of $\sigma = \Delta$ to the simulated 8-bit ADCs shown in Figure 6.3. The effect is clear: the peaks in the spectrum of the ideal ADC are gone whereas the low frequency components introduced by the non-ideal ADC still remain. In Figure 6.6 (top) the shape of the *dither filter* is shown together with the frequency components of an ideal ADC.

⁵ ξ is the Fourier-conjugate variable of v , and is accordingly measured in 2π volts⁻¹.

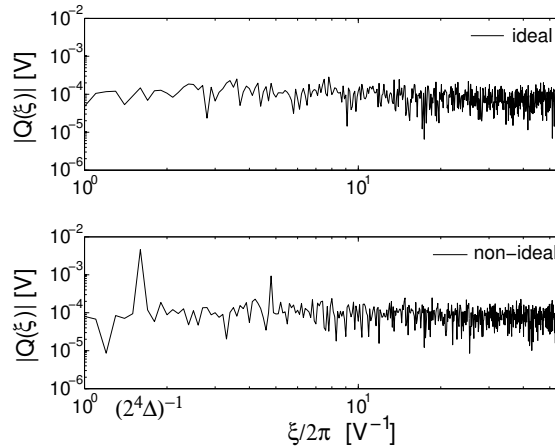


Figure 6.4: *Idem* as Figure 6.3. However, this time Gaussian noise with $\sigma = \Delta$ has been added to the signal before the quantisation process. All the peaks of both quantisers vanish except those at low frequency introduced by the faulty bit of the non-ideal ADC.

6.1.1.3 Dither signal effect on non-ideal quantisers

The error of a real ADC is formed by the ideal quantisation error function —see Eq. (6.10)— plus a term related to the non-idealities of the ADC, i.e.,

$$q(v) = q_i(v) + q_k(v) \quad (6.17)$$

where $q_i(v)$ and $q_k(v)$ are the ideal quantisation error and the quantisation error due to the faulty bits, respectively. As seen in the previous section, the ideal quantisation error is filtered out by the analog noise in the measurement chain, which acts as a dither signal of Gaussian pdf. Instead, the quantisation error due to the non-ideality of the ADC is not reduced by the same analog noise, which causes it to show up as extra noise. In this section we show how it can be identified in the temperature measurements and how it limits the performance of the system. The quantisation error caused by faulty bits, $q_k(v)$, is the waveform shown in Figure 6.5.

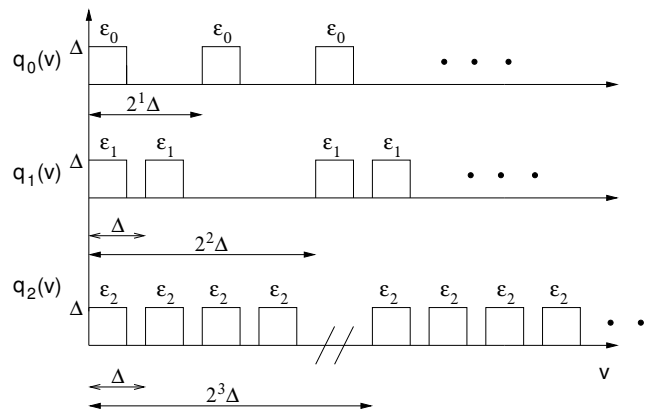


Figure 6.5: $q_k(v)$. This signal is the difference between the quantisation error of an ideal ADC and the quantisation error of a real ADC. ϵ_k is given in Eq. (6.6).

The modulus of the Fourier transform of the non-ideal noise for a single defective bit, k , say, is [152]

$$|\mathcal{Q}_k(\xi)| = \Delta \sum_{n=-\infty}^{\infty} \frac{\sin \frac{n\pi\epsilon_k}{2^{k+1}\Delta}}{n} \frac{\sin \frac{n\pi}{2}}{\sin \frac{n\pi}{2^{k+1}}} \delta\left(\xi - \frac{\pi n}{2^k\Delta}\right) \quad (6.18)$$

where ϵ_k is given in Eq. (6.6). The effect of Gaussian dither on $q_k(v)$ is readily calculated with Eq. (6.9):

$$|\mathcal{Q}_k(\xi)| = \Delta e^{-\xi^2\sigma^2/2} \sum_{n=-\infty}^{\infty} \frac{\sin \frac{n\pi\epsilon_k}{2^{k+1}\Delta}}{n} \frac{\sin \frac{n\pi}{2}}{\sin \frac{n\pi}{2^{k+1}}} \delta\left(\xi - \frac{\pi n}{2^k\Delta}\right) \quad (6.19)$$

Equations (6.18) and (6.19) are plotted in Figure 6.6 (centre and bottom). The plot in the top represents the components introduced by an ideal ADC. The plot in the centre corresponds to errors associated to $k = 0$, i.e., the LSB. Here, the fundamental period is 2Δ . The plot in the bottom shows the same for $k=3$ (the 4-th bit) with a fundamental period of 16Δ . For each plot, the low-pass filter generated by Gaussian dither of $\sigma = \Delta$ is also plotted (dashed lines). It can be seen that the dither signal suffices to suppress the noise associated to a faulty LSB, $k=0$ (this corresponds to the DNL effect which, is readily mitigated). However, it cannot attenuate the low frequency lines due to errors in the higher bits. In fact, when $k = 3$ the dithering with $\sigma = \Delta$ is clearly insufficient.

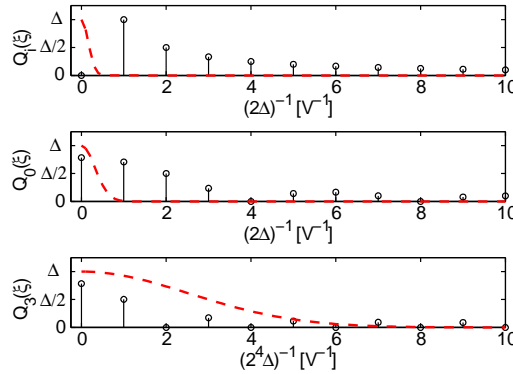


Figure 6.6: Top: quantisation error for an ideal ADC, $\mathcal{Q}_1(\xi)$. Centre: quantisation error for a non-ideal ADC with $k = 0$ as the faulty bit. The error is $\epsilon_0 = 0.5\Delta$. Bottom: same as the plot in the middle but for $k = 3$. The error is $\epsilon_3 = 0.5\Delta$. Note that the x -axis scale of the plot in the bottom is different from the one in the top and the centre plots; for instance, the main frequency component for \mathcal{Q}_0 is $1/2\Delta$ while for \mathcal{Q}_3 is $1/2^4\Delta$. This implies that errors in the MSBs appear at lower frequencies than those in the LSBs errors. The dashed red trace is the equivalent low-pass filter of the dither signal which is Gaussian noise with $\sigma = \Delta$. The filter is sufficient to reduce the frequency components of the ideal ADC and of the non-ideal ADC with the faulty bit $k=0$. However, it is useless for the faulty bit $k=3$. The term at “dc” is only a constant error, and therefore does not affect the measurement.

From Figure 6.6 we note how faulty bits introduce spectral components in the measurement if the signal spans a large enough fraction of the range of the ADC transfer curve. Conversely, if the input signal is a constant dc then no extra noise will be seen, since no bit, whether faulty or not, will change its state. Therefore, the INL effect becomes perceptible in our system only when the input signal runs through a sufficiently wide fraction of the ADC range.

6.1.1.4 INL effect on general signals

As we have just seen, when the input signal, v , is not a dc constant (e.g., a ramp), the errors related to the INL of the ADC tend to introduce low frequency components which degrade the performance of the system. In fact, this is seen to happen in our device for voltage variations in the order of few milli-volts. Moreover, if the input signal changes rate, i.e., $\dot{v} \neq 0$, the frequency components introduced by the INL errors spread across the frequency band.

In order to deal with non-constant signals and to estimate INL induced noise, a simplification is expedient. First, let us assume the input signal in straight line for a certain time interval, i.e.,

$$v(t) = \begin{cases} a + bt & \text{if } 0 \leq t \leq t_{\max} \\ 0 & \text{if } t \leq 0 \text{ or } t > t_{\max} \end{cases} \quad (6.20)$$

where a is the initial value of the signal $v(t)$, and b is the slope of the input signal [Vs^{-1}]. If we note $\tilde{q}_k(\omega)$ the usual time-frequency Fourier transform of the non-ideal quantisation noise, it immediately follows from Eq. (6.20) that

$$\tilde{q}_k(\omega) = \frac{e^{i\omega a/b}}{|b|} \mathcal{Q}_k \left(\frac{\omega}{|b|} \right). \quad (6.21)$$

In this case, Eq. (6.18) becomes

$$|\tilde{q}_k(\omega)| = \frac{\Delta}{|b|} \sum_{n=-\infty}^{\infty} \frac{\sin \frac{n\pi\epsilon_k}{2^{k+1}\Delta}}{n} \frac{\sin \frac{n\pi}{2}}{\sin \frac{n\pi}{2^{k+1}}} \delta \left(\omega - \frac{\pi n |b|}{2^k \Delta} \right) \quad (6.22)$$

and the main frequency component for an ADC with an error in the k -th bit is located at:

$$\omega_{1_k} = \frac{\pi |b|}{2^k \Delta} \quad (6.23)$$

Before we proceed further, a technical comment is in order. In several equations above, Dirac δ -functions appear. They are the result of infinite length integration intervals in Fourier transform calculations, which are of course idealisations. In any practical situation, such intervals are limited to the experimentally available data ranges, so that the δ -functions are actually sinc-functions: they have identical centre points but spread around those centres depending on the integration interval lengths. In order to make sense of e.g. Eq. (6.22) we must ask which is the minimum required integration time to obtain a meaningful spectrum or, in other words, which is the minimum duration, t_{\max} , of the ramp signal in Eq. (6.20). This is easily inferred from the frequency of the lowest spectral line ω_{1_k} in Eq. (6.23): for a conventional ten cycle integration time we get

$$t_{\max} > 10 \frac{2\pi}{\omega_{1_k}} = 10 \frac{2^{k+1} \Delta}{|b|} \quad (6.24)$$

These considerations apply to the analysis of the ADC response to signals which drift slowly with time, where *slow drift* means such signals can be conveniently approximated by a series of concatenated ramps with suitable slopes, and lengths complying with Eq. (6.24). In these circumstances, we can generalise Eq. (6.23) as follows:

$$\omega_{1_k} = \frac{\pi 2^N}{2^k V_{\text{FS}}} |\dot{v}(t)|, \quad \dot{\omega}_{1_k} = \frac{\pi 2^N}{2^k V_{\text{FS}}} |\ddot{v}(t)| \quad (6.25)$$

From Eqs. (6.23) and (6.25) some conclusions can be drawn:

- High-slope signals at the ADC input translate into high-frequency components at the output of the ADC.
- Errors in the higher bits show up as noise at low frequency.
- Consequently, high-slope input signals combined with errors in high bits may show as noise peaks in the measurement bandwidth.
- The fundamental frequency associated to a faulty bit varies with the variations of $\dot{v}(t)$, hence the error in a faulty bit spreads across the frequency band when $\ddot{v} \neq 0$.

The above can be validated by looking at real data from the TMS. We took a long time series of temperature data, about $4 \cdot 10^5$ sec, and subdivided it into shorter stretches of 16 000 sec. With this, we calculated the short-time Fourier transform (STFT) [100], also known as *spectrogram*, and plotted the results as shown in Figure 6.7 — see caption for details. The data are amenable to the analysis described above, and the results indicate the presence of the foreseen frequency peaks associated to faulty bits. They are clearly visible in Figure 6.7, bottom graph as the darker areas, which show how the fundamental frequency of the INL errors for different faulty bits is varying with time. A straightforward fit to the first Eq. (6.25) permits the identification of the corresponding faulty bit, thus confirming that the extra noise in the temperature measurements is indeed due to the INL errors of the ADC.

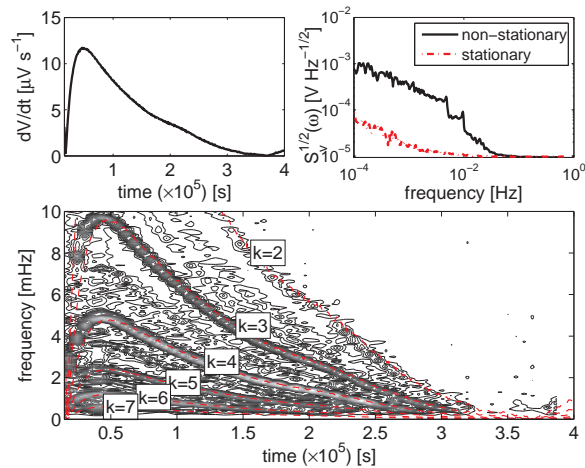


Figure 6.7: Top left: Absolute value of the input signal slope, $|\dot{v}(t)|$, of the measurement. It varies between 0 and $12.5 \mu\text{V s}^{-1}$. The sensitivity at the input of the ADC is $\simeq 1.35 \text{ V K}^{-1}$, hence the values of the voltage slope almost directly provide the actual temperature drifts in $[\text{K s}^{-1}]$. Top right: power spectral density for: (i) the signal shown in the top left plot, i.e., a non-*dc* signal (solid black trace) and, (ii) a *dc* signal (dashed red trace), i.e., with $|\dot{v}(t)| \lesssim 0.5 \mu\text{V s}^{-1}$. The excess noise when measuring non-constant signals is very noticeable, and degrades the performance of the measurement by about one order of magnitude. Bottom: STFT (or spectrogram) of the measurement. The energy of the signal is concentrated in specific frequencies which change with time precisely following $|\dot{v}(t)|$, as predicted by Eq.(6.25). The latter is represented by dashed superimposed traces, and are labelled by the order of the corresponding faulty bit (from $k=2$ to $k=7$). Experimental results and theoretical estimates are in excellent agreement.

Once the problem has been identified, we focus on possible solutions to solve it. The following section describes two different methods tested successfully to avoid the consequences of INL errors in real ADCs.

6.1.2 Mitigation of ADC errors

Two different techniques have been used to deal with the non-linearities of the ADCs. The first one is based on the injection of Gaussian noise out of the MBW, taking advantage of the oversampling involved in the measurement. The second option is based on the addition of a triangular wave of *high* frequency to the signal of interest before quantisation. The following sections describe both techniques as well as their practical implementation.

6.1.2.1 Gaussian noise dither injection

In §6.1.1.2 we saw that Gaussian noise can be used as a dither signal in order to mitigate the non-idealities of the ADC transfer curve. We have also seen that the amount of noise generated by the measurement system itself ($\sigma \simeq \Delta$) is not enough to suppress the periodic components of erroneous bits for $k \gtrsim 2$ —see Figure 6.7. Thus, a natural solution is to add more Gaussian noise to the ADC input. Obviously, this noise should be added out of the MBW in order not to disturb the frequency range of interest. The ADC sampling frequency is 38.4 kHz (in the prototype), thus leaving a large frequency slot to accommodate the required additional noise. Care must however be taken to also place it away from the fundamental frequency of the modulating square wave (and its harmonics) so as to avoid bringing the Gaussian noise back into the MBW in the demodulation process. The required amount of noise to be injected, characterised by σ , basically, depends on the input signal slope, $\dot{v}(t)$, and on the frequencies of interest, and is limited by the digital processing performed after quantisation —see below. Figure 6.8 shows the relationship between the input signal slope and the main frequency component for each of the faulty bits. It is useful to identify the faulty bits potentially affecting the measurement as a function of the input signal slope.

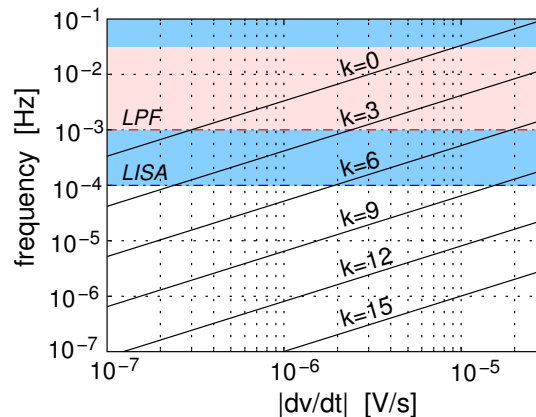


Figure 6.8: Relationship between the input signal slope, the faulty bit and the fundamental frequency affected by the error in the k -th bit. When high input signal slopes are present, more faulty bits will affect the measurement quality in the MBW. Clearly, LSBs show up at higher frequencies than MSBs. The shaded areas span the MBWs of LISA and LPF, as indicated. Note that LPF's MBW is a subset of LISA's.

Once the problematic bits are identified, the needed amount of Gaussian dither must be calculated. For this, we define the σ needed to filter out the noise components associated to the k -th faulty bit. If we (conventionally) adopt a damping factor of 10 for the first harmonic then σ is easily derived from the condition —see Eq. (6.19),

$$e^{-\xi^2 \sigma^2 / 2} \leq \frac{1}{10} \quad \text{for} \quad \xi = \frac{2\pi}{2^{k+1} \Delta} \quad (6.26)$$

whence

$$\sigma \geq \frac{\sqrt{2 \ln 10}}{2\pi} 2^{k+1} \Delta \quad (6.27)$$

Practical implementation In this section we briefly describe the hardware implementation of the Gaussian dithering scheme. The circuit scheme is given in Figure 6.9 (left panel). The first stage amplifies the noise of an operational amplifier (OP-07 of Analog Devices); the second stage is a high-pass filter of 4-th order (two Sallen-Key filters in cascade) with a cut-off frequency of 100 Hz; the third stage is an adder that sums the signal of interest (the amplified output of the Wheatstone bridge) to the dither signal. In the fourth stage, the sum of signal and dither are low-pass filtered with a 4-th order low-pass filter (again, two Sallen-Key filters in cascade) with cut-off frequency 3 kHz. The output of this chain is fed to a 16-bit SAR ADC. The noise shape of the dither signal is given in Figure 6.9 (right panel) where the characteristic frequencies of the high- and low-pass filters are clearly visible.

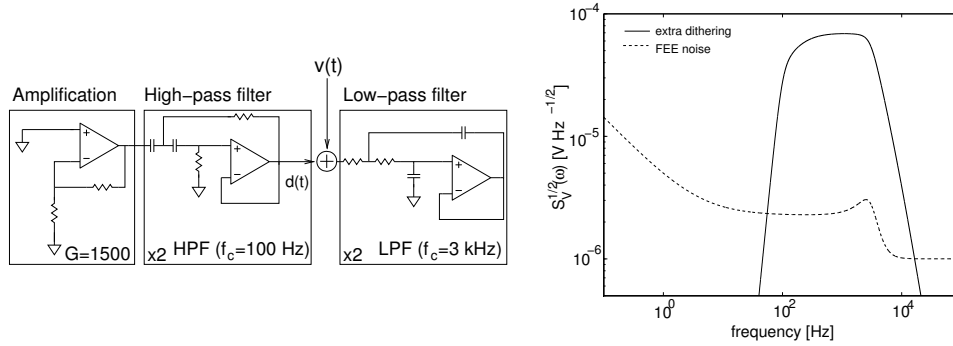


Figure 6.9: Gaussian noise dither signal generator. $d(t)$ is the Gaussian noise dither and $v(t)$ is the amplified output of the Wheatstone bridge. Right: PSD of the Gaussian noise (solid trace). The dashed trace shows the floor noise of the measurement system.

As mentioned before, the amount of Gaussian dither must be kept under control to avoid excessive noise folding back into the MBW during the digital demodulation stage. The limit of usable Gaussian noise amplitude, σ , can be easily estimated assuming a flat spectrum, $S_{V,\text{dither}}$, from $\omega_m/2\pi$ (the corner frequency of the high-pass filter) to $\omega_M/2\pi$ (the corner frequency of the low-pass filter). The demodulation by a square wave of frequency ω_c entails a certain gain at dc of the odd harmonics of ω_c of the dither noise which, under the just mentioned assumption, results in the following —see §2.3 and §3.2:

$$S_{V,\text{extra}}(\omega \rightarrow 0) \simeq S_{V,\text{dither}} \cdot \frac{4}{\pi^2} \sum_{n=\lfloor \omega_m/2\omega_c \rfloor}^{\lfloor \frac{\omega_M}{2\omega_c} \rfloor} \frac{1}{(2n+1)^2} \quad (6.28)$$

where $\lfloor \cdot \rfloor$ is the floor function.

In order to cut down the noise leaking into the MBW, we impose a requirement that it be less than 10% the floor noise, in the absence of ADC errors, $S_{V,\text{FEE}}$, i.e.,

$$S_{V,\text{extra}}(\omega \rightarrow 0) \leq \frac{S_{V,\text{FEE}}(\omega)}{10} \quad (6.29)$$

In our case, $\omega_m/2\pi \simeq 100$ Hz, $\omega_M/2\pi \simeq 3$ kHz, and $\omega_c/2\pi \simeq 5.55$ Hz, so that the term multiplying $S_{V,\text{dither}}$ is approximately 0.015, hence $S_V(\omega \rightarrow 0) \simeq 0.015 S_{V,\text{dither}}$. The value of $S_{V,\text{FEE}}$ is 1.5 ·

$10^{-11} \text{ V}^2 \text{ Hz}^{-1}$ in the MBW. The maximum value for $S_{V,\text{dither}}$ compliant with the criterion in Eq. (6.29) is therefore $3 \cdot 10^{-11} \text{ V}^2 \text{ Hz}^{-1}$ which corresponds to $\sigma \simeq 0.3 \text{ mV}$.

In §6.1.3, we present the tests and results obtained with this technique.

6.1.2.2 Triangular wave dither injection

Another implemented and tested technique consists in using a deterministic signal instead of random Gaussian noise as the dither signal. Different signals can be used for this purpose, but we have used a triangular wave form for simplicity in the generation of the signal —see below. In this section we describe the theoretical basis and the hardware implementation details.

The dither signal is now a triangular wave, which can be represented by the Fourier series

$$d(t) = \frac{D_o}{2} - \frac{4D_o}{\pi^2} \sum_{n=0}^{\infty} \frac{1}{(2n+1)^2} \cos(2n+1)\omega_{\text{tr}}t \quad (6.30)$$

where D_o and ω_{tr} are the amplitude and the angular frequency, respectively —see Figure 6.11. Its pdf is [103]

$$p(d) = \begin{cases} \frac{1}{D_o} & 0 \leq d \leq D_o, \\ 0 & d < 0 \text{ and } d > D_o \end{cases} \quad (6.31)$$

whose Fourier transform is

$$\mathcal{P}(\xi) = \frac{\sin(D_o/2)\xi}{(D_o/2)\xi}. \quad (6.32)$$

As shown in §6.1.1, the averaged quantisation error is

$$\langle \mathcal{Q}(\xi) \rangle = \mathcal{Q}(\xi)\mathcal{P}^*(\xi) \quad (6.33)$$

whence we realise that the triangular wave is equivalent to a low-pass filter of the form $\frac{\sin x}{x}$. Evaluation of Eq. (6.33) is graphically evaluated in Figure 6.10 for different faulty bits and triangular wave amplitudes. For comparison, we also have plot the equivalent filter of a sine wave. The pdf of a sine wave of amplitude A is

$$p(d) = \frac{1}{\pi\sqrt{A^2 - d^2}}, \quad -A < d < A \quad (6.34)$$

and its characteristic function is

$$\tilde{p}(\xi) = \frac{2}{\pi} K_0(A\xi) \quad (6.35)$$

where K_0 is the modified Bessel function of the second kind. The attenuations obtained using a sine wave or a triangular wave are very similar, as one would expect.

Like we did with the Gaussian noise, we can give an expression to determine the required triangular wave amplitude, D_o , to attenuate by 10 the effect of the k -th bit, or

$$|\text{sinc}(D_o/2)\xi| \leq \frac{1}{10} \quad (6.36)$$

where $\xi = \frac{2\pi}{2^{k+1}\Delta}$ stands for the fundamental component. In this case it is not possible to give a closed form for the amplitude of the triangular wave, which requires a numerical solution to Eq. (6.36) in each specific case. The amplitude D_o needed to attenuate the errors coming from the $k=6$ bit is $\sim 20 \text{ mV}$.

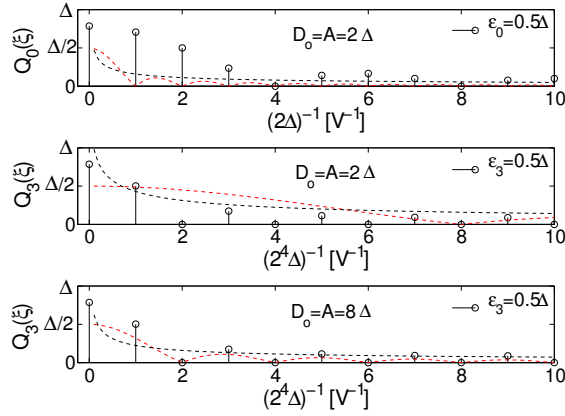


Figure 6.10: Top: quantisation error for a real ADC with a faulty bit in $k=0$ ($\epsilon_0 = 0.5\Delta$) and the low-pass filter when using a triangular wave (red dashed trace) or a sine wave (black dot-dashed trace) as dither signals, with $D_o = A = 2\Delta$ in both cases. Middle: same as the plot in the top for an error in the bit $k=3$ ($\epsilon_3 = 0.5\Delta$). Bottom: same as the plot in the middle but with $D_o = A = 8\Delta$ instead of 2Δ . Note that x -axis scales are different for q_0 and q_3 —see Figure 6.6. The differences between using a triangular wave and a sine wave are small.

Practical implementation Figure 6.11 shows the triangular wave added to the system. It is important to note that the addition of the triangular signal will not perturb the temperature measurement within the MBW. The digital demodulation involved in the measurement —see §2.3 and §3.2— is done by averaging 6144 samples: 3072 samples during one polarity and 3072 samples during the opposite polarity. Afterwards, they are subtracted and divided by 2. Thus, if we inject exactly the same signal in both polarities the contribution of the added dither signal to the output is zero —see Eq. (6.37).

The output signal after the digital processing is

$$v_o = \frac{[\bar{v}_{\text{pos}}(t) + \bar{d}(t)] - [\bar{v}_{\text{neg}}(t) + \bar{d}(t)]}{2} = \frac{\bar{v}_{\text{pos}} - \bar{v}_{\text{neg}}}{2} \quad (6.37)$$

where here $d(t)$ stands for the triangular wave —see Figure 6.11— and $\bar{}$ means average over 3072 samples.

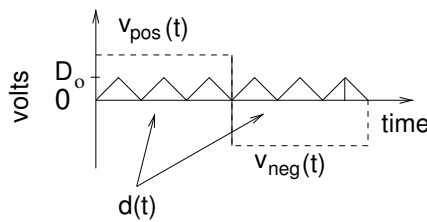


Figure 6.11: Signals at the input of the ADC: triangular wave dither signal (solid trace) and signal coming from the measurement chain (dashed trace).

Equation 6.37 indicates that there is no limit on the amplitude of the triangular dither, provided triangular waves in both polarities are identical. Therefore that non-linearities of MSBs can be reduced without degrading the measurement. This happens for an analog dither signal, but ours is

actually generated with a DAC, which imposes some limits on the validity of the previous statement—see below.

The circuit which implements the triangular signal is shown in Figure 6.12, and consists in an 8-bit up-and-down counter followed by a 12-bit DAC where only the 8 LSBs are used. The circuit is configured such that the quantisation step of the DAC closely matches that of the 16-bit ADC. Mismatches here result in actual performance diverging from the predictions of the theoretical analysis described above.

The output signal from the DAC is added to the signal of interest and both are low-pass filtered (a 4-th order Sallen-Key filter with a cut-off frequency of 3 kHz), then quantized by the 16-bit SAR ADC. The triangular wave is low-pass filtered to eliminate high-frequency components related to the digital quantization of the DAC. Nevertheless, the previous analysis is still valid since the fundamental frequency of the triangular wave is 50 Hz and the low-pass filter cut-off frequency is 3 kHz. Thus, the dither signal will go almost unaltered through the filter (except for some distortion in its high-frequency components).

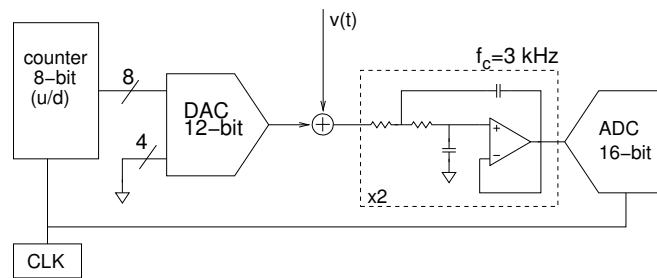


Figure 6.12: Triangular wave dither signal, $d(t)$, generator. $v(t)$ is the output of the Wheatstone bridge after being amplified. Both signals [$d(t)$ and $v(t)$] are added, low-pass filtered and quantised.

6.1.3 Test set up and results

Both methods described in §6.1.2 have been put to test using a 16-bit SAR ADC (AD977 of Analog Devices⁶). For comparison, a 24-bit Delta-Sigma ADC (LTC2440 of Linear Technology) which, in principle, should exhibit lower problems of non-linearity has also been tested although it is not qualified for space applications. The test has been also done for the 16-bit SAR ADC without dither signals. In this section we first give a brief description of the test set up and then the obtained results are discussed.

6.1.3.1 Test set up

The test set up is composed by different parts. Temperature sensors are placed inside a thermal insulator able to screen ambient temperature fluctuations to the required level in the MBW, i.e., $S_T^{1/2}(\omega) \lesssim 10^{-5} \text{ KHz}^{-1/2}$ for $\omega/2\pi \gtrsim 1 \text{ mHz}$ [84]—see chapter §4. A temperature control is included to implement different temperature profiles inside the insulator; basically, a set of temperature ramps with different slopes is generated in order to assess whether or not the methods to overcome the INL errors of the ADC work—see Figure 6.13 (right). The temperature control consists in a heater commanded by a programmable power which is in turn controlled by the computer calculated value of the difference between the desired temperature and the actual measurement—see Figure 6.13.

⁶Actually, the ADC used in the flight model is the Texas Instruments ADS7809 which is based on the same structure.

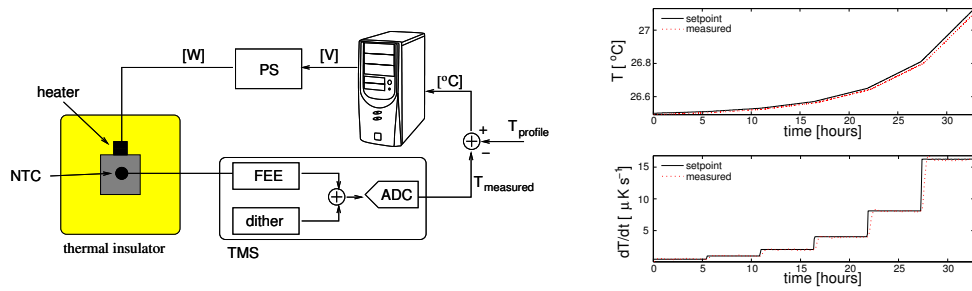


Figure 6.13: Left: set up scheme. The temperature of aluminium block is controlled using a feedback control loop. The temperature profile consists in temperature ramps of different slope. The temperature of the thermistor is measured with the TMS. The injection of the dither signals is done before the discretisation. Right top: desired and experimental temperature profiles. Right bottom: time derivative of the signals shown in the top plot. Slopes are: $0.5, 1, 2, 4, 8$ and $16 \mu\text{K s}^{-1}$.

The nominal and actual profiles are shown in Figure 6.13. The experiment has been repeated for the two dithering techniques, and for the 24-bit Delta-Sigma ADC as well. Prior to that, the 16-bit SAR ADC with no dither signal has been tested in order to provide a reference measurement with the INL effects in it.

6.1.3.2 Test results

The power spectral density in the different tested configurations (no dither, Gaussian noise, triangular wave and 24-bit Delta-Sigma ADC) are given in Fig. 6.15 for three different slopes, more specifically, for $1, 4$ and $8 \mu\text{K s}^{-1}$ (or $\mu\text{V s}^{-1}$). The measurements performed with the 16-bit SAR ADC are clearly affected by the INL errors when no dither signal is used. The noise in the MBW increases by more than one order of magnitude when slopes are around $1 \mu\text{K s}^{-1}$ and above. Figure 6.15 shows how the INL errors appear in the MBW, spanning wider frequency regions as slopes increase, thus confirming the predicted behaviour. For instance, when the slope is $4 \mu\text{K s}^{-1}$ the INL effect is only noticeable at frequencies below 6 mHz , while for a slope of $8 \mu\text{K s}^{-1}$ the noise appears at frequencies as high as 10 mHz .

When the dither signal is Gaussian noise, the INL effects can be satisfactorily reduced down to 1 mHz for drifts under $8 \mu\text{K s}^{-1}$. Looking up Figure 6.8, we see that faulty bits up to $k=5$ will create additional noise in the band. Then, using Eq. (6.27), we find that the necessary dither requires $\sigma \simeq 22 \Delta$, or $\sigma \simeq 3 \text{ mV}$. This is however a factor of 6 larger than the maximum estimated after Eq. (6.29), which means some extra noise will be added to the system floor noise, if we insist on applying a $\sigma = 3 \text{ mV}$ dither, as discussed in Section 6.1.2.1. We did take this option, with the result that the floor noise becomes a factor ~ 1.5 larger than nominal [in good agreement with predictions calculated using Eq. (6.28)], with the advantage that good damping of the ADC's INL errors obtains —see Figure 6.15.

The use of a triangular wave as the dither signal appears as the most robust option to deal with the non-idealities of the ADC: on the one hand, the floor noise is left untouched and, on the other hand, immunity to faulty bits and high signal slopes can be tuned essentially at will. The 24-bit Delta-Sigma ADC exhibits a behavior similar to that observed in the measurements performed by the 16-bit ADC with added dither signals. Non-linearity errors in this ADC are not noticeable when measuring signals drifting up to $8 \mu\text{K s}^{-1}$. The generated triangular wave had the following properties: $D_o=155 \text{ mV}$ and a period of 20 ms , which is an integer sub-multiple of the duration of each polarity (80 ms) —see Figure 6.11. This amplitude is almost 8 times higher than the one estimated towards the end of Section 6.1.2.2 (20 mV) to attenuate errors up the $k=6$ bit. This

means that immunity to faulty bits under higher temperature drifts is accomplished. Figure 6.14 provides a clear display of the superiority of triangular wave over Gaussian noise dither.

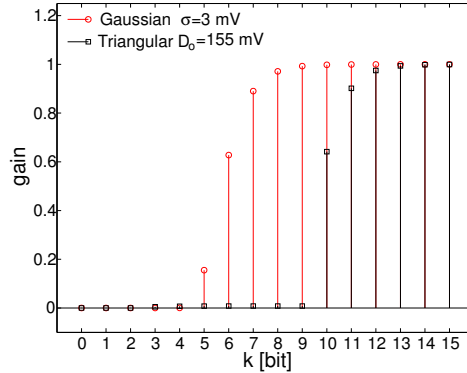


Figure 6.14: Gain of the equivalent filters of the Gaussian noise dither and the triangle wave dither. The gain for each bit corresponds to the fundamental frequency. Gaussian noise dither mitigates the error of the bits $k \leq 5$ whereas the triangular wave reduces the error of the bits $k \leq 9$.

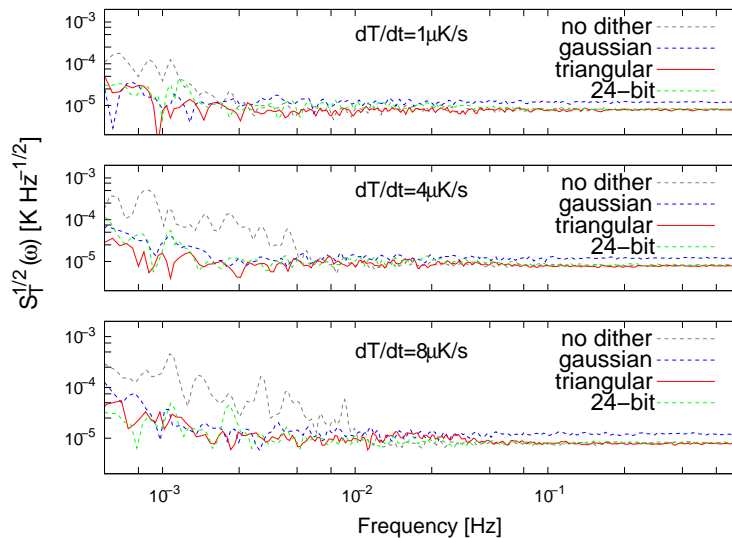


Figure 6.15: Power spectral density (in amplitude units) for the different configurations (16-bit ADC without dither, 16-bit ADC with Gaussian dither, 16-bit ADC with triangular wave dither and 24-bit Sigma-Delta ADC) involved in the test under different input signals (slopes from 1 to $8 \mu\text{K s}^{-1}$). In the absence of dither, the noise increases (in amplitude and bandwidth) with the slope of the input signal. The solutions tested work properly for slopes up to $\sim 10 \mu\text{K s}^{-1}$ level. The 24-bit Sigma-Delta does not exhibit non-linearity problems.

Figure 6.15 confirms the analysis in this paper, and shows that when slopes of $\sim 10 \mu\text{K s}^{-1}$ are present, the effects of the non-idealities can be made negligible by use of proper dither. For higher slopes, e.g., $16 \mu\text{K s}^{-1}$, some increase in the power spectrum near one milli-Hertz is detected. We

believe this is probably due to the relative simplicity of the model used. Further research is ongoing to clarify these matters. Nevertheless, such drifts look unlikely both in LISA and LPF.

In conclusion, extra noise has been detected when measuring drifting temperatures. This fact totally hinders compliance with the demanding required performance for LISA, i.e., noise levels in terms of temperature about the $\mu\text{K Hz}^{-1/2}$ in the submilli-Hertz range. The source of the noise has been identified and ascribed to the non-idealities of the ADC which, due to space qualification constraints can be a 16-bit SAR ADC at best. We have laid down the theoretical basis of the problem, which has been validated with experimental measurements⁷. Two different options to mitigate this effect have been proposed, analysed and tested. Both are based on the addition of a dither signal to the signal of interest prior to the ADC quantisation. On the one hand, we have used Gaussian noise, which certainly reduces the INL errors of the ADC, although in our case its performance is limited by the demodulation process, which sets an upper limit on the noise amplitude, σ , which can be injected in the system. On the other hand, the use of a triangular wave as the dither signal circumvents this problem. In this case the amplitude can be as large as desired and, thus, the errors of the MSBs of the ADC can also be attenuated up to a point. Furthermore, a 24-bit Delta-Sigma ADC has been compared to the 16-bit ADCs plus dither. A 16-bit ADC plus averaging (to increase the resolution) and proper dither reaches the same performance as a 24-bit Delta-Sigma ADC.

In summary, a method capable to suppress the INL errors of the ADC in the TMS of the LPF mission has been described. The results obtained are important in view of LISA, which will work at lower frequencies and will need a lower noise in the measurement. The method described here might be useful for other subsystems of the mission where ADC non-linearities appear as a limitation in the performance of the measurement.

6.2 Floor noise reduction

LISA is one order of magnitude more demanding than LPF. This implies that very roughly we can set the temperature stability required around $10^{-5} \text{K Hz}^{-1/2}$ from 0.1 mHz to 0.1 Hz instead of the $10^{-4} \text{K Hz}^{-1/2}$ from 1 mHz to 30 mHz of the LTP. Consequently, the noise of the TMS should be reduced by one order of magnitude. In this section we explore the options to do this and discuss the limits of measuring temperature fluctuations with thermistors.

The floor noise of the prototype system is $\simeq 8 \mu\text{K Hz}^{-1/2}$ when the sampling frequency is 1.3875 Hz, i.e., when measuring four channels ($5.5/4=1.3875$ Hz). This has been theoretically and experimentally stated in §2 and §5. In this section we discuss the possibility of reducing the floor noise by minor modifications in the system. There are essentially three options to accomplish this purpose. They are:

- to reduce or increase the equivalent resistance of the Wheatstone bridge,
- to increase the power dissipated in the sensor and,
- to avoid channel multiplexing.

From the options above only the increase of power in the sensor and the use of a non-multiplexed system actually reduces the floor noise as will be shown later. Finally, we analyse the theoretical limits of noise equivalent temperature when measuring with thermistors in a resistive Wheatstone bridge.

The noise of electronic nature of the TMS is modelled as —see §2.3.2,

$$S_T(\omega) = S_{T,b}(\omega) + S_{T,b+IA_i}(\omega) + S_{T,IA_v}(\omega) + S_{T,ADC}(\omega) \quad (6.38)$$

⁷The solution and results have been obtained for the LTP measurement bandwidth. However, the solution is also valid for the LISA band.

where

- $S_{T,b}$ is the Johnson noise of the Wheatstone bridge,
- $S_{T,b+IA_i}$ is the noise caused by the current noise of the instrumentation amplifier (IA) together with the equivalent resistance of the Wheatstone bridge,
- S_{T,IA_v} is the inherent voltage noise of the IA,
- $S_{T,ADC}$ is the noise introduced by the analog-to-digital converter (transition noise).

Equation (6.38) can be expressed as⁸

$$S_T^{1/2}(\omega) = \frac{2T^2}{(RP)^{1/2}\beta} \left[4k_B T R + i_n^2(\omega) \frac{R^2}{2} + e_n^2(\omega) + e_{ADC}^2(\omega) \right]^{1/2} \quad (6.39)$$

where R and β are the nominal resistance and the temperature characteristic of the thermistor, respectively, T is the temperature in Kelvin, P is the power dissipated in the sensor, i_n^2 and e_n^2 are the noise figures of the IA —cf. §2.3.2.4, e_{ADC}^2 is the noise of the ADC —cf. §2.3.2.4— and k_B is Boltzmann's constant. For a given IA and ADC, the noise is inversely proportional to the square root of the power, and also depends on the nominal resistance of the thermistor. The effect of these two variables, P and R is analysed in the following sections.

6.2.1 Thermistor nominal resistance

The optimum value of R that minimises Eq. (6.39) is found by

$$\frac{\partial S_T}{\partial R} = 0 \quad (6.40)$$

which yields

$$R_{opt} = \left(\frac{2}{i_n^2(\omega)} [e_n^2(\omega) + e_{ADC}^2(\omega)] \right)^{1/2}. \quad (6.41)$$

The optimum value of the thermistor nominal resistance, R_{opt} , depends only on the IA noise properties and on the noise introduced by the ADC. The expressions of e_n^2 , i_n^2 and e_{ADC}^2 are [102] —see §2.3.2.4 and §2.3.2.5,

$$e_n^2(\omega) = K_v^2 \left(1 + \frac{\omega_{cv}}{\omega} \right) \quad (6.42a)$$

$$i_n^2(\omega) = K_i^2 \left(1 + \frac{\omega_{ci}}{\omega} \right) \quad (6.42b)$$

$$e_{ADC}^2(\omega) = \left[\frac{\sigma}{2^{16}} V_{FS} \frac{1}{\sqrt{6} f_s} \frac{1}{G_{IA}} \right]^2 \quad (6.42c)$$

For the case of the IA AD624 the values of e_n^2 and i_n^2 at $f_c=5.55$ Hz are $2.47 \cdot 10^{-17} \text{ V}^2 \text{ Hz}^{-1}$ and $1.71 \cdot 10^{-24} \text{ A}^2 \text{ Hz}^{-1}$, respectively. The noise introduced by the ADC⁹ is $e_{ADC}^2 = 3 \cdot 10^{-17} \text{ V}^2 \text{ Hz}^{-1}$. Substituting these values into Eq. (6.41) yields $R_{opt} \simeq 8 \text{ k}\Omega$ which is very close to the value used in the TMS, $10 \text{ k}\Omega$. However, the IA in the FM system is the AD620 which is slightly different from the AD624. The AD620 noise figures are: $e_n^2 = 2.26 \cdot 10^{-16} \text{ V}^2 \text{ Hz}^{-1}$ and $i_n^2 = 2.1 \cdot 10^{-25} \text{ A}^2 \text{ Hz}^{-1}$ and the optimum nominal resistance is $\simeq 50 \text{ k}\Omega$. However, differences in the noise figure when using a $50 \text{ k}\Omega$ thermistor or a $10 \text{ k}\Omega$ one are tiny. Figure 6.16 shows the floor noise when using the AD624 and the AD620 IAs for different nominal resistance thermistors.

⁸For simplicity, we assume $R_1 = R_2 = R_{ref} = R(T)$.

⁹Considering a gain in the amplification stage of 200 and the sampling frequency 38.4 kHz .

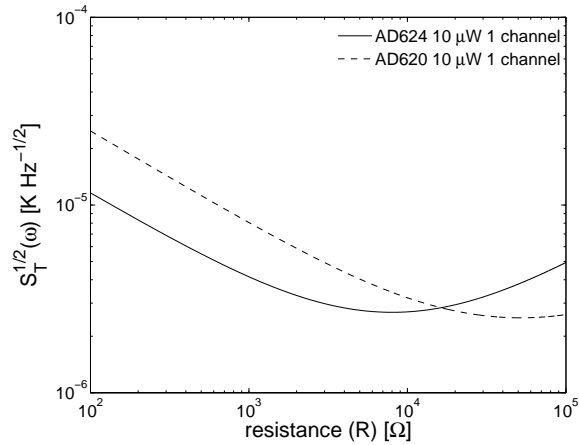


Figure 6.16: Noise levels as a function of the nominal resistance of the thermistor. Two instrumentation amplifiers are considered: AD624 (the one used in the prototype design) and AD620 (the one used in the flight model system).

The analysis shown in this section indicates that the noise of the system is already at its minimum for a given power and that the only chance to reduce it is by dissipating more power to increase the sensitivity of the Wheatstone bridge. This possibility is discussed in the next section.

6.2.2 Power increase in thermistors

Equation (6.39) indicates that the floor noise of the temperature measurement is inversely proportional to \sqrt{P} . In order to assess this, the electronics was modified to dissipate $100 \mu\text{W}$ in the thermistor, instead of $10 \mu\text{W}$. Moreover, only one channel was acquired, i.e., no multiplexing was present. Differential measurements were taken since they (i) reduce the stabilisation time in the measurement, (ii) reduce the effect of the ambient temperature fluctuations and (iii) increase the immunity to the problems of non-linearity in the ADC since the slopes of the measurement are very small. The results for a $10 \mu\text{W}$ -1 channel measurement and for a $100 \mu\text{W}$ -1 channel measurement are shown in Figure 6.17. The floor noise is reduced by a factor of $\sqrt{100/10} = 3.3$, thus, Eq. (6.39) is validated. The noise is flat for frequencies down to $\approx 1 \text{ mHz}$ in both measurements. At lower frequencies the effect of the temperature coefficient (TC) of the electronics degrades the measurement in both configurations. The dashed grey traces represent the projection of the laboratory temperature fluctuations in the aluminium block when measuring differential temperature¹⁰. The magenta dashed trace is the effect of the TC of the electronics and it is the one limiting the measurement for $f < 1 \text{ mHz}$. At frequencies close to $f_s/2$ the noise increases slightly due to the differentiation process involved in the measurement —see §2.3.4.

¹⁰ $S_{T,\text{ins}}(\omega) = k_{\text{NTC}}^2 \omega^2 |H_{\text{ins}}(\omega)|^2 S_{T,\text{lab}}(\omega)$ —see §4.1.2 and §4.2.2.

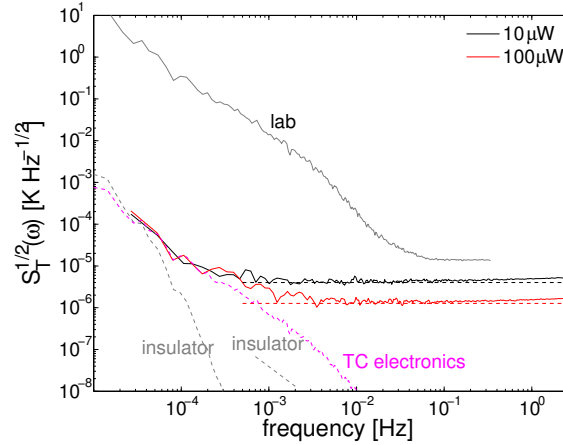


Figure 6.17: Noise levels when sampling only one channel, i.e., with no multiplexing, and for $P = 10 \mu\text{W}$ and $P = 100 \mu\text{W}$. The measurement sensitivity is limited at low frequency ($f < 1 \text{ mHz}$) by the TC of the electronics (magenta trace).

The results in Figure 6.17 lead to the following conclusions:

- the noise in the measurement is reduced by dissipating more power in the thermistor,
- measurement with no multiplexing avoids aliasing —see §2.3.4,
- no excess noise has been detected in the thermistors or electronics at $1 \mu\text{K Hz}^{-1/2}$ and at $\sim 1 \text{ mHz}$.

The noise in the measurement in terms of power and number of multiplexed channels can be expressed as

$$S_T^{1/2}(\omega) \simeq 4 \mu\text{K Hz}^{-1/2} \left(\frac{10 \mu\text{W}}{P} \right)^{1/2} N_{\text{ch}}^{1/2} \quad (6.43)$$

where P is the power dissipated in the thermistor and N_{ch} is the number of channels multiplexed.

However, noise cannot be reduced as much as desired by increasing the power. The self-heating effect (SHE) restricts the amount of power dissipated in the thermistor; if this limit is exceeded the noise introduced by the SHE is higher than the noise modelled by Eq. (6.43). The SHE has been described in §2.3.2.3. Here we use the same analysis to estimate the maximum power permitted in the thermistor. The temperature fluctuations caused by the SHE are

$$S_T(\omega) = \theta^2 S_P(\omega) \simeq \left[\theta \frac{2V}{R(T)} \right]^2 S_V(\omega) \quad (6.44)$$

where $R(T)$ is the resistance of the thermistor, θ is the thermal resistance between the sensor and the body, S_V are the voltage fluctuations in the thermistor and V is the voltage in the NTC, $V = \sqrt{PR}$. Substituting $V = \sqrt{PR}$ into Eq. (6.44) yields

$$S_T^{1/2}(\omega) = 2\theta \left(\frac{P}{R} \right)^{1/2} S_V^{1/2}(\omega). \quad (6.45)$$

Combining Eq. (6.43) and (6.45) we obtain an expression for the maximum power, i.e.,

$$P \leq 4 \mu\text{K Hz}^{-1/2} \cdot (10 \mu\text{W})^{1/2} \frac{R^{1/2}}{2\theta S_V^{1/2}(\omega)} = 1.25 \cdot 10^{-8} \frac{R^{1/2}}{2\theta S_V^{1/2}(\omega)} \quad (6.46)$$

where we notice that the maximum power is (i) inversely proportional to the thermal resistance, θ , and to the voltage fluctuations in the thermistor, S_V , and, (ii) proportional to the square root of the nominal resistance of the thermistor, R . Consequently, the better the voltage reference the higher the power that can be dissipated in the thermistor and, therefore, the lower the noise in the measurement. The thermal resistance even assuming an ideal contact between the thermistor head and the body is $\sim 50 \text{ K W}^{-1}$ due to the inherent properties of the thermistor —see appendix §B. Large values of R permit higher values of P . However, the range of resistance values of space qualified NTC thermistors is from $2 \text{ k}\Omega$, to $20 \text{ k}\Omega$. In our system we are using $R=10 \text{ k}\Omega$. The total noise in the temperature measurements considering the electronics noise and the SHE can be expressed, in general, as:

$$S_T^{1/2}(\omega) = \frac{2}{R^{1/2}} \left\{ \frac{T^4}{P\beta^2} \left[4k_B T R + i_n^2(\omega) \frac{R^2}{2} + e_n^2(\omega) + e_{\text{ADC}}^2(\omega) \right] + \theta^2 P S_V(\omega) \right\}^{1/2} \quad (6.47)$$

Equation (6.47) is plotted in Figure 6.18 for different values of R and P for a given IA (AD624), ADC (AD977), θ ($=100 \text{ K W}^{-1}$) and S_V ($=10^{-10} \text{ V}^2 \text{ Hz}^{-1}$). We notice that for a given R the power cannot be increased arbitrarily since then the SHE becomes important. However, large values of R permit higher values of P since in this case the SHE becomes less critical. If S_V and θ are large, the measurement is dominated by the SHE.

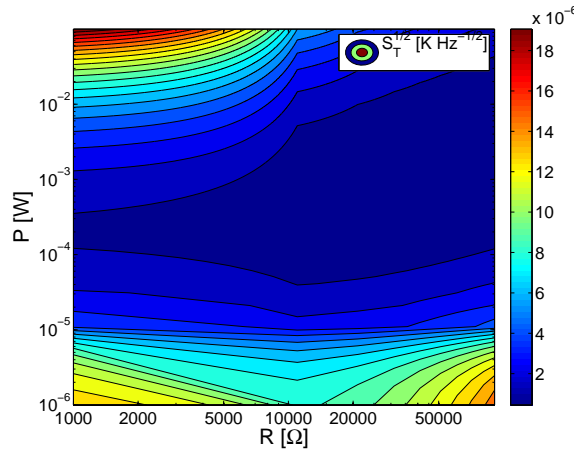


Figure 6.18: Noise in temperature measurements for different values of R and P . The dark blue region is the one exhibiting the lowest noise.

In order to assess this analysis, measurements with $P=1 \text{ mW}$ and $P=10 \text{ mW}$ (both with $R=10 \text{ k}\Omega$) were performed. The results are shown in Figure 6.19. In both measurements the SHE was detected. When $P=1 \text{ mW}$ (solid black trace) the noise differed from the expected one (dash-dotted black trace) at $\sim 20 \text{ mHz}$. The projection of the ambient temperature in the measurement (dashed grey traces) and the TC of the electronics (dashed magenta trace) could not explain such behaviour between 1 mHz and 20 mHz . For $P=10 \text{ mW}$ the noise due to the SHE starts to dominate at 200 mHz and at 30 mHz is already higher than the one for $P=1 \text{ mW}$, thus confirming the fact that the power cannot be increased arbitrarily: it becomes counterproductive due to the voltage fluctuations in the thermistors which in turn cause temperature fluctuations due to the SHE. This is specially noticeable at the milli-Hertz range.

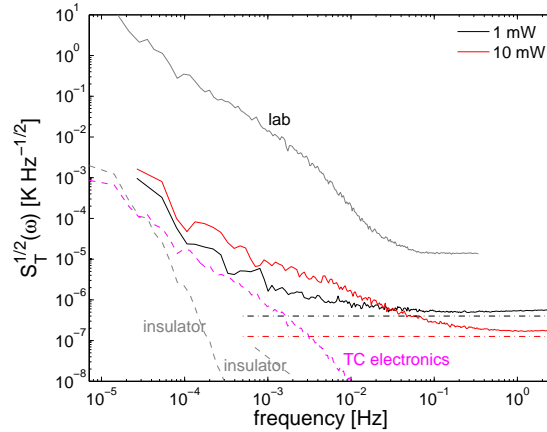


Figure 6.19: Noise levels of the TMS with $P = 1$ mW and $P=10$ mW (in both cases only one channel is sampled). The projection of the ambient temperature fluctuations through the insulator (grey dashed trace) and the TC of the electronics (magenta dashed trace) are also shown. None of them explain the extra noise from ~ 1 mHz to ~ 50 mHz. The extra noise comes from the SHE which dominates the measurement when *high* power is dissipated in the sensor.

Finally, there is a physical limitation independent of the method of measurement imposed by the fluctuation-dissipation theorem which states that for a thermodynamic system in equilibrium the fluctuations around the equilibrium point are random. Thus, they limit the temperature measurement to a certain level. The limit is given by [29, 35]

$$S_T(\omega) = 4\theta k_B T^2 \quad (6.48)$$

where θ is the thermal resistance, T is the absolute temperature and k_B is Boltzmann's constant. In the case of thermistors the minimum thermal resistance is $\sim 50 \text{ K W}^{-1}$ —see appendix §B— and the temperature we are interested in is $\sim 300 \text{ K}$. This leads to a limit of $16 \text{ nK Hz}^{-1/2}$. The TMS achieves noise levels of $\simeq 1 \text{ } \mu\text{K Hz}^{-1/2}$ in the milli-Hertz region when dissipating $100 \text{ } \mu\text{W}$ and of $\simeq 0.2 \text{ } \mu\text{K Hz}^{-1/2}$ at 1 Hz with $P=10 \text{ mW}$. We are still a factor of ~ 60 above the theoretical limits in the milli-Hertz band and a factor of 12 at $\sim 1 \text{ Hz}$. All in all, it seems difficult to achieve measurements with noise levels below $1 \text{ } \mu\text{K Hz}^{-1/2}$ in the milli-Hertz with the measurement method described in this thesis. The SHE spoils the measurement when increasing the power to improve the temperature sensitivity of the system.

In summary, we have shown that the noise of the TMS is compatible with the measurement of temperature fluctuations at the level of $\mu\text{K Hz}^{-1/2}$ in the milli-Hertz band if the power is increased by a factor of 10 with respect to the one in the LTP ($10 \text{ } \mu\text{W}$), and if no multiplexing is used. However, the power dissipated in the thermistor does not only concern the SHE. The power also must be small enough not to perturb other subsystems nearby. In the LTP it has been limited to $10 \text{ } \mu\text{W}$. Such fears mainly concern the GRS since the power dissipated in the thermistors can generate thermal fluctuations in the walls of the EH and thus, exert forces in the TMs. A simple approach to obtain an idea about the effect in the temperature stability of the GRS is presented herein. First we consider that the temperature evolution of one wall of the EH is described by (during the transient response)

$$P = C\dot{T} \quad (6.49)$$

where C is the thermal mass of the EH wall, T is the temperature of the EH wall and P is the power dissipated in the thermistor. We consider that the cut-off frequency of the transfer function

between power and temperature increase (of the EH walls) is, in principle, lower than the MBW¹¹. Therefore, we Fourier transform Eq. (6.49) to obtain the transfer function in the MBW. In power spectral density it is¹²:

$$S_P(\omega) = \omega^2 C^2 S_T(\omega) \quad (6.50)$$

Power fluctuations, S_P , can be approximated to:

$$S_P(\omega) = \left(\frac{2V}{R}\right)^2 S_V(\omega) \stackrel{V=\sqrt{PR}}{=} 4\frac{P}{R} S_V(\omega) \quad (6.51)$$

where P is the power dissipated in the thermistor, R is the resistance of the thermistor and S_V are the voltage fluctuations in the thermistor. Now we combine Eqs. (6.50) and (6.51) to obtain the relationship between voltage fluctuations and increase of temperature of the EH walls, i.e.,

$$S_T(\omega) = \frac{4P}{RC^2\omega^2} S_V(\omega) \quad (6.52)$$

The value of C has been estimated by simulations performed with the CGS thermal model. Details on the thermal model and the simulations can be found in [50, 51, 97]. The value is $C \sim 70 \text{ J K}^{-1}$, R is $10 \text{ k}\Omega$ and $S_V^{1/2}$ is $\sim 10^{-4} \text{ V Hz}^{-1/2}$ in the LTP MBW in the very worst-case. Evaluation of Eq. (6.52) yields temperature fluctuations of $\sim 10^{-8} \text{ K Hz}^{-1/2}$ and $\sim 5 \cdot 10^{-8} \text{ K Hz}^{-1/2}$ at 1 mHz for $P=10 \mu\text{W}$ and $P=100 \mu\text{W}$, respectively. The stability in the GRS must be kept lower than $10^{-4} \text{ K Hz}^{-1/2}$ —cf. §1.5. From this analysis it is clear that the effect of the power dissipated in the thermistors should not pose a problem to the required temperature stability in the GRS and thus, higher power (at least $100 \mu\text{W}$) can be dissipated in the thermistors in order to achieve higher sensitivity in the temperature measurements. Dedicated experiments to assess the effect of dissipating power through a thermistor attached to the walls of the EH will provide accurate information on the thermal response of the EH walls. Such tests must be performed in view of the definition of the thermal experiments in the GRS which are described in chapter §7. Anyway the effect of the power fluctuations in the thermistor of the TMS can be considered negligible.

¹¹Simulations performed with the LCA thermal model provided by CGS suggest this hypothesis [50, 51, 97].

¹²This expression is valid in the MBW if and only if the cut-off frequency of the thermal response of the EH walls is smaller or of the same order than 1 mHz . The cut-off frequency is approximated to $f_c = 1/(2\pi C\theta)$ where C is the thermal mass of the EH wall and θ is the thermal resistance with the surroundings

Chapter 7

Thermal experiments in the GRS

A set of 14 heaters will fly in the LTP as a part of the thermal diagnostic subsystems. Their objective is to generate thermal gradients in thermally sensitive locations on-board the LTP. The purpose of these controlled disturbances is to induce a perturbing signal of high amplitude in different subsystems to then estimate the relationship between the temperature and the subsystem thermally perturbed. The temperature disturbances are monitored by 24 thermistors distributed across the LTP. The final scope of such measurements is to characterise the thermal noise contribution to the LTP noise performance curve.

In the following sections we focus on the definition of the thermal experiments in the GRS. Thermal effects in the GRS are those causing a force on the test mass when a temperature gradient is present across the opposite faces of the electrode housing. The most relevant derived effects in the LTP conditions are: the radiation pressure, the radiometer effect and the outgassing from the housing walls [84, 26] —cf. §1.5.1.

We mainly discuss the possibility of disentangling two thermal effects (radiation pressure and radiometer effect) by using suitable thermal signals generated by the heaters. The analysis is a continuation of the work presented in [97]. The first part focuses on the definition of suitable signals. The second part of the chapter describes simulations within the LTP dynamics control loop in order to assess the quality in the estimation of the parameters and to determine the motion of the TMs within the control loops when thermally perturbing them.

7.1 Estimation of errors on parameters: the Cramér-Rao bound

The approach followed to design experiments on-board the LTP is based on the evaluation of the errors in the estimation of the parameters. The figure of merit is the variance of the parameters in terms of the experiment variables, i.e., the power dissipated in the heaters and the integration time (duration of the experiment). A suitable tool for this purpose is the Fisher information matrix, whose inverse sets lower bounds on the variance of the parameters [63, 163].

In order to introduce the notation and the main concepts required for the analysis, we consider a known deterministic signal $s[n, \theta]$ with an unknown parameter θ , to produce an output, $y[n]$, which is measured with a noisy component, $w[n]$, i.e.,

$$y[n] = s[n, \theta] + w[n], \quad n = 0, 1, \dots, N - 1. \quad (7.1)$$

where N is the number of samples. If we can assign a probability density function to the process $y[n]$, i.e., $p(y; \theta)$, then the Cramér-Rao bound (CRB) states that the variance of any unbiased

estimator $\hat{\theta}$, satisfies

$$\text{var}(\hat{\theta}) \geq - \frac{1}{\mathcal{E} \left[\frac{\partial^2 \ln p(y; \theta)}{\partial^2 \theta} \Big|_{\theta=\theta_{\text{true}}} \right]} \quad (7.2)$$

where $\mathcal{E}\{-\}$ stands for the expectation value taken with respect to $p(y; \theta)$ and the derivative is evaluated at the *true* value of θ , θ_{true} . The term $\ln p(y; \theta)$ is also known as the log-likelihood ratio and, in the case of a set of parameters $\Theta = \{\theta_1, \theta_2, \dots, \theta_M\}$, the denominator of Eq. (7.2) becomes a matrix, known as the Fisher information matrix

$$\mathbf{I}(\Theta) = -\mathcal{E} \left[\frac{\partial^2 \ln p(y; \Theta)}{\partial^2 \Theta} \Big|_{\Theta=\Theta_{\text{true}}} \right] \quad (7.3)$$

and the CRB is

$$\text{var}(\hat{\Theta}) \geq \text{diag}[\mathbf{I}(\Theta)]^{-1} \quad (7.4)$$

saying that the lower bound for the variance in the estimation of the parameters Θ is the inverse of the Fisher matrix.

7.2 Purpose of the thermal experiments in the GRS

The *nominal* thermal feedthrough factor for the case of infinite planes, α , is¹ [84] —cf. §1.5:

$$\alpha(T, p) = \frac{A_{\text{TM}}}{m_{\text{TM}}} \left[\frac{16}{3} \frac{\sigma}{c} T^3 + \frac{1}{2} \frac{p}{T} + \frac{Q(T)}{C_{\text{eff}}} \frac{\Theta}{T^2} \right] \quad (7.5)$$

where the three terms correspond to the known effects: radiation pressure, radiometer effect and outgassing processes. The acceleration caused by this joint effect in a free floating test mass is proportional to the thermal gradient between the faces of the walls of the EH, or

$$a_{\text{TM}} = \alpha \Delta T. \quad (7.6)$$

In Eqs. (7.5) and (7.6) the variables stand for (see also Figure 7.1):

- A_{TM} : surface of each of the TM faces,
- m_{TM} : mass of the TMs,
- σ : the Stefan-Boltzmann constant,
- c : the speed of the light,
- p : the pressure inside the vacuum enclosure,
- $Q(T)$, Θ and C_{eff} : parameters to describe the outgassing effect,
- T : absolute temperature of the EH walls facing the TM,
- ΔT : differential temperature between the EH walls facing the TM.

¹Other factors can be found in the literature that are slightly different [26, 67].

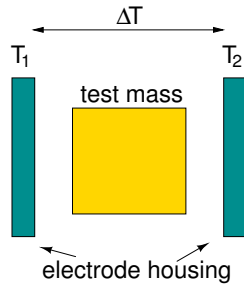


Figure 7.1: Scheme of the TM and EH walls surrounding it.

We assume a constant pressure, p , and ignore the outgassing effect due to the uncertainty of this effect which, in principle, will be negligible —see §1.5.1. Thus, the feedthrough factor, α , is simplified to

$$\alpha(T) \simeq \frac{A_{\text{TM}}}{m_{\text{TM}}} \left[\frac{16}{3} \frac{\sigma}{c} T^3 + \frac{1}{2} \frac{p}{T} \right]. \quad (7.7)$$

In addition, the temperature surrounding each of the TMs, T , will be *quasi*-constant during the experiment. The increase of this temperature should be around $\sim 0.5 - 1$ K maximum during each run —see Figure 7.11. This fact suggests considering the absolute temperature constant during the experiments, whence, Eq. (7.7) can be further simplified:

$$\alpha \simeq \frac{A_{\text{TM}}}{m_{\text{TM}}} \left[\frac{16}{3} \frac{\sigma}{c} T_o^3 + \frac{1}{2} \frac{p}{T_o} \right] \quad (7.8)$$

where T_o is the temperature of the EH walls during the experiment (assumed constant). However, this assumption does not allow to discern the radiation pressure effect and the radiometer effect since the parameter α becomes a mere constant.

In order to resolve both effects we must know accurately the value of α and consider T is not constant. The accuracy needed is determined by the change of α with respect to the absolute temperature, and the variation of the latter during the experiment², or

$$\frac{d\alpha}{dT} = \frac{A_{\text{TM}}}{m_{\text{TM}}} \left(16 \frac{\sigma}{c} T^2 - \frac{1}{2} \frac{p}{T^2} \right) \quad (7.9a)$$

$$\Delta\alpha_{\text{GRS}}(T) = \frac{1}{\alpha_o} \frac{d\alpha}{dT} [T(t_f) - T(t=0)] \quad (7.9b)$$

where $[T(t_f) - T(t=0)]$ is the variation of the absolute temperature during the experiment and α_o is α at $T(t=0)$. If the accuracy in the estimation of the parameter is higher than the change observed in α during the experiment due to absolute temperature changes —Eq. (7.9b)— then we will be able to disentangle the two effects. Now we evaluate Eqs. (7.8), (7.9a) and (7.9b) to have an idea about the needed accuracy. The values used are [99]:

- $A_{\text{TM}} = (46 \cdot 10^{-3})^2 \text{ m}^2$
- $m_{\text{TM}} = 1.96 \text{ kg}$
- $T_o = 293 \text{ K}$
- $p = 10^{-5} \text{ Pa}$

²The change in absolute temperature permits to distinguish between the T^3 behaviour from the $1/T$ one in Eq. (7.7).

- $[T(t_{\text{tot}}) - T(t = 0)] \simeq 0.5 \text{ K}$

and the numbers obtained are:

$$\alpha(T = 293 \text{ K}) = \left(\overbrace{27.37}^{\text{r.p.}} + \overbrace{18.42}^{\text{rm.}} \right) \cdot 10^{-12} = 45.79 \cdot 10^{-12} \text{ m s}^{-2} \text{ K}^{-1} \quad (7.10)$$

$$\left. \frac{d\alpha}{dT} \right|_{T=293 \text{ K}} = (0.280 - 0.062) \cdot 10^{-12} = 0.217 \cdot 10^{-12} \text{ m s}^{-2} \text{ K}^{-2} \quad (7.11)$$

$$\Delta\alpha(T)|_{0.5 \text{ K}} = 2.37 \cdot 10^{-3} \text{ (0.23\%)} \quad (7.12)$$

where “r.p.” stands for radiation pressure and “rm.” for radiometer.

From Eq. (7.12) we notice that the accuracy in the estimation of α must be better than 0.23%. In other words, if the accuracy is worse than 0.23% the absolute temperature can be considered constant and therefore the hope of discerning the two effects vanishes. This is analysed in the following sections.

7.3 Thermal coupling within the LTP dynamics

Following the notation in [148], we can describe the LTP dynamics in terms of the following set of equations

$$\mathbf{D}\vec{q} = \vec{g}, \quad (7.13a)$$

$$\vec{g} = -\mathbf{C}\vec{o} - \vec{g}_n, \quad (7.13b)$$

$$\vec{o} = \mathbf{S}\vec{q} + \vec{o}_n \quad (7.13c)$$

where \mathbf{D} is the TMs dynamical matrix (2×2), \mathbf{C} is the 2×2 controller matrix (drag-free and low-frequency suspension), and \mathbf{S} is the matrix translating the position of the TMs, \vec{q} ($= \{q_1, q_\Delta\}$), into interferometer read out \vec{o} ($= \{o_1, o_\Delta\}$). \vec{o}_n ($= \{o_{n1}, o_{n\Delta}\}$) and \vec{g}_n ($= \{g_{n1}, g_{n\Delta}\}$) are noise of the interferometer and stray forces on the TM, respectively —see §7.4. The subscript “1” is related to the position of one TM with respect to the SC, whereas the subscript “ Δ ” stands for the differential motion between one TM and the other one. A more detailed description is given in §7.4.

As seen before, the effect of the heaters in this location will be a direct force applied on the TM, which we name \vec{g}_T . With this term, Eq. (7.13b) becomes

$$\vec{g} = -\mathbf{C}\vec{o} - \vec{g}_n - \vec{g}_T. \quad (7.14)$$

At the same time, the applied force, \vec{g}_T , needs to be expressed in terms of the EH thermal transfer function (or feedthrough factors), i.e.,

$$\vec{g}_T = \mathbf{G}\vec{T}. \quad (7.15)$$

This notation allows for different models, depending on the assumptions made on the dependence of the thermal force exerted on the test mass. Two different cases are considered:

1. Thermal force depends only on ΔT across the EH —see §7.2. We thus consider the whole equation in (7.5) as a unique factor, or

$$\mathbf{G} = \begin{pmatrix} \alpha_1 & 0 \\ -\alpha_1 & \alpha_2 \end{pmatrix}, \quad \vec{T}_{\text{IS}} = \begin{pmatrix} \Delta T_1 \\ \Delta T_2 \end{pmatrix} \quad (7.16)$$

where α is the thermal feedthrough factor defined in Eq. (7.5), and we assume that a heat input in TM-1 is seen in both interferometers o_1 and o_Δ , but a heat pulse in TM-2 only affects the o_Δ measurement. ΔT is the temperature gradient across the EH.

2. The thermal feedthrough factor is split into the radiation pressure and the radiometer effect —see §7.2, i.e.,

$$\mathbf{G} = \begin{pmatrix} \beta_1 & \gamma_1 & 0 & 0 \\ -\beta_1 & -\gamma_1 & \beta_2 & \gamma_2 \end{pmatrix}, \quad \vec{T} = \begin{pmatrix} T_1^3 \Delta T_1 \\ \frac{\Delta T_1}{T_1} \\ T_2^3 \Delta T_2 \\ \frac{\Delta T_2}{T_2} \end{pmatrix} \quad (7.17)$$

where now β is defined to be the radiation pressure factor and γ is the radiometer one. This model can help disentangle both contributions as shown in §7.3.5.

Introducing now the thermal contribution into (7.13b) and working out the dynamics equation we end up with one equation gathering all the relevant information, i.e.,

$$(\mathbf{DS}^{-1} + \mathbf{C})\vec{o} = \vec{g}_n + \vec{g}_T + \mathbf{DS}^{-1}\vec{o}_n \quad (7.18)$$

or equivalently, the output acceleration is:

$$\vec{a} = \vec{g}_n + \vec{g}_T + \mathbf{DS}^{-1}\vec{o}_n \quad (7.19)$$

where the first component of \vec{a} , i.e., the acceleration of TM-1 with respect to the spacecraft (SC) is fully dominated by the SC motion $[G_{\text{SC}}(s)]$ —see §7.4 and appendix §G. Consequently, we only focus on the differential acceleration, $a_\Delta(s)$ (the second component of \vec{a}), which is (considering the absolute temperature-independent model)

$$a_\Delta = (g_2 - g_1) - \alpha_1 \Delta T_1 + \alpha_2 \Delta T_2 + (s^2 + \omega_{p2}^2)o_{n\Delta} + \Delta\omega_p^2 o_{n1} \quad (7.20)$$

where $(s^2 + \omega_{p2}^2)$ and $\Delta\omega_p^2$ are components of the dynamical matrix, \mathbf{D} —see §7.4 and appendix §G. Different thermal perturbation combinations can be applied to the TMs in order to extract the maximum information. On the one hand, applying a perturbation to TM-1 implies that:

$$a_\Delta = (g_2 - g_1) - \alpha_1 \Delta T_1 + (s^2 + \omega_{p2}^2)o_{n\Delta} + \Delta\omega_p^2 o_{n1} \quad (7.21)$$

and, on the other hand, a perturbation on TM-2 results in

$$a_\Delta = (g_2 - g_1) + \alpha_2 \Delta T_2 + (s^2 + \omega_{p2}^2)o_{n\Delta} + \Delta\omega_p^2 o_{n1}. \quad (7.22)$$

Other combinations lead to different expressions that can be useful. For instance, we can apply the same thermal gradient for the two TMs, or an opposite thermal gradient, i.e.,

$$\Delta T_1 = \Delta T_2, \quad [\text{same thermal gradient}], \quad (7.23)$$

$$\Delta T_1 = -\Delta T_2, \quad [\text{opposite thermal gradient}]. \quad (7.24)$$

The differential accelerations for the two cases are

$$a_\Delta|_{\Delta T_1 = \Delta T_2} = (g_2 - g_1) + (\alpha_2 - \alpha_1)\Delta T + (s^2 + \omega_{p2}^2)o_{n12} + \Delta\omega_p^2 o_{n1}, \quad (7.25)$$

$$a_\Delta|_{\Delta T_1 = -\Delta T_2} = (g_2 - g_1) + (\alpha_2 + \alpha_1)\Delta T + (s^2 + \omega_{p2}^2)o_{n12} + \Delta\omega_p^2 o_{n1} \quad (7.26)$$

where we see that the differential feedthrough factor, $\alpha_1 - \alpha_2$, can be measured by applying the same thermal gradient to both TMs.

7.3.1 Available hardware description

The temperature sensors and heaters in the GRS have been described in §2 and in appendix §B. However, here we briefly describe how they can be used in order to properly excite the TM.

The thermal feedthrough factor will be determined by enhancing the *thermally induced acceleration* in the TMs, which will be generated by applying a train of heat pulses. Given that the thermal coupling must be characterised in the measurement bandwidth, a suitable activation period will lead to a periodic force with the main frequency component in the MBW [97] —see §7.3.2. The number of heaters in each EH is 4, 2 in each face, but the heaters attached to the same face of the same EH are connected together. Thus, the number of commanded heaters in each GRS is actually two instead of four. We call the former *physical* heaters (four per EH) and the latter *logical* heater (two per EH). This is schematised in Figure 7.2. Four temperature sensors are also present in each EH —see §2.4.

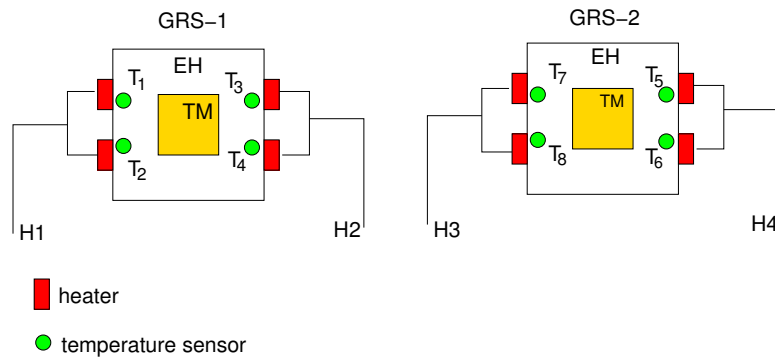


Figure 7.2: Heaters and temperature sensors locations in the EHS of the two GRSs —see also Figure 3.1.

The activation scheme to induce a net force in one of the TMs consists in switching on/off the heaters H1 and H2 for TM-1, and H3 and H4 for TM-2 —see Figure 7.3. With this activation scheme a thermal gradient between opposite faces of the EH is generated —see Figure 7.4.

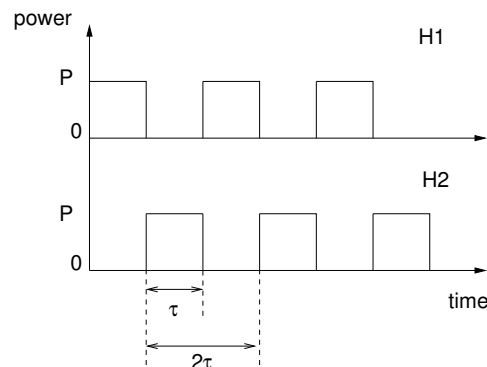


Figure 7.3: Scheme of the power dissipated in the heaters of one of the EHS. Note that, actually, the power dissipated in each of the faces of the EH is $2P$ instead of P since H1 stands for one logical heater that contains two physical heaters. The same applies to H2.

Since the thermal effects are mainly dependent on ΔT , this variable will be the figure of merit

to characterise the heating scheme. The definition of ΔT in both EHs is [99, 97]

$$\Delta T_1 = \frac{T_1 + T_2}{2} - \frac{T_3 + T_4}{2}, \quad (7.27)$$

$$\Delta T_2 = \frac{T_7 + T_8}{2} - \frac{T_5 + T_6}{2} \quad (7.28)$$

where T_i corresponds to each of the temperature sensors placed in the EH —see Figure 7.2. The absolute temperature of the EH surfaces is defined as the semisum of the temperature read out of the two sensors at the same face.

7.3.2 Signals definition

The power dissipated in the heaters causes a temperature increase of the walls of the EHs with a constant slope (since we are far from the steady state —see Figure 7.5),

$$P = mc\dot{T} = C\dot{T} \quad (7.29)$$

where C is the specific heat in JK^{-1} of each of the walls of the EH and \dot{T} is the slope of the temperature increase in the walls of the EH. We now define a new parameter which is the inverse of C [97]:

$$Q = \frac{1}{C} \quad [\text{K W}^{-1} \text{s}^{-1}] \quad (7.30)$$

The parameter Q relates energy dissipated in the heaters to the increase of temperature of the EH walls.

The positive temperature slope when the heaters are switched on is higher than the negative temperature slope when the heaters are switched off. Therefore, a net increase in the absolute temperature will be present. The thermal gradient between the two opposite faces of the TM is a triangular wave —see Figure 7.4. Simulations performed with the thermal model of the LTP provided by Carlo Gavazzi Space (CGS) [50, 51, 97] confirmed this behaviour —see Figure 7.5.

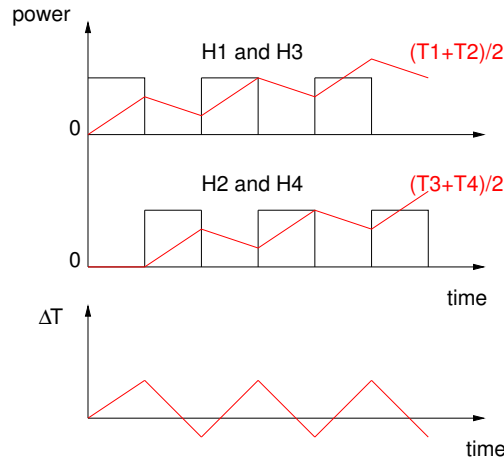


Figure 7.4: Scheme of the power dissipated in the heaters and the increase of temperature in the EH walls. A simulation with the CGS LTP thermal model is shown in see Figure 7.5.

The absolute temperature drift in each of the EH walls can be described, in a very simplified

form, as³

$$T(t) = \frac{1}{2}Q\bar{P}t + T_o \quad (7.31)$$

where $T(t)$ is the temperature of each of the walls of the EH, T_o is the temperature at the beginning of the experiment and \bar{P} is the average power dissipated during the experiment in a *physical* heater, i.e., $P/2$.

The differential temperature between the EH walls, ΔT , can be roughly approximated by a sine wave (useful for analytical calculations —see §7.3.5)

$$\Delta T(t) = \frac{1}{2}QP\tau \sin \frac{2\pi}{2\tau}t \quad (7.32)$$

or more accurately by a triangular wave (useful for simulations —see §7.3.5) [97]:

$$\Delta T(t) = \sum_{k=1}^N \Delta T_k(t) \quad (7.33)$$

with

$$\Delta T_k(t) = \begin{cases} \frac{2\Delta T_{p-p}}{2\tau}t + (\frac{3}{2} - 2k)\Delta T_{p-p} & (k-1)2\tau < t < (k-\frac{1}{2})2\tau \\ -\frac{2\Delta T_{p-p}}{2\tau}t + (2k - \frac{1}{2})\Delta T_{p-p} & (k-\frac{1}{2})2\tau < t < k2\tau \end{cases}$$

where ΔT_{p-p} ($=Q\tau P$) and N are the peak-to-peak (p-p) amplitude of ΔT and the number of cycles, respectively. The Fourier transform of this signal when integrating during a time $2\tau N$ is

$$|\widetilde{\Delta T}(\omega)|^2 = \frac{\Delta T_{p-p}^2}{4\tau^2\omega^4} \sin^2(N\tau\omega) \left[2\tau\omega - 4 \tan\left(\frac{\tau\omega}{2}\right) \right]^2 \quad (7.34)$$

which will be useful for the calculation of the signal-to-noise ratio (SNR) later on.

The CGS LTP core assembly (LCA) thermal model allows us to compute the evolution of the temperature when dissipating power in the heaters. Results for a concrete simulation are given in Figure 7.5. The parameters chosen for that simulation are: 20 mW dissipated in each of the heaters of the EH, $\tau=500$ s is the time each heater is switched on/off, and the total amount of time of the experiment is 3000 s —details of the simulations and the thermal model can be found in [50] and [97].

³We assume that $T = (T_1 + T_2)/2 = (T_3 + T_4)/2$, i.e., the temperature of each of the walls is the same. Obviously, there is always a differential temperature, ΔT , between both faces, however here we are only interested in the *drift* of the absolute temperature. We also omit the *ripples* in the absolute temperature evolution.

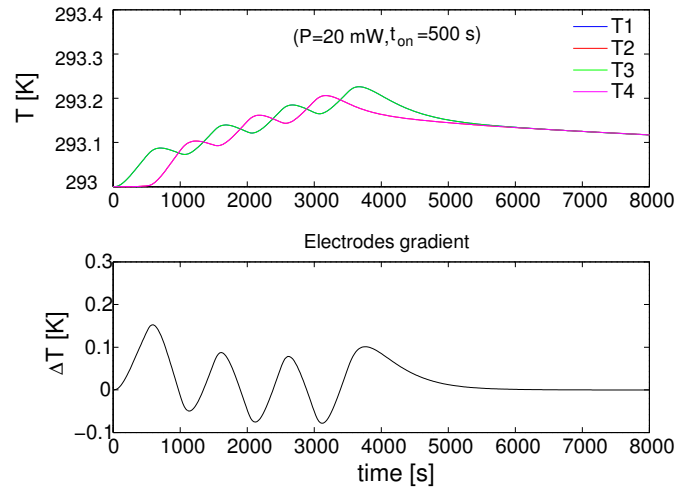


Figure 7.5: Simulation performed with the CGS thermal model [97]. The power dissipated in each *physical* heater is 20 mW with $\tau=500$ s and total running time of 3000 s.

According to the results displayed in Figure 7.5, the subtraction described in Eq. (7.27) leads to a nearly triangular signal —as previously argued qualitatively.

7.3.3 Parameters estimation

In this section we analyse the error in the determination of the thermal feedthrough factors. First, we assume a constant absolute temperature and only a global feedthrough factor, α . Since this parameter can be determined with high accuracy —see §7.3.4—, we, in §7.3.5, will also address the possibility of disentangling the two thermal effects (radiation pressure and radiometer effect). The analysis of the accuracy in the parameter estimation is based on the Cramér-Rao lower bound —see §7.1.

7.3.4 Estimation of α

The parameter estimation is based on the following equation

$$a_{\Delta}(t) = \alpha \Delta T(t) + n(t) \quad (7.35)$$

where $n(t)$ is the differential acceleration noise of the LTP and we assume the read out of the temperature, ΔT , is noiseless⁴.

⁴For instance, the SNR between the temperature signal and the noise of the temperature read out for $\Delta T_{\text{p-p}}=1 \text{ mK}$, $\tau=100 \text{ s}$ and 40 cycles is about 500 (assuming a temperature noise read out of $10^{-4} \text{ KHz}^{-1/2}$ in the MBW). This noise has been taken into account in the simulations shown in §7.4.

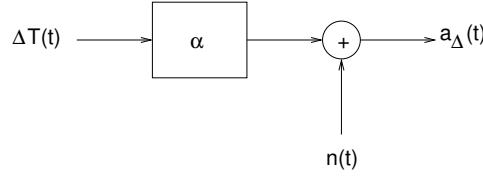


Figure 7.6: Parameter estimation scheme. The temperature read out is assumed noiseless.

The estimation of the parameter α is done by the likelihood ratio approach. If we assume a zero-mean, stationary Gaussian random process (not necessarily white), the optimum signal-to-noise ratio, ρ^2 , in the estimation of the parameter α is [63, 163]

$$\rho^2 \doteq \frac{\partial^2 \ln \Lambda}{\partial \alpha^2} \quad (7.36)$$

where in the Gaussian noise case the log-likelihood function is

$$\ln \Lambda = \ln p_n(a_\Delta - \alpha \Delta T) = -\frac{N}{2} \ln \pi - \frac{1}{2} \det |\mathbf{C}| - \frac{1}{2} \sum_{i,j} \mu_{i,j} (a_{\Delta,i} - \alpha \Delta T_i)(a_{\Delta,j} - \alpha \Delta T_j) \quad (7.37)$$

where \mathbf{C} is the covariance matrix of the Gaussian noise and $\mu_{i,j} \equiv (\mathbf{C}^{-1})_{i,j}$. Substituting Eq. (7.37) in (7.36) results in

$$\rho^2 = \sum_{i,j} \mu_{i,j} \Delta T_i \Delta T_j \quad (7.38)$$

which can be approximated to the frequency domain, i.e.,

$$\rho^2 = 4 \int_{MBW} \frac{|\widetilde{\Delta T}(\omega)|^2 d\omega}{S_{a_\Delta}(\omega) 2\pi} \quad (7.39)$$

The standard deviation in the estimation of the parameter is set by the Cramér-Rao bound,

$$\sigma \geq \rho^{-1} \quad (7.40)$$

The relative error ($1-\sigma$) in the determination of the parameter is calculated by using Eq. (7.39). Triangular waves of different amplitudes and frequencies are considered, and the nominal parameter is $\alpha = 45.79 \cdot 10^{-12} \text{ m s}^{-2} \text{ K}^{-1}$. The obtained values are shown in Table 7.1.

ΔT_{p-p} [mK]	$\tau = 1000 \text{ s}$ ($f=0.5 \text{ mHz}$)	$\tau = 500 \text{ s}$ ($f=1 \text{ mHz}$)	$\tau = 50 \text{ s}$ ($f=10 \text{ mHz}$)	$\tau = 10 \text{ s}$ ($f=50 \text{ mHz}$)
1	3.62%	1.16%	1.9%	45.8%
5	0.72%	0.23%	0.4%	91.6%
10	0.36%	0.12%	0.2%	45.8%
20	0.18%	0.06%	0.1%	22.9%
40	0.09%	0.03%	0.05%	11.45%

Table 7.1: $1-\sigma$ relative error of $\hat{\alpha}$ considering $\alpha = 45.79 \cdot 10^{-12} \text{ m s}^{-2} \text{ K}^{-1}$. f is the frequency of the triangular wave.

Now we can calculate the amount of power necessary in each of the heaters to attain the desired thermal gradient, ΔT_{p-p} , shown in Table 7.1. Simulations done with the CGS thermal model lead

to an estimate of the parameter $Q \sim 15 \text{ mK s}^{-1} \text{ W}^{-1}$. This coefficient is used to calculate the power per *physical* heater needed to attain $\Delta T_{\text{p-p}}$ in a certain time τ , i.e.,

$$P \simeq \frac{1}{Q} \frac{\Delta T_{\text{p-p}}}{\tau}. \quad (7.41)$$

Table 7.2 shows the power needed for different test configurations. It is clear that for triangular waves of low frequency (0.5 mHz and 1 mHz) small levels of power are needed. For instance, with $P=3 \text{ mW}$ and $\tau=1000 \text{ s}$ we obtain a triangular wave of frequency 0.5 mHz and $\Delta T_{\text{p-p}}=40 \text{ mK}$ which translates into a 0.09% error in the estimation of α . However, if $\tau=50 \text{ s}$ ($f=10 \text{ mHz}$) the required power to obtain $\Delta T_{\text{p-p}}=40 \text{ mK}$ is 50 mW.

$\Delta T_{\text{p-p}}$ [mK]	$\tau = 1000 \text{ s}$ ($f=0.5 \text{ mHz}$)	$\tau = 500 \text{ s}$ ($f=1 \text{ mHz}$)	$\tau = 50 \text{ s}$ ($f=10 \text{ mHz}$)	$\tau = 10 \text{ s}$ ($f=50 \text{ mHz}$)
1	67 μW	133 μW	1.3 mW	6.7 mW
5	333 μW	667 μW	6.5 mW	33 mW
10	667 μW	1.5 μW	13.5 mW	66 mW
20	1.5 mW	3 mW	26 mW	133 mW
40	3 mW	5 mW	52 mW	266 mW

Table 7.2: Power per physical heater needed for the configurations given in Table 7.1.

In summary, it is clear that α can be determined with high accuracy. Therefore to disentangle the two effects involved in the thermal acceleration coupling might be possible.

7.3.5 Resolving radiation pressure and radiometer effect

An accuracy of $\sim 0.03\%$ is possible in the determination of the parameter α —see Table 7.1. The required accuracy in order to disentangle radiation pressure from radiometer effect is 0.23%, assuming a variation in the absolute temperature of the EH walls of 0.5 K —see §7.2.

The easiest way to disentangle the thermal effects would be to perform the experiments at two different temperatures, for example, 15°C and 25°C in order to obtain a system of two equations with two unknowns. This can be done by switching on the four heaters in one of the EH at a constant power and wait for temperature stabilisation. Once the temperature is stable, the switching scheme described in section 7.3.2 can be performed (maintaining the power to increase the temperature as an offset). Simulations done with the CGS thermal model tool applying a constant power in one of the EH walls led to a very long time constant prior to stabilisation ($>10 \text{ ks}$) [50, 51]. Therefore, this option is not the optimum approach for our purpose, due to time constraints. However, the two effects can be discerned in another way. We assume we have three measurements: the differential temperature, ΔT , the absolute temperature of the EH walls, T , and the output acceleration, a_{Δ} . The TM acceleration as a function of ΔT and T is —see §7.2:

$$a_{\Delta}(T, \Delta T, t) = \beta T(t)^3 \Delta T(t) + \gamma \frac{\Delta T(t)}{T(t)} + n(t) \quad (7.42)$$

where β is the radiation pressure parameter, γ is the radiometer effect parameter and $n(t)$ is the noise of the acceleration measurement. Figure 7.7 shows this process schematically.

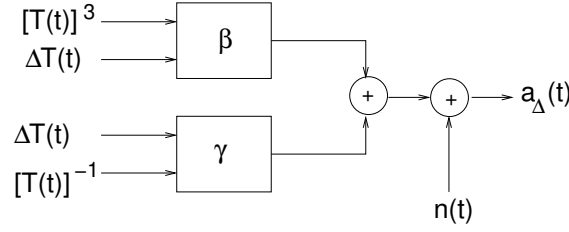


Figure 7.7: Parameter estimation scheme considering T and ΔT as inputs. The temperature read out is assumed noiseless.

In this case the log-likelihood function is (assuming a zero-mean white Gaussian noise with variance σ_n^2)⁵:

$$-\log \Lambda = N \ln \sqrt{2\pi\sigma_n^2} + \frac{1}{2\sigma_n^2} \int_0^{2N\tau} \left[a_\Delta(t) - \beta \Delta T(t) T(t)^3 - \gamma \frac{\Delta T(t)}{T(t)} \right]^2 dt \quad (7.43)$$

and the Fisher matrix is defined as:

$$\mathbf{I} = \frac{1}{\sigma_n^2} \begin{pmatrix} \frac{\partial^2(-\log \Lambda)}{\partial \beta^2} & \frac{\partial^2(-\log \Lambda)}{\partial \beta \partial \gamma} \\ \frac{\partial^2(-\log \Lambda)}{\partial \gamma \partial \beta} & \frac{\partial^2(-\log \Lambda)}{\partial \gamma^2} \end{pmatrix}. \quad (7.44)$$

The variance of the parameters are the diagonal terms of the inverse Fisher matrix, which are the Cramér-Rao lower bounds —cf. §7.1. The inverse Fisher matrix is:

$$\mathbf{I}^{-1} = \frac{1}{\det(\mathbf{I})} \begin{pmatrix} \int_0^{2N\tau} [\Delta T(t)/T(t)]^2 dt & -\int_0^{2N\tau} [\Delta T(t)T(t)]^2 dt \\ -\int_0^{2N\tau} [\Delta T(t)T(t)]^2 dt & \int_0^{2N\tau} [\Delta T(t)T(t)^3]^2 dt \end{pmatrix}. \quad (7.45)$$

In order to evaluate the numbers above, we come back to the equations describing (in a very simplified way) the temperature evolution in the GRS —see §7.3.2,

$$T(t) = \frac{1}{4} Q P t + T_o, \quad (7.46a)$$

$$\Delta T(t) = \frac{1}{2} Q P \tau \sin \frac{2\pi}{2\tau} t. \quad (7.46b)$$

The variance in the estimation is obtained by substituting Eq. (7.46a) and (7.46b) into the diagonal terms of Eq. (7.45). In this manner we can express the variance as a function of the variables of the test, i.e.,

$$\sigma_{\beta,\gamma}^2 = f(Q, P, \tau, N, T_o) \quad (7.47)$$

where Q is a constant determined by the physical properties of the EH, P is the power dissipated in each of the *physical* heaters, τ is the amount of time the heater is switched on in each cycle (a duty cycle of 50% is considered), N is the total number of cycles and T_o is the absolute temperature of the EH walls at the starting of the test.

If we want to estimate the parameters β and γ with a 10% accuracy we have to solve the following inequalities:

$$\sigma_\beta^2(Q, P, \tau, N, T_o) \leq \left(\frac{\alpha}{10} \right)^2, \quad (7.48a)$$

$$\sigma_\gamma^2(Q, P, \tau, N, T_o) \leq \left(\frac{\beta}{10} \right)^2. \quad (7.48b)$$

⁵Actually, the noise of the differential acceleration is not white, however, due to the high signal-to-noise ratio present in the measurements, we have assumed it is. Simulations performed with the expected non-white acceleration noise are shown in §7.4.

We evaluate Eqs. (7.48a) and (7.48b) under different scenarios in order to conclude whether or not it is possible to distinguish between β and γ with a reasonable power, P , and time, τ . The *nominal* values for β and γ are —see §7.2:

$$\beta = \frac{A_{\text{TM}}}{m_{\text{TM}}} \frac{16}{3} \frac{\sigma}{c} = 1.08 \cdot 10^{-18} \text{ m s}^{-2} \text{ K}^{-4}, \quad (7.49)$$

$$\gamma = \frac{A_{\text{TM}}}{m_{\text{TM}}} \frac{1}{2} p = 5.40 \cdot 10^{-9} \text{ m s}^{-2}. \quad (7.50)$$

Now we express Eqs. (7.48a) and (7.48b) in terms of N (the number of cycles). For this purpose we consider the following numbers:

- $Q \simeq 0.015 \text{ K W}^{-1} \text{ s}^{-1}$ (extracted from the CGS thermal model) for all the calculations,
- $T_o = 293 \text{ K}$,
- different values of τ have been considered: 1000 s, 500 s and 50 s which correspond to ΔT signals (sine waves) of frequency ($= 1/2\tau$) 0.5 mHz, 1 mHz and 10 mHz, respectively,
- different values of power dissipated in each of the *physical* heaters are considered (15 mW, 20 mW, 30 mW and 40 mW),
- the only free parameter is N , i.e., the number of cycles of the ΔT signal or, in other words the total duration of the test,
- the noise of the differential acceleration is assumed white with $\sigma_n^2 = (3 \cdot 10^{-14})^2 \cdot (30 \cdot 10^{-3}) = 2.7 \cdot 10^{-29} (\text{m s}^{-2})^2$.

Case 1: $\tau=1000 \text{ s}$ ($f=0.5 \text{ mHz}$). We set $\tau=1000 \text{ s}$ and sweep the power from 15 mW to 40 mW. Afterwards, Eqs. (7.48a) and (7.48b) are solved for N (the required number of cycles, or total amount of time, needed to resolve β and γ). The solutions of the inequalities above are given in Figure 7.8: the zero-crossing indicates the solution, N .

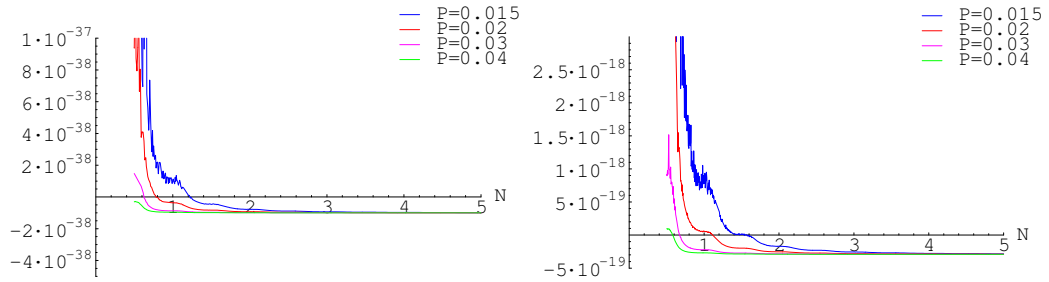


Figure 7.8: Number of cycles, N , needed for β (left) and γ (right) estimation with a 10% accuracy. τ is set to 1000 s ($f=0.5 \text{ mHz}$).

Table 7.3 summarises the results for $\tau=1000 \text{ s}$.

P [mW]	N	total time ($2N\tau$) [s]	ΔT_{p-p} [K]	$T(t_{\text{tot}}) - T(t=0)$ [K]
15	1.6	3200	0.22	0.180
20	1.2	2400	0.30	0.180
30	0.7	1400	0.45	0.1575
40	0.6	1200	0.60	0.180

Table 7.3: Results for $\tau = 1000$ s. ΔT_{p-p} is the peak-to-peak value of the differential temperature signal. $T(t_{\text{tot}}) - T(t=0)$ is the absolute temperature increase of the walls of the EH.

Case 2: $\tau=500$ s ($f=1$ mHz). We performed the same analysis presented in the “Case 1” for $\tau=500$ s. Results are shown in Figure 7.9 and in Table 7.4.

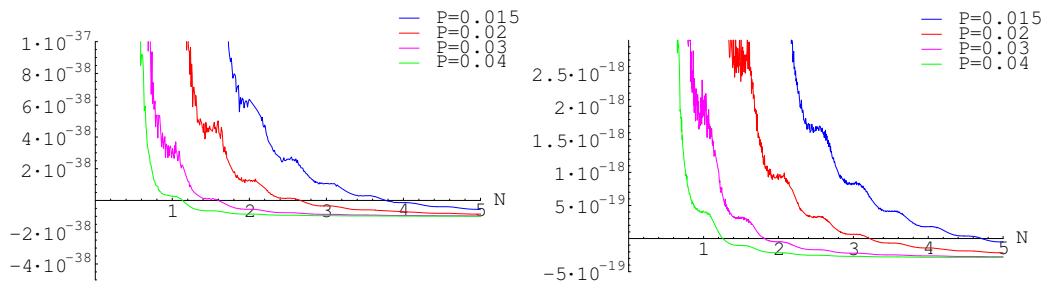


Figure 7.9: *Idem* as Figure 7.8 with $\tau=500$ s ($f=1$ mHz).

P [mW]	N	total time ($2N\tau$) [s]	ΔT_{p-p} [K]	$T(t_{\text{tot}}) - T(t=0)$ [K]
15	4.8	4800	0.11	0.270
20	3.2	3200	0.15	0.240
30	1.8	1800	0.22	0.202
40	1.2	1200	0.30	0.180

Table 7.4: *Idem* as Table 7.3 for $\tau = 500$ s.

Case 3: $\tau= 50$ s ($f=10$ mHz). *Idem* of “Case 1” and “Case 2” for $\tau = 50$ s. Results are shown in Figure 7.10 and Table 7.5.

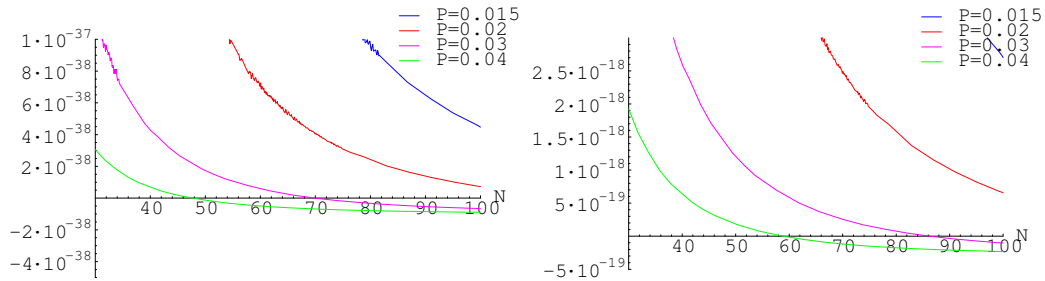


Figure 7.10: *Idem* as Figure 7.8 with $\tau=50$ s ($f=10$ mHz)

P [mW]	N	total time ($2N\tau$) [s]	ΔT_{p-p} [K]	$T(t_{tot}) - T(t=0)$ [K]
15	—	—	—	—
20	—	—	—	—
30	60	6000	0.02	0.675
40	90	9000	0.03	1.350

Table 7.5: *Idem* as Table 7.3 for $\tau = 50$ s.

These results suggest that low frequency signals, i.e., large τ are more convenient for our purpose. For instance, if $\tau=1000$ s and $P = 40$ mW the required total time for the experiment is 1200 s, however, for $\tau=50$ s the required experiment time is 9000 s.

The results of this analysis have been obtained assuming white Gaussian noise, noiseless temperature read out and sine waves as the ΔT signals. Such simplifications lead to results biased in an optimistic sense. These aspects have been included in the simulations presented in §7.4.

In view of this analysis, the proposed temperature profile to excite the test masses of the GRS is shown in Figure 7.11. Two different heater switching schemes are used: the first results in a triangular ΔT of frequency 0.5 mHz while the second one is a triangular wave of 1 mHz. The most important aspect in order to distinguish between radiation pressure and radiometer effects is the absolute temperature drift which in the proposed experiment is of 1 K.

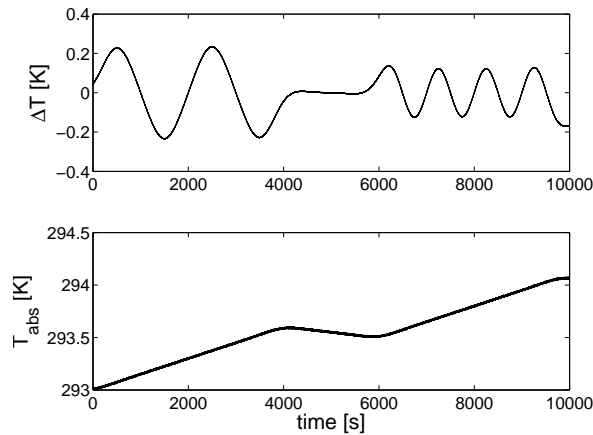


Figure 7.11: Possible temperature profile in the walls of the EH for the thermal experiments in the GRS. The signals in this plot are very simplified, however, they give a fair idea about the temperature evolution during the test.

The experiments should be performed independently at both test masses to estimate the parameters for both GRSs. Moreover, if the same thermal gradient is applied to both TMs then we can measure directly the *asymmetries* of thermal feedthrough factors between both GRSs. This measurement would be useful to check the prior estimates of α_1 and α_2 which are estimated independently. It would be also convenient to repeat this set of experiments at three different moments of the mission, i.e., at the beginning, at the middle and at the end of the mission.

In summary, the results conclude that the thermal feedthrough factor in each of the GRS can be very well known due to the high signal-to-noise ratio present in the experiments. The fact that this parameter can be known so accurately implies that we might be able to distinguish between the radiometer effect and the radiation pressure effect.

The most important issue, though, is the assessment of the temperature response of the walls

of the EHs when dissipating power in the heaters. So far, the temperature evolution of the EH has been *guessed* by means of simulations done with the thermal model of CGS. However, in order to assess such behaviour, on ground tests are mandatory. These tests must be done using an exact replica of the system. Depending on the results of this test, the heaters activation scheme might be different from the one proposed here. This test is, thus, intended to obtain the transfer function relating a heat pulse applied on the GRS with respect to the temperature read out of the sensors attached to the electrode housing.

7.4 Simulations

The accuracy in the estimation of the parameters obtained by the inverse of the Fisher matrix has also been assessed by means of simulations, as we now describe. In order to do so a *simple* model of the LTP dynamics in the x -axis and working in the science mode (M3)⁶ was implemented in Simulink⁷. In the following we describe the LTP dynamics in the x -axis and the implementation using Simulink. Once the model is implemented in Simulink we can apply thermal excitations in the GRS and estimate the parameters coupling temperature and TM motion.

7.4.1 x -axis LTP dynamics

The dynamics of the LTP are⁸ (in the s -domain) —cf. §7.3 [148, 147]

$$(s^2 + \omega_{p1}^2)x_1 = \frac{f_1}{m} - \frac{F}{M} - H_{DF}(s)o_1, \quad (7.51a)$$

$$(s^2 + \omega_{p2}^2)\Delta x + (\omega_{p2}^2 - \omega_{p1}^2)x_1 = \frac{f_2 - f_1}{m} - h_{lfs}(s)o_\Delta \quad (7.51b)$$

with

$$\Delta x = x_1 - x_2, \quad (7.52a)$$

$$o_1 = x_1 + o_{n1}, \quad (7.52b)$$

$$o_\Delta = \Delta x + o_{n\Delta} + \delta s x_1, \quad (7.52c)$$

$$F/M = G_{SC}, \quad (7.52d)$$

$$f_1/m = g_1, \quad (7.52e)$$

$$f_2/m = g_2 \quad (7.52f)$$

where x_1 and Δx are the displacement of the TM-1 with respect to the spacecraft (SC) and the relative position of TM-1 with respect to TM-2, respectively. f_1 and f_2 are the stray forces present in each of the test masses, for instance, due to thermal and magnetic phenomena. F stands for the external forces perturbing the spacecraft. H_{DF} and h_{lfs} are the drag-free and low-frequency suspension controllers: the former maintains the TM-1/SC distance constant while the latter forces TM-2 to follow TM-1. ω_{p1}^2 and ω_{p2}^2 are the parasitic stiffness of the TMs. o_1 , o_Δ , o_{n1} , $o_{n\Delta}$, δs are the interferometric read out of x , Δx and their noise, and the cross-talk between both read out. M (=436 kg) is the mass of the SC and m (=1.96 kg) is the mass of the TM. The system described by Eqs. (7.51a) and (7.51b) is schemed in the block diagram of Figure 7.12.

⁶Mode M3 consists in: the spacecraft position is controlled with respect to the TM-1 by the drag-free controller and the thrusters, and TM-2 position is controlled with respect to TM-1 by the low frequency suspension and the electrostatic actuator [148].

⁷Simulink is an environment for multidomain simulation and Model-Based Design for dynamic and embedded system that runs under Matlab.

⁸Actually this is the system of equations given in §7.3.

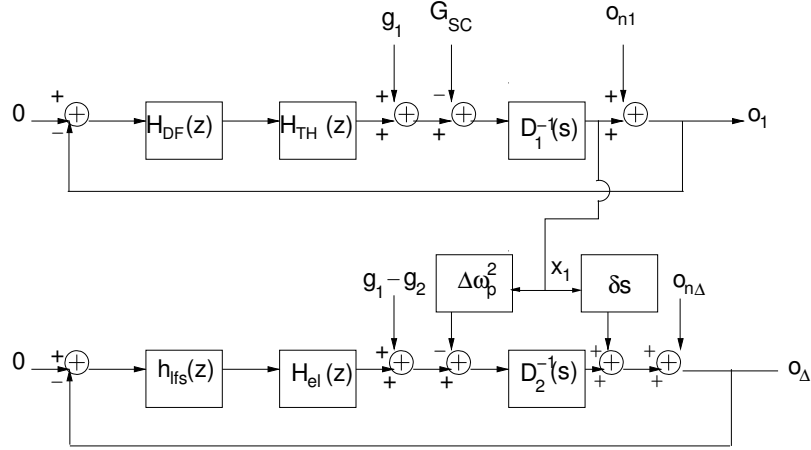


Figure 7.12: Block diagram of the LTP dynamics in the x -axis. The branches in the top represent the control of the position of TM-1 with respect to the SC by means of the drag-free control. The branches in the bottom represent the control of the TM-2 position by the so-called low-frequency suspension, which forces TM-2 to follow TM-1.

The read out of the interferometer, o_1 , is

$$o_1(s) = o_{n1}(s) + D_1^{-1}(s) [-G_{SC}(s) + g_1(s) - H_{DF}(s)o_1(s)] \quad (7.53)$$

where $D_1 = s^2 + \omega_{p1}^2$ stands for the dynamics of TM-1. If $G_{SC}(s) \gg g_1(s)$ —see appendix §G— Eq. (7.53) becomes

$$o_1(s) \simeq -\frac{1}{s^2 + \omega_{p1}^2 + H_{DF}(s)} G_{SC}(s) + \frac{s^2 + \omega_{p1}^2}{s^2 + \omega_{p1}^2 + H_{DF}(s)} o_{n1}(s) \quad (7.54)$$

where o_1 is dominated by the motion of the SC caused by the forces acting on it, G_{SC} .

The differential measurement of the interferometer is

$$o_\Delta(s) = o_{n\Delta}(s) + \delta s x_1(s) + D_2^{-1}(s) [-\Delta\omega_p^2 x_1(s) + g_2(s) - g_1(s) - h_{lfs}(s)o_\Delta(s)] \quad (7.55)$$

where assuming $G_{SC}(s) \gg g_1(s)$ and that the interferometer is ideal, $\delta s = 0$, we have that

$$\begin{aligned} o_\Delta(s) &= \frac{1}{s^2 + \omega_{p2}^2 + h_{lfs}(s)} [g_2(s) - g_1(s)] + \frac{s^2 + \omega_{p2}^2}{s^2 + \omega_{p2}^2 + h_{lfs}(s)} o_{n\Delta}(s) \\ &+ \frac{\Delta\omega_p^2}{[s^2 + \omega_{p1}^2 + H_{DF}(s)][s^2 + \omega_{p2}^2 + h_{lfs}(s)]} G_{SC}(s) \\ &+ \frac{H_{DF}(s)\Delta\omega_p^2}{[s^2 + \omega_{p1}^2 + H_{DF}(s)][s^2 + \omega_{p2}^2 + h_{lfs}(s)]} o_{n1}(s). \end{aligned} \quad (7.56)$$

This is the expected output of the differential displacement between TM-1 and TM-2, where we can see that the external forces exerted by the SC are minimised, and for $\Delta\omega_p^2 = 0$ fully suppressed.

The data available in the experiment are the two outputs of the interferometer, o_1 and o_Δ . However, we are interested in the acceleration, not in the position⁹. From Eqs. (7.54) and (7.56)

⁹The purpose of the thermal experiments in the GRS is to determine the feedthrough factor between temperature gradient and TM acceleration (or force).

we express the acceleration in terms of the interferometer read out as

$$a_1(s) = [s^2 + \omega_{p1}^2 + H_{DF}(s)]o_1(s), \quad (7.57a)$$

$$a_\Delta(s) = [s^2 + \omega_{p2}^2 + H_{ifs}(s)]o_\Delta(s). \quad (7.57b)$$

Substituting Eqs. (7.54) and (7.56) into Eqs. (7.57a) and (7.57b) we obtain the different terms in the acceleration measurement:

$$a_1(s) \simeq -G_{SC}(s) + (s^2 + \omega_{p1}^2)o_{n1}(s) \quad (7.58)$$

and

$$\begin{aligned} a_\Delta(s) \simeq & g_1(s) - g_2(s) + (s^2 + \omega_{p2}^2)o_{n\Delta} + \frac{\Delta\omega_p^2}{s^2 + \omega_1^2 + H_{DF}(s)}G_{SC}(s) \\ & + \frac{H_{DF}(s)\Delta\omega_p^2}{s^2 + \omega_1^2 + H_{DF}(s)}o_{n1}(s). \end{aligned} \quad (7.59)$$

From Eq. (7.59) we notice that any disturbance exerted upon TM-1 or TM-2 (g_1 or g_2) appears directly as a differential acceleration, thus it can be considered in open-loop if the conversion from displacement to acceleration is properly done, i.e., if the transfer functions involved in Eq. (7.57b), H_{ifs} and ω_{p2} , are well known. However, the closed loop response of the system, in terms of displacement, when applying a heat pulse is of interest since the displacement of the TM must be kept below $1 \mu\text{m}$ in any case.

7.4.2 Implementation in Simulink

The system described in the previous section has been implemented in Simulink. The goal of such simulations is to observe the response of the system when exciting the test masses by means of thermal shocks, and then check if it is possible to estimate the parameters related to the thermal effects in the GRS. The proposed thermal excitation has been obtained by means of analytical calculations based on the Fisher matrix —see Figure 7.11 and §7.3.3. In the analytical calculations some simplifications were made. The simulations described herein overcome such simplifications, i.e., they take into account coloured noise, noise in the temperature read out and non-sinusoidal ΔT signals. Another important outcome of the simulations is to check the actual motion of the test masses within the LTP control loops. The motion of the TMs is restricted to $1 \mu\text{m}$, therefore, when exerting a force in the masses we must ensure that the displacement will be less than that.

For the simulations, we have used the following values [148, 147]: $\omega_{p1}^2 = -1.2996 \cdot 10^{-6} \text{ s}^{-2}$, $\omega_{p2}^2 = -1.9881 \cdot 10^{-6} \text{ s}^{-2}$, $\Delta\omega_p^2 = -7 \cdot 10^{-7} \text{ s}^{-2}$ and $\delta s = 10^{-4}$. All the transfer functions and noise sources involved in the system are described in detail in appendix §G.

First of all, the nominal response of the system was simulated, i.e., no excitation of any kind was applied to the system and only the *nominal* noise sources were considered. Figure 7.13 shows the outputs of the interferometer: o_1 (top plot) and o_Δ (bottom plot). Red traces in the power spectral density plots are the theoretical noise curves of o_1 and o_Δ [Eqs. (7.54) and (7.56)]. Results agree quite well.

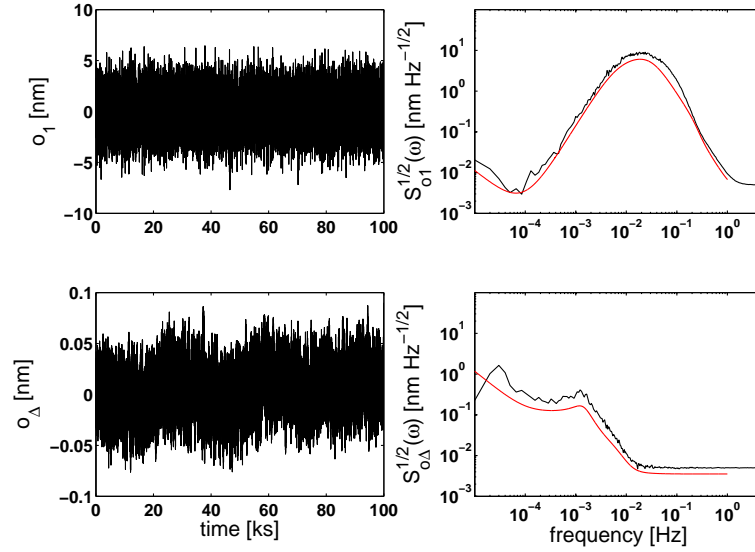


Figure 7.13: Results of the simulations in nominal conditions. The plots in the top correspond to the displacement of the TM-1 with respect to the SC, o_1 . The plots in the bottom are the displacement of TM-1 with respect to TM-2, o_{Δ} . The red traces in the power spectral density plots are the theoretical noise curves.

Figure 7.14 shows the acceleration calculated from the displacements shown in Figure 7.13, o_1 and o_{Δ} . The conversion from displacement to acceleration is done using Eqs. (7.57a) and (7.57b) for the absolute measurement and the differential measurement, respectively. Note that the conversion requires perfect knowledge of the transfer functions present in the system: the drag-free, H_{DF} , and low-frequency controllers, h_{lfs} , and the parasitic stiffness in both test masses, ω_{p1}^2 and ω_{p2}^2 . Poor knowledge in any of these parameters, specially in the gain of the drag-free and low-frequency controllers, lead to errors in the determination of the acceleration. Dedicated experiments in-flight to determine accurately these transfer functions will be done, and they are actually key experiments in the LTP [148]. The results of the simulations were compared with the theoretical curves [red traces in Figure 7.14, which correspond to Eqs (7.58 and (7.59) in PSD]. The agreement is good.

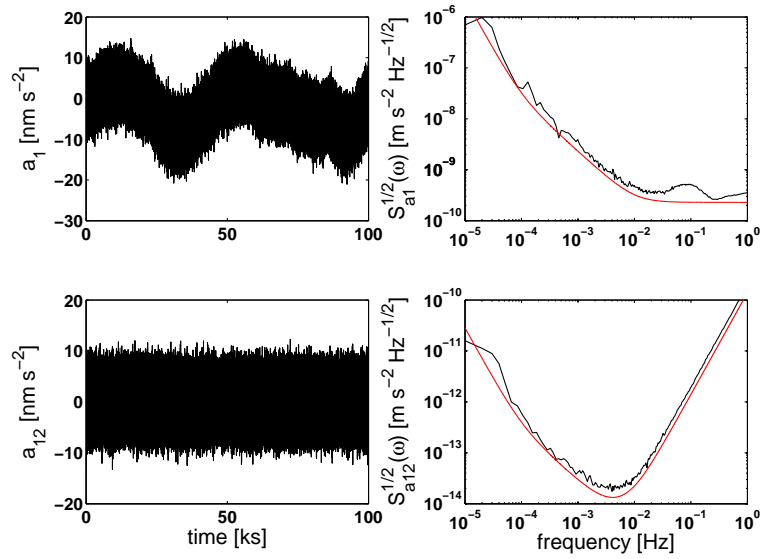


Figure 7.14: *Idem* as Figure 7.13 for the accelerations, a_1 and a_{Δ} . The acceleration is obtained by using Eqs. (7.57a) and (7.57b). Note that the noise in the differential acceleration is about four orders of magnitude lower (in the MBW) than the absolute acceleration noise, since the latter is dominated by the external forces disturbing the SC. The red traces are the theoretical curves.

The results of these simulations were useful in order to assess the validity of the model implemented in Simulink. Once we assessed the correctness of the model, we proceeded to the excitation of the system by means of heat pulses.

7.4.3 Thermal excitation and parameters estimation

The heat pulses in this simulation were applied to TM-2. The temperature profile was the one shown in Figure 7.15.

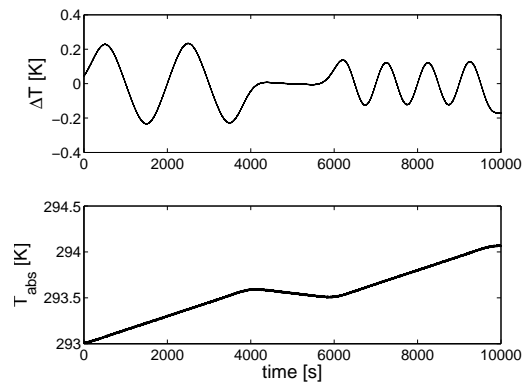


Figure 7.15: Thermal excitation profile applied to TM-2 —see §7.3.5. The noise in the measurement of the temperature is added, but the temperature signal is orders of magnitude larger than the noise read out and it becomes negligible.

As has been shown in §7.2 the acceleration of the TMs due to the thermal effects can be modelled as —see Figure 7.7,

$$a_{\Delta}(t) = \beta T(t)\Delta T(t) + \gamma \frac{\Delta T}{T} + n(t). \quad (7.60)$$

For the simulations we have set $\beta = 1.088 \cdot 10^{-18} \text{ m s}^{-2} \text{ K}^{-4}$ and $\gamma = 5.4 \cdot 10^{-9} \text{ m s}^{-2}$ —see §7.3.5. The noise of the temperature read out has been modeled as white Gaussian noise of $10^{-4} \text{ K Hz}^{-1/2}$ and $10^{-3} \text{ K Hz}^{-1/2}$ for ΔT and T , respectively. The noise levels have been considered higher than the ones exhibited by the actual TMS —cf. §5— in order to work in the safe side. The rest of noise sources and transfer functions are described in appendix §G.

The results of the simulations are shown in Figure 7.16 both in displacement and in acceleration [by using the conversion given in Eqs. (7.57a) and (7.57b)]. The interferometer output o_1 is the blue trace in the top figure, while o_{Δ} is the black trace. The former is dominated by the SC motion, whereas the latter is fully commanded by the force exerted on TM-2 by the temperature pulses. The displacement of TM-2 with respect to the SC is approximately o_{Δ} since $o_{\Delta} \gg o_1$; the maximum displacement of TM-2 with respect to the SC is $\simeq 50 \text{ nm}$ —see Figure 7.16 (top)— which is within the permitted limit ($\simeq 1 \mu\text{m}$) and causes a sufficiently high signal-to-noise ratio. The acceleration is shown in the bottom panel of Figure 7.16. The colour code is the same: the blue trace stands for a_1 and the black one for a_{Δ} . Both acceleration measurements are dominated by the high frequency noise of the interferometer when converting from displacement to acceleration due to the effect of the double derivative —see the noise acceleration curve in Figure 7.14. However, by proper filtering the high frequency noise is eliminated and the effect of the thermal perturbations is clearly seen in the differential acceleration —see Figure 7.18.

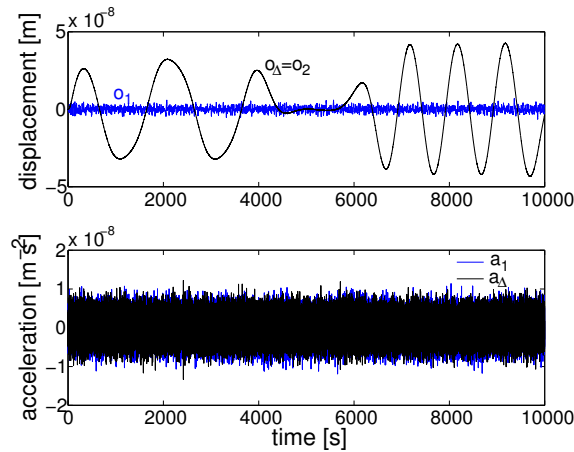


Figure 7.16: Interferometer read out (TM-1/SC motion is the blue trace and TM-1/TM-2 motion is the black trace) of a simulation when applying the heat pulses shown in Figure 7.15. The plot in the top is the displacement where we note that displacement of TM-2 with respect to TM-1 (and thus with respect the SC) is about 50 nm (peak-to-peak). The motion of TM-1 with respect to the SC is one order of magnitude lower —see Figure 7.13. When converting to acceleration (plot in the bottom) the measurement is fully dominated by the high frequency noise coming from the interferometer which must be removed by proper filtering —see Figure 7.17.

The next step is the estimation of the parameters, β and γ , from the temperature and interferometric read out. This is done by the maximum likelihood approach presented in §7.1. The system is [63, 163]

$$a(t) = \beta x(t) + \gamma y(t) + n(t) \quad (7.61)$$

where $a(t)$ is the differential acceleration between both test masses, a_Δ , $n(t)$ is the differential acceleration noise of the system —see Figure 7.14 and, for the sake of clarity we have defined $x(t)$ and $y(t)$ as

$$x(t) = T^3(t)\Delta T(t), \quad (7.62a)$$

$$y(t) = \frac{\Delta T(t)}{T(t)}. \quad (7.62b)$$

If $n(t)$ is considered zero mean, white Gaussian noise, the log-likelihood function is

$$-\ln \Lambda = N \ln (2\pi\sigma_n^2)^{1/2} + \frac{1}{2\sigma_n^2} \sum_{i=1}^N (a_i - \beta x_i - \gamma y_i)^2 \quad (7.63)$$

whence the parameters are estimated by solving the following system of equations

$$\frac{\partial(-\ln \Lambda)}{\partial \beta} = 0, \quad (7.64a)$$

$$\frac{\partial(-\ln \Lambda)}{\partial \gamma} = 0. \quad (7.64b)$$

The solution to the system is

$$\hat{\gamma} = \frac{\sum a_i x_i \sum x_i y_i - \sum x_i^2 \sum a_i y_i}{(\sum x_i y_i)^2 - \sum x_i^2 \sum y_i^2}, \quad (7.65a)$$

$$\hat{\beta} = \frac{\sum a_i x_i - \hat{\gamma} \sum x_i y_i}{\sum x_i^2}. \quad (7.65b)$$

where it is clear that $\hat{\beta}$ and $\hat{\gamma}$ are correlated. The inverse of the Fisher matrix given in Eq. (7.45) shows this fact.

Eqs. (7.65a) and (7.65b) only make sense if the noise, $n(t)$, is uncorrelated since the solution has been derived from the log-likelihood function in Eq. (7.63) where white Gaussian noise was assumed. This is not true in our case, the curve noise of the differential acceleration is the V-shaped one shown in Figure 7.14. Consequently, in order to make use of Eqs. (7.65b) and (7.65a) the differential acceleration must be *whitened*, as must the terms $x(t)$ and $y(t)$, too.

The non-white behaviour in a_Δ is mainly due to the interferometer noise when converting position to acceleration since this conversion implies a double derivative. The noise of the interferometer converted to acceleration is

$$a_{\Delta, \text{ifo}}(s) = H_{\text{ifo}}(s) = (s^2 - \omega_{p2}^2) o_{n\Delta}(s) \quad (7.66)$$

where $o_{n\Delta}$ is the interferometer displacement noise —see appendix G. Thus, the whitening filter is

$$W(s) = H_{\text{ifo}}^{-1}(s). \quad (7.67)$$

Once the whitening filter is in place, the differential acceleration output, a_Δ and the two temperature read out [$x(t) = \Delta T(t)T(t)$ and $y(t) = \Delta T(t)/T(t)$] are filtered. The effect of the whitening filter on the differential acceleration is shown in Figure 7.17. The ω^2 dependence of the acceleration noise vanishes when applying the filter. The $1/f$ noise at low frequencies coming from the internal disturbances in the GRS does not disappear since the whitening filter designed only took into account the noise of the interferometer. A slightly more sophisticated filter can be designed to *white* the low frequency part of the spectrum.

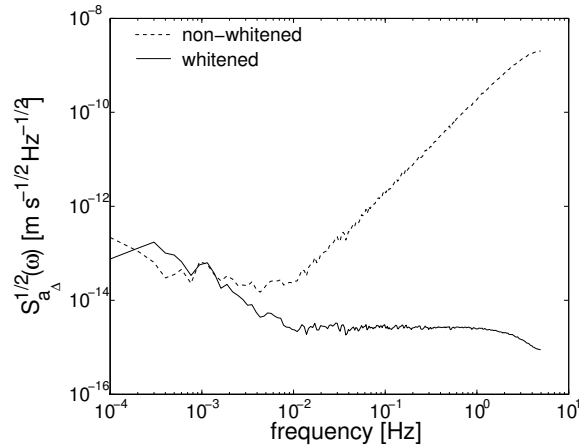


Figure 7.17: Power spectral density of the differential acceleration. The dashed trace is the one standing for a_{Δ} , i.e., no filtered, while the solid trace is the differential acceleration after the whitening filter.

The signals $x(t)$, $y(t)$ and $a_{\Delta}(t)$ after being filtered by $W(s)$ are shown in Figure 7.18 in time-domain. The acceleration modulated by the temperature excitation is now clear since the high frequency noise of the interferometer has been attenuated by the whitening filter. Now, the parameters β and γ can be estimated by using Eqs. (7.65b) and (7.65a), respectively. Figure 7.19 shows the simulated acceleration and the one obtained with the estimated parameters and the temperature signals, $x(t)$ and $y(t)$. In the bottom panel the residuals are shown which are two orders of magnitude smaller than the signal.

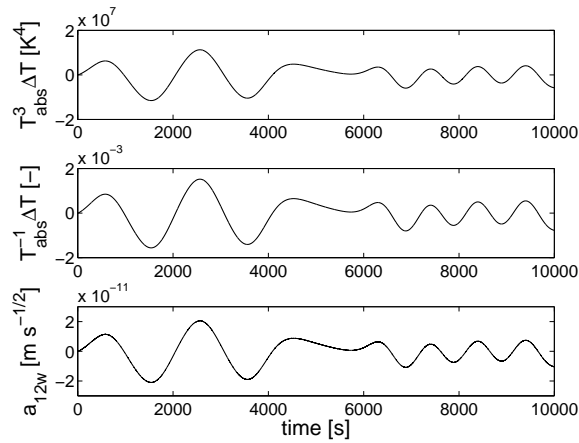


Figure 7.18: Whitened outputs used for the estimation of the parameters β and γ . The bottom plot is the differential acceleration, a_{Δ} , where now the effect of the heat pulses can be observed since the high frequency noise of the interferometer is attenuated by the whitening filter. The acceleration prior to being filtered is the one shown in Figure 7.16.

A total of 1000 simulations were computed in order to obtain the statistics of the parameters. The histograms are shown in Figure 7.20 which show a Gaussian distribution as one might expect since all the noise sources in the simulation were Gaussian. The mean of $\hat{\beta}$ is

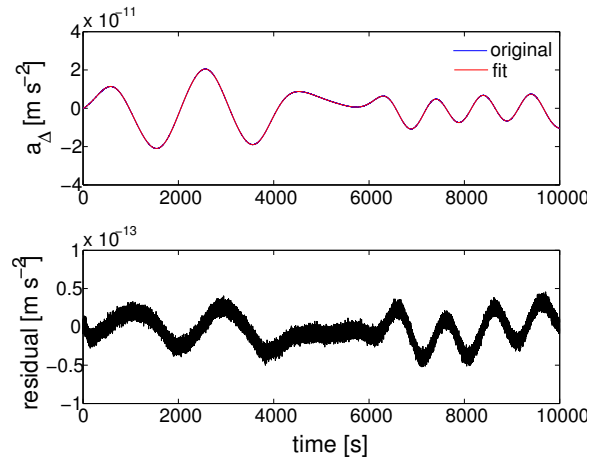


Figure 7.19: Simulated acceleration and acceleration using estimated parameters. The agreement is very good. The residuals are shown in bottom panel.

$1.053 \cdot 10^{-18} \text{ m s}^{-2} \text{ K}^{-4}$ with a standard deviation of $6.5 \cdot 10^{-20} \text{ m s}^{-2} \text{ K}^{-4}$. The *real* parameter was set to $1.088 \cdot 10^{-18} \text{ m s}^{-2} \text{ K}^{-4}$. The maximum error was $\sim 20\%$. On the other hand, the mean of $\hat{\gamma}$ is $5.7 \cdot 10^{-9} \text{ m s}^{-2}$ with a standard deviation of $4.8 \cdot 10^{-10} \text{ m s}^{-2}$. The *real* value in the simulations was $5.4 \cdot 10^{-9} \text{ m s}^{-2}$. In this case the maximum error was $\sim 25\%$. The correlation between both parameters is also shown in Figure 7.20 (bottom).

So far we have shown that the thermal feedthrough factor, α , can be estimated, in principle, accurately. Such accuracy permits to split it into two parts, one describing the radiation pressure effect (β), and the other one, describing the radiometer effect (γ). This is possible provided the absolute temperature of the walls of the EH changes $\sim 1 \text{ K}$ during the thermal experiments. The results of the simulations have confirmed this and we have assessed that the absolute displacement of the TMs when exciting them with heat pulses does not exceed in any case 100 nm , thus within the requirement of $1 \mu\text{m}$. Obviously, the Fisher matrix analysis and the simulations give an idea about the goodness in the estimation of the parameters if the model assumed for the thermal effects is correct. However, if the the outgassing effect or other unforeseen effect is present in the experiments, the estimation of the parameters will be poorer and it will be detected since the residuals of the fit (or χ^2) will be much higher than the ones shown in Figure 7.19. Hence, a new model for the thermal effects would be required.

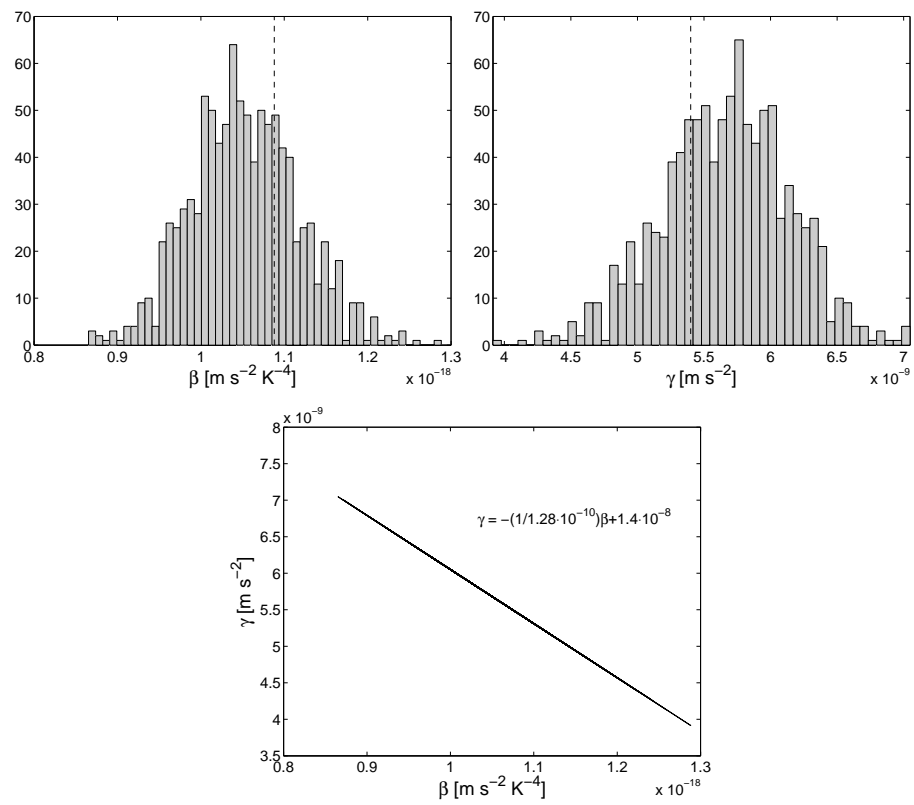


Figure 7.20: Histogram of the estimated parameters, $\hat{\beta}$ and $\hat{\gamma}$, after 1000 simulations. The correlation in the estimated parameters is shown in the bottom panel.

Chapter 8

Conclusion

In the present work we have investigated in depth the main aspects of the measurement of temperatures in LPF and the definition of suitable experiments to be performed in the gravity reference sensor of the LTP. These two issues are fundamental to characterise accurately the coupling between temperature and test mass motion and afterwards estimate the amount of noise in the LTP due to temperature fluctuations by proper noise apportioning. These functionalities (measurement and generation of temperature perturbations), like the rest of the diagnostics elements in LPF, as a technology precursor of LISA, are intended to help design a quieter environment in the LISA spacecraft. The role of the thermal diagnostics (and the rest of diagnostics) in LISA is still to be fully concreted, but they will likely work as a noise debugging tool which will provide house-keeping data and assist in future gravitational wave signal dig-out. In view of this, during this work we also have investigated different issues in order to deal with the requirements for LISA which, although still vague, can be assumed to be one order of magnitude more demanding both in noise amplitude and in frequency range than those set for LPF. In the following we review the most relevant results of the investigations appearing during the development and validation of the thermal diagnostic subsystem.

The first task, for obvious reasons, is the definition of the functionality and the performance required for the thermal diagnostic subsystem, e.g., maximum permitted noise, frequency band, number of measurements needed, temperature range of operation, etc. These requirements are a direct consequence of the foreseen thermal effects that can disturb the main subsystems of the LTP: the gravitational reference sensor and the optical metrology system. Both systems are sensitive to temperature for different reasons. The effects on the GRS cause real motion of the test masses due to radiation pressure or the radiometer effect, while the OMS is affected by the temperature causing changes of index of refraction and causing dilatation (and contraction) of optical elements, hence pathlength variations which, in turn, translate into an error in the measurement of the displacements of the test masses. Thermal effects have been tentatively quantified, and the thermally sensitive points have been identified. As a result, the requirements on the thermal diagnostic subsystem appear naturally. On the one hand, the system must be able to measure fluctuations of very low amplitude, below $10^{-4} \text{ K Hz}^{-1/2}$, in the frequency band of the milli-Hertz, in a temperature range between 10°C and 30°C with a total number of measurements of 32. On the other hand, the system must be capable of applying controlled thermal perturbations at specific spots in the LTP by means of heaters, which will be useful to estimate the transfer functions between temperature and acceleration.

The design and the validation of a temperature measurement system exhibiting noise levels of $10^{-5} \text{ K Hz}^{-1/2}$ for $f \geq 1 \text{ mHz}$ and at room temperature has been one of the nuclear aspects of the study. The requirement for the noise in the measurement is a direct consequence of the expected fluctuations in the LTP, $10^{-4} \text{ K Hz}^{-1/2}$. In addition, restrictions of different kinds, such as availability of space qualified components, electrical power, connection limitations, etc., have

had to be taken into consideration. The system proposed to cope with such requirements and constraints consisted in a Wheatstone bridge with a temperature sensor in it and the use of the lock-in amplification technique in order to avoid $1/f$ noise during the amplification of the signal. The temperature sensors initially considered were NTC thermistors and platinum RTDs. The RTDs were discarded due to their insufficient sensitivity. The only possible option was the use of thermistors because of their *high* sensitivity profile. However, thermistors are of semiconductor nature and their stability and noise performance at low frequency needed specific assessment. The different test campaigns confirmed their usability.

The prototype was designed to meet the requirements. The theoretical noise analysis showed that the noise levels of the system should be around $6 \cdot 10^{-6} \text{ K Hz}^{-1/2}$ in the MBW. Obviously, prior to their implementation in the engineering model of the DMU and, later on, in the flight model, the performance of the prototype was tested. The validation of the temperature measurement subsystem (electronics chain plus thermistors) was not a trivial task. The concept of the test consisted in isolating the temperature sensors from ambient temperature fluctuations and, thus, measure only electronic noise. The required stability was set to $10^{-6} \text{ K Hz}^{-1/2}$ at 1 mHz. Such stability is not available in standard climatic chambers, therefore, an insulator designed *ad hoc* for the test was needed.

Once the insulator jig and the temperature measurement system were in place, the first test campaign was done. The results were in very good agreement with the theoretical predictions calculated with the noise models of the electronic components. One important result from these tests was the assessment of the noise model of the thermistor. The thermistor was considered, *a priori*, as a pure resistive element and, thus, it was modelled as a Johnson noise source. Such hypothesis was validated during this test. However, noise in the LTP MBW was detected when measuring *drifting* temperatures. Temperature slopes higher than $0.4\text{-}0.5 \mu\text{K s}^{-1}$ were sufficient to deteriorate the performance of the measurement. The source of this effect was identified: the non-ideal transfer curve of the 16-bit analog-to-digital converter. In principle this effect should not limit the measurements in the LTP: (i) the differential measurements (of interest in the GRS) are free of this problem since they exhibit very low temperature slopes and, (ii) the absolute temperature in the LTP (absolute measurements are of interest, specially, for the OMS components) should exhibit slopes lower than $0.4\text{-}0.5 \mu\text{K s}^{-1}$. At this moment, the temperature measurement subsystem was ready to be implemented by NTE¹ in the engineering model of the DMU and, afterwards, in the flight model. The system was exactly the same with slight variations due to space component constraints. The EM and FM systems were also put to test. Both systems exhibited identical results to those obtained with the prototype system. However, during the tests another unforeseen effect was detected which required further investigations. Four of the 24 thermistor used during the EM and FM tests campaigns revealed unacceptable levels of noise for our purposes. The origin of such noise could not be determined with certainty. After discarding several possibilities, the only plausible hypothesis was that they came *damaged* from the manufacturer due to the fabrication process itself, or due to the tests that the space qualification process requires. In any case, an important conclusion emerged from this fact: a screening process is mandatory not to install *non-compliant* sensors in the LTP.

With an eye on LISA, a set of investigations in order to achieve a measurement system more robust and exhibiting lower levels of noise was performed. First the same system designed for the LTP was put under test at the frequency range of LISA, i.e., at 0.1 mHz. This investigation required the design of an improved test bed. At 0.1 mHz a passive insulator like the one constructed for the LTP measurement bandwidth tests became inefficient. The only realistic solution to reach a stability of $10^{-6} \text{ K Hz}^{-1/2}$ at 0.1 mHz was the use of a combination of a passive insulator together with an active temperature control. This was the adopted solution to perform meaningful tests: the passive insulator was the one constructed for the tests in the LTP MBW whereas the active control was based on a feedback-feedforward scheme. The results of this test campaign revealed

¹The LTP Spanish contractor industry.

that no $1/f$ noise is present in the thermistors nor in any other component of the measurement chain down to 0.1 mHz and $10^{-5} \text{ K Hz}^{-1/2}$, provided the temperature slope is kept close to zero. From here we assessed that the temperature fluctuations in the LTP, and concluded they can be reliably measured even at frequencies of 0.1 mHz, which is very interesting for debugging systems in view of LISA.

An effect that can limit the measurement of temperature in the LISA measurement bandwidth is the non-ideal analog-to-digital converter. At 0.1 mHz the effect of the non-idealities of the ADC is much more important than at 1 mHz. Investigations focused on the mitigation of this problem have been also done. The method used was based on the so-called *dithering* technique which, in a word, consists in injecting specific signals (or noise) out of band to reduce the effect of the non-ideal transfer curve of the ADC. The results obtained were satisfactory and this solution can be easily implemented in the same measurement system designed for the LTP. Finally, investigations on the reduction of the floor noise of the measurements were done. The minimum noise levels that can be achieved when measuring with the system developed in this work are in the order of $10^{-6} \text{ K Hz}^{-1/2}$. Lower noise levels are not feasible due to counterproductive effects related to the self-heating effect when trying to reduce the noise by increasing the power dissipated in the thermistor.

With respect to the temperature measurement system still two more considerations were discussed. The first one was the detection of remanent magnetic moment in the thermistors. This was of importance since eight thermistors (four as temperature sensors and four as heaters) are surrounding each test mass at a distance of 13 mm. The magnetic cleanliness required inside the GRS, i.e., in the surroundings of the test masses is very restrictive. For this reason, a magnetic characterisation of the thermistors and the evaluation of their impact on the noise acceleration was investigated. The results revealed that, under the most unfavourable conditions, the noise due to magnetic issues will be increased by $\sim 65\%$ which is still within the budgeted magnetic noise limits. Also, it was found that demagnetisation of the thermistors produces very good results. The magnetic moment can be reduced to a level which induces negligible noise in the test masses. The second consideration concerns the possible interferences that can appear in the temperature measurement. A detailed analysis of the effect of potential interferences was done. The presence of such problem cannot be confirmed until tests with the whole system are performed. Anyway, the analysis is of interest in case some unforeseen signal is detected during the final tests in the satellite.

Aside from the issues related to the measurement system, we also focused on different aspects of the thermal experiments to be carried out in the GRS during the mission. The next step was the definition of the proper signals to be applied in the GRS. The study focused on the possibility of discerning the different thermal effects prevailing in the GRS. A theoretical analysis based on the calculation of the Fisher matrix and the Cramér-Rao bound was performed. The results were promising although some simplifications (with an optimistic bias) were done. In order to assess these results a simplified model of the x -axis dynamics of the LTP was implemented in Simulink. The simplifications used for the Fisher matrix and the Cramér-Rao bound calculations were considered. The results confirmed the previous analysis, i.e., the radiation pressure and the radiometer effect can be distinguished by proper thermal excitation. Therefore, simulations validated, momentarily, the heaters activation scheme defined during the Cramér-Rao bound analysis. However, it is important to note that the definition of the heaters activation scheme was based on the simulations performed with thermal model provided by CGS. The thermal model was used to estimate the evolution of temperature when dissipating power in the heaters of the EH walls and it is not very unlikely that the actual response of the system varies to some extent from the one obtained with the model. In consequence, the power or activation scheme might differ from the one presented here in order to achieve the temperature profile proposed during this study, which should not change.

The most significant outcomes presented in the thesis are summarised in the following items:

1. The definition of the temperature measurement subsystem (TMS) requirements in view of the foreseen thermal effects in LPF. The figure of merit of the TMS is the noise equivalent temperature levels which must be below $10^{-5} \text{ K Hz}^{-1/2}$ in the LTP MBW (between 1 mHz and 30 mHz).
2. The design of the TMS and the selection of the appropriate temperature sensor. The designed electronics are based in a Wheatstone bridge together with the lock-in amplification technique. The chosen temperature sensors are NTC thermistors of nominal resistance of $10 \text{ k}\Omega$ since we have shown that they are suitable for low-frequency high-sensitivity measurements.
3. The design and construction of a test bed suitable for the validation of the TMS. Such test bed has consisted in constructing an insulator able to keep the temperature fluctuations lower than $10^{-6} \text{ K Hz}^{-1/2}$ in the LTP MBW.
4. The tests of the prototype TMS, the engineering model TMS and the flight model system. The results of the tests were satisfactory, i.e., the system exhibited noise levels of $10^{-5} \text{ K Hz}^{-1/2}$ in the LTP MBW. However, two unexpected sources of noise were detected:
 - non-uniform performance of the thermistor's batch. Some of the thermistors are noisier than others and thus, a screening process is required to choose only the ones working OK,
 - excess noise at low-frequency when measuring *drifting* temperatures. The source of this noise was identified: the non-ideal transfer curve of the ADC. A detailed analysis of this effect on the TMS has been presented together with a method to mitigate it.
5. The assessment of the compatibility of the thermistors with the magnetic cleanliness required in the surroundings of the TMs.
6. Thermal experiments to be performed in-flight in the GRS have been proposed. Such experiments should be able to determine the coupling between temperature fluctuations and TMs acceleration.
7. In view of LISA, the TMS has been also put to test at the sub-milli Hertz range (0.1 mHz). We have shown that the noise of the TMS is kept white at such frequencies and with an amplitude of $10^{-5} \text{ K Hz}^{-1/2}$. We have also explored the possibility of reducing the floor noise of the system: levels of $10^{-6} \text{ K Hz}^{-1/2}$ at 1 mHz has been achieved.

Appendix A

Temperature coefficient and uncertainty analysis

This appendix details the analysis of the temperature coefficient and the uncertainty of the TMS. A worst-case condition analysis has been performed for all the stages of the measurement chain. It is of special interest the temperature coefficient: its value limits the maximum permitted temperature fluctuations in the electronics not to degrade the measurement. The uncertainty is not so important since we are interested in relative changes of temperature and not in very accurate absolute temperature measurements. However, it is also presented for completeness.

A.1 Voltage level adaption

The first stage of the electronics is the voltage applied to the Wheatstone bridge. The reference voltage used is the one of the ADC. The needed voltage is 0.63 V. The voltage reference of the ADC is, though, 2.5 V, hence, a voltage divider is needed. The voltage level adaption consists of a voltage follower (to avoid loading effects) and a voltage divider. Figure A.1 shows the voltage level adaption stage.

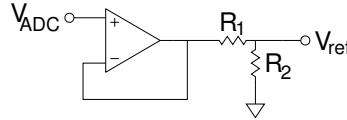


Figure A.1: Voltage level adaption stage. The output voltage feeds the Wheatstone bridge.

The following sections determine the temperature coefficient (TC) and uncertainty introduced by the voltage follower and the voltage divider.

A.1.1 Voltage follower

The uncertainty caused by the voltage follower is due to the finite open-loop gain, A_d , and the common-mode rejection ratio, $CMRR$, of the operational amplifier (OA). The model used is shown in Figure A.2 and the expression for the uncertainty is (in units of Volt)

$$\epsilon_1 \simeq V_b \left(\frac{1}{|CMRR|} + \frac{1}{|A_d|} \right) \Delta R_b \quad (\text{A.1})$$

where V_b is voltage of the Wheatstone bridge and¹

$$\Delta R_b = \frac{R_{NTC}}{R + R_{NTC}} - \frac{R_{ref}}{R + R_{ref}}. \quad (\text{A.2})$$

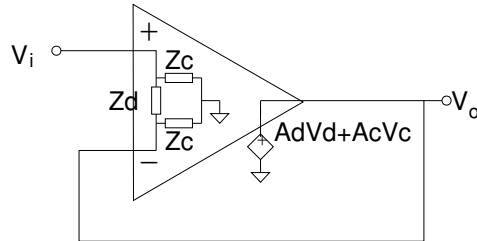


Figure A.2: Equivalent circuit used to analyse the TC and the uncertainty in the voltage follower.

The OA used is an OP-07 of Analog Devices. The error for different temperatures is shown in Figure A.3.

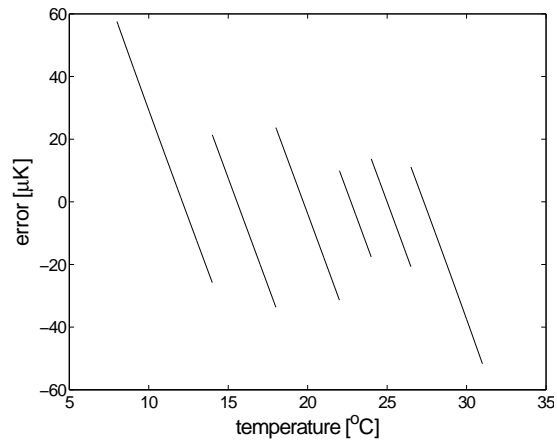


Figure A.3: Uncertainty in temperature due to the voltage follower (finite open-loop gain and $CMRR$ of the operational amplifier).

¹This expression is valid for the rest of the chapter.

A.1.2 Voltage divider

The voltage divider circuit is given in Figure A.4.

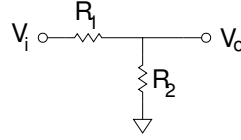


Figure A.4: Voltage divider circuit.

The resistors of the voltage divider have a tolerance specified by the manufacturer, tol . When analysing the circuit assuming the worst-case condition, i.e., $R_1 = R(1 - tol)$ and $R_2 = R(1 + tol)$, the expression for the uncertainty is

$$\begin{aligned} \epsilon_2 &= 2V_{\text{ADC}} \left[\frac{R_2(1 + tol)}{R_1(1 - tol) + R_2(1 + tol)} - \frac{R_2}{R_1 + R_2} \right] \Delta R_b \\ &\simeq 2V_{\text{ADC}} \left[\frac{2R_1 R_2}{(R_1 + R_2)^2} \right] tol \Delta R_b. \end{aligned} \quad (\text{A.3})$$

Figure A.5 (left) shows the uncertainty caused by the voltage divider. The values used are: $R_1=7\text{ k}\Omega$, $R_2=1.120\text{ k}\Omega$ and $tol=0.01\%$. *Mutatis mutandi*, we obtain the expression for the temperature coefficient in units of V K^{-1} , i.e.,

$$\epsilon_{\text{TC},2} \simeq 2V_{\text{ADC}} \left[\frac{2R_1 R_2}{(R_1 + R_2)^2} \right] \alpha \Delta R_b \quad (\text{A.4})$$

where α ($= 0.6\text{ ppm K}^{-1}$) is the TC of the resistors. Figure A.5 (right) shows the TC of this stage.

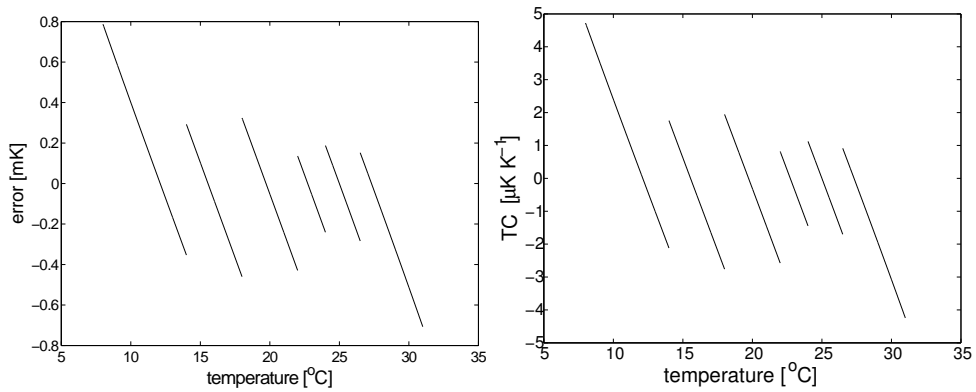


Figure A.5: Effect of the tolerance and TC of the resistors forming the voltage divider. Left: uncertainty. Right: temperature coefficient.

A.2 Drive bridge circuit

The drive bridge circuit generates the square wave signal used to excite the Wheatstone bridge. The circuit is shown in Figure A.6.

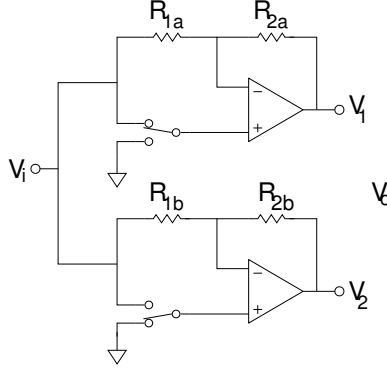


Figure A.6: Drive bridge circuit.

The output voltage for each polarity is

$$V_{o+} = V_{o1} - V_{o2} = V_{\text{ref}} \left(1 + \frac{R_{2b}}{R_{1b}} \right), \quad (\text{A.5a})$$

$$V_{o-} = V_{o1} - V_{o2} = -V_{\text{ref}} \left(1 + \frac{R_{2a}}{R_{1a}} \right) \quad (\text{A.5b})$$

and the final output is the average difference, or

$$V_o = \frac{V_{o+} - V_{o-}}{2} = \frac{V_{\text{ref}}}{2} \left(2 + \frac{R_{2b}}{R_{1b}} + \frac{R_{2a}}{R_{1a}} \right). \quad (\text{A.6})$$

Ideally, $R_{2b}/R_{1b} = R_{2a}/R_{1a} = 1$. However, due to non-idealities of the OAs and tolerance of the resistors, the values can be slightly different, and thus introduce a gain error in the measurement. The effect of the resistors and the OAs in this stage are analysed in the following sections.

A.2.1 Resistors

The tolerance of the drive bridge circuit resistors causes a gain error in the measurement. Assuming the worst case and taking into account that $R_{1a} = R_{2a} = R_{1b} = R_{2b}$ we find:

$$\epsilon_3 = V_b \left(\frac{1}{1 - \text{tol}} \right) \simeq V_b \text{tol} \Delta R_b \quad (\text{A.7})$$

where tol is the tolerance of the resistors specified by the manufacturer. Likewise, the temperature coefficient, α , of the resistors results in (in V K^{-1})

$$\epsilon_{\text{TC},3} \simeq V_b \alpha \Delta R_b. \quad (\text{A.8})$$

The uncertainty and the TC of this stage are shown in Figure A.7.

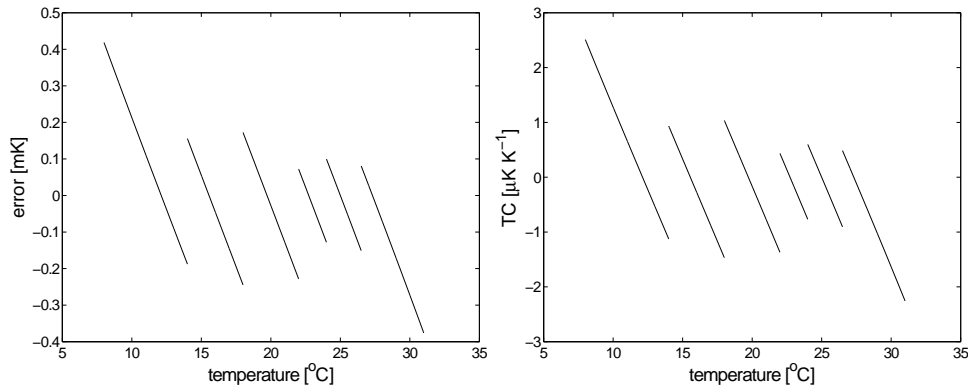


Figure A.7: Uncertainty and temperature coefficient due to the resistors (of 10 kΩ) of the drive bridge circuit. The tolerance is 0.01% and $\alpha=0.6 \text{ ppm K}^{-1}$.

A.2.2 Operational amplifiers

The finite open-loop gain, A_d , and the $CMRR$ of the OAs in the drive bridge circuit cause, also, a gain error in the measurement. After the averaged difference measurement the uncertainty is

$$\epsilon_4 = \frac{V_b}{2}(e_{\text{no-inv}} + e_{\text{inv}})\Delta R_b \quad (\text{A.9})$$

where $e_{\text{no-inv}}$ and e_{inv} are the errors in the non-inverting and inverting configuration —see Figure A.8.

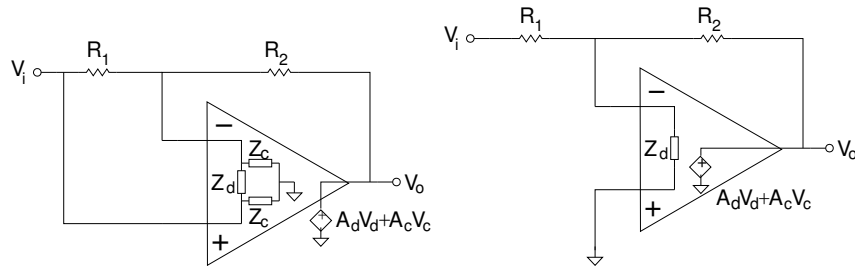


Figure A.8: Left: non-inverter operational amplifier circuit model. Right: inverter operational amplifier circuit model.

From these models the uncertainty due to the open-loop gain and the $CMRR$ is (assuming in both cases $R_1 = R_2 = R$ and $Z_d \gg R$)

$$e_{\text{inv}} = \frac{1}{1 + \frac{A_d R}{2 + \frac{R}{Z_d}}} \simeq \frac{2}{A_d}, \quad (\text{A.10a})$$

$$e_{\text{no-inv}} = 2 \left(\frac{1}{|CMRR|} + \frac{1}{|A_d|} \right) + \frac{R}{Z_c}. \quad (\text{A.10b})$$

The values obtained are shown in Figure A.9 for an OP-177F with $A_{d0} = 5 \cdot 10^6$ (min. value), $CMRR_0=315000$ (min. value), $Z_{c0}=200 \text{ G}\Omega$ (typ. value) and $R=10 \text{ k}\Omega$.

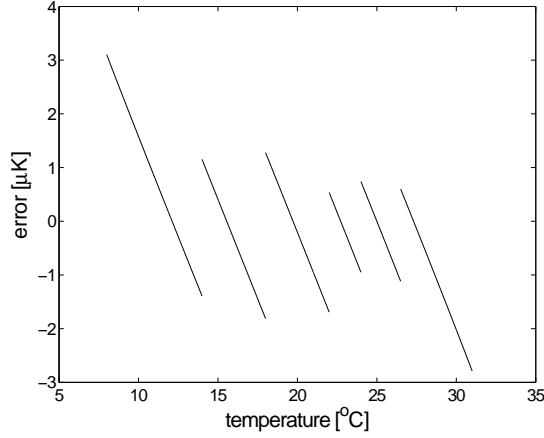


Figure A.9: Uncertainty due to the finite open-loop gain and $CMRR$ of the OAs.

A.3 Wheatstone bridge

The uncertainty in this stage comes from: (i) the zero error due to the tolerance of the resistors (tol) and, (ii) the temperature coefficient, α , of the resistors. The Wheatstone bridge is formed of two resistors of $10\text{ k}\Omega$ and one variable resistor, R_{ref} . Assuming the worst-case condition the zero error is

$$\begin{aligned}
 \epsilon_5(T) &= V_b \left[\frac{2RR_{\text{ref}}tol}{(R + R_{\text{ref}})[R(1 + tol) + R_{\text{ref}}(1 - tol)]} + \right. \\
 &\quad \left. + R_{\text{NTC}}(T) \left(\frac{1}{R(1 - tol) + R_{\text{NTC}}(T)} - \frac{1}{R_{\text{NTC}} + R} \right) \right] \\
 &\simeq V_b R \left[\frac{2R_{\text{ref}}}{(R + R_{\text{ref}})^2} + \frac{R_{\text{NTC}}(T)}{[R + R_{\text{NTC}}(T)]^2} \right] tol
 \end{aligned} \tag{A.11}$$

and likewise the temperature coefficient, i.e.,

$$\epsilon_{\text{TC},5}(T) \simeq V_b R \left[\frac{2R_{\text{ref}}}{(R + R_{\text{ref}})^2} + \frac{R_{\text{NTC}}(T)}{[R + R_{\text{NTC}}(T)]^2} \right] \alpha. \tag{A.12}$$

The uncertainty and TC of this stage is shown in Figure A.10 for $tol=0.01\%$ and $\alpha=0.6\text{ ppm K}^{-1}$.

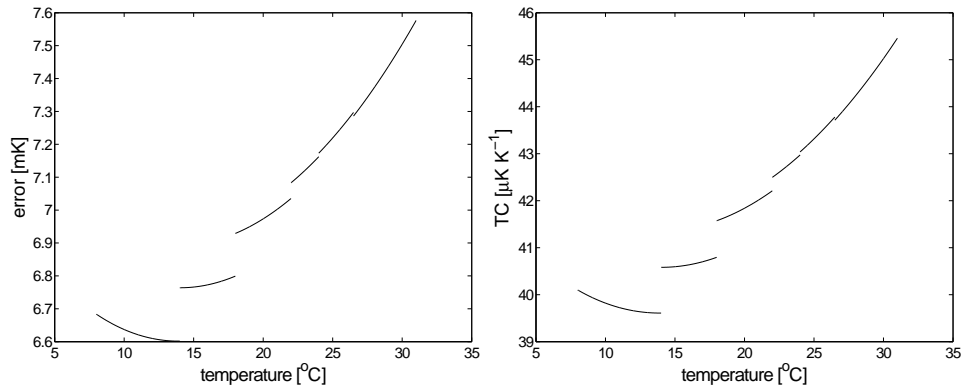


Figure A.10: Effects related with the tolerance and TC of the resistors in the Wheatstone bridge. Left: zero error. Right: temperature coefficient.

A.4 2-wire configuration

Temperature measurement is done by using the 2-wire configuration —see Figure A.11.

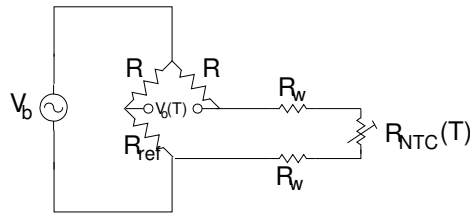


Figure A.11: 2-wire configuration circuit.

The error due to this configuration is

$$\epsilon_6 = V_b \frac{2RR_w(1 + \alpha_w \Delta T_w)}{[R + R_{NTC}][R + R_{NTC} + 2R_w(1 + \alpha_w \Delta T_w)]}. \quad (\text{A.13})$$

Assuming 24 AWG copper wire ($84.1976 \Omega \text{ km}^{-1}$ and $\alpha_w = 0.00393 \text{ K}^{-1}$) and a length of 5 m per cable, the resultant R_w is 0.042Ω . Substituting into Eq. (A.13) we obtain the results shown in Figure A.12 (assuming $\Delta T_w \rightarrow 0$ since the error due to the temperature coefficient of the copper wire is considered negligible).

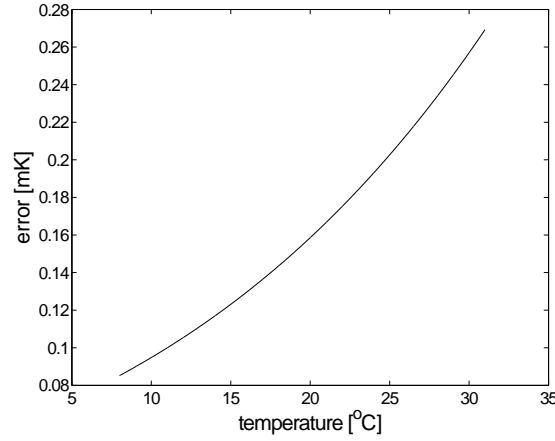


Figure A.12: Errors in the measurement due to the 2-wire configuration.

A.5 Multiplexers

The multiplexers+IA equivalent circuit is given in Figure A.13. R_{ON} mismatch is important for differential signals. Each channel resistance forms a voltage divider with load's common-mode input impedance. This results in a limited $CMRR$ which for a worst-case condition is

$$\frac{1}{CMRR_{MUX}} = \frac{R_{ON}}{Z_c} \left(\left| \frac{\Delta Z_c}{Z_c} \right| + \left| \frac{\Delta R_{ON}}{R_{ON}} \right| \right) \simeq \frac{\Delta R_{ON}}{Z_c} \quad (\text{A.14})$$

where

$$R_{ON} \doteq \frac{R_{ON} + R'_{ON}}{2}, \quad (\text{A.15a})$$

$$\Delta R_{ON} \doteq R_{ON} - R'_{ON}. \quad (\text{A.15b})$$

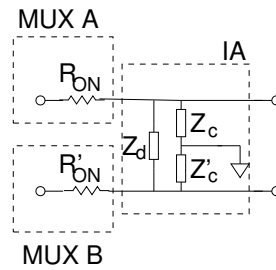


Figure A.13: Multiplexers+IA equivalent circuit. Mismatch between R_{ON} and R'_{ON} reduces the $CMRR$ of the IA.

This effect reduces the effective $CMRR$ of the instrumentation amplifier (IA) placed next to the multiplexers. The multiplexers used are DG-408 (in the prototype) with $R_{ON} = 100 \Omega$ (max. value), $\Delta R_{ON} = 15 \Omega$ (max. value) and $Z_c = 1 \text{ G}\Omega$ (AD624AD min. value). The degradation of the $CMRR$ of the IA due to this effect is analysed in the next section —see Eq. (A.17).

A.6 Instrumentation amplifier

The IA stage presents two different measurement errors: on the one hand, the offset error due to the common-mode voltage and the finite $CMRR$ and, on the other hand, the gain error due to the tolerance and temperature coefficient of the IA gain.

The difference averaged common-mode voltage at the input of the IA is

$$v_c(T) = \frac{V_b}{4} \left(\frac{R_{NTC}(T) - R}{R_{NTC}(T) + R} + \frac{R_{ref} - R}{R_{ref} + R} \right). \quad (\text{A.16})$$

The effective $CMRR$ taking into account the previous multiplexers is

$$\frac{1}{CMRR_e} = \frac{1}{CMRR_{MUX}} + \frac{1}{CMRR_{IA}} \simeq \frac{1}{CMRR_{IA}}. \quad (\text{A.17})$$

Hence, the offset error due to common-mode voltage is calculated as

$$\epsilon \simeq \frac{v_c}{CMRR_{IA}}. \quad (\text{A.18})$$

The uncertainty of this stage is given in Figure A.14 for the AD624A with $CMRR_0=10^5$ (min. value).

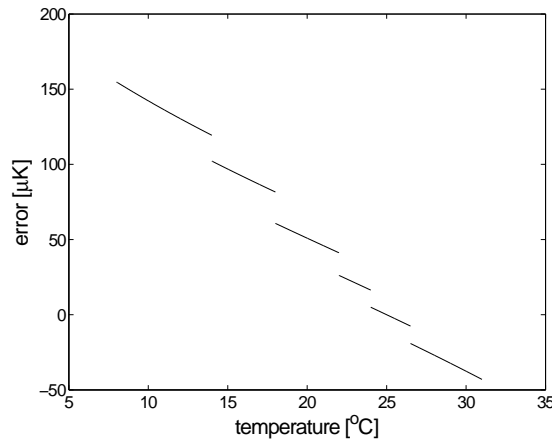


Figure A.14: Uncertainty due to the common voltage at the input of the IA and its finite $CMRR$.

The temperature coefficient of the $CMRR$, α_{CMRR} , is $\sim 550 \text{ K}^{-1}$ at room temperature. The effect on the measurement is approximated by

$$S_T^{1/2}(\omega) \simeq \frac{v_c}{CMRR_{T_0}} \alpha_{CMRR} S_{T,FEE}^{1/2}(\omega) \quad (\text{A.19})$$

where $CMRR_{T_0}$ is the $CMRR$ at 300 K which is around 10^5 , v_c is the common-mode voltage at the input of the IA —see Figure A.14— and $S_{T,FEE}^{1/2}$ are the temperature fluctuations of the electronics. Evaluation of Eq. (A.19) leads to comfortable requirements for the temperature stability required. Thus, this effect is considered negligible

The gain error referred to the input due to the gain tolerance of the IA is

$$\epsilon_7 = V_b \text{tol}_{G_{IA}} \Delta R_b. \quad (\text{A.20})$$

The values are shown in Figure A.15 (left) for the AD642A with a gain tolerance of 0.5%. In addition, the gain also depends on the temperature of the IA. The error due to the temperature coefficient is (in $V K^{-1}$)

$$\epsilon_{TC,7} = V_b \alpha_{G_{IA}} \Delta R_b \quad (A.21)$$

where $\alpha_{G_{IA}} = -3.5 \text{ ppm } K^{-1}$. Figure A.15 shows the error due to the temperature coefficient of the IA gain.

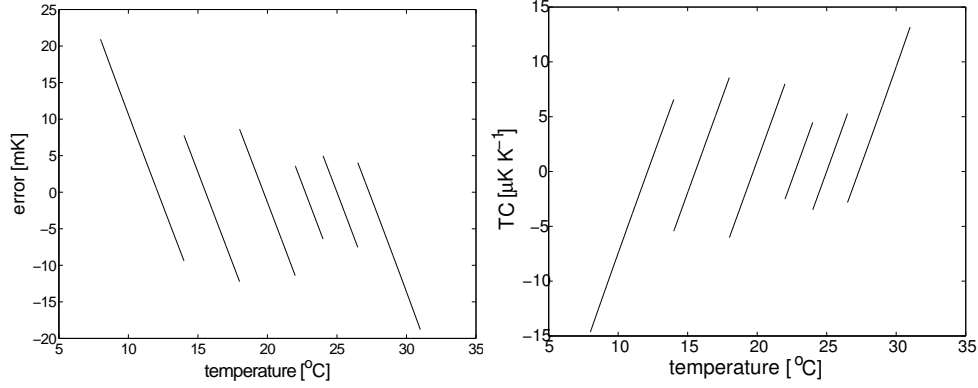


Figure A.15: Left: Errors due to the IA gain tolerance. Right: temperature coefficient of the IA stage.

A.7 Low-pass filter

The low-pass filter —see Figure A.16— causes two different errors: one due to the finite open-loop gain and $CMRR$ of the operational amplifier, and another one due to the time response of the filter itself.

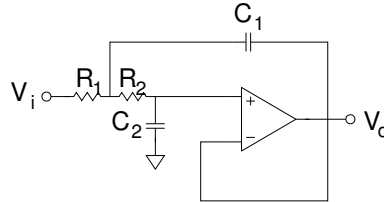


Figure A.16: Second-order Butterworth active low-pass filter circuit.

The error due to the OA referred to the input is

$$\epsilon_8 = V_b \left(\frac{1}{|CMRR|} + \frac{1}{|A_d|} + \frac{R_1 + R_2}{Z_c} \right) \Delta R_b. \quad (A.22)$$

The error values obtained are shown in Figure A.17. The OA is an OP-27GZ with $A_{d0} = 6 \cdot 10^5$ (min. value), $CMRR_0 = 10^5$ (min. value) and $Z_c = 2 \text{ G}\Omega$ (typ. value). The resistors values are $R_1 = 2.84 \text{ k}\Omega$ and $R_2 = 10.7 \text{ k}\Omega$.

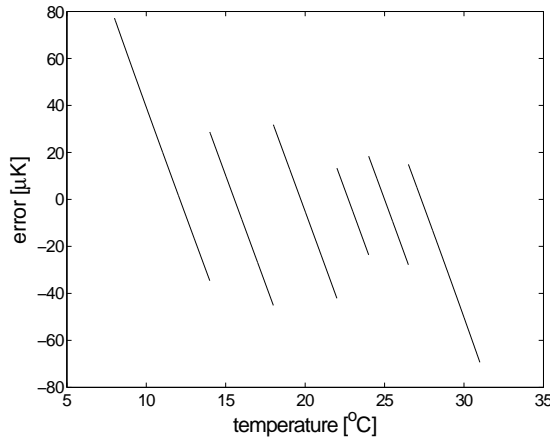


Figure A.17: Error due to the operational amplifiers non-idealities of the low-pass filter.

The settling time error is caused by the finite time response of the filter —see figure A.18. If the integration starts at $t=0$ (“start 0”) the filter transient will introduce an error in the average voltage estimation. However, if the integration starts after the filter has settled down (“start 1”), the error is minimised.

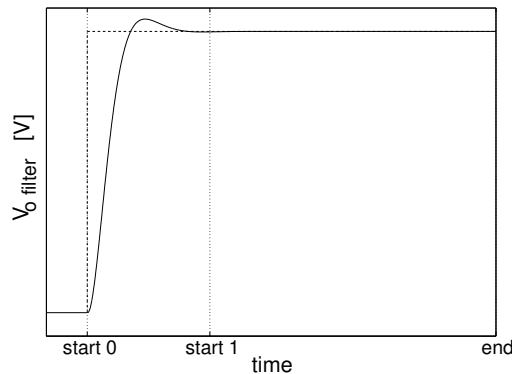


Figure A.18: Low pass filter time response. The dashed line is the ideal response. Solid trace is the real time-response of the filter.

The settling error has two terms, one due to the cross-talk (the previous voltage, V_{old} , contributes to the new sample), and the other due to the response of the new voltage (V_{new}). They are:

$$\epsilon_{c-t} = V_{\text{old}} \left[1 - \frac{U(t_{\text{end}}) - U(t_{\text{start}})}{t_{\text{end}} - t_{\text{start}}} \right], \quad (\text{A.23a})$$

$$\epsilon_{s-t} = V_{\text{new}} \left[1 - \frac{U(t_{\text{end}}) - U(t_{\text{start}})}{t_{\text{end}} - t_{\text{start}}} \right] \quad (\text{A.23b})$$

where

$$U(t) = \int_0^t u(\tau) d\tau = \tau + \frac{e^{-\frac{\tau\omega_0}{2q}}}{\omega_0 \sqrt{1 - \frac{1}{4q^2}}} \cdot \sin \left[\omega_0 \sqrt{1 - \frac{1}{4q^2}} \tau + \arcsin \left(\sqrt{1 - \frac{1}{4q^2}} \right) + \arctan \left(\sqrt{4q^2 - 1} \right) \right] \quad (\text{A.24})$$

with

$$\omega_0 = \sqrt{\frac{1}{R_1 R_2 C_1 C_2}}, \quad (\text{A.25a})$$

$$q = \omega_0 C_1 \frac{R_1 R_2}{R_1 + R_2} \quad (\text{A.25b})$$

where $R_1 = 2.84 \text{ k}\Omega$, $R_2 = 10.7 \text{ k}\Omega$, $C_1 = 100 \text{ nF}$ and $C_2 = 33 \text{ nF}$. The start and end time have been fixed to $t_{\text{start}1} = 10 \text{ ms}$ and $t_{\text{end}} = 90 \text{ ms}$ —see Figure A.18. The error obtained when using these parameters are negligible (around the pK) as shown in Figure A.19.

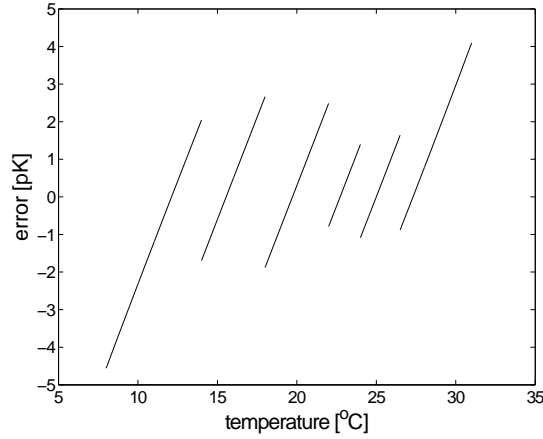


Figure A.19: Error due to the dynamic response of the LPF.

A.8 Analog-to-digital converter

The error introduced by the ADC converter is mainly due to the full scale error (includes gain and zero errors). The maximum error is 0.5% of full scale. As already mentioned, the zero error in this application is eliminated. However, we will keep this value as the maximum gain error of the ADC converter.

$$\epsilon_9 = V_b \text{tol}_{G_{\text{ADC}}} \Delta R_b. \quad (\text{A.26})$$

The error obtained is given in Figure A.20. The error due to the temperature dependence of the ADC converter gain is

$$\epsilon_{\text{TC},9} = V_b \alpha_{G_{\text{ADC}}} \Delta R_b \quad (\text{A.27})$$

where $\alpha_{G_{\text{A/D}}} = 2 \text{ ppm K}^{-1}$. Figure A.20 shows the uncertainty and TC of this stage.

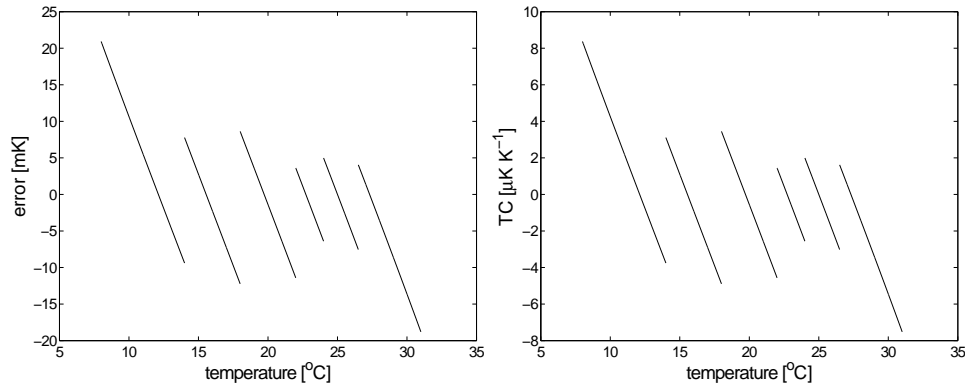


Figure A.20: Left: gain error of the ADC. Right: temperature coefficient of the ADC.

A.9 Temperature sensor

The NTC thermistor (G10K4D372—BetaTherm) tolerance given by the manufacturer is $\epsilon = \pm 0.5$ K.

A.10 TC and uncertainty of the measurement chain

A summary of the different error sources and their values is given in Table A.1.

source	gain uncertainty [K]	zero error [K]	TC [K K ⁻¹]
voltage follower	$\epsilon_1 = 8.7 \cdot 10^{-6} \Delta R_b$	—	—
voltage divider	$\epsilon_2 = 1.2 \cdot 10^{-4} \Delta R_b$	—	$\epsilon_{TC,2} = 7.1 \cdot 10^{-7} \Delta R_b$
drive b. R	$\epsilon_3 = 6.3 \cdot 10^{-5} \Delta R_b$	—	$\epsilon_{TC,3} = 3.8 \cdot 10^{-7} \Delta R_b$
drive b. OA	$\epsilon_4 = 2.3 \cdot 10^{-6} \Delta R_b$	—	—
WB	—	$\epsilon_5 = 7 \cdot 10^{-3}$	$\epsilon_{TC,5} = 42 \cdot 10^{-6}$
wires	—	$\epsilon_6 = 2 \cdot 10^{-4}$	—
CMRR IA	—	see Figure A.14	—
IA gain	$\epsilon_7 = 3.2 \cdot 10^{-3} \Delta R_b$	—	$\epsilon_{TC,7} = -2.2 \cdot 10^{-6} \Delta R_b$
LPF	$\epsilon_8 = 1.2 \cdot 10^{-5} \Delta R_b$	—	—
ADC	$\epsilon_9 = 3.2 \cdot 10^{-3} \Delta R_b$	—	$\epsilon_{TC,9} = 1.3 \cdot 10^{-6} \Delta R_b$
thermistor	—	$\epsilon_{10} = \pm 0.5$	—

Table A.1: Uncertainty sources and temperature coefficient for the different stages of the electronics involved in the temperature measurement system summary.

In order to obtain a *global* uncertainty and temperature coefficient for the temperature measurement chain we use (worst-case condition)

$$\begin{aligned}
 \epsilon_t &= \sum \epsilon_c + \sqrt{\sum \epsilon_i^2} \\
 &= \epsilon_6 + \left(\sum_{i=1, i \neq 6}^{10} \epsilon_i^2 \right)^{1/2}
 \end{aligned} \tag{A.28}$$

where subscripts c and i refer, respectively, to systematic errors with a common source and independent systematic errors. All the errors analysed in the previous sections are considered as

independent systematic errors, except for the 2-wire configuration error which must be added linearly to the other errors.

Figure A.21 (left) shows the *global* error due to all the sources of error except for the NTC thermistor uncertainty. Figure A.21 (right) shows the *global* error adding the tolerance sensor uncertainty which dominates the error.

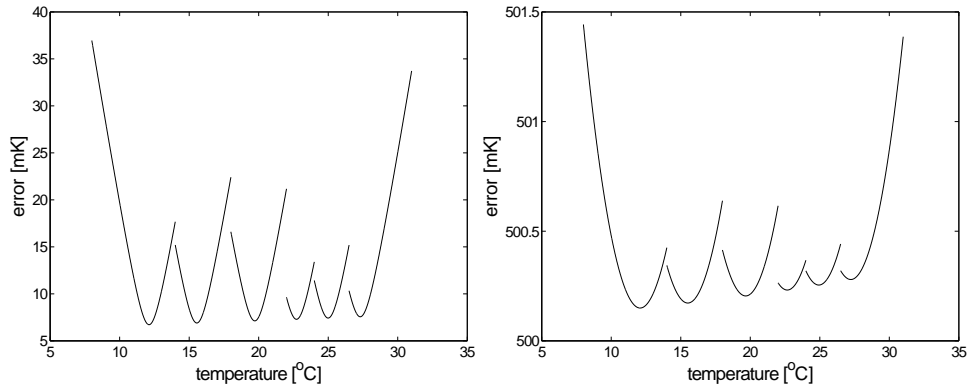


Figure A.21: Left: temperature error introduced by the electronic components. Right: temperature error introduced by the electronics plus the thermistor tolerance. The thermistor tolerance dominates the error, however, this is a systematic error that can be eliminated by proper calibration.

Finally, the *global* temperature coefficient of the FEE is given in Figure A.22 which has been calculated using Eq. (A.28): we added quadratically all the errors due to the temperature coefficient of the different stages except the one from the IA which was added linearly since its sign is known.

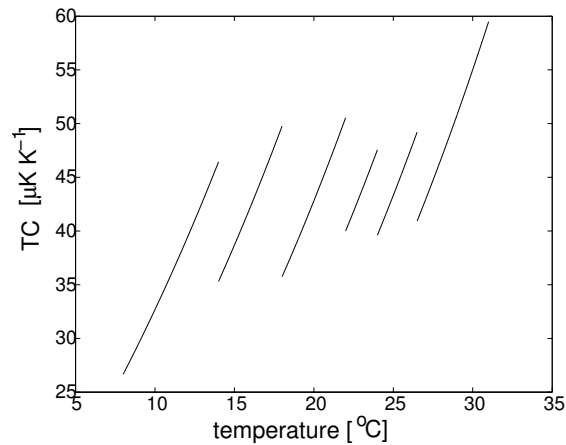


Figure A.22: *Global* temperature coefficient of the temperature measurement system.

Appendix B

Heaters in the GRS

In this appendix we analyse the possibility of using thermistors as heaters in the GRS. The function of these heaters is to produce a thermal signal that must be well above the noise background in the measuring bandwidth. Such perturbations must be measured to provide a direct construction of the temperature-TM motion transfer function. The proposed thermal experiments in the GRS are detailed in chapter §7.

The idea of using thermistors as heaters in the GRS rose up due to the difficulties of using *standard* heaters —see Figure B.1— for different reasons, such as magnetic incompatibilities (ferromagnetic materials are present in such heaters) and outgassing related problems (*rubbers* are forbidden in the GRS). On the contrary, thermistors are suitable to be placed in the GRS¹ and for that reason this technology can be used, in principle, as a heater due to its resistive properties. Nevertheless, first we have to ensure the ability of such devices to manage power of $\simeq 50$ mW (this power is a consequence of the thermal experiments defined in §7).

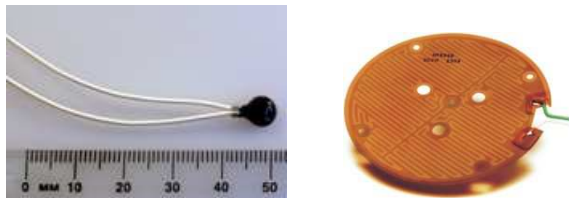


Figure B.1: Left: BetaTherm thermistor. Right: MINCO Kapton Heater (*standard* heater).

In the following sections we discuss the problems and potential errors related with using thermistors as heaters. The circuit used is based on a voltage source. As it will be shown such circuit is not the best option. However, when the impossibility of using standard heaters came up the circuit was already design. Due to the low power needed in the thermal experiments in the GRS the possibility of keeping such circuit was considered. Nevertheless, a circuit based on a current source or a circuit able to apply an independent-load power had been more appropriate.

Due to the high resistance-temperature dependence of the thermistor —cf. §2.2.2—, the electrical power applied to the sensor is not constant when applying a constant voltage [114, 121]. Mainly, the power evolution in the thermistor depends on the sensitivity of the sensor, on the thermal resistance between the sensor and the body where it is attached and, obviously, on the voltage

¹The magnetic moment of the thermistors is compatible with the required magnetic cleanliness in the GRS —see §3.1— and the outgassing effect is also within the required limits [122].

applied to the thermistor. Other factors to consider are the time constant of the system and the nominal resistance of the thermistor.

B.1 Thermistor temperature increase due to the SHE

When power is dissipated in the sensor this is not able to evacuate it all and, in consequence, the sensor starts to increase its temperature until it reaches equilibrium with the environment. The temperature rise due to this fact for a *standard* heater (with no resistance variation with temperature) is

$$\Delta T = P\theta \quad (\text{B.1})$$

where

- ΔT is the increase in temperature of the sensing element due to the self-heating effect (SHE),
- P is the electric power that heats up the heater due to the Joule effect and
- θ is the thermal resistance between the heater and the body.

However, when using thermistors the power dissipated, P , is not constant and the analysis of this effect is slightly more complicated. The thermal resistance, θ , depends on different aspects, such as the mounting, the thermal mass of the thermistor, the thermal dynamics of the environment, etc. and, also, this value is very sensitive to these factors [132, 30, 143]. Indicative values of thermal resistances are given by the thermistors' manufacturer and are shown in Table B.1.

still air	well stirred oil bath	attached to aluminium block
1000 to 2000 K W ⁻¹	125 to 142 K W ⁻¹	$\lesssim 100$ K W ⁻¹

Table B.1: Thermal resistance, θ , values given by the manufacturer (BetaTherm) for different systems and Epoxy Coated BetaTherm thermistor.

The thermistor temperature evolution determines the power dissipated in the thermistor. When voltage is supplied to the thermistor this increases its temperature and, therefore, its resistance decreases. For this reason the final power supplied to the thermistor differs from the initial one. This effect is called *power slippage* through the following sections —see Figures B.7. The factors that conditionate it are: (i) mass and heat capacitance of the thermistor and, (ii) thermal coupling between the thermistor and the body.

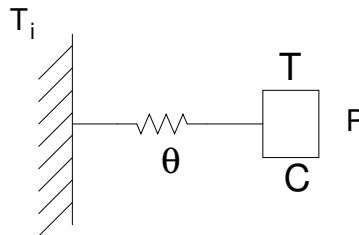


Figure B.2: First-order model for the sensor-body system.

The temperature evolution of the system can be modelled using the differential equation in (B.2) which can be inferred from Figure B.2.

$$P(T, t) = C \frac{dT(t)}{dt} + \frac{T(t) - T_i}{\theta} \quad (\text{B.2})$$

where T is the sensor temperature, T_i is the temperature of the body² and the initial temperature of the whole system, θ is the thermal resistance, C is the heat capacitance of the sensor and

$$P(T) = \frac{V^2}{R(T)}, \quad (\text{B.3})$$

and $R(T)$ is —cf. §2.2.2,

$$R(T) = R_o e^{\beta(\frac{1}{T} - \frac{1}{T_o})}. \quad (\text{B.4})$$

The solution of the first-order differential equation given in (B.2) is found by expanding $P(T)$ in a Taylor series. We first re-define Eq. (B.2) as

$$C\dot{\mu} + \frac{1}{\theta}\mu = P(\mu + T_i) \quad (\text{B.5})$$

where $\mu \equiv T(t) - T_i$ and $\mu(0) = 0$. The term $P(\mu + T_i)$ is expanded in a Taylor series, i.e.,

$$P(\mu + T_i) = F(\mu) = P_i + P'_i\mu + \frac{1}{2}P''_i\mu^2 + \dots \quad (\text{B.6})$$

where $P_i = P(T = T_i)$, $P'_i = \partial P_i / \partial T|_{T=T_i}$ and so on.

Figure B.3 shows the difference between the approximation of $P(T)$ at first-order and at second-order with respect to the exact function. The first-order approximation (solid trace) is only valid when μ (the temperature increase of the thermistor) is lower than ~ 20 K. The second-order approximation is accurate up to $\mu \sim 80$ K. From these results we conclude that the first-order approximation is adequate for our purpose since the increase of temperature will be small due to the low power dissipated in the heaters (~ 50 mW).

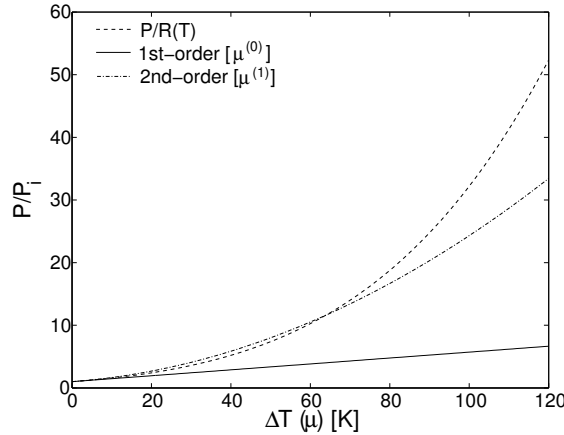


Figure B.3: Comparison between the function $P(T)$ and the Taylor series approximations (first- and second-order).

The solution of Eq. (B.5) with $P(\mu + T_i) = P_i + P'_i\mu$ (first-order approximation) and $\mu(0) = 0$ is

$$\mu^{(0)}(t) = \frac{P_i}{aC}(1 - e^{-at}) \quad (\text{B.7})$$

²The temperature of the body is assumed constant due to its large heat capacitance and for small times. Obviously, the purpose of the heaters is to change the temperature of the body but this is assumed to be very slow in comparison with thermistor response.

with

$$a = \frac{1}{C} \left(\frac{1}{\theta} - P'_i \right) \quad (\text{B.8})$$

where

$$P'_i = P_i \frac{\beta}{T_i^2}, \quad (\text{B.9})$$

The parameter a in Eq. (B.8) can be negative. If so the temperature of the thermistor will increase exponentially and will not reach a steady-state. In practise, if this happens, the thermistor will be damaged by an excess of current through it which will be limited by the power supply. Therefore, the maximum initial power permitted when using a voltage source not to damage the sensor is

$$P_i < \frac{T_i^2}{\beta\theta} \longrightarrow V < T_i \left(\frac{R_i}{\beta\theta} \right)^{1/2}. \quad (\text{B.10})$$

In normal conditions, i.e., at $T=300\text{ K}$, $\beta=3694\text{ K}$ and $\theta < 200\text{ K W}^{-1}$ (in a worst-case), the power must be lower than 120 mW in order to keep the temperature of the sensor within safe values. Actually, tests have result on thermistor failure when applying $\sim 14\text{ V}$ to $2\text{ k}\Omega$ thermistor with a current limitation of 1 A and with $\theta=130\text{ K W}^{-1}$ and $T_i = 300\text{ K}$: the resistance of the sensor decreased at such level that the current through it reached 1 A . As stated previously the power needed in the GRS thermal experiments is no more than 50 mW which is well below the 120 mW limit.

The thermal resistance, θ , is the only unknown parameter in order to determine the final power in thermistor as a function of the initial power. Moreover, the knowledge of this parameter is also important for other issues related with low noise temperature measurements as it has been stated in §4.1.3 and §6.2. Using Eq. (B.7) together with adequate measurements we can estimate the value of the thermal resistance of the thermistor-body system:

$$\theta = \frac{T_i^2 \mu_{t \gg \tau}}{P_i (T_i^2 + \beta \mu_{t \gg \tau})}, \quad (\text{B.11})$$

where $\mu_{t \gg \tau}$ stands for the increase of the thermistor temperature once the system is in steady-state. All the variables in Eq. (B.11) can be measured, thus, the thermal resistance can be estimated.

Once the thermal resistance is known, the power slippage when applying a constant voltage to the sensor can be estimated using Eq. (B.12). This equation gives the relationship between the initial power, P_i , and the final power, P_f . Therefore, it can be used to calculate the required initial power to reach the desired final power in steady-state. This equation is plotted in Figure B.4 for $\theta=100\text{ K W}^{-1}$ and $T_i=300\text{ K}$. The final power when using a voltage source increases exponentially with the initial power:

$$P_f = P_i e^{\beta \left(\frac{P_i \theta}{P_i \theta (T_i - \beta) + T_i^2} \right)}, \quad (\text{B.12})$$

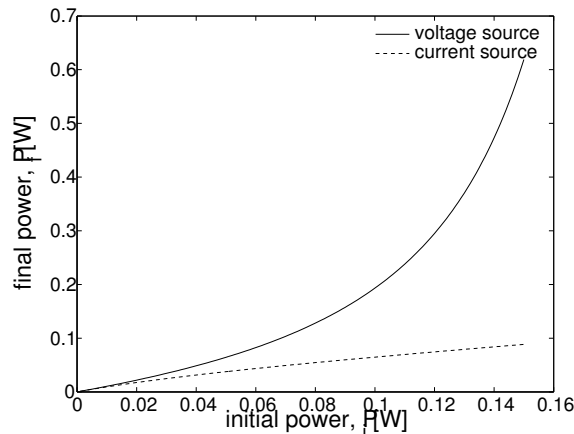


Figure B.4: Final power as a function of the initial power for a voltage and current source (plotted for comparison). Values used are: $T_i=300$ K, $\theta=100$ K W $^{-1}$ and $\beta=3694$ K. When using a voltage source the final power is always higher than the initial one whereas when using a current source occurs the contrary. For this reason when using a current source the final power is always bounded, however, when using a voltage source the system can become unstable which in practise means damaging of the thermistor.

The calculation of the initial power required to reach a concrete final power demands good knowledge of the temperature of the system and of the thermal resistance between the sensor and the body. Uncertainty in the temperature, T_i , and in the thermal resistance, θ , translate into deviations of the desired final power. Such deviations (or errors) are shown in Figure B.5. On one hand, the errors in the power due to uncertainty in the thermal resistance are quite small, for instance, 50% error in θ translates into $\sim 10\%$ error in the final power. On the other hand, the errors in T_i appear in an important manner in the final power deviation: 3% error in the determination of the initial temperature is equivalent to an error of the $\sim 50\%$ in the final power. The errors shown in Figure B.5 have been calculated assuming the desired final power, P_f , is 45 mW and the thermistors are of 2 k Ω .

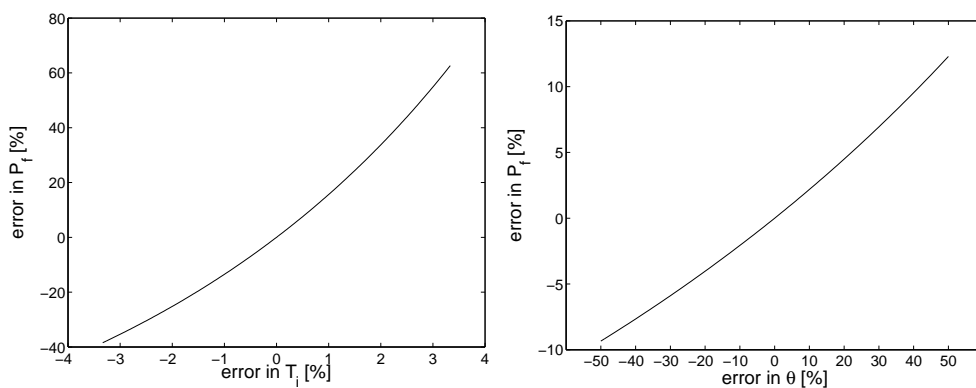


Figure B.5: Left: error in the final power dissipated due to initial temperature uncertainty. Right: *idem* for uncertainty in the thermal resistance. Values used for the calculations are: $P_f=45$ mW, $T_i=300$ K, $\theta=100$ K W $^{-1}$, $R_o=2$ k Ω and $\beta=3694$ K.

The next step is the selection of the proper nominal resistance of the thermistor. The available voltage in the DAU is 10 V, thus, in order to dissipate the needed power, the nominal resistance cannot be chosen arbitrarily. Figure B.6 shows the required voltage using a 10 k Ω and a 2 k Ω NTCs to reach 45 mW in steady-state for different initial temperatures, the thermal resistance value used is 100 K W⁻¹. It is clear that 10 k Ω thermistors must be discarded and that the 2 k Ω NTCs are suitable for our purpose although for $T < 15^\circ\text{C}$ the available voltage is not sufficient and, thus, the dissipated power will be slightly lower than the desired.

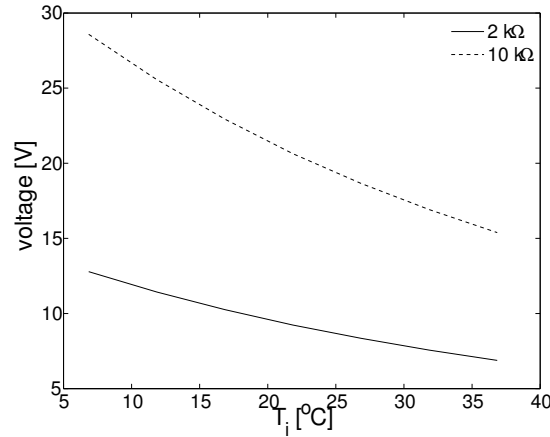


Figure B.6: Voltage needed to reach 45 mW in steady-state for different temperatures and for two different thermistors: 2 k Ω and 10 k Ω ; $\theta = 100 \text{ K W}^{-1}$. The voltage available in the DAU is 10 V.

Finally, another aspect to take into account is the time constant of the sensor. It is from 100 ms to few seconds depending on test conditions. We have found that the thermal constant when attaching a thermistor to an aluminium block by means of thermal grease is lower than 3-4 s —see Figure B.7. Nevertheless, this value depends on how the sensor is attached, increasing with the thermal resistance, θ [$\tau = 1/a$ —see Eq. (B.8)]. The time constant of the system is not a problem at all since the proposed thermal experiments in the GRS involve heat pulses of 500–1000 s, thus, a transient response of a few seconds is negligible.

Tests were done to assess the validity of the previous analysis. Thermistors were attached to an aluminium block and covered with an insulating material. Different voltage levels were applied to them while the current through the thermistors was measured. Figure B.7 shows the results for $V=10 \text{ V}$ (top), and $V=5 \text{ V}$ (bottom) The panel in the left represents the increase of temperature during the test, $\mu (= T_f - T_i)$, while the panel in the right stands for the power dissipated in the thermistor. See caption for details.

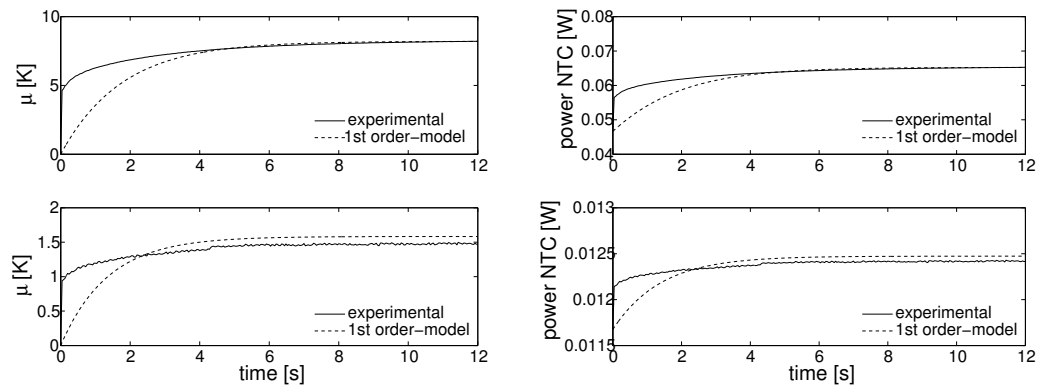


Figure B.7: Thermistor response for a voltage input of 10 V (plots in the top) and 5 V (plots in the bottom). The thermal resistance was estimated using Eq. (B.11). The value obtained was $\theta=100 \text{ K W}^{-1}$. The theoretical response was calculated using Eq. (B.7) considering $C=0.01 \text{ J K}^{-1}$ and $T_i=23^\circ\text{C}$. The power in both tests is low: 50 mW for the 10 V test and 10 mW for the 5 V, thus, the first order approximation is appropriate — Eq. (B.7). The experimental results and the theoretical calculation are in agreement in the steady state, however, they differ in the transient region. This happens due to the simplicity of the model —see Figure B.2— that only considers a time constant for the whole system whereas the actual system has, at least, two time constant: one related to the thermistor chip which exhibits a very fast response (milli-seconds) and the other one related with the thermistor encapsulation, contact, environment, etc. The analysis of the system considering both responses is presented in §B.2.

B.2 Second-order model for the thermistor response

Figure B.7 shows that the first-order model represented in Figure B.2 does not reproduce accurately the thermistor temperature response at short times since it considers only one time constant whereas at least two are present in the system: the one of the thermistor chip itself and the one related to the encapsulation, contact, etc. —see Figure 4.3 in §4.1.3. The system is more accurately modelled by a second-order system —see Figure B.8. In this model θ_1 and C_1 stand for the thermal resistance and specific heat of the chip of the thermistor and θ_2 and C_2 are the same for the encapsulation of the sensor, the contact, etc.

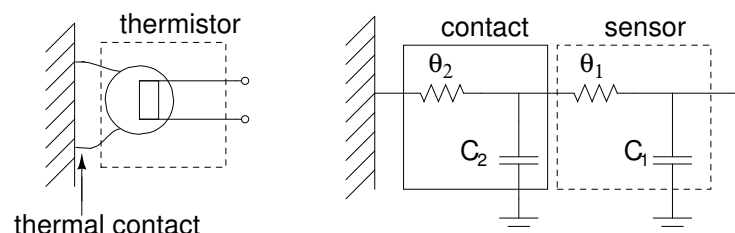


Figure B.8: Left: Physical system scheme: body-contact-thermistor (dimensions exaggerated). Right: Equivalent second-order model of the system.

The differential equation describing the temperature of the thermistor chip (the one that changes

its resistance with temperature) using the second-order model shown in Figure B.8 is³

$$\ddot{\mu} + \frac{b}{a}\dot{\mu} + \frac{c}{a}\mu = P_1\frac{d}{a} \quad (\text{B.13})$$

where $\mu = T - T_i$ and

$$a = \theta_1 C_1 C_2, \quad (\text{B.14a})$$

$$b = C_1(1 + \theta_1/\theta_2) + C_2(1 - P_1'\theta_1), \quad (\text{B.14b})$$

$$c = \theta_2^{-1} - P_1'(1 + \theta_1/\theta_2), \quad (\text{B.14c})$$

$$d = 1 + \theta_1/\theta_2. \quad (\text{B.14d})$$

The initial conditions are defined as

$$\mu(0) = 0, \quad (\text{B.15a})$$

$$\dot{\mu}(0) = \frac{P_1}{C_1}. \quad (\text{B.15b})$$

The solution of the differential equation is

$$\mu^{(0)}(t) = P_1(-B - C + Be^{-Dt} + Ce^{-Et}) \quad (\text{B.16})$$

where

$$B = \frac{C_1 db - 2ac - C_1 d\sqrt{b^2 - 4ac}}{2cC_1\sqrt{b^2 - 4ac}}, \quad (\text{B.17a})$$

$$C = \frac{-C_1 db + 2ac - C_1 d\sqrt{b^2 - 4ac}}{2cC_1\sqrt{b^2 - 4ac}}, \quad (\text{B.17b})$$

$$D = \frac{1}{2a} \left(b + \sqrt{b^2 - 4ac} \right), \quad (\text{B.17c})$$

$$E = \frac{1}{2a} \left(b - \sqrt{b^2 - 4ac} \right). \quad (\text{B.17d})$$

Now by fitting the experimental results using Eq. (B.16) we obtain the values of B , C , D and E . Then by solving the system of Eqs. (B.14) and (B.17) we estimate the values of θ_1 , θ_2 , C_1 and C_2 . In this manner we determine the intrinsic properties of the thermistor, i.e., its specific heat and its thermal resistance which sets the minimum thermal resistance in any measurement with thermistors. Tests were done to assess the quality of the second-order model. Results are shown in Figure B.9. The values obtained for θ_1 , θ_2 , C_1 and C_2 are given in Table B.2 for different sensors and configurations —see caption for details. The experimental data and the fit obtained by using Eq. (B.16) are in well agreement.

³The term $P(T)$ has been approximated in Taylor series at first order —see §B.1.

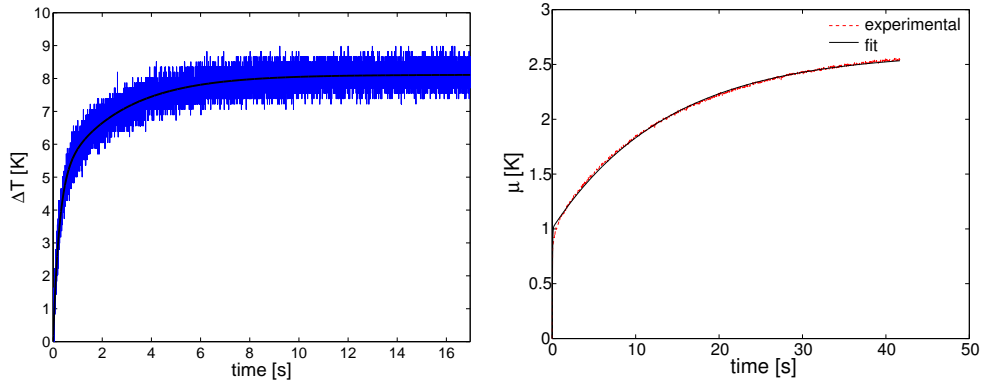


Figure B.9: Experimental data and fitted curve using Eq. B.16. Left: good thermal contact and 12 V. Right: poor thermal contact and 5 V. The obtained parameters are given in Table B.2.

Theoretically, θ_1 and C_1 should be the same under different scenarios since they are intrinsic properties of the thermistor and θ_2 and C_2 should change when attaching the thermistor in different manners. A measurement attaching the sensor with a poor thermal contact was performed in order to assess the *immutability* of the parameters θ_1 and C_1 and the dependence of θ_2 and C_2 with the attaching method. The experimental data and the fitted curve are shown in Figure B.9 (right panel). The fitted curve reproduces precisely the experimental data. Table B.2 shows the values obtained of θ_1 , θ_2 , C_1 and C_2 for the different tests. We notice how the values of θ_2 and C_2 change considerably when a poor contact is present in the measurement, whereas θ_1 and C_1 are still similar to the ones estimated with a good thermal contact.

sensor	[K W ⁻¹]		[mJ K ⁻¹]	
	θ_1	θ_2	C_1	C_2
2 k Ω (3 samples)	61 \pm 14	38 \pm 6.5	3.6 \pm 1	54 \pm 8.7
2 k Ω (p.c.)	86.5	124	3	100
10 k Ω (7 samples)	48 \pm 7.4	32 \pm 3.3	2.2 \pm 1.6	36 \pm 12

Table B.2: Parameters obtained for the fitted curves shown in Figures B.9. “p.c.” stands for poor thermal contact. It is clear that the parameters describing the contact are similar in all the cases except in the one with a poor thermal contact. The results are sound even though the estimated parameters are very sensitive to the accuracy in the determination of P_1 ($= v^2/R_i$).

The second-order model reproduces with excellent accuracy the temperature-time evolution of the thermistor. However, the results obtained using the first-order model are still useful and the results and conclusions obtained in §B.1 are valid anyway since the stationary state conditions are very well predicted by the first-order model and the error in the transient response is acceptable and of less importance.

In summary, the analysis presented herein concludes that thermistors are suitable to be used as heaters if low power is required. The heaters in the GRS will dissipate no more than 45 mW — see §7— which can be considered as “low power”. The thermistors used as heaters in the GRS will be of 2 k Ω of nominal resistance and they will be feed by means of a voltage source of 10 V. However, different aspects must be considered: (i) the unknown thermal resistance, θ , introduces a small error

in the power applied to the thermistor —see Figure B.5 (left); (ii) absolute temperature uncertainty causes an important error in the power dissipated by the thermistor —see Figure B.5 (right). This fact, though, should not be a problem since the temperature of the GRS is continuously measured by the $10\text{ k}\Omega$ thermistors. Therefore, prior to decide the voltage supplied to the thermistors it will be necessary to check the temperature in order to choose the adequate voltage value. (iii) at temperatures lower than $\simeq 20^\circ\text{C}$, 45 mW cannot be dissipated in the thermistor since the required voltage at those temperatures is higher than 10 V —see Figure B.6. The most unfavourable situation is at $T=10^\circ\text{C}$ where the maximum power is $\simeq 25\text{ mW}$ (assuming $\theta=100\text{ K W}^{-1}$).

Appendix C

Bit rate reduction

This appendix describes the digital downsampling (anti-alias filter + downsampling) to be implemented in the software of the data management unit (DMU) in order to reduce the bit rate of the thermal diagnostics in the data and diagnostic subsystem (DDS).

The sampling frequency of the thermal diagnostics is 1/1.2 Hz. The bit rate is calculated as

$$\begin{aligned} \textit{bit rate} &= \overbrace{[(4 \text{ byte} + 1 \text{ byte}) \cdot 24]}^{\text{absolute meas.}} + \overbrace{3 \text{ byte} \cdot 2}^{\text{heaters}} + \overbrace{4 \text{ byte} \cdot 12}^{\text{diff. and ref.}} + \overbrace{17 \text{ byte} \cdot 2}^{\text{headers}} \cdot 8 \cdot \frac{1}{1.2} \\ &= 800 \text{ bps} + 320 \text{ bps} + 226.67 \text{ bps} + 40 \text{ bps} = 1386.67 \text{ bps} \end{aligned} \quad (\text{C.1})$$

where the absolute, the differential and the reference measurements are 32 bit signed integers¹. The absolute measurement, in addition to the measurement data also includes the resistor reference used in the bridge, otherwise it would not be possible to convert the data to temperature —see §2.3.2.1. This adds an extra byte. The bytes used for the heaters contain information about the state and the voltage applied to them.

Such bit rate is considered too large taking into account that the measurement bandwidth of the system is from 1 mHz to 30 mHz. In order to reduce the bit rate the sampling frequency has been reduced by a factor of 4, i.e., 1/4.8=0.2083 Hz. Therefore, the bit rate is also reduced by a factor of 4, or

$$\textit{bit rate}_{41} = \frac{1386.67}{4} = 346.67 \text{ bps} \quad (\text{C.2})$$

A digital anti-alias filter has to be implemented prior to the downsampling in order to avoid aliasing. The chosen filter is a Butterworth of third order with a cut-off frequency of 80 mHz in order to respect the Nyquist criteria (the new sampling frequency is $\simeq 200$ mHz). The square modulus of the Butterworth filter is [105]

$$|H(\omega)|^2 = \frac{1}{1 + (\omega/\omega_c)^{2N}} \quad (\text{C.3})$$

where ω_c is the -3 dB frequency and N is the order of the filter. The filter is converted to the digital domain by use of the bilinear transform with frequency prewarping [105], i.e.,

$$s = i\omega = \frac{\omega_c}{\tan \pi \frac{\omega_c}{\omega_s}} \frac{z - 1}{z + 1} \quad (\text{C.4})$$

¹Actually, the useful data of each measurement is $\simeq 22$ bit ($\simeq 3$ byte), however, due to the available parameter types, for signed integers, defined by the LISA Pathfinder Packet Utilisation Standard [57] it is not possible to send packages of 3 bytes but of 4.

where ω_s ($= 2\pi/T_s$) is the sampling frequency (in rad s^{-1}) and ω_c is the angular cut off frequency of the filter. The digital filter is an IIR of the form

$$H(z) = \frac{Y(z)}{X(z)} = \frac{b_0 + b_1z^{-1} + b_2z^{-2} + b_3z^{-3}}{1 + a_1z^{-1} + a_2z^{-2} + a_3z^{-3}} \quad (\text{C.5})$$

and in the time domain is

$$y[n] = b_0x[n] + b_1x[n-1] + b_2x[n-2] + b_3x[n-3] - (a_1y[n-1] + a_2y[n-2] + a_3y[n-3]). \quad (\text{C.6})$$

For the case of the thermal diagnostics the coefficients of the filter with $f_s=1/1.2\text{ Hz}$ and $f_c=80\text{ mHz}$ are

$$\begin{aligned} a_1 &= -1.80858343266616, \\ a_2 &= +1.23230378937989, \\ a_3 &= -0.293244969120982, \\ b_0 &= +0.0163094234490924, \\ b_1 &= +0.0489282703472773 (= 3b_0), \\ b_2 &= +0.0489282703472773 (= b_1), \\ b_3 &= +0.0163094234490924 (= b_0). \end{aligned} \quad (\text{C.7})$$

The Bode plot of the filter is shown in Figure C.1. The plot in the right is a zoom of the filter response in the measurement bandwidth. It is clear that the signals in the measurement bandwidth are not attenuated and, also, that the phase is linear, which is very convenient for the thermal experiments proposed in the LTP —see §7.

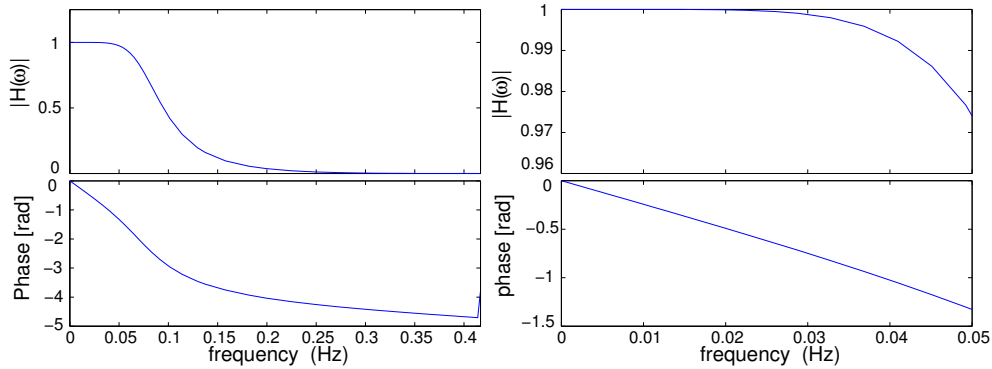


Figure C.1: Digital filter for the temperature measurements. Left: from 0 to $(1/1.2)/2\text{ Hz}$. Right: zoom of the MBW in the LTP. It is important to note that the phase is linear in the MBW which is needed in order to do meaningful thermal tests.

Once the filter is implemented the downsampling consists in dumping one out of four samples to the on board computer (OBC) mass memory where the downlink to Earth is managed.

The Butterworth filter algorithm needs CPU resources for its implementation, which raises the question of whether this will result in excess CPU loads. The answer to this is that the downsampling process is the one which really alleviates the CPU. Indeed, thermal data packages will be

produced 4 times less often. Managing a data package involves several operations, e.g., package creation, data accommodation, check-sums and dispatch to the bus, which are very significantly CPU demanding compared to the filter operations. The downsampling of the temperature measurements will free bandwidth that can be used for other subsystems.

Appendix D

Spectral density function for the fluctuating force due to magnetic disturbances

From

$$\delta F_x = V \langle \mathbf{M} \cdot \delta(\nabla B_x) \rangle + \frac{\chi V}{\mu_0} \langle \delta \mathbf{B} \cdot \nabla B_x \rangle + \frac{\chi V}{\mu_0} \langle \mathbf{B} \cdot \delta(\nabla B_x) \rangle \quad (\text{D.1})$$

the power spectral density of the force fluctuations, i.e., $S_{\delta F_x}(\omega)$, is to be determined. For simplicity let us assume Eq. (D.1) is only

$$\delta F_x = V \langle \mathbf{M} \cdot \delta(\nabla B_x) \rangle. \quad (\text{D.2})$$

Now we assume the temporal fluctuations of the magnetic field gradient, $\delta \nabla B_x$, are *homogeneous* across the TM volume, i.e.,

$$\delta F_x = V \langle \mathbf{M} \cdot \delta(\nabla B_x) \rangle = V \langle \mathbf{M} \rangle \cdot \delta(\nabla B_x). \quad (\text{D.3})$$

The spectral density function of Eq. (D.3) is defined by [13]

$$S_{\delta F_x}(\omega) = \int_{-\infty}^{\infty} R_{\delta F_x}(\tau) e^{-i\omega\tau} d\tau \quad (\text{D.4})$$

where $R_{\delta F_x}(\tau)$ is the auto-correlation function of δF_x , i.e.,

$$R_{\delta F_x}(\tau) = \mathcal{E}\{\delta F_x(t)\delta F_x(t+\tau)\}. \quad (\text{D.5})$$

Here, $\mathcal{E}\{\text{---}\}$ is the expectation value operator. Substituting Eq. (D.3) into Eq. (D.5) and assuming \mathbf{M} is a time independent quantity we obtain

$$R_{\delta F_x}(\tau) = V^2 \mathcal{E} \left\{ \sum_{i,j=1}^3 \langle M_i \rangle \langle M_j \rangle \delta \left(\frac{\partial B_x(t)}{\partial x_i} \right) \delta \left(\frac{\partial B_x(t+\tau)}{\partial x_j} \right) \right\}. \quad (\text{D.6})$$

We now assume cross-terms in Eq. (D.6) are uncorrelated and, consequently, cross-terms in Eq. (D.6) vanish:

$$R_{\delta F_x}(\tau) = V^2 \mathcal{E} \left\{ |\langle \mathbf{M} \rangle|^2 \sum_{i=1}^3 \delta \left(\frac{\partial B_x(t)}{\partial x_i} \right) \delta \left(\frac{\partial B_x(t+\tau)}{\partial x_i} \right) \right\}. \quad (\text{D.7})$$

Substituting Eq. (D.7) into Eq. (D.4) we obtain

$$S_{\delta F_x}(\omega) = V^2 |\langle \mathbf{M} \rangle|^2 \cdot S_{\nabla B_x}(\omega) \quad (\text{D.8})$$

assuming fluctuations in the components of the field gradient are equal (in power spectral density) and uncorrelated, or

$$S_{\partial B_x / \partial x_i} = S_{\partial B_x / \partial x}(\omega), \quad \text{for } i = 1, 2, 3. \quad (\text{D.9})$$

Mutatis mutandi, we obtain the same expression for: (i) the term $(\chi V / \mu_0) \langle \mathbf{B} \cdot \delta(\nabla B_x) \rangle$, where $\langle \mathbf{M} \rangle$ is substituted by $\langle \mathbf{B} \rangle$, and (ii) for the term $(\chi V / \mu_0) \langle \delta \mathbf{B} \cdot \nabla B_x \rangle$, where the constant term is $\langle \nabla B_x \rangle$ instead of $\langle \mathbf{M} \rangle$, and also assuming equality and uncorrelation of the fluctuations of the three components of the magnetic field:

$$S_{B_i}(\omega) = S_{B_x}(\omega), \quad \text{for } i = 1, 2, 3. \quad (\text{D.10})$$

By linearly adding these spectral density functions we obtain Eq. (3.8).

Appendix E

Insulator construction

The design and construction of the insulator is shown in the following pages. Figure E.1 shows the concept of the layout. Several slabs of polyurethane are used to build a cube that can be opened easily. Once all the pieces are joint, the cube is filled with insulating wool and the aluminium block is placed in the centre. The construction of the insulator is shown in Figure E.2. The aluminium block is shown in Figure E.3.

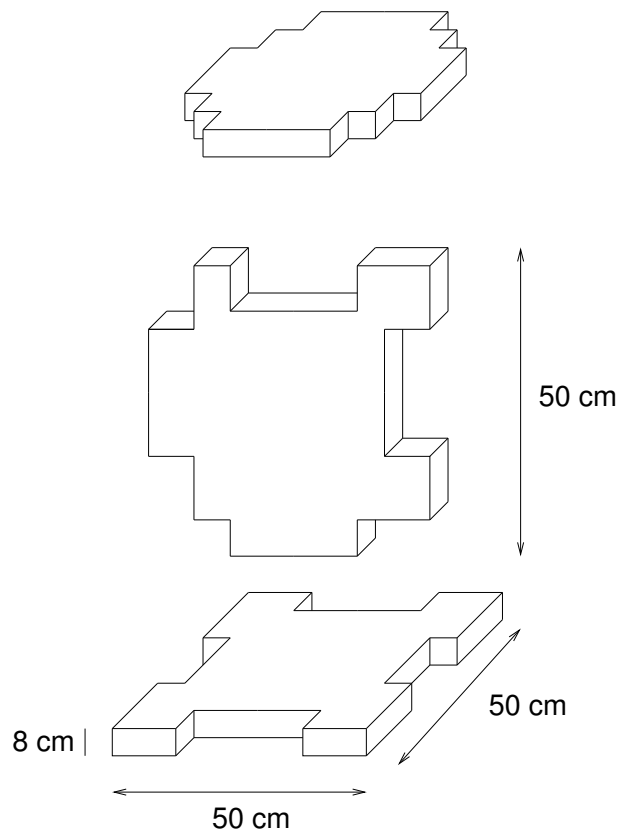


Figure E.1: Insulator jig design. Slabs of polyurethane are used to construct a cube which is filled with insulating wool. The slab in the middle is repeated four times.



Figure E.2: Construction of the insulator.

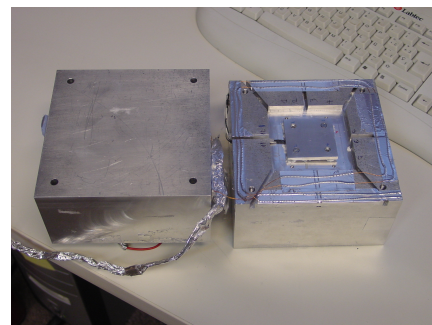
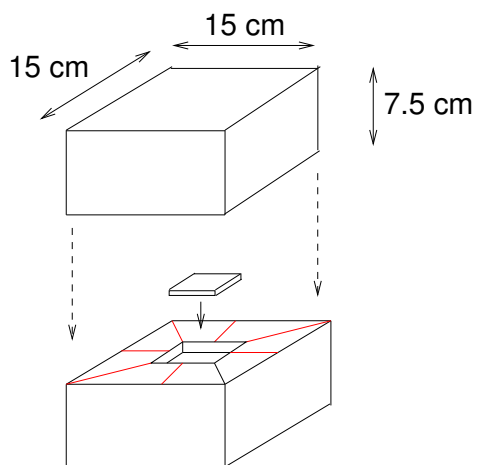


Figure E.3: Aluminium block. The temperature sensors are placed in the centre and pressed with a small lid. The block is placed in the centre of the polyurethane cube surrounded by insulating wool (Superwool 607).

Appendix F

Heater transfer function

In this appendix we describe the analysis to obtain the transfer function relating a heat pulse in a face on an aluminium block and the temperature increase along the block. First we find the transfer function in the frequency domain to, then, obtain the response of the system to a heat step in the time domain. The problem is shown in Figure 4.12. It is solved assuming linear flow in the x direction, i.e., the isothermal surfaces are planes parallel to $x = 0$, and the heat flow is unidirectional, the lines of heat flow being parallel to the x -axis. Under the conduction-only hypothesis, $T(x, t)$ satisfies Fourier's partial differential equation,

$$\rho c \frac{\partial^2 T(x, t)}{\partial x^2} = \kappa \frac{\partial T(x, t)}{\partial t}, \quad 0 \leq x \leq \ell \quad (\text{F.1})$$

where ρ , c , κ and T are the density, the specific heat, the thermal conductivity and the temperature of the aluminium block, respectively. Initial conditions are:

$$T = T_o(x) = 0, \quad t = 0, \quad 0 \leq x \leq \ell. \quad (\text{F.2})$$

The boundary conditions are defined on the basis of: (i) the heat flux in the surface at $x = 0$ is related with the total amount of power dissipated in the heater, P^1 , minus the power heating up the insulating material, P_2 ; and (ii) the surface at $x = \ell$ is adiabatic, i.e.,

$$-\kappa \left. \frac{\partial T(x, t)}{\partial x} \right|_{x=0} = \frac{1}{A} [P - P_2], \quad (\text{F.3a})$$

$$-\kappa \left. \frac{\partial T(x, t)}{\partial x} \right|_{x=\ell} = 0 \quad (\text{F.3b})$$

where A is the contact area of the heater with the aluminium block. The transfer function is calculated by taking advantage of the Laplace transform of Eqs. (F.1), (F.3a) and (F.3b).

F.1 Frequency-domain analysis

The equation of linear flow (in the s -domain) considering the initial conditions in Eq. (F.2) is:

$$\frac{d^2 \tilde{T}(x)}{dx^2} - q^2 \tilde{T}(x) = 0 \quad (\text{F.4})$$

¹ $P = V^2/R_h$ where $R_h=95 \Omega$ is the electrical resistance of the heater.

where $q^2 = s/K$ and $K = \kappa/\rho c$. The boundary conditions in the s-domain are

$$-\kappa \frac{d\tilde{T}(x)}{dx} \Big|_{x=0} = \frac{1}{A} \left[\tilde{P} - \tilde{T}(x=0) \left(\frac{1 + \theta C s}{\theta} \right) \right], \quad (F.5a)$$

$$-\kappa \frac{d\tilde{T}(x)}{dx} \Big|_{x=\ell} = 0. \quad (F.5b)$$

where θ and C are the lumped thermal models for the insulating material. The solution of Eq. (F.4) is

$$\tilde{T}(x) = C_1 e^{-qx} + C_2 e^{qx} \quad (F.6)$$

where C_1 and C_2 are calculated by using the boundary conditions given in Eqs. (F.5a) and (F.5b). They are:

$$C_1 = \tilde{P}\theta \frac{e^{q\ell}}{2[A\kappa\theta q \sinh q\ell + (q^2\theta KC + 1) \cosh q\ell]}, \quad (F.7a)$$

$$C_2 = \tilde{P}\theta \frac{e^{-q\ell}}{2[A\kappa\theta q \sinh q\ell + (q^2\theta KC + 1) \cosh q\ell]}. \quad (F.7b)$$

Substituting Eqs. (F.7a) and (F.7b) into Eq. (F.6) we obtain the transfer function which relates the power dissipated in the heater and the increase of temperature at any point of the aluminium block, i.e.,

$$H(x, s) = \frac{\tilde{T}(x, s)}{\tilde{P}(s)} = \theta \frac{\cosh q(\ell - x)}{A\kappa\theta q \sinh q\ell + (q^2\theta KC + 1) \cosh q\ell}. \quad (F.8)$$

F.2 Time-domain analysis

We are interested in the response of the system to a heat step (in time domain) at $x = \ell/2$. The power step is $\tilde{P} = P/s$, thus the temperature response is

$$\tilde{T}(x, s) = \frac{P\theta}{s} \frac{\cosh q(\ell - x)}{A\kappa\theta q \sinh q\ell + (q^2\theta KC + 1) \cosh q\ell}. \quad (F.9)$$

The time-domain response is obtained using the Inversion theorem which states that

$$T(t) = \frac{1}{i2\pi} \int_{\gamma-i\infty}^{\gamma+i\infty} e^{\lambda t} \tilde{T}(\lambda) d\lambda \quad (F.10)$$

where γ is to be so large that all the singularities of $\tilde{T}(\lambda)$ lie to the left of the line $(\gamma - i\infty, \gamma + i\infty)$. Applying the Inversion theorem to Eq. (F.10) leads to

$$T(t) = \frac{1}{i2\pi} \int_{\gamma-i\infty}^{\gamma+i\infty} \frac{e^{\lambda t}}{\lambda} \frac{\cosh \mu(\ell - x)}{A\kappa\theta \mu \sinh \mu\ell + (\mu^2\theta KC + 1) \cosh \mu\ell} d\lambda \quad (F.11)$$

where $\mu = \sqrt{\lambda/K}$.

The integral in Eq. (F.11) is solved by using the Cauchy theorem, i.e.,

$$\int_{\gamma-i\infty}^{\gamma+i\infty} \frac{e^{\lambda t}}{\lambda} \frac{\cosh \mu(\ell - x)}{A\kappa\theta \mu \sinh \mu\ell + (\mu^2\theta KC + 1) \cosh \mu\ell} d\lambda = i2\pi \sum_{n=0}^{\infty} \text{Residual}(\lambda_n) \quad (F.12)$$

where λ_n are the poles of the integrand. In our case the poles are

$$\lambda_0 = 0, \quad (F.13a)$$

$$\lambda_n = -\kappa\alpha_n^2, \mu = i\alpha_n, \quad n = 1, 2, 3, \dots \quad (F.13b)$$

where α_n for $n \neq 0$ are the roots of

$$\alpha_n \tan \alpha_n \ell = \frac{1 - \alpha_n^2 \theta K C}{\kappa A \theta}. \quad (\text{F.14})$$

Residues of λ_n are calculated as

$$\text{Residue}(\lambda_n) = \lim_{\lambda \rightarrow \lambda_n} \frac{e^{\lambda t}}{\lambda} \frac{\cosh \mu(\ell - x)}{A \kappa \theta \mu \sinh \mu \ell + (\mu^2 \theta K C + 1) \cosh \mu \ell} (\lambda - \lambda_n). \quad (\text{F.15})$$

Evaluation of Eq. (F.15) yields

$$\text{Residue}(\lambda_0) = 1, \quad n = 0, \quad (\text{F.16a})$$

$$\text{Residue}(\lambda_n) = \lim_{\lambda \rightarrow \lambda_n} \frac{e^{\lambda t}}{\lambda} \cosh \mu(\ell - x) \frac{1}{f'(\lambda_n)}, \quad n = 1, 2, 3, \dots \quad (\text{F.16b})$$

where

$$f(\lambda) = A \kappa \theta \mu \sinh \mu \ell + (\mu^2 \theta K C + 1) \cosh \mu \ell \quad (\text{F.17})$$

and

$$f'(\lambda_n) = \frac{1}{2K\mu} [\theta \mu (A \kappa \ell + 2K C) \cosh \mu \ell + (\ell + A \kappa \theta + \ell \theta K \mu^2 C) \sinh \mu \ell]. \quad (\text{F.18})$$

Substituting Eq. (F.18) into Eq. (F.16b) results in

$$\text{Residue}(\lambda_n) = \frac{-2e^{-K\alpha_n^2 t}}{\alpha_n} \frac{\cos \alpha_n(\ell - x)}{\theta \alpha_n (A \kappa \ell + 2K C) \cos \alpha_n \ell + (\ell + A \kappa \theta - \ell \theta K \alpha_n^2 C) \sin \alpha_n \ell}, \quad (\text{F.19})$$

and finally we find $T(t)$ by using Eqs. (F.11), (F.12), (F.16a) and (F.19),

$$T(x, t) = P\theta \left[1 - 2 \sum_{n=1}^{\infty} \frac{e^{-K\alpha_n^2 t}}{\alpha_n} \frac{\cos \alpha_n(\ell - x)}{\theta \alpha_n (A \kappa \ell + 2K C) \cos \alpha_n \ell + (\ell + A \kappa \theta - \ell \theta K \alpha_n^2 C) \sin \alpha_n \ell} \right] \quad (\text{F.20})$$

where

$$\alpha_n \tan \alpha_n \ell = \frac{1 - \alpha_n^2 \theta K C}{\kappa A \theta} \quad (\text{F.21})$$

Appendix G

Transfer functions and noise sources of the x -axis LTP dynamics

This appendix describes the transfer functions and noise sources [148, 147] used for the numerical simulations of the LTP x -axis dynamics together with some details related with the implementation in the Simulink software. The equations of motion of the system are given in §7.4. It is assumed that we are always working in the science mode (M3).

G.1 Drag-free control and low-frequency suspension

The spacecraft (SC) position is commanded by the position of the TM-1 with respect to the SC. This measurement is performed by the interferometer, o_1 . The control is performed by the drag-free (DF) subsystem which commands the thrusters of the SC. The drag-free transfer function is (in the s -domain):

$$H_{\text{DF}}(s) = \frac{0.0004659s^6 + 0.1349s^5 + 4.37s^4 + 0.8304s^3 + 0.07499s^2 + 0.002978s + 4.403 \cdot 10^{-5}}{s^6 + 5.046s^5 + 9.604s^4 + 11.05s^3 + 0.01221s^2 + 3.401 \cdot 10^{-6}} \quad (\text{G.1})$$

In the science mode, the position of TM-2 is controlled by means of the low-frequency suspension (LFS) control that forces TM-2 to follow TM-1. The force is exerted on TM-2 by means of the capacitive actuator in the GRS. The low-frequency suspension control transfer function is:

$$h_{\text{LFS}}(s) = \frac{-2.726 \cdot 10^{-7}s^3 + 1.665 \cdot 10^{-5}s^2 + 1.303 \cdot 10^{-7}s + 8.381 \cdot 10^{-10}}{s^4 + 0.2189s^3 + 0.01922s^2 + 7.803 \cdot 10^{-4}s} \quad (\text{G.2})$$

Figure G.1 shows these two transfer functions.

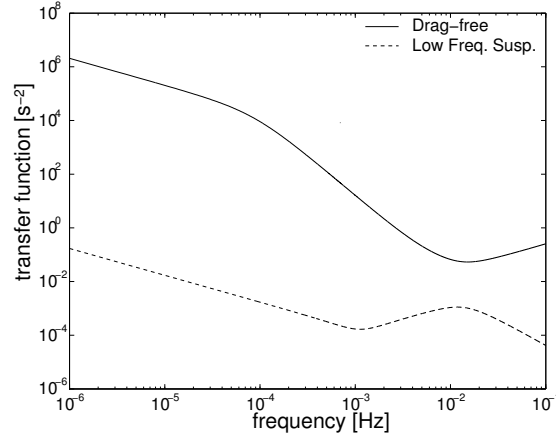


Figure G.1: Drag-free control and low-frequency suspension control transfer functions. These controls convert measurement of displacement in force (acceleration) to be exerted to the SC or to the TM-2.

G.2 Noise sources

The main sources of noise expected in the LTP are modelled in this section. Here we present the transfer functions used to generate the desired noise profile which is obtained by filtering white noise with the corresponding transfer functions. First, we have to consider the internal forces perturbing TM-1. They are modeled as:

$$g_1(s) = \sqrt{\frac{0.5}{10.089}} \cdot 30 \cdot 10^{-15} \frac{(s + 2\pi(3 \cdot 10^{-3}))(s + 2\pi 10^{-4})}{(s + 2\pi 10^{-6})(s + 2\pi 10^{-7})} \quad (\text{G.3})$$

and we assume that the internal forces in TM-1 and TM-2 exhibit the same (but uncorrelated) fluctuations, thus, the transfer function is the same for both TMs, i.e.,

$$g_2(s) = g_1(s) \quad (\text{G.4})$$

The forces perturbing the SC are modeled as:

$$G_{\text{SC}}(s) = \frac{10^{-7}}{436} \frac{(s + 2\pi 10^{-2})(s + 2\pi 10^{-4})}{(s + 2\pi 10^{-6})(s + 2\pi 10^{-7})} \quad (\text{G.5})$$

Figure G.2 shows the acceleration noise (in terms of PSD) due to the forces perturbing the SC and the internal disturbances perturbing the TMs. The theoretical and numerical simulations are shown.

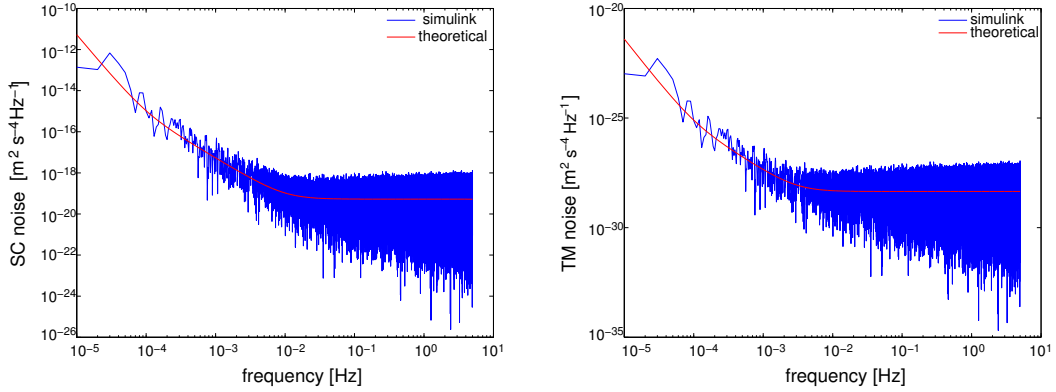


Figure G.2: Left: SC acceleration noise. Right: TMs acceleration noise. Note that the noise perturbing the SC is orders of magnitude higher than the stray forces in the TM.

The noise of the interferometer is modelled by (for both channels, o_1 and o_Δ) —see Figure G.3:

$$o_{n1,n\Delta}(s) = \sqrt{0.5} \cdot 5 \cdot 10^{-12} \frac{(s + 2\pi \cdot 10^{-2})(s + 2\pi \cdot 3.33 \cdot 10^{-4})}{(s + 2\pi \cdot 10^{-6})(s + 2\pi \cdot 10^{-7})} \quad (\text{G.6})$$

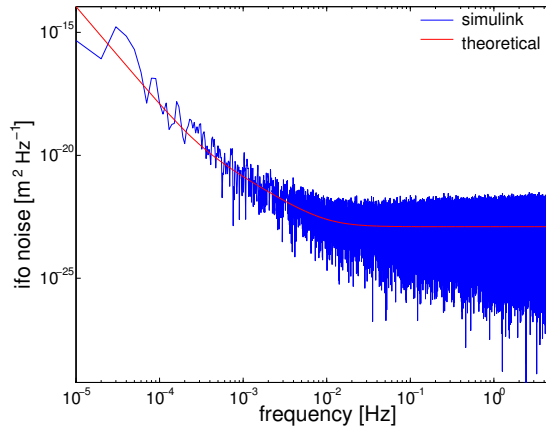


Figure G.3: Interferometer noise (o_{n1} and o_{n12}).

G.3 Closed-loop transfer functions and noise apportioning

In this section we show the closed-loop transfer functions (both in position and acceleration) in the drag-free control and low-frequency suspension control. Then, the noise contribution of each source to the total displacement (or acceleration) is broken down for the two measurements, o_1 and o_Δ .

G.3.1 Drag-free control: o_1

Figure G.4 shows the closed-loop transfer functions in terms of displacement (left) and acceleration (right) in the drag-free control system. They are obtained by evaluation of Eqs. (7.54) and (7.58). See caption for details.

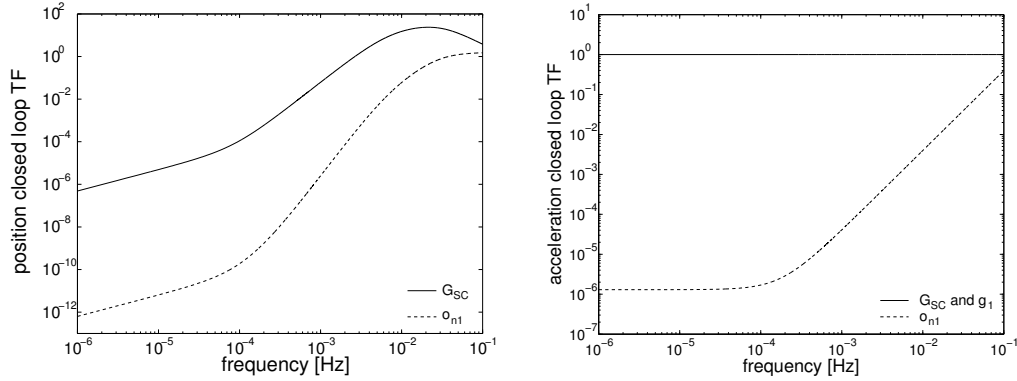


Figure G.4: Drag-free control. Left: closed-loop transfer functions in terms of position. The solid trace is the transfer function that relates force on the SC, G_{SC} , and displacement of TM-1 with respect to the SC. This function is the one accompanying the term G_{SC} in Eq. (7.54). The dashed trace is the same for the noise of the interferometer which is also feedbacked and appears in the measurement through this transfer function. Right: *idem* for the case of the acceleration. The solid trace ($=1$) is applied to G_{SC} and g_1 , this means, that the acceleration of the SC and TM-1 appear in the measurement of acceleration as they were in open-loop. The noise of the interferometer, o_{n1} , is filtered by the dashed trace to appear as acceleration noise in the read out.

Figure G.5 shows the noise apportioning of the total displacement (panel in the left) and of the total acceleration (panel in the right) noise in the SC/TM-1 system.

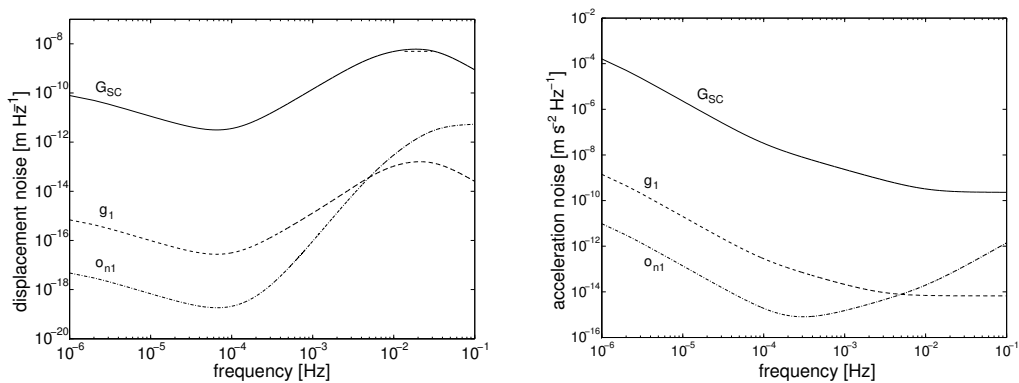


Figure G.5: Measurement o_1 (and a_1). Left: apportioning of the noise sources in the measurement o_1 . The noise sources have been defined in §G.2. Right: *idem* in terms of acceleration. In both cases the forces perturbing the SC are the ones that dominate the measurement.

G.3.2 Low-frequency suspension control: o_{Δ}

This section is exactly the same that shown in §G.3.1 but for the low-frequency suspension and the differential measurement case. Figure G.6 shows the closed-loop transfer functions in terms of displacement (left) and acceleration (right) involved in the low-frequency suspension control. They are obtained by evaluation of Eqs. (7.56) and (7.59). See caption for details.

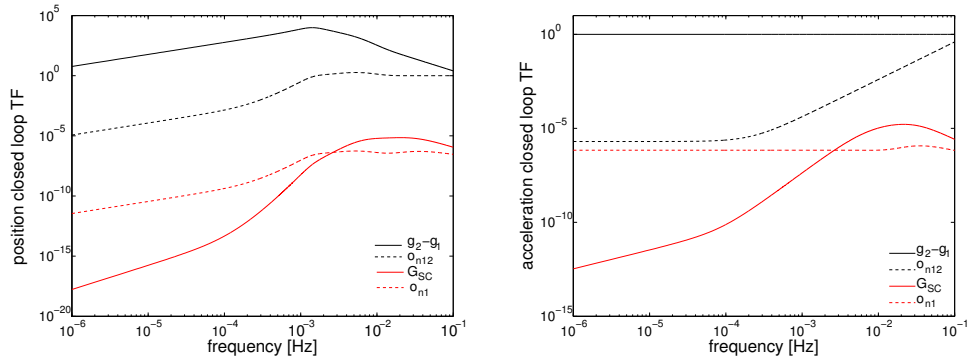


Figure G.6: Low-frequency suspension. Left: the solid black trace is the transfer function that converts forces acting on TM-1 and TM-2 into o_{Δ} . The dashed black trace is the same for the noise of the interferometer. The red traces, ideally, should both be zero since the forces perturbing the SC are common for both TMs and, thus, the differential measurement should reject them all. However, due to the stiffness mismatch the common mode is not fully rejected. The same applies to the noise of the interferometer o_{n1} : due to cross-talk between the measurement o_1 and o_{Δ} , the former leaks into the latter. These two effects should not contribute in a noticeable manner in the differential measurement. Right: *idem* for the acceleration measurement, a_{Δ} . The differential forces perturbing both TMs appear with unity gain in the measurement whereas the forces perturbing the SC are well attenuated.

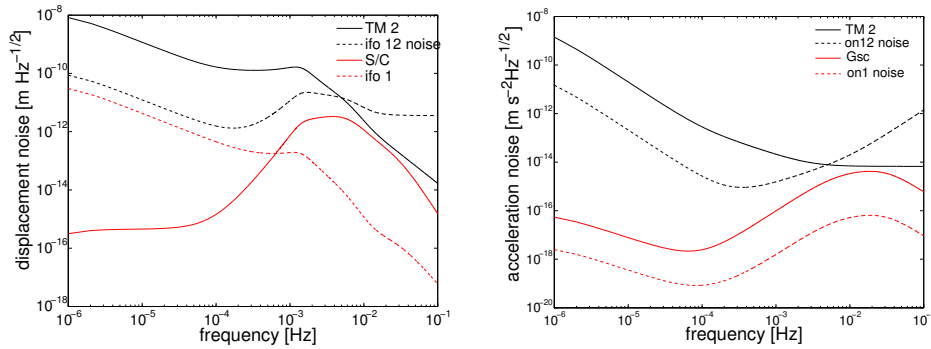


Figure G.7: Differential measurement, o_{Δ} . Left: apportioning of the noise sources in the measurement o_{Δ} . Right: *idem* in terms of acceleration. At low-frequency the differential acceleration measurement is dominated by the internal forces in the TMs. For $f \gtrsim 3$ mHz the noise of the interferometer is the one limiting the measurement. The sum of the solid and dashed black traces one results in the typical noise curve required/expected for the LTP. The forces perturbing the SC are well attenuated and should not contribute significantly to the differential measurement.

G.4 DF and LFS controls: implementation in discrete domain

The drag-free control, however, is a discrete system. In this section we give the expressions in the z -domain. The transfer functions in the s -plane have been converted to the z -domain by means of the bilinear transform. The sampling frequency is 10 Hz for both control systems. The drag-free control was implemented in three stages in cascade, otherwise the filter became unstable, i.e.,

$$H_{DF}(z) = kH_1(z)H_2(z)H_3(z) \quad (\text{G.7})$$

where

$$\begin{aligned} k &= 0.0004659 \\ H_1(z) &= \frac{1.00356822789509 - 1.99988233906499z^{-1} + 0.996328288186069z^{-2}}{1 - 1.99988942603276z^{-1} + 0.999889429113384z^{-2}} \\ H_2(z) &= \frac{0.909149649134965 - 1.80755075311414z^{-1} + 0.898465712564196z^{-2}}{1 - 1.79146095571032z^{-1} + 0.823705159102989z^{-2}} \\ H_3(z) &= \frac{33.5832877231938 + 38.6438243582394z^{-1} + 8.5245978657927z^{-2}}{1 - 1.73203061537316z^{-1} + 0.732030615373157z^{-2}} \end{aligned} \quad (\text{G.8})$$

The LFS is implemented in the discrete domain as:

$$H_{lfs}(z) = 10^{-8} \frac{2.770671 + 2.699583z^{-1} - 8.234474z^{-2} - 2.699578z^{-3} + 5.463807z^{-4}}{1 - 3.978157334z^{-1} + 5.934663271z^{-2} - 3.934853767z^{-3} + 0.9783478304z^{-4}} \quad (\text{G.9})$$

The digital implementation of H_{DF} and h_{lfs} in comparison with the theoretical ones are shown in Figure G.8.

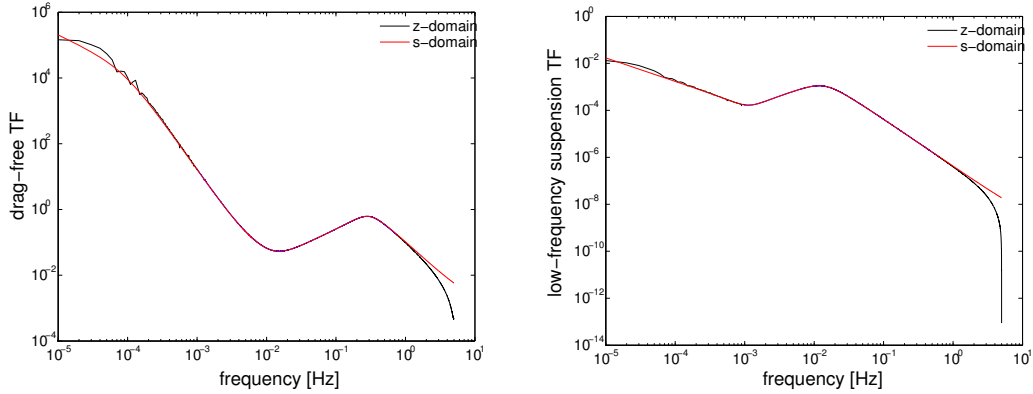


Figure G.8: Left: drag-free control, H_{DF} , implementation in the z -domain. Right: *idem* for the low-frequency suspension control, h_{lfs} .

Imperfections in the actuators commanded by the outputs of the drag-free control and low-frequency suspension control have been also included in the model. They are basically a delay plus a low-pass filter.

G.5 Position to acceleration conversion

The output obtained through the simulations is the read out of the interferometer, i.e., o_1 and o_Δ . However, we are interested in the acceleration since we want to estimate the forces perturbing the TMs. The conversion from displacement to acceleration has been performed by using the scheme shown in Figure G.9 —see Eqs. (7.57a) and (7.57b).

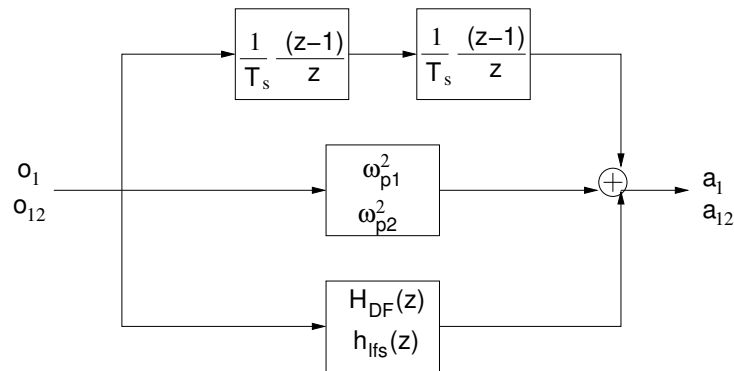


Figure G.9: Position to acceleration: $o_{1,\Delta} \rightarrow a_{1,\Delta}$. $(1/T_s)(z-1)/z$ is a simple discrete derivative.

Bibliography

- [1] A Abramovici *et al.* LIGO: the laser interferometer gravitational-wave observatory. *Science*, 256:325–333, 1992.
- [2] F Acernese *et al.* Status of VIRGO detector. *Class. Quantum Grav.*, 24:S381–S388, 2007.
- [3] Y Acker *et al.* The VIRGO interferometer for gravitational wave detection. *Nucl. Phys. B*, 54B:167–175, 1997.
- [4] OD Aguiar *et al.* The gravitational wave detector Mario Schenberg: status of the project. *Brazilian Journal of Physics*, 32:866–869, 2002.
- [5] S Anza *et al.* The LTP experiment on the LISA Pathfinder mission. *Class. Quantum Grav.*, 22:S125–S138, 2005.
- [6] H Araújo *et al.* LISA and LISA pathfinder, the endeavour to detect low frequency GWs. *J. Phys: Conf. Ser.*, 66:012003, 2007.
- [7] M Armano *et al.* LISA Pathfinder: the experiment and the route to LISA. *Class. Quantum Grav.*, 26(9):094001, 2009.
- [8] P Arpaia, P Daponte, and L Michaeli. Influence of the architecture on ADC error modeling. *IEEE Trans. Instrum. Meas.*, 48(5):956–966, 1999.
- [9] P Astone *et al.* The gravitational wave detector NAUTILUS operating at $T=0.1$ K. *Astroparticle physics*, 7:231–243, 1997.
- [10] P Astone *et al.* The EXPLORER gravitational wave antenna: recent improvements and performances. *Class. Quantum Grav.*, 19:1905–1910, 2002.
- [11] E Balestrieri, P Daponte, and S Rapuano. A state of the art on ADC error compensation methods. *IEEE Trans. Instrum. Meas.*, 54(4):1388–1394, 2005.
- [12] J Bechhoefer. Feedback for physicists: a tutorial essay on control. *Rev. Mod. Phys.*, 77(3):783–836, 2005.
- [13] JS Bendat and AG Piersol. *Random data: analysis & measurement procedures*. John Wiley & Sons, 2000.
- [14] P Bender *et al.* LISA for the detection and observation of gravitational waves. Pre-phase A. Technical Report 244, Max Plank für Quantenoptik, 1998.
- [15] E Berti, A Buonanno, and CM Will. Testing general relativity and probing the merger of massive black holes with LISA. *Class. Quantum Grav.*, 22:S943–S954, 2005.
- [16] Betatherm Ireland ltd. Ballybrit Business Park, Galway, Ireland.

- [17] DG Blair *et al.* High sensitivity gravitational wave antenna with parametric transducer readout. *Phys. Rev. Lett.*, 74(11):1908–1911, 1995.
- [18] D Bortoluzzi *et al.* Testing LISA drag-free control with the LISA technology package flight experiment. *Class. Quantum Grav.*, 20:S89–S97, 2003.
- [19] B Brannon. Overcoming converter nonlinearities with dither. Technical report, Analog Devices, Inc., 1995.
- [20] JA Burgos. DAU design description. Technical Report S2-NTE-RP-3012 v1.1, NTE, 2006.
- [21] X Canalias. Technical Report LTP-IEEC-1185-MagACEdata, IEEC, 2003.
- [22] JC Candy and GC Temes. *Oversampling delta-sigma data converters : theory, design, and simulation*. IEEE Press, 1999.
- [23] L Carbone. *Ground based investigation of force noise sources for LISA*. PhD thesis, Universtà degli studi di Trento, 2005.
- [24] P Carbone, C Narduzzi, and D Petri. Dither signal effects on the resolution of nonlinear quantisers. *IEEE Trans. Instr. Meas.*, 43(2):139–145, 1994.
- [25] L Carbone *et al.* Characterisation of disturbance sources for LISA: torsion pendulum results. *Class. Quantum Grav.*, 22:S509–S519, 2005.
- [26] L Carbone *et al.* Thermal gradient-induced forces on geodetic reference masses for LISA. *Phys. Rev. D*, 76:102003, 2007.
- [27] HS Carslaw and JC Jaeger. *Conduction of heat in solids*. Oxford University Press, 1986.
- [28] PNR Childs, JR Greenwood, and CA Long. Review of temperature measurement. *Rev. Sci. Instrum.*, 71(8):2959–2978, 2000.
- [29] TCP Chui, DR Swanson, MJ Adriaans, JA Nissen, and JA Lipa. Temperature fluctuations in the canonical ensemble. *Phys. Rev. Lett.*, 69(21):3005–3008, 1992.
- [30] MG Cooper, BB Mikic, and MM Yovanovich. Thermal contact conductance. *Int. J. Heat Mass Transfer*, 12:279–300, 1969.
- [31] RJ Cruz, JI Thorpe, M Hartman, and G Mueller. Time delay interferometry using the UF LISA benchtop simulator. *AIP Conf. Proc.*, 873:319–325, 2006.
- [32] K Danzmann. Laser interferometric gravitational wave detectors. *Proceedings of the Thirteenth International Conference on General*, pages 3–20, 1992.
- [33] K Danzmann and A Rüdiger. LISA technology—concept, status, prospects. *Class. Quantum Grav.*, 20:S1–S9, 2003.
- [34] R Davis. Magnetic susceptibility (d.c.) of FM TMs and EM TM. Technical Report S2-BIP-TR-3001, Bureau International des Poids et Mesures (BIPM).
- [35] P Day, I Hahn, TCP Chui, AW Harter, D Rowe, and JA Lipa. The fluctuation-imposed limit for temperature measurement. *J. of Low Temp. Phys.*, 107(3-4):359–370, 1997.
- [36] A de Waard *et al.* MiniGRAIL progress report 2004. *Class. Quantum Grav.*, 22:S215–S219, 2005.
- [37] M Devlin *et al.* A dc-coupled high-sensitivity bolometric detector system for the infrared telescope in space. *IEEE Trans. Nucl. Sci.*, 40(2):162–165, 1993.

- [38] D DiBartolomeo and JH Klems. Simple phase-sensitive detector for wheatstone bridge resistance measurements. *Rev. Sci. Instrum.*, 56(5):755–757, 1985.
- [39] R Dolesi *et al.* Gravitational sensor for LISA and its technology demonstration. *Class. Quantum Grav.*, 20(S99-S108), 2003.
- [40] J Dratler. A proportional thermostat with 10 microdegree stability. *Rev. Sci. Instrum.*, 45(11):1435–1444, 1974.
- [41] TJ Edwards. Observations on the stability of thermistors. *Rev. Sci. Instrum.*, 54(5):613–617, 1983.
- [42] JR Engstrom and WH Weinberg. Design and construction of a digital temperature controller for use in surface studies. *Rev. Sci. Instrum.*, 55(3):404–409, 1984.
- [43] CC Enz and GC Temes. Circuit techniques for reducing the effects of op-amps imperfections: autozeroing, correlated double sampling, and chopper stabilisation. *Proceedings of the IEEE*, 84(11):1584–1614, 1996.
- [44] ESA. ESCC qualified part list. Technical report, ESA, 2009.
- [45] RD Esman and DL Rode. 100- μ K temperature controller. *Rev. Sci. Instrum.*, 54(10):1368–1370, 1983.
- [46] V Fafone. Resonant-mass detectors: status and perspectives. *Class. Quantum Grav.*, 21:S377–S383, 2004.
- [47] WM Folkner *et al.* Disturbance reduction system: testing technology for precision formation control. *Proceedings of SPIE*, 4860:221–228, 2003.
- [48] EM Forgan. On the use of temperature controllers in cryogenics. *Cryogenics*, 14(4):207–213, 1974.
- [49] S Franco. *Design with operational amplifiers and analog integrated circuits*. McGraw-Hill, 2001.
- [50] A Franzoso. Assessment on the DDS heaters power on the electrode housing. Technical Report S2-CGS-TN-3013, CGS, 2005.
- [51] A Franzoso. LISA core assembly thermal analysis report. Technical Report S2-CGS-TN-3031, CGS, 2007.
- [52] G Frossati. Ultra-low temperature resonant gravitational wave detectors. present and future prospects. *Adv. Space Res.*, 32:1227–1232, 2003.
- [53] H Fu *et al.* A high-resolution thermometer for the range 1.6 to 5 K. *J. of Low Temp. Phys.*, 111:49–71, 1998.
- [54] S Gaertner *et al.* A new readout system for bolometers with improved low frequency stability. *Astron. Astrophys. Suppl. Ser.*, 126:151–160, 1997.
- [55] JR Gair *et al.* Event rate estimates for LISA extreme mass ratio capture sources. *Class. Quantum Grav.*, 21:S1595–S1606, 2004.
- [56] M Galeazzi *et al.* Non-ideal effects in doped semiconductor thermistors. *Ninth International Workshop on Low Temperature Detectors. AIP Conference Proceedings*, 605:83–86, 2002.
- [57] H García. DMU software ICD. Technical Report S2-NTE-ICD-3004, NTE, 2008.

- [58] AF García Marín. *Minimisation of optical pathlength noise for the detection of gravitational waves with the spaceborne laser interferometer LISA and LISA Pathfinder*. PhD thesis, AEI, Hannover, 2007.
- [59] RM Gray and TG Stockham. Dithered quantisers. *IEEE Trans. Inf. Theory*, 39(3):805–812, 1993.
- [60] B Guillet, D Robbes, and L Méchin. Low noise temperature control: Application to an active cavity radiometer. *Rev. Sci. Instrum.*, 74(1):243–249, 2003.
- [61] G Heinzel *et al.* Interferometry for the LISA technology package (LTP) aboard SMART-2. *Class. Quantum Grav.*, 20:S153–S161, 2003.
- [62] G Heinzel *et al.* The LTP interferometer and phasemeter. *Class. Quantum Grav.*, 21:S581–S587, 2004.
- [63] CW Helstrom. *Statistical theory of signal detection*. Pergamon Press, 1968.
- [64] IS Heng. Allegro: noise performance and the ongoing search for gravitational waves. *Class. Quantum Grav.*, 19:1889–1895, 2002.
- [65] S Higuchi *et al.* High-stability temperature control for ST-7/LISA Pathfinder gravitational reference sensor ground verification testing. *Journal of Physics: Conference Series*, 32:125–131, 2006.
- [66] DF Hoeschele. *Analog-to-digital and digital-to-analog conversion techniques*. John Wiley & Sons, 1994.
- [67] M Hueller. *Geodesic motion of LISA test masses: development and testing of drag-free position sensors*. PhD thesis, Università degli Studi di Trento, 2003.
- [68] SA Hughes. Listening to the universe with gravitational-wave astronomy. *Ann. Phys. (NY)*, 303:142–178, 2003.
- [69] RA Hulse and JH Taylor. Discovery of a pulsar in a binary system. *Astrophys. J. Lett.*, 195:L51–L53, 1975.
- [70] Cygnal Integrated Products Inc. Improving ADC resolution by oversampling and averaging. Technical report, 2001.
- [71] FP Incropera and DP DeWitt. *Fundamentals of heat and mass transfer*. John Wiley & Sons, 2002.
- [72] Innovative sensor technology, IST AG. Industriestrasse 2, 9630 Wattwil, Switzerland.
- [73] JD Jackson. *Classical electrodynamics*. John Wiley & Sons, 1998.
- [74] PGA Jespers. *Integrated converters*. Oxford University Press, 2001.
- [75] W Kester. *Practical design techniques for sensor signal conditioning*. Analog Devices Inc., 1999.
- [76] W Kester. *Analog-digital conversion*. Analog Devices Inc., 2004.
- [77] B Lange. *The control and use of drag-free satellites*. PhD thesis, SUDAER, 1964.
- [78] KM Lawton and SR Patterson. A high-stability air temperature control system. *Elsevier: Precision Engineering*, 24:174–182, 2000.

- [79] KM Lawton and SR Patterson. Long-term relative stability of thermistors. *Elsevier: Precision Engineering*, 25:24–28, 2001.
- [80] KM Lawton and SR Patterson. Long-term relative stability of thermistors: Part 2. *Elsevier: Precision Engineering*, 26:340–345, 2002.
- [81] X Llamas. DDS design description. Technical Report S2-NTE-RP-3002 v2.2, NTE, 2006.
- [82] X Llamas. DDS design specification. Technical Report S2-NTE-DS-3001 v1.3, NTE, 2006.
- [83] A Lobo. DDS science requirements document. Technical Report S2-IEEC-RS-3002, IEEC, 2005.
- [84] A Lobo, M Nofrarias, J Ramos-Castro, and J Sanjuán. On-ground tests of the LISA Pathfinder thermal diagnostic system. *Class. Quantum Grav.*, 23:5177–5193, 2006.
- [85] JA Lobo. Effect of a weak plane GW on a light beam. *Class. Quantum Grav.*, 9:1385–1394, 1992.
- [86] JA Lobo *et al.* In-flight diagnostics in LISA Pathfinder. *AIP Conference Proceedings*, 873, 2006.
- [87] H Lück *et al.* Status of the GEO600 detector. *Class. Quantum Grav.*, 23:S71–S78, 2006.
- [88] TT Lyons, MW Regehr, and FJ Raab. Shot noise in gravitational-wave detectors with Fabry-Perot arms. *Appl. Opt.*, 39(36):6761–6770, 2000.
- [89] F Marc, D Dallet, and Y Danto. Fault and diagnosis on a successive approximation ADC. *Instrumentation and Measurement Technology Conference*, 2(19-21):1460–1463, 1997.
- [90] D McCammon *et al.* $1/f$ noise in doped semiconductor thermistors. *Low temperature detectors. AIP Conference proceedings*, 605:91–94, 2002.
- [91] BJ Meers. Recycling in laser-interferometric gravitational-wave detectors. *Phys. Rev. D*, 38(8):2317–2326, 1988.
- [92] L Michaeli, P Michalko, and J Sálga. Unified ADC nonlinearity error model for SAR ADC. *Measurement, Elsevier*, 41:198–204, 2008.
- [93] CW Misner, KS Thorne, and JA Wheeler. *Gravitation*. WH Freeman and Company, 1973.
- [94] CD Motchenbacher and JA Connelly. *Low-noise electronic design*. John Wiley & Sons, 1993.
- [95] J Neylon. ESA/SCC qualification report for NTC thermistors. Technical report, BetaTherm Ireland Ltd., 2001.
- [96] AM Nobili, D Bramanti, G Comandi, and R Toncelli. Radiometer effect in space missions to test the equivalence principle. *Phys. Rev. D*, 63, 2001.
- [97] M Nofrarias. *Thermal diagnostic in the LISA technology package experiment*. PhD thesis, Universitat de Barcelona, 2007.
- [98] M Nofrarias, AF García Marín, A Lobo, G Heinzl, J Ramos-Castro, J Sanjuán, and K Danzmann. Thermal diagnostic of the optical window on board LISA Pathfinder. *Class. Quantum Grav.*, 24:5103–5121, 2007.
- [99] M Nofrarias and J Sanjuán. Thermal experiments on board the LTP. Technical Report S2-IEC-TN-3042 v0.5, IEEC, 2009.

- [100] AV Oppenheim, RW Schafer, and JR Buck. *Discrete-time signal processing*. Prentice-Hall, 1999.
- [101] R Pallàs and JG Webster. *Sensors and signal conditioning*. John Wiley & Sons, 2000.
- [102] R Pallàs and JG Webster. *Analog signal processing*. John Wiley & Sons, 2001.
- [103] A Papoulis. *Probability, random variables, and stochastic processes*. McGraw-Hill, 1985.
- [104] CL Phillips and RD Harbor. *Feedback control systems*. Prentice Hall, 1996.
- [105] JG Proakis and DK Manolakis. *Digital signal processing*. Prentice Hall, 1996.
- [106] J Ramos-Castro and J Sanjuán. DDS thermal diagnostic prototype design. Technical Report S2-UPC-DDD-3001, UPC, 2005.
- [107] J Ramos-Castro and J Sanjuán. Temperature sensors and FEE prototype test report. Technical Report S2-IIEEC-TR-3001, IIEEC, 2005.
- [108] D Reitze. Ground based GW detectors (presentation). 7th International LISA Symposium, Barcelona, Spain, 2008.
- [109] F Ricci and A Brillet. A review of gravitational wave detectors. *Annual Review of Nuclear and Particle Science*, 47:111–156, 1997.
- [110] JP Rice *et al.* Antenna-coupled high Tc air-bridge microbolometer on silicon. *Appl. Phys. Lett.*, 65(6):773–775, 1994.
- [111] FM Rieke, AE Lange, JW Beeman, and EE Haller. An ac bridge readout for bolometric detectors. *IEEE Trans. Nucl. Sci.*, 36(1):946–949, 1989.
- [112] D Robertson *et al.* LTP interferometer - noise sources and performance. *Class. Quantum Grav.*, 22:S155–S163, 2005.
- [113] J Sanjuán. Diagnostic-DAUs interface configuration. Technical Report S2-IEC-TN-3023 v1.4, IIEEC.
- [114] J Sanjuán. Feasibility analysis of using a NTC thermistor as a heater on the IS and the OW. Technical Report S2-IEC-TN-3022 v1.0, IIEEC.
- [115] J Sanjuán. Noise performance test report for the DMU thermal diagnostic subsystem. Technical Report S2-IEC-TR-3064 v1.0, IIEEC, 2008.
- [116] J Sanjuán. Noise performance test report for the FM DMU thermal diagnostic subsystem. Technical Report S2-IEC-TR-3068 v1.0, IIEEC, 2008.
- [117] J Sanjuán, J Ramos-Castro, and A Lobo. ADC non-linear errors correction in thermal diagnostics for the LISA mission. submitted to *Rev. Sci. Instrum.*, 2009.
- [118] J Sanjuán, J Ramos-Castro, and A Lobo. Extension of the LTP temperature diagnostics to the LISA band: first results. *Class. Quantum Grav.*, 26(9):094009, 2009.
- [119] J Sanjuán, J Ramos-Castro, A Lobo, M Nofrarias, and PJ Riu. Thermal diagnostics front-end electronics for LISA Pathfinder. *Rev. Sci. Instrum.*, 78, 2007.
- [120] J Sanjuán *et al.* Magnetic polarization effects of temperature sensors and heaters in LISA pathfinder. *Rev. Sci. Instrum.*, 79:084503, 2008.
- [121] M Sapoff and RM Oppenheim. Theory and application of self-heated thermistors. *Proceedings of the IEEE*, 51(10):1292–1305, 1963.

- [122] P Sarra. DDS thermistors gas load measurements. Technical Report S2-CGS-TN-3035 v1.0, CGS, 2007.
- [123] RW Scarr and RA Settingington. Thermistors, their theory, manufacture and application. *IRE Transactions on Components Parts*, 8(1):6–22, 1961.
- [124] A Schnabel, L Trounoux, and E Balaguer. LTP EM TM remnant magnetic moment measurements. Technical Report S2-EST-TR-3002, ESA-ESTEC, 2007.
- [125] L Schuchman. Dither signals and their effect on quantisation noise. *IEEE Trans. Comm. Tech.*, 12(4):162–165, 1964.
- [126] BL Schumaker. Disturbance reduction requirements for LISA. *Class. Quantum Grav.*, 20:S239–S253, 2003.
- [127] BF Schutz. Gravitational waves on the back of an envelope. *Am. J. Phys.*, 52(5), 1984.
- [128] JH Scofield. A frequency-domain description of a lock-in amplifier. *Am. J. Phys.*, 62(2):129–133, 1994.
- [129] FW Sears and MW Zemansky. *College Physics*. Addison-Wesley, 1991.
- [130] D Sigg *et al.* Status of the LIGO detectors. *Class. Quantum Grav.*, 25, 2008.
- [131] MLC Sing, E Lesquey, C Dolabdjian, and D Robbes. A high stability temperature controller based on a superconducting high-Tc sensor. *IEEE Transactions on Applied Superconductivity*, 7(2):3087–3090, 1997.
- [132] B Snaith, PW O’Callaghan, and SD Probert. Interstitial materials for controlling thermal conductances across pressed metallic contacts. *Applied Energy*, 16:175–191, 1984.
- [133] JS Steinhart and SR Hart. Calibration curves for thermistors. *Deep Sea Res.*, 15:497–503, 1968.
- [134] A Stroeer and A Vecchio. The LISA verification binaries. *Class. Quantum Grav.*, 23:S809–S817, 2006.
- [135] R Takahashi *et al.* Status of TAMA300. *Class. Quantum Grav.*, 21:S403–S408, 2004.
- [136] JH Taylor, LA Fowler, and PM McCullough. Measurements of general relativistic effects in the binary pulsar PSR1913 + 16. *Nature*, 277:437–440, 1979.
- [137] JH Taylor and JM Weisberg. A new test of general relativity: gravitational radiation and the binary pulsar PSR1913 + 16. *Astrophys. J.*, 253:908–920, 1982.
- [138] Advanced LIGO team. Advanced LIGO reference design. Technical Report LIGO-060056-08-M, Caltech, MIT, LIGO Hanford, LIGO Livingston, 2007.
- [139] M Tinto, DA Shaddock, J Sylvestre, and JW Armstrong. Implementation of time-delay interferometry for LISA. *Phys. Rev. D*, 67:122003, 2003.
- [140] M Tröbs and G Heinzel. Improved spectrum estimation from digitized time series on a logarithmic frequency axis. *Measurement*, 39:120–129, 2006.
- [141] L Trounoux. Impact of LTP thermal diagnostics on magnetic acceleration budget. Technical Report S2-EST-TN-3026, ESA-ESTEC, 2008.
- [142] L Trounoux. Personal communication, February 2008.

- [143] RP Tye. *Thermal conductivity*. Academic Press, 1969.
- [144] PKM Unni, MK Gunasekaran, and A Kumar. $\pm 30 \mu\text{K}$ temperature controller from 25 to 103°C : study and analysis. *Rev. Sci. Instrum.*, 74(1):231–242, 2003.
- [145] S Vitale. LISA technology package architect final report. Technical Report ESTEC contract no. 15580/01/NL/HB, Università degli Studi di Trento, 2002.
- [146] S. Vitale. LISA pathfinder report. Technical Report LTPA-UTN-ScRD-Iss003-Rev1, Università degli Studi di Trento, 2005.
- [147] S Vitale. Measurement of differential acceleration noise on LISA Pathfinder. Technical Report S2-UTN-TN-3053 v1.0, Università degli Studi di Trento, 2007.
- [148] S Vitale. Measurement of LTP dynamical coefficients by system identification. Technical Report S2-UTN-TN-3045 v1.1, Università degli Studi di Trento, 2007.
- [149] MF Wagdy. Effect of various dither forms on quantization errors of ideal A/D converters. *IEEE Trans. Instr. Meas.*, 38(4):850–855, 1989.
- [150] MF Wagdy. Correction of capacitor errors during the conversion cycle of self calibrating A/D converters. *IEEE Transactions on Circuits and Systems*, 1990.
- [151] MF Wagdy. Linearizing average transfer characteristics of ideal ADCs via analog and digital dither. *IEEE Trans. Instr. Meas.*, 43(2):146–150, 1994.
- [152] MF Wagdy. Effect of additive dither on the resolution of ADCs with single-bit or multibit errors. *IEEE Trans. Instr. Meas.*, 45(2):610–615, 1996.
- [153] RA Wannamaker, SP Lipshitz, J Vanderkooy, and JN Wright. A theory of nonsubtractive dither. *IEEE Transactions on Signal Processing*, 48(2):499–516, 2006.
- [154] C Warren. Personal communication, February 2009.
- [155] D Wealthy. LTP mission performance budgets. Technical Report S2-ASU-RP-2007, ASU, 2004.
- [156] J Weber. Detection and generation of gravitational waves. *Phys. Rev.*, 117:306–313, 1960.
- [157] J Weber. Evidence for discovery of gravitational radiation. *Phys. Rev. Letters*, 22:1320–1324, 1969.
- [158] P Welander *et al.* A new small nano-kelvin resolution thermometer for low temperature experiments. *Instrumentation and measurement technology conference, 1999. Proceedings of the 16th IEEE*, 1:413–416, 1999.
- [159] T Wilbanks, M Devlin, AE Lange, S Sato, JW Beeman, and EE Haller. Improved low-frequency stability of bolometric detectors. *IEEE Transactions on Nuclear Science*, 37(2):566–572, April 1990.
- [160] H Yamamoto *et al.* The development of high sensitivity NTC thermistors. *Proc. of the ninth IEEE international symposium on Applications of ferroelectrics*, pages 735–738, 1994.
- [161] F Yang, L Mechin, J-M Routoure, and B Guillet. Low-noise LaSrMnO thermometers for uncooled bolometric applications. *J. Appl. Phys.*, 99, 2006.
- [162] J-P Zendri *et al.* Status report and near future prospects for the gravitational wave detector AURIGA. *Class. Quantum Grav.*, 19:1925–1933, 2002.
- [163] VD Zubakov and LA Wainstein. *Extraction of signals from noise*. Dover, 1962.